LBL-3500
c.1

INTERFEROMETRY OF ELECTROCHEMICAL MASS TRANSFER BOUNDARY LAYERS

Frank Raymond McLarnon
(Ph. D. thesis)

December 1974

Prepared for the U. S. Atomic Energy Commission
under Contract W-7405-ENG-48

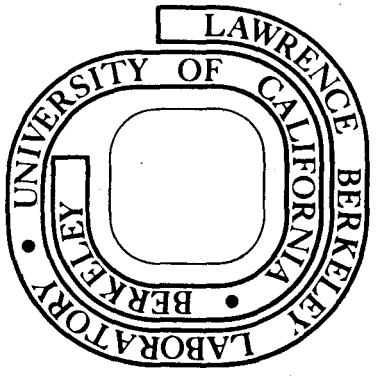

LBL-3500
c.1

DISCLAIMER

I dedicate this work to the memory of my sister

Jane McLarnon-Browne

INTERFEROMETRY OF ELECTROCHEMICAL MASS TRANSFER BOUNDARY LAYERS

Contents

INTERFEROMETRY OF ELECTROCHEMICAL MASS TRANSFER BOUNDARY LAYERS*

Frank Raymond McLarnon

Inorganic Materials Research Division, Lawrence Berkeley Laboratory and Department of Chemical Engineering; University of California Berkeley, Calififfornia 94720

ABSTRACT

A travelling, double-beam interferometer has been used to study the development of electrochemical mass transfer boundary layers along horizontal electrodes in a rectangular duct. The interferometric fringe patterns (interferograms) of refractive-index fields formed by constant-current Cu deposition from 0.1 M $CuSO_4$ were converted to $CuSO_4$ concentration profiles.

When interferograms are obtained from boundary layers in which the refractive-index varies between the bulk electrolyte and interface, refraction causes the light beam to curve in the direction of increasing index. Conventional interpretation of such interferograms, which assumes light propagation along a straight line, leads to serious errors in the evaluation of the concentration field. Reflection from the even slightly rounded edge of a planar surface has been identified as another source of error. These optical aberrations are accounted for in new iterative methods for the quantitative interpretation of interferograms, and the practical limitations and capabilities of interferometry are defined. Graphical correlations are also presented for a practical range of variables to facilitate convenient estimation of errors incurred due to light-deflection. Studies of transient diffusion layers served to verify portions of the optical analysis.

---

*Ph. D. Thesis, research conducted under the direction of R. H. Muller and C. W. Tobias.

Investigations of the concentration boundary layers in laminar flow at downward-facing and upward-facing electrodes revealed the expected two modes of mass transfer control: forced convention and combined free and forced convection, respectively. Transient and steady-state boundary layer thicknesses and interfacial concentrations for laminar forced convection derived from interferograms show good agreement with asymptotic solutions to the convective diffusion equation. Onset of natural convection effects is correlated with a critical Rayleigh Number.

A comparative study of turbulent forced convection boundary layers demonstrates the practicality of increasing mass transfer rates by using small obstacles on the surface to promote local turbulence in an otherwise laminar stream.

INTRODUCTION

Industrial electrochemical processes are generally carried out at low current densities because of slow liquid-phase mass transport. Forced convection (e.g., in brine electrolysis) or natural convection (e.g., in copper plating) is employed to enhance mass transfer rates. The limiting current technique is the standard method in the experimental analysis of problems involving ionic transport to and from electrodes. However, this method gives no direct information about the nature of mass transfer processes at current densities of practical significance, i.e., below the limiting current.

Interferometry is an alternative to the limiting current technique that provides direct visualization of the concentration boundary layer at any current level. The interferogram gives (a) quantitative information about local current density, interfacial concentration and boundary layer thickness in two-dimensional concentration fields and (b) qualitative information about three-dimensional concentration fields, such as those occurring in combined forced and free convection.

The prupose of this work was two-fold: (1) to define the practical capabilities and limitations of the interferometric technique and (2) to use the method to study convective electrochemical mass transfer boundary layers. K. W. Beach* began this project by constructing the flow channel and interferometer and describing the light-deflection effects that complicate interpretation of interferograms.

---

*K. W. Beach, Optical Methods for the Study of Convective Mass Transfer Boundary Layers on Extended Electrodes (Ph. D. Thesis), UCRL-20324, July 1971.

Chapter 1 describes the experimental set-up and explains the operation of the system. An optical analysis of the light-deflection problem is presented in Chapter 2. Part 2.1 presents the various methods for solution of the problem and part 2.2 illustrates the large errors that can result if light-deflection effects are neglected. Part 2.3 presents a numerical iterative method for the interpretation of interferograms and discusses the useful range and limitations of interferometry.

Chapter 3 examines another problem in the quantitative interpretation of interferograms: reflection from the even slightly rounded edge of the electrode surface. Surprisingly large distortions can result from this optical aberration.

The results of an experimental study of the transient diffusion layers associated with constant-current electrolysis are presented in Chapter 4. This work provides experimental verification of parts of the optical analysis given in Chapter 2.

Chapter 5 gives the results of an experimental study of convective electrochemical mass transfer boundary layers. Part 5.1 contains an interferometric analysis of laminar forced convection mass transfer boundary layers, and part 5.2 examines the effects of laminar natural convection superimposed on forced convection. Part 5.3 presents a comparative study of turbulent boundary layers. Turbulence induced by small promoters attached to the electrode surface is compared to that due to increased electrolyte flow rate.

1. EXPERIMENTAL

All interferometric experiments were carried out using the flow channel and interferometer built and described[1,2] by K. W. Beach. The channel and interferometer are described briefly in part 1.1; the reader who seeks more detailed descriptions should consult Refs. 1 and 2. The special electrode preparation required to minimize edge reflection (Chapter 3) is described in part 1.2. Part 1.3 deals with electrolyte preparation and correlation of refractive-index with electrolyte concentration. Part 1.4 explains the operation of the interferometer and the method of beam alignment.

1.1. The Flow Channel and Interferometer

The three meter long flow channel is shown in part in Figs. 1 and 2. Gravity feed from a storage tank (which can be pressurized) provides an even flow of electrolyte to the rectangular duct for Reynolds Numbers up to at least 10,000. A cross-sectional sketch of the duct is shown in Fig. 1 of Chapter 4: the duct is 1.00 cm wide and 2.54 cm high, and the electrodes fully occupy the space between the two parallel optically flat glass sidewalls. Seventy hydraulic diameters (d_e = 1.44 cm) of entry length are provided, where lucite replaces copper upstream of the 1.00 meter long electrodes. Table 1 gives the relationship between average flow velocity and Reynolds Number for this flow channel, using the density and viscosity of 0.1 M $CuSO_4$ at 25°C (see Ref. 3 and part 1.3).

A cross-section of the modified Mach-Zehnder interferometer is also depicted in Fig. 1 of Chapter 4. Note that the He-Ne laser is specially modified to emit light (at λ = 632.8) nm from each end. Interferograms are recorded on Kodak 7278 Tri-X film in a Bolex Pillard 16 mm movie camera,

Table 1. Reynolds Numbers for various volume average flow velocities through the duct.

Average Flow Velocity v(cm/s)	Reynolds Number Re = $\rho v d_e / \mu$
0.70	100
3.49	500
6.98	1,000
10.5	1,500
13.9	2,000
34.9	5,000
69.8	10,000

which is mounted on a micrometer slide to permit reproducible positioning.

1.2. Electrode Preparation

The copper electrodes were designed with two goals in mind: (a) the electrode working surfaces should be flat and smooth and (b) the test beam should traverse the cell parallel to the working surface. These requirements suggested the following scheme: polish one side of each electrode flat and optically smooth. Then, construct a right-angle polishing jig and prepare the electrode working surfaces perpendicular to the reflecting sides. Align the cell so that the test beam strikes the reflecting side of an electrode at exactly normal incidence (check that the reflected beam retraces its path back to the laser light source), and the beam will then traverse the cell parallel to the working surface.

The original 99.999% pure copper metal was milled to form a pair of bars 1.0 meter long, 1.0 cm wide and 3.8 cm high. One side (3.8×100 cm) of each bar was polished in three stages as detailed in Table 2. The resulting reflecting surface profiles were measured with a profileometer[4] and are depicted in Fig. 3a and 3c. These surfaces were then coated with urethane for protection; and the profiles of the coated surfaces are shown in Fig. 3b and 3d. The localized scratches visible in Fig. 3b and 3d were caused by the use of the polishing jig to prepare the electrode working surfaces (the jig rides against the reflecting surface, see Fig. 5), and the humps were caused by unequal draining of the urethane coating while it dried. The test beam is usually reflected from the coated side surface about 5 mm away from the edge of the electrode working surface, where the profile is flat to within 0.03°.

Table 2. Polishing procedures for the electrode side surfaces.

Stage #	Abrasive	Rubbing Material	Holder for Rubbing Material
1	Brilliantshine Metal Polish (Ref. 5)	#250, #400 carbide paper	A flat, rectangular metal block slightly smaller than the 3.8 cm electrode height (to avoid edge rounding).
2	1-5 μm chromium oxide powder (Ref. 6) with kerosene as a carrier	#600 carbide paper	Same as Stage 1
3	1 μm Diamond Polishing Compound (Ref. 6) with kerosene as a carrier	A fine polishing cloth	A rotating metal cylinder, its flat contact surface diameter slightly smaller than the 3.8 cm electrode height.

The right-angle polishing jig is shown in Fig. 4 and its use is illustrated in Fig. 5. Note that the Teflon® legs of the jig ride against parts of the polished side of the electrode that are not used for reflection. Carbide paper can be used as a course abrasive material on the face of the jig, and chromium oxide on paper with kerosene can be used as a fine abrasive. The resulting electrode working surface profiles are shown in Fig. 6. The profiles are not perfectly flat, and the consequences of this are discussed in Chapter 3. The overall accuracy of the beam alignment parallel to the electrode working surfaces is limited by the flatness of the reflecting and working surface profiles and the resolution of the reflected test beam at its original source. The estimated overall accuracy is ±0.1°.

1.3. Electrolyte Preparation

Aqueous $CuSO_4$ electrolyte was prepared by mixing reagent grade $CuSO_4 \cdot 5H_2O$ crystals with twice-distilled water in a 25 gallon polyethylene container. The solution was agitated and sparged with inert gas (e.g., argon) until all of the crystals were dissolved. Selected physical properties[3] of $CuSO_4$ electrolytes are listed in Table 3.

The dependence of electrolyte refractive-index on $CuSO_4$ concentration was determined by preparing a small batch of 1.0 M electrolyte as above and diluting portions to samples of different concentration. The refractive-index of each sample was measured with an Abbe critical angle refractometer, and the concentration of each sample was found by gravimetric analysis. Linear correlations of measured refractive-index vs concentration are presented in Fig. 7 for two wavelengths: sodium

Table 3. Physical properties[3] of the $CuSO_4$ electrolyte at 25°C.

C (M $CuSO_4$)	ρ (gm/cm^3)	μ/μ_{water}
0	0.997	1.0
0.009	0.999	1.007
0.284	1.041	1.200

yellow (λ = 589.2 nm) and that of the He-Ne laser (λ = 632.8 nm) for the range $0 \leq C \leq 0.2$ M at 25°C. For the range $0 \leq C \leq 0.1$ M, a least squares analysis provides the linear correlations shown in Fig. 7:

$$\lambda = 589.2 \text{ nm}: \quad n = 1.33238 + 0.0294 \cdot C \tag{1}$$

$$\lambda = 632.8 \text{ nm}: \quad n = 1.33110 + 0.0290 \cdot C \tag{2}$$

The actual measured value of refractive-index for water was 1.33243 at the sodium yellow wavelength, which may be compared to the value of 1.33250 given in Landolt-Boernstein[7] for the same wavelength and temperature. Equation (2) is used to correlate refractive-index with $CuSO_4$ concentration throughout this thesis. A polynomial correlation for the range $0 \leq C \leq 1.0$ m $CuSO_4$ has been presented elsewhere.[8] Figure 8 illustrates the measured variations of aqueous $CuSO_4$ refractive-indices with light wavelength.

1.4. System Operation

A step-by-step procedure is presented for the operation of the interferometer and flow channel.

1. Electrode preparation. Use the right-angle polishing jig with mild detergent solution to clean and polish the electrode working surfaces (see Fig. 5). Insure that the glass walls and flow channel are clean.

2. Assemble the flow channel and check for leaks. Turn on the laser and check the film in the camera.

3. Align the channel in its lengthwise (flow) direction. Adjust the cell jacks until the electrode/electrolyte interface is visible through the

camera as the interferometer is moved from one end of the electrode to the other.

4. Lower or raise the channel until the test beam strikes the reflecting face of an electrode and adjust the cell jacks until the beam is reflected right back to its source at the laser head. Repeat steps 3 and 4 until both criteria are met. The accuracy of this alignment is about 0.03°.

5. Adjust the interference fringes until they appear perpendicular to the electrode/electrolyte interface, as described by Beach.[1]

6. Focus the camera by moving it back and forth on its micrometer slide until a suitable target appears in focus. For the observation of cathodic concentration boundary layers (refractive-index decreasing near the electrode surface), the recommended[1] plane focus is on the inside of the glass wall farther from the camera. Eleven sets of scale lines spaced 10 cm apart in the horizontal direction have been inscribed on this wall for ease of focusing. The lines are spaced 0.5 mm apart in the vertical direction to provide a calibration for distance on the interferogram. See Chapter 3 for details on the determination of the true electrode/electrolyte interface location by variation of the plane of focus.

7. Set the electrolyte flow rate and pass current through the cell.

8. The resulting interferograms can be recorded on 16 mm movie film and analyzed later by projecting the film onto a table. An example is shown in Fig. 9, in which the above-mentioned scale lines are visible. The phase depicted by the interferogram can be directly related

to electrolyte concentration by the following well-known equation:[9]

$$\Delta C = \frac{N\lambda}{w \frac{dn}{dC}} \tag{3}$$

or,

$$\Delta C/N = 0.002182 \text{ M/fringe} \tag{4}$$

The numerical value 0.002182 was determined using Eq. (2) for the value of dn/dC.

REFERENCES

1. K. W. Beach, Optical Methods for the Study of Convective Mass Transfer Boundary Layers on Extended Electrodes (Ph. D. Thesis), UCRL-20324, July 1971. K. W. Beach, R. H. Muller and C. W. Tobias J. Opt. Soc. Am. 63, 559 (1973).
2. K. W. Beach, R. H. Muller and C. W. Tobias, Rev. Sci. Instr. 40, 1248 (1969).
3. T. W. Chapman and J. S. Newman, A Compliation of Selected Thermodynamic and Transport Properties of Binary Electrolytes in Aqueous Solution, UCRL-17767, May 1968, pp. 37-39.
4. Surfanalyzer 150 System, Clevite Corporation, El Monte, CA.
5. Afta Solvents Corporation, San Francisco, CA.
6. Buehler Ltd, Evanston, Illinois.
7. W. A. Roth and K. Scheel, eds., Landolt-Boernstein, Physikatisch-Chemische Tabellen (Springer Verlag, Berlin, 1923), p. 28512.
8. Inorganic Materials Research Division, Annual Report 1971 (LBL-425), p. 39.
9. R. H. Muller in Advances in Electrochemistry and Electrochemical Engineering, R. H. Muller, ed. (Wiley-Interscience, New York, 1972), Vol. 9, pp. 326-353.

NOMENCLATURE

C	concentration (M $CuSO_4$)
d_e	hydraulic diameter (cm)
n	refractive-index
N	phase change (fringes)
Re	Reynolds Number
v	average velocity (cm/s)
w	electrode width (cm)
λ	light wavelength (nm)
μ	viscosity ($gm\text{-}cm^{-1}\text{-}s^{-1}$)
ρ	density ($gm\text{-}cm^{-3}$)

FIGURE CAPTIONS

Fig. 1. End view of the flow channel and interferometer. The interferometer is mounted on a lathe bed to permit travel of the instrument along the length of the electrodes.

Fig. 2. Side view of the electrodes and interferometer with one glass sidewall installed in the flow channel.

Fig. 3. Electrode reflecting surface profiles. These profiles were measured at z = 50 cm from the electrode leading edges, but they are similar at other locations.

Abscissa: distance parallel to the electrode reflecting surface (cm)

Ordinate: distance normal to the electrode reflecting surface (μm)

The electrode working surface is perpendicular to the reflecting surface and is located at the indicated origin of the abscissa scale. The origins of the ordinate scales are at arbitrary locations.

a Upper electrode after final polishing

b Upper electrode after coating

c Lower electrode after final polishing

d Lower electrode after coating

Fig. 4. The right-angle polishing jig.

Fig. 5. Polishing the lower electrode working surface with the right-angle polishing jig.

Fig. 6. Electrode working surface profiles.

Abscissa: distance parallel to the electrode working surface (cm)

Ordinate: distance normal to the electrode working surface (μm)

These profiles were measured at z = 50 cm from the electrode leading edges, but they are similar at other locations. The electrode reflecting surface is perpendicular to the working surface and is located at the indicated origin of the abscissa scale. The origins of the ordinate scales are at arbitrary locations.

a Upper electrode working surface after final polishing

b Lower electrode working surface after final polishing

Fig. 7. Linear correlation of refractive-index with electrolyte concentration.

o o o refractive-index vs concentration data for sodium yellow (λ = 589.2 nm) light source.

• • • refractive-index vs concentration data for a He-Ne laser (λ = 632.8 nm) light source.

_____ linear correlations for the range $0 \leq C \leq 0.1$ M $CuSO_4$ (see text).

Fig. 8. Variation of electrolyte refractive-index with light wavelength.

Ordinate: measured refractive-index

Abscissa: light wavelength (nm)

■ 0.602 M $CuSO_4$

▲ 0.2009 M $CuSO_4$

▲ 0.0829 M $CuSO_4$

○ 0.0419 M $CuSO_4$

● 0 M $CuSO_4$ (water)

Fig. 9. Measurement of interferograms.

Vertical scale determined by etched markings (separated by 0.5 mm). Each fringe spacing along the vertical line corresponds to one wavelength of phase difference.

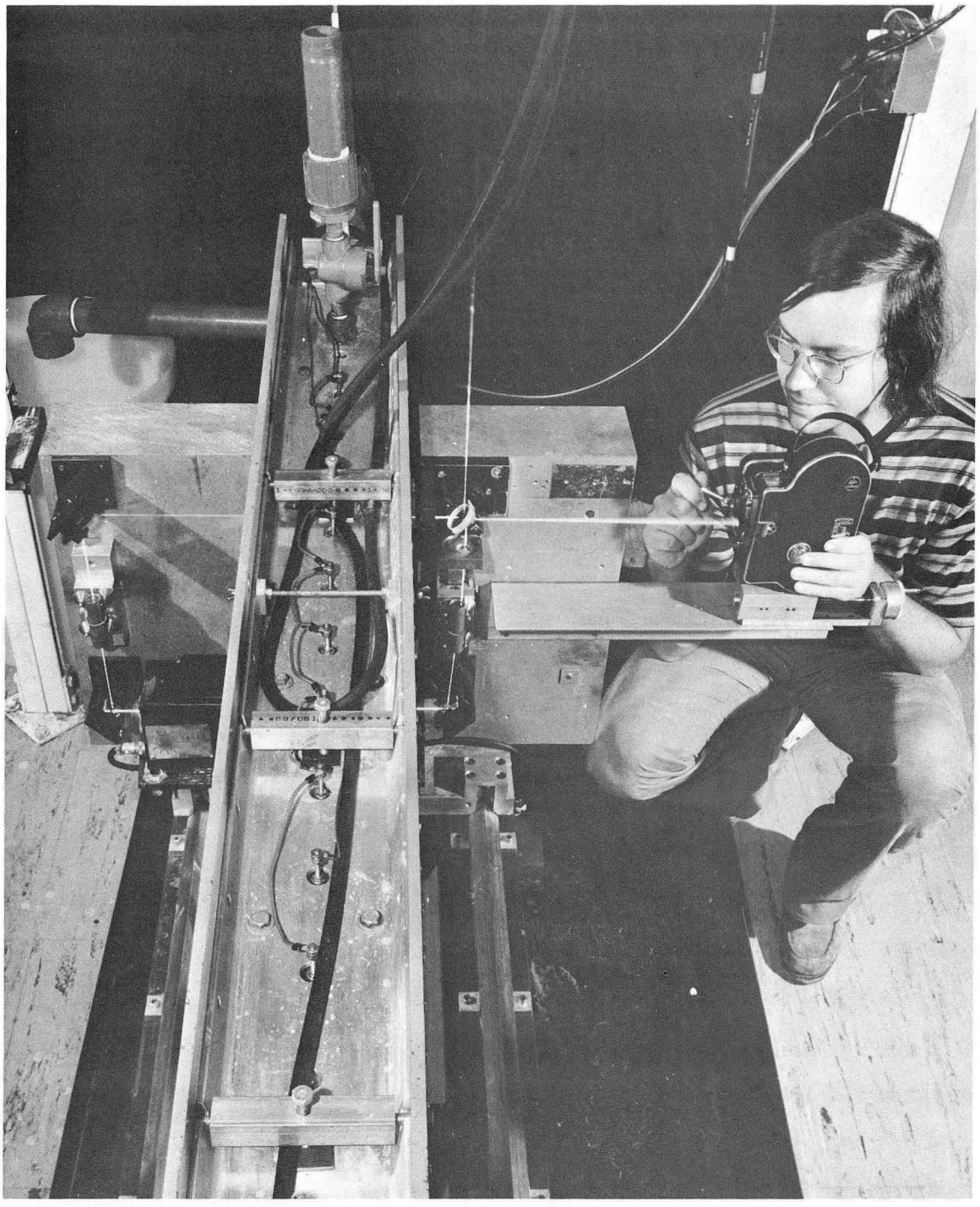

CBB 7410-7137

Fig. 1

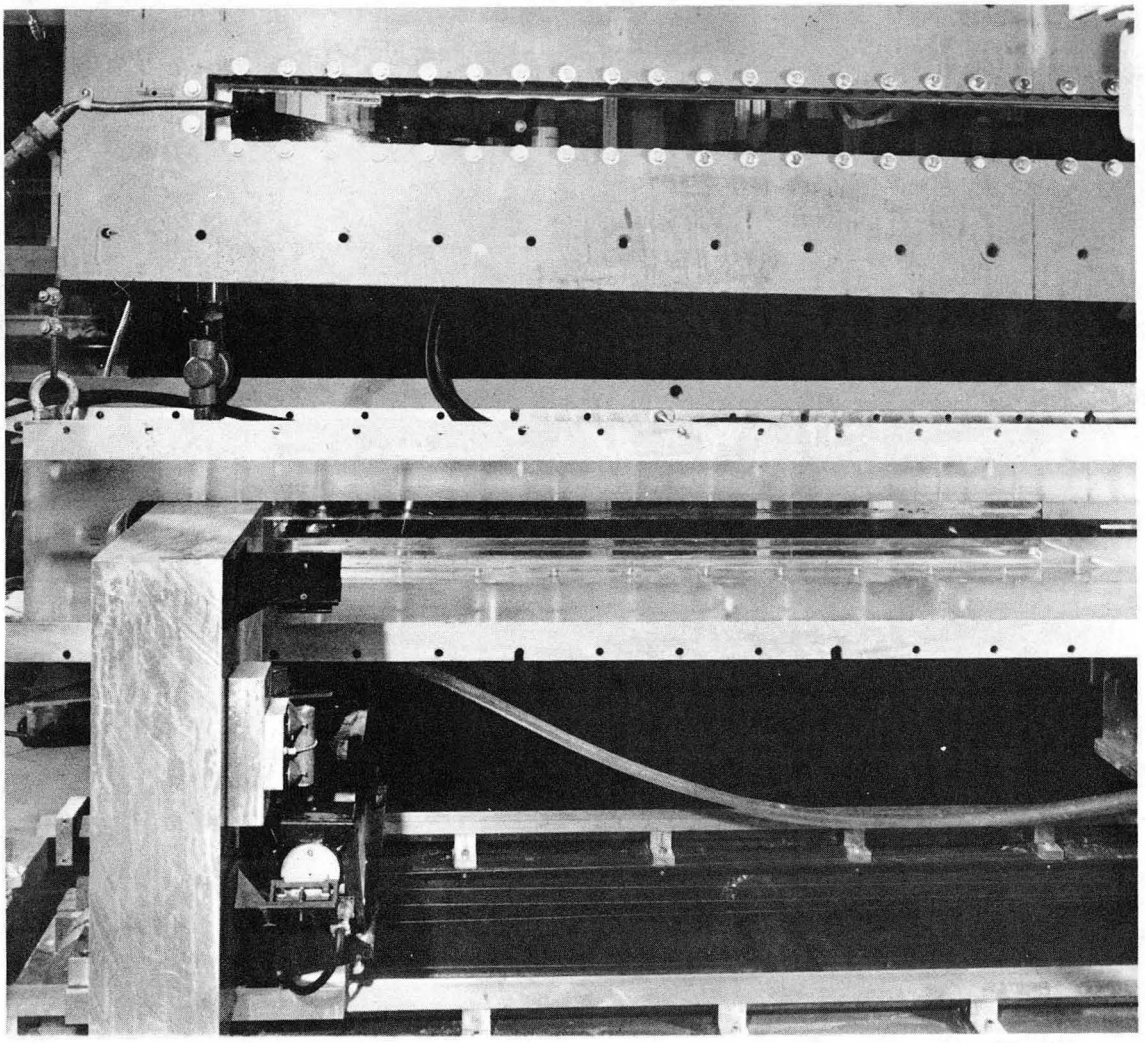

CBB 7410-7141

Fig. 2

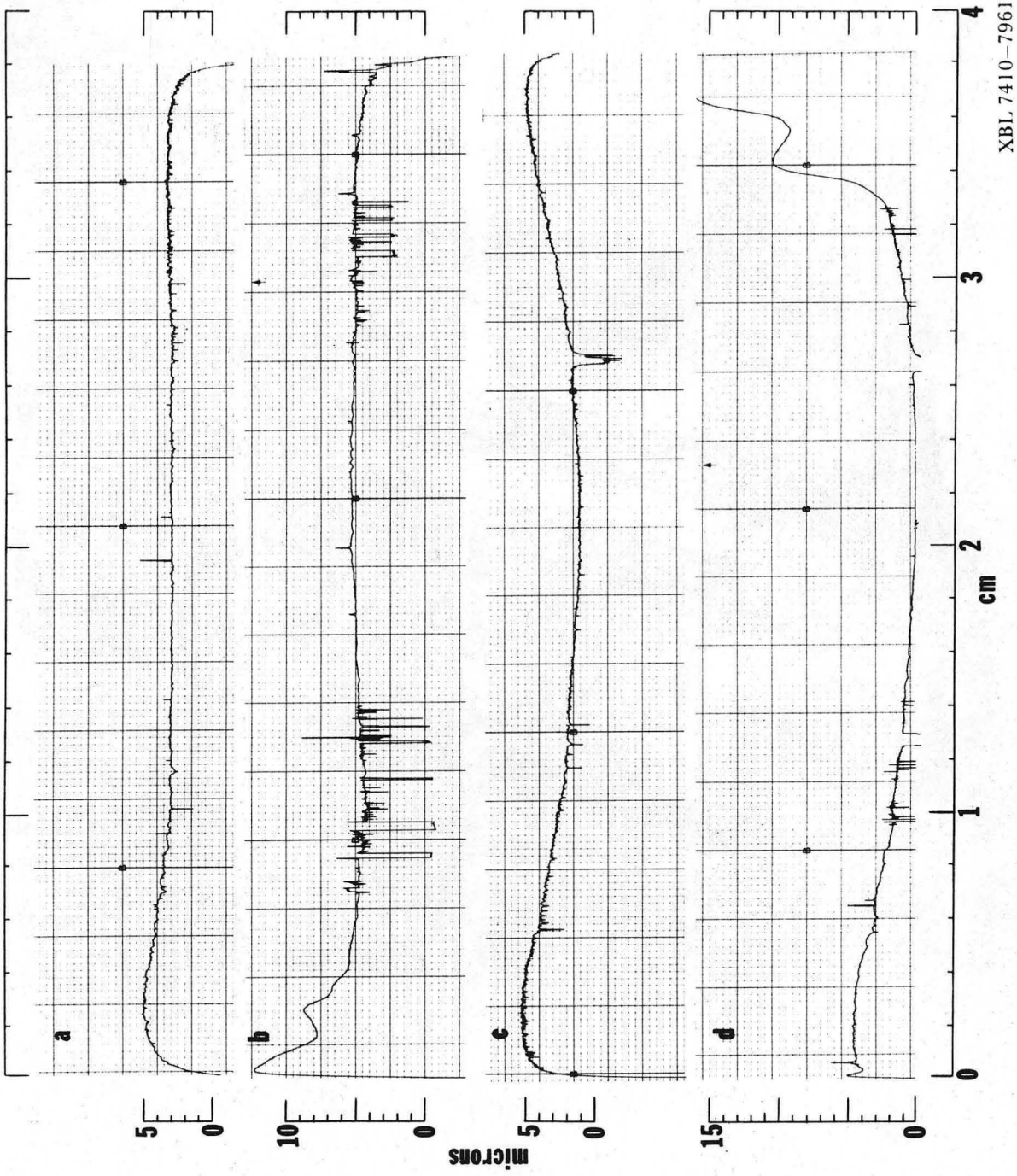

XBL 7410-7961

Fig. 3

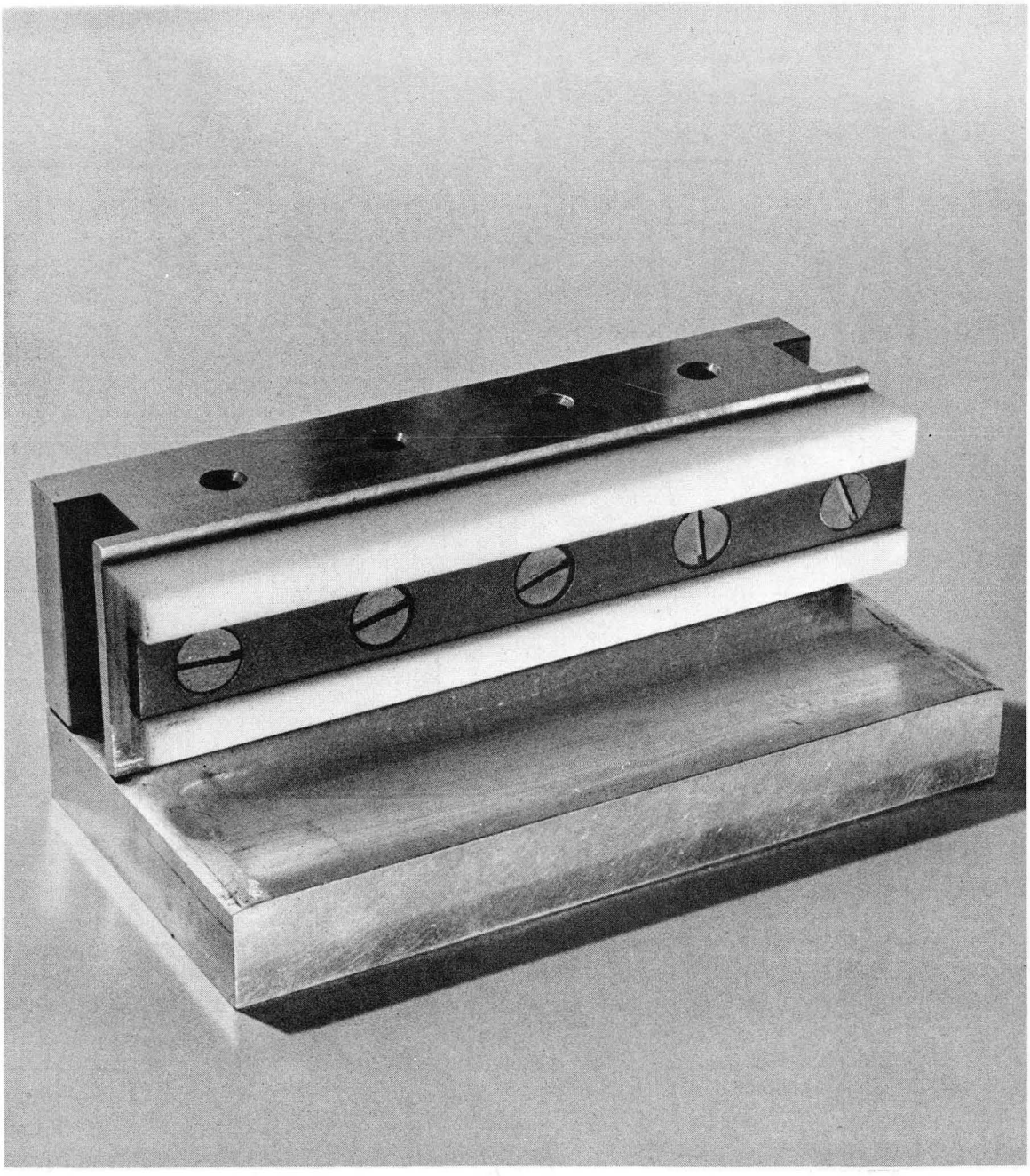

CBB 7410-7139

Fig. 4

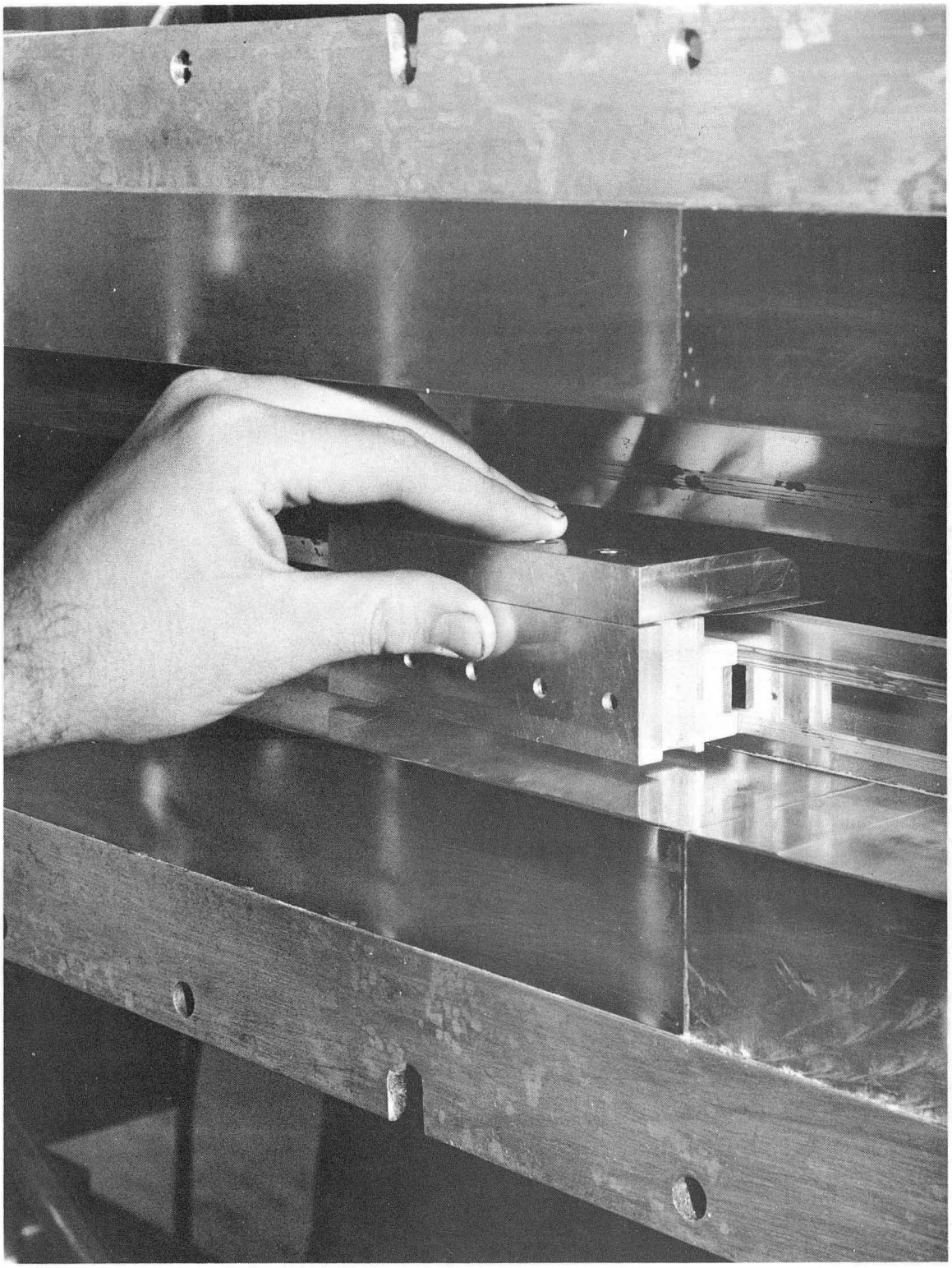

CBB 7410-7143

Fig. 5

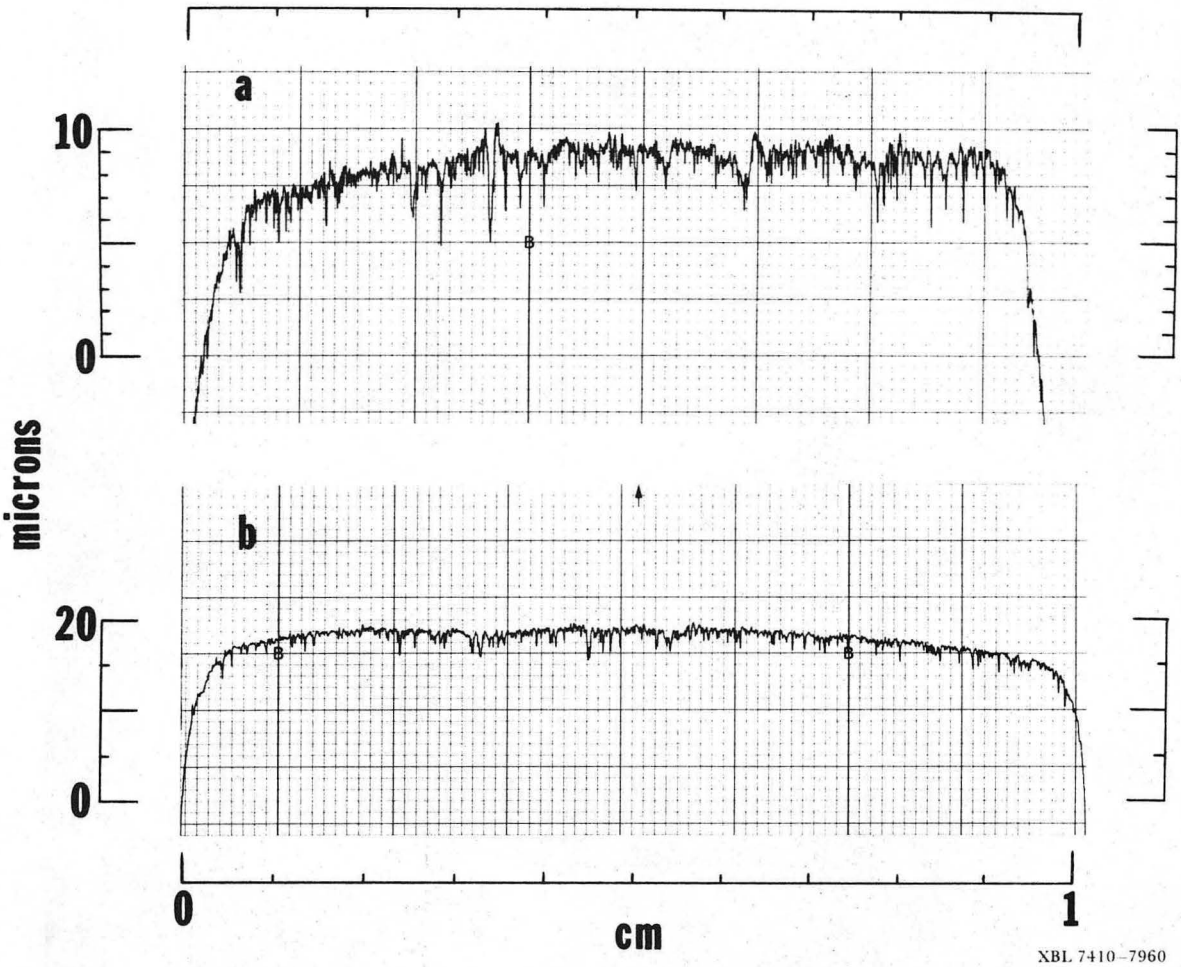

Fig. 6

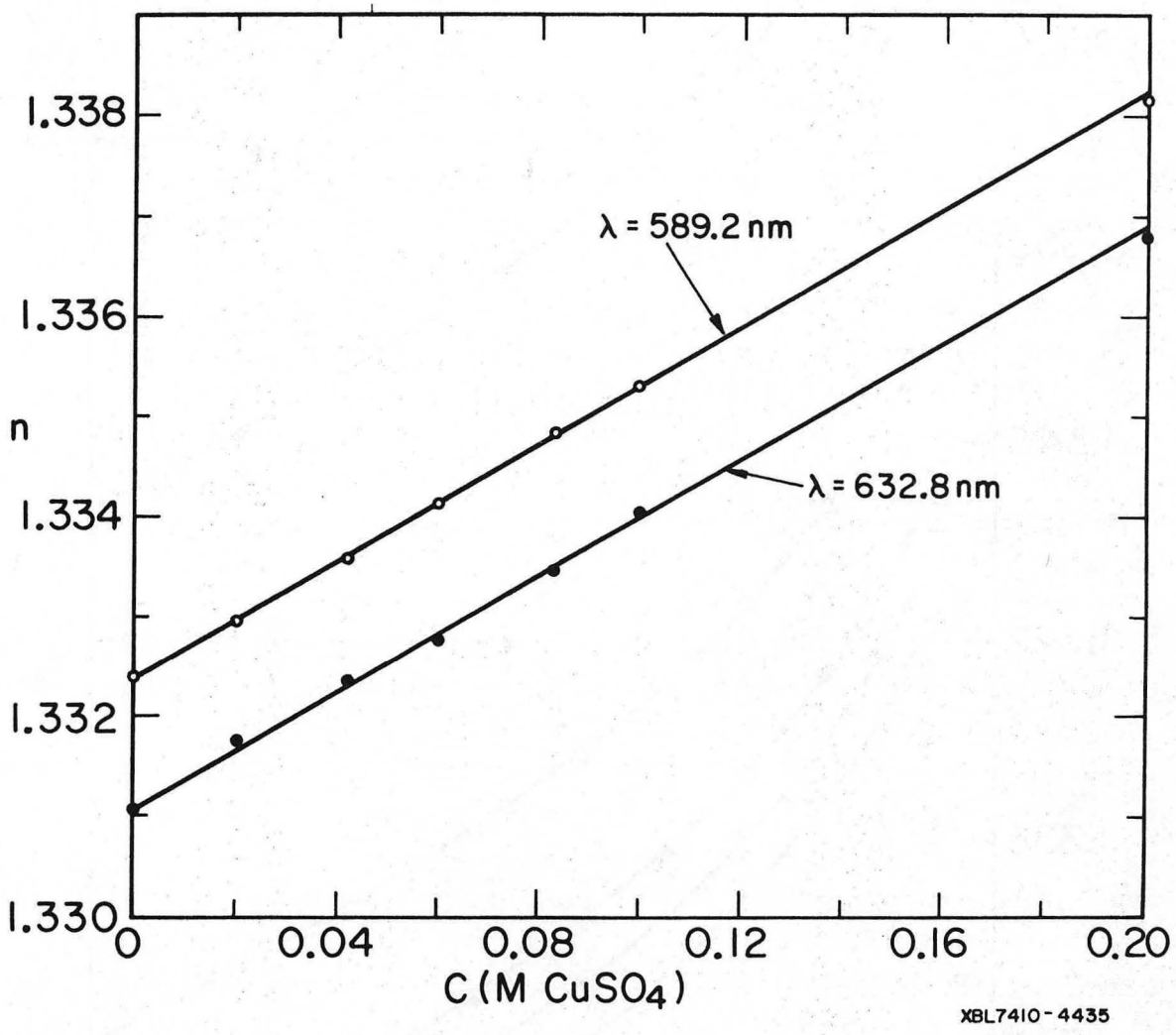

Fig. 7

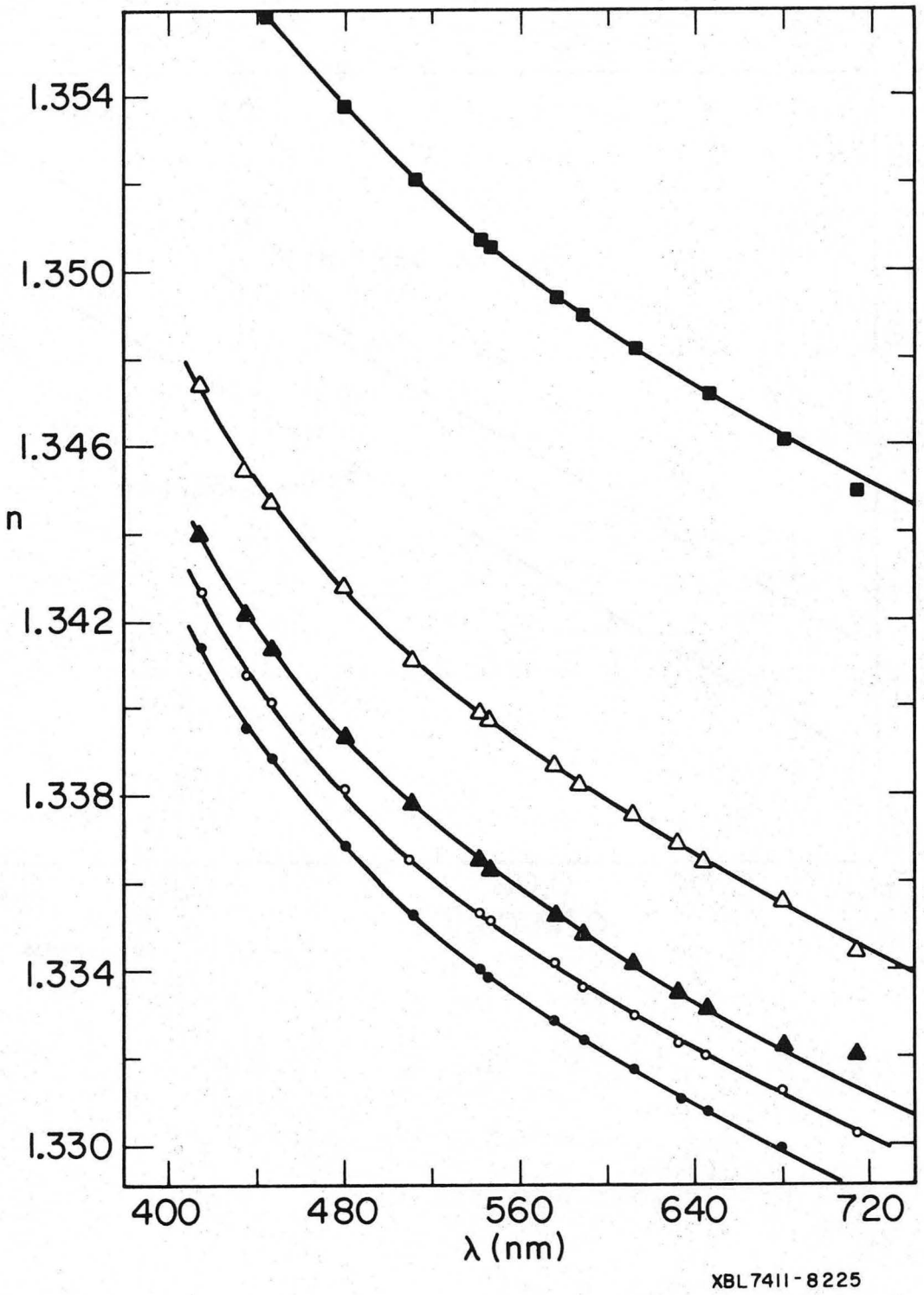
1.354
1.350
1.346
n
1.342
1.338
1.334
1.330
400
480
560
640
720
λ (nm)
XBL7411-8225

Fig. 3

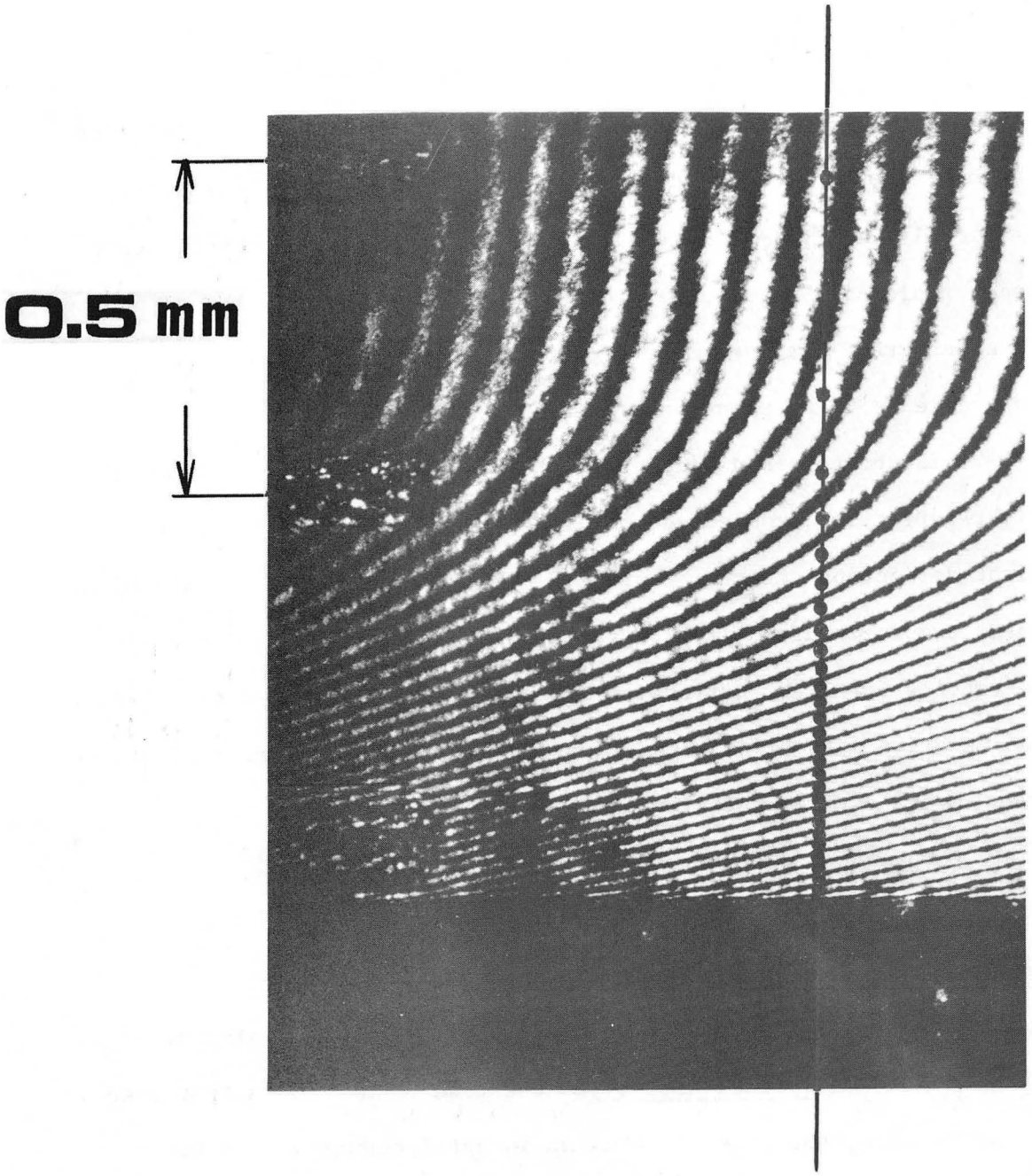

XBB 7411-3119

Fig. 9

2. LIGHT-DEFLECTION EFFECTS IN INTERFEROMETRY

The nature and interpretation of "ideal" interferograms obtained in double-beam (Mach-Zehnder) experiments has been well-described previously.[1] Light-refraction (Schlieren effect) in the refractive-index field in typical experimental situations distorts the resulting interferogram, leading to severe problems in the reduction of the interference fringes to concentration profiles.

This chapter is divided into three parts. Part 2.1 defines the light-deflection problem and outlines several methods to correct for light-deflection effects. Part 2.2 (LBL-2240) presents, in graphical form, errors incurred if interferograms were to be interpreted without correcting for light-deflection effects. Part 2.3 (LBL-3141) presents an iterative method for the derivation of one-dimensional refractive-index profiles from interferograms.

2.1. Solutions of the light-Deflection Problem

An experimental interferogram (e.g., Fig. 2 in part 2.2) produced by a double-beam interferometer depicts a one-dimensional phase vs distance relationship. The phase information is a measure of the optical history of the test beam. For a test specimen of finite size, the phase is thus an integral quantity, related (see part 2.3) to the optical path length of some ray as it traverses the specimen. If the ray had propagated along a straight line, its optical path length would be simply the product of the local refractive-index and the specimen width. The local refractive-index within the specimen could then be calculated directly from the experimental interferogram.

Refraction of the beam within the refractive-index field, however, alters the propagation direction. Figure 2 in part 2.1 and Fig. 1 of part 2.3 illustrate typical beam deflections. In each case, the specimen (electrolyte) refractive-index increases in the (positive) y-direction, and the beam AB is deflected toward the same direction. The slope dy/dx of the rays continuously increases from zero at x = 0 (plane of light-entrance into the specimen) to a positive value at x = w (plane of light-exit from the specimen). The crux of the problem is now evident; the phase depicted on the interferogram is not related to a refractive-index value at any particular location within the specimen. Rather, the phase is related to the optical path length of a deflected ray:

$$p(x) = \int_0^x n(x,y) \sqrt{1 + \left(\frac{dy}{dx}\right)^2}\, dx \qquad (1)$$

The ray trajectory must be calculated in order to solve Eq. (1), requiring solution of the light-deflection equation for a Cartesian coordinate system:[2-4]

$$\frac{d^2y}{dx^2} = \frac{1}{n(x,y)} \left[1 + \left(\frac{dy}{dx}\right)^2\right] \left[\frac{\partial n}{\partial y} - \left(\frac{dy}{dx}\right) \frac{\partial n}{\partial x}\right] \qquad (2)$$

Equations (1) and (2) are derived in Appendix IV.

Solution of Eqs. (1) and (2) requires knowledge of the refractive-index function n(x,y). This leads to an iterative method for the interpretation of interferograms; the refractive-index function must be guessed and the associated interferogram calculated. This process is then repeated until there is agreement between the computed and

experimental interferograms. This technique, by itself, does not guarantee that the unique refractive-index profile has been found. See part 2.3 for further discussion of this point.

One-Dimensional Refractive-Index Profiles

When refractive-index is a function of y only, n = n(y), the last term on the right-hand side of Eq. (2) vanishes. Equations (1) and (2) can then be solved by a numerical integration method[1,2] for any refractive-index profile. For specific polynomial-type refractive-index profiles, closed-form solutions to the light-deflection equations can be obtained, as outlined in part 2.3.

Two-Dimensional Refractive-Index Profiles

Solution of the light-deflection equations for any two-dimensional refractive-index profile requires a numerical integration. The refractive-index field is divided into a large (e.g., 100) number of intervals, one of which is depicted in Fig. 1. The solid arc AB represents the trajectory of a deflected ray over a small distance dx. If this arc is approximated by a straight segment AOB of slope

$$s = \frac{dy}{dx} \tag{3}$$

we can write Eq. (2) in another form:

$$\frac{ds}{dx} = \frac{1 + s^2}{n} \left(\frac{\partial n}{\partial y} - s \frac{\partial n}{\partial x} \right) \tag{4}$$

Casting Eqs. (1), (3) and (4) in finite difference form permits computation of the position y_{j+1}, slope s_{j+1} and segment optical path $p(x_{j+1})$ from the position y_j, slope s_j and optical path $p(x_j)$ of the previous segment:

$$y_{j+1} = y_j + s_j \cdot dx \tag{5}$$

$$s_{j+1} = s_j + \frac{dx}{n(x_a,y_a)} \cdot \left(1 + s_j^2\right) \cdot \left(\frac{\partial n}{\partial y} - s_j \cdot \frac{\partial n}{\partial x}\right) \tag{6}$$

$$p_{j+1} = p_j + n(x_a,y_a) \cdot \sqrt{1 + s_j^2} \cdot dx \quad , \tag{7}$$

where

$$\frac{\partial n}{\partial x} = \left.\frac{n(x_{j+1}) - n(x_j)}{dx}\right|_{y=y_a} \quad . \tag{8}$$

A formula similar to Eq. (8) could be used for the gradient $(\partial n/\partial y)$. Note that the subscript "a" refers to average values at the center of the segment. Use of Eqs. (5) through (8) is demonstrated in Appendix II for a two-dimensional refractive-index field.

Focusing Effects

The real plane of focus within the specimen is optically conjugate to the film plane of the camera. In other words, there is a one-to-one relationship between a point at the real plane of focus and a point on the film plane of the camera, as illustrated by the dashed line in Fig. 1 of Chapter 4.

Given the location $x = x_f$ of the real plane of focus within the specimen, the location of the virtual plane of focus can be computed[1] as a distance F relative to the outside of the glass sidewall nearest to the camera):

$$F = \frac{w - x_f}{n_b} + \frac{d}{n_g} \tag{9}$$

The distance F is depicted in Fig. 2. All rays, provided they are accepted by the objective lens of the interferometer imaging optics, appear to emanate from the virtual plane of focus. Thus, on the interferogram the apparent location of the interface will not, in general, coincide with the true position.* Figure 2 of part 2.2 illustrates this effect.

For every refractive-index field, there exists a real plane of focus at $x = x_o$ for which the location of the interface is not distorted on the interferogram. Choice of such a plane of focus would guarantee a true representation of the extent of the refractive-index variations on the interferogram (far from the interface, the refractive-index variations greatly diminish and light-deflection distortions are negligible).

Figure 2 depicts a light ray trajectory AB within a cathodic boundary layer. The refractive-index increases continuously from its minimum value $n_s(C = C_s)$ at the electrode surface $y = 0$ to its maximum value $n_b(C = C_b)$ at $y = \delta$, the edge of the boundary layer. The refractive-index is uniform for $y > \delta$. The real plane of focus GH is the above-mentioned plane for which the deflected ray ABC appears to emanate from its virtual origin Q right at the electrode surface. This condition of no interfacial distortion is met when

$$y(x = w + d) = y_C = S = F \cdot \tan\phi_a \tag{10}$$

*The image of the electrode surface in the absence of any optical aberrations.

The exit location y_C and exit angle ϕ_a of a deflected ray must be calculated in order to find the desired plane of focus x_o by using Eqs. (9) and (10):

$$x_o = w - n_b\left(\frac{y_C}{\tan\phi_a} - \frac{d}{n_g}\right) \tag{11}$$

Computation of the exit location y_C requires, in general, numerical integration of the light-deflection equation (Eq. (2)). The exit angle ϕ_a and the ray trajectory in the glass sidewall are then easily calculated by Snell's law, as shown in Appendix I.

Ray trajectories were calculated for two diffusional concentration profiles (as outlined in part 2.2), and the results are shown in Figs. 3 through 6. As in part 2.2, the interfacial refractive-index gradient (current density) was chosen as the abscissa. The ordinate is the function $1 - x_o/w$, representing a dimensionless distance from the inside of the glass sidewall nearest to the camera to the focal plane location x_o. If this function were unity, the plane of focus would correspond to $x = 0$, the recommended[2,3] plane of focus for observation of cathodic boundary layers.

The curves in Fig. 3 show the dependence of the focal plane location x_o on both concentration difference $(C_b - C_s)$ and the type of diffusional concentration profile (potentiostatic or galvanostatic). The curves "a" and "b" correspond to 0.1 and 0.2 M $CuSO_4$ concentration difference, respectively. The inflection points at (a) 7 mA/cm^2 and (b) 10 mA/cm^2 correspond to the interfacial refractive-index gradients at which the light ray entering the electrolyte right at the electrode

surface has been deflected so much that it leaves the boundary layer before entering the glass sidewall nearer to the camera. This effect is discussed more fully in the next section. The relatively small effect of the particular type of diffusional concentration profile (solid lines, potentiostatic; dashed lines, galvanostatic) reflect the similarity of the respective concentration profiles. A similar conclusion is drawn from the computations presented in the next section.

Figure 4 illustrates the effect of specimen width. Only for thin specimens (less than a few mm) does the focal plane location x_o remain near the center of the specimen for a range of current densities. Similar, but less conclusive results were presented earlier by Muller.[1]

As suggested by Beach,[5] the asymptotic behavior of the curves in Figs. 3 and 4 should not be interpreted strictly. In the limit as the interfacial refractive-index gradient vanishes, there is no single focal plane location that eliminates interfacial distortion; all locations give no distortion in this limit. Figures 5 and 6 illustrate this point. The cross-hatched area in each figure corresponds to focal plane locations that produce no more than ±0.001 mm distortion in interfacial location.

While Figs. 3 through 6 may be used to estimate an advantageous focal plane location for the observation of cathodic boundary layers, the variation of this location with current density suggests that choice of a fixed location is preferable for the sake of simplicity of interpretation.

REFERENCES

1. R. H. Muller in Advances in Electrochemistry and Electrochemical Engineering, R. H. Muller, ed. (Wiley-Interscience, N. Y., 1973), Vol. 9, pp. 326-353.

2. K. W. Beach, R. H. Muller and C. W. Tobias, J. Opt. Soc. Am. 63, 559 (1973).

3. K. W. Beach, Optical Methods for the Study of Convective Mass Transfer Boundary Layers on Extended Electrodes (Ph. D. Thesis), UCRL-20324, July 1971.

4. F. P. Kapron, J. Opt. Soc. Am. 60, 1433 (1970).

5. K. W. Beach, private communication, 1973.

NOMENCLATURE

C	electrolyte concentration (M $CuSO_4$)
C_b	bulk concentration (M $CuSO_4$)
C_s	interfacial concentration (M $CuSO_4$)
d	glass sidewall width (mm)
F	location of virtual plane of focus (mm) (see Fig. 2)
i	current density (mA cm^{-2})
n	refractive-index
n_b	refractive-index of bulk electrolyte
n_g	refractive-index of glass walls
n_s	refractive-index of electrolyte at the electrode surface
p	optical path length (mm)
s	slope of a deflected light ray
S	see Fig. 2 (mm)
w	specimen (electrode or electrolyte) width (mm)
x	horizontal distance (mm)
x_f	location of real plane of focus (mm)
x_o	location of plane of focus giving no interfacial distortion (mm)
y	vertical distance (mm)
y_C	see Fig. 2 (mm)
ϕ_a	deflected ray angle in surrounding medium (rad)

FIGURE CAPTIONS

Fig. 1. Numerical solution of the light-deflection equation.

Abscissa: horizontal distance (mm)

Ordinate: vertical distance (mm)

AB deflected light ray trajectory

AOB straight segment used to approximate arc AB

dx interval width

x_j, x_a, x_{j+1}
y_j, y_a, y_{j+1} } see text

Fig. 2. Determination of focal plane location giving no distortion of the interfacial location on an interferogram.

ABC deflected light ray

GH real plane of focus

RQ virtual plane of focus

F,S see text

d glass wall width

w electrode width

x horizontal distance

y vertical distance

x_o location of real plane of focus giving no interfacial distortion

δ boundary layer edge

Fig. 3. Focal plane position x_o for different concentration differences.

$w = 10$ mm, $C_s = 0$.

Abscissa: interfacial refractive-index gradient (cm^{-1})

Ordinate: dimensionless focal plane location, $1 - x_o/w$

_____ potentiostatic diffusional concentration profile Eq. (6) in part 2.2.

- - - - - galvanostatic diffusional concentration profile (Eq. (13) in part 2.2).

a $C_b = 0.1$ M $CuSO_4$, $(C_b - C_s) = 0.1$ M

b $C_b = 0.2$ M $CuSO_4$, $(C_b - C_s) = 0.2$ M

Fig. 4. Focal plane position x_o for different electrode widths.

$C_b = 0.1$ M $CuSO_4$, $C_s = 0$

a $w = 20$ mm

b 10 mm

c 5 mm

d 2.5 mm

e 1 mm

Other designations as in Fig. 3.

Fig. 5. Focal plane positions x_o for which the distortions in interfacial location are not larger than ±0.001 mm.

$w = 10$ mm

$C_b = 0.1$ M $CuSO_4$

$C_s = 0$

Potentiostatic diffusional concentration profile.

Fig. 6. Focal plane positions x_o for which the distortions in interfacial location are not larger than ±0.001 mm. $w = 1$ mm, other designations as in Fig. 5.

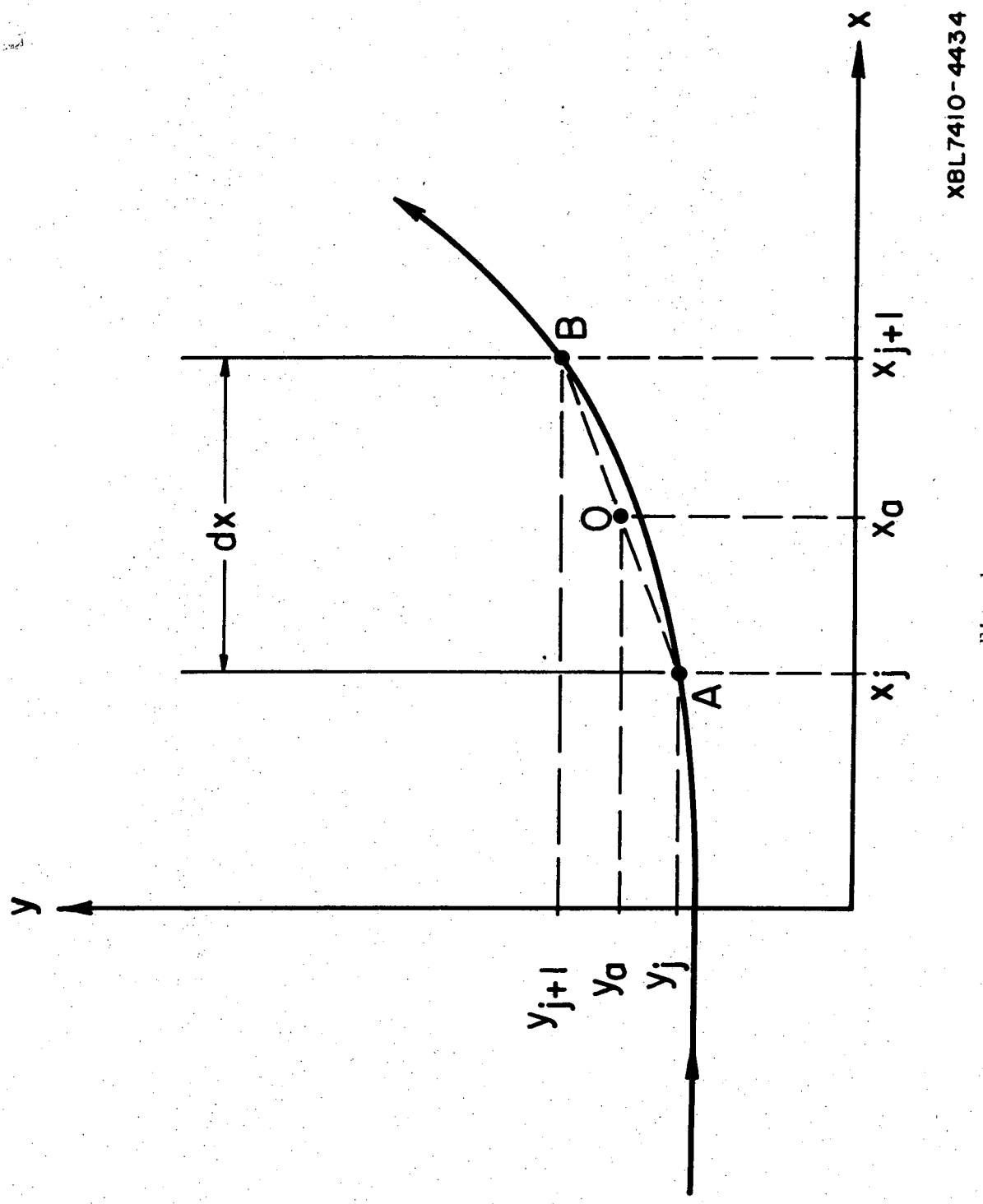

Fig. 1

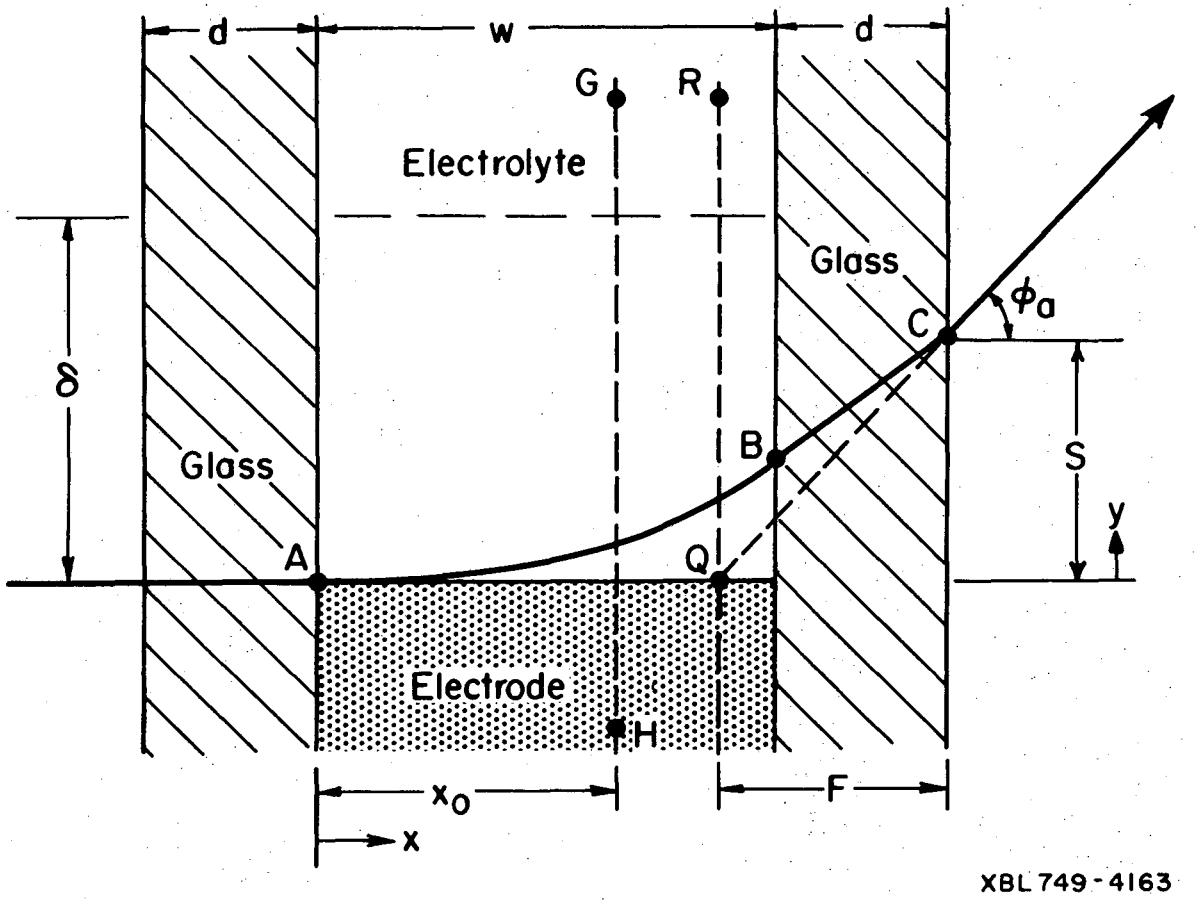
d
w
d
G
R
Electrolyte
Glass
ϕ_a
C
δ
B
S
Glass
A
Q
y
Electrode
H
x_o
F
x
XBL 749-4163

Fig. 2

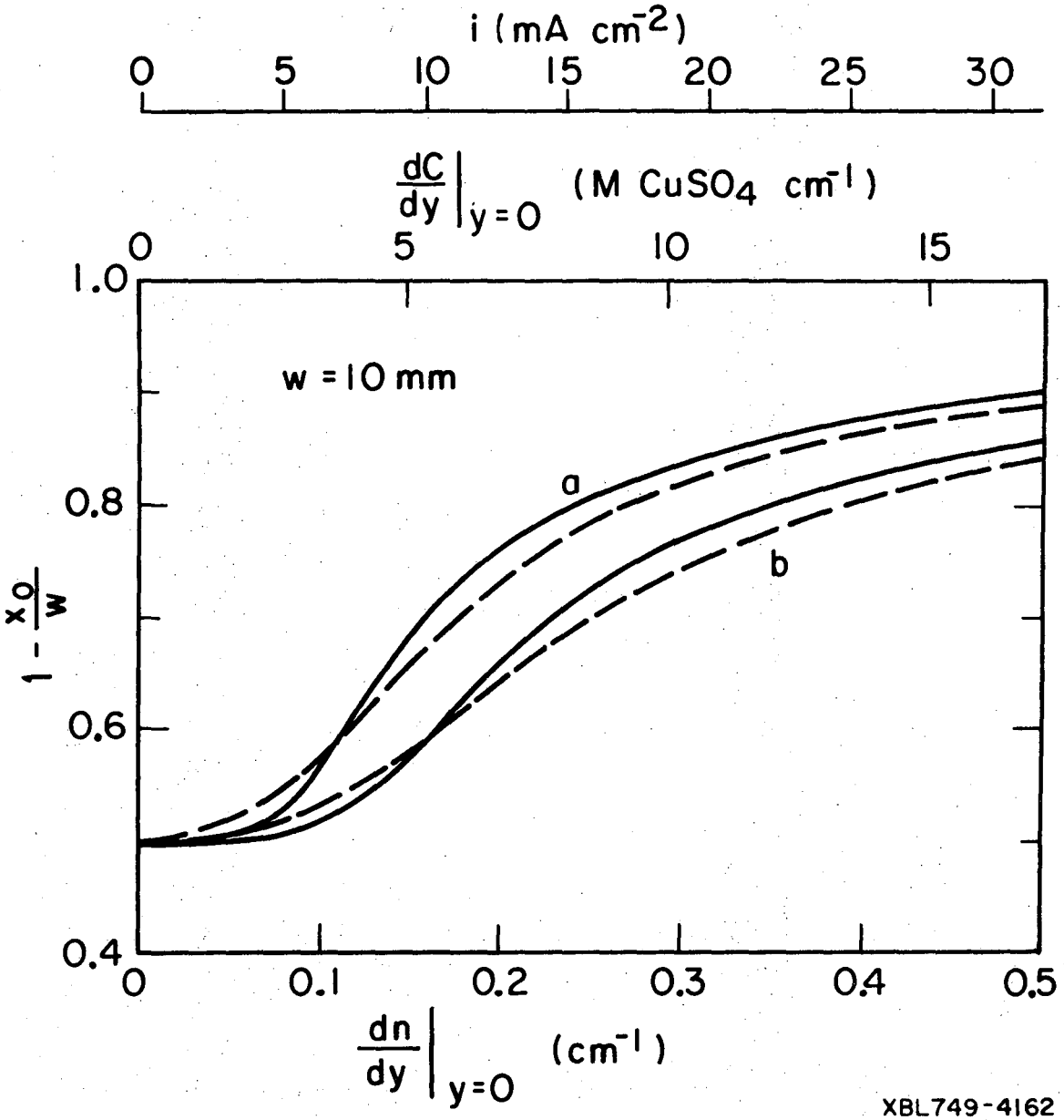

Fig. 3

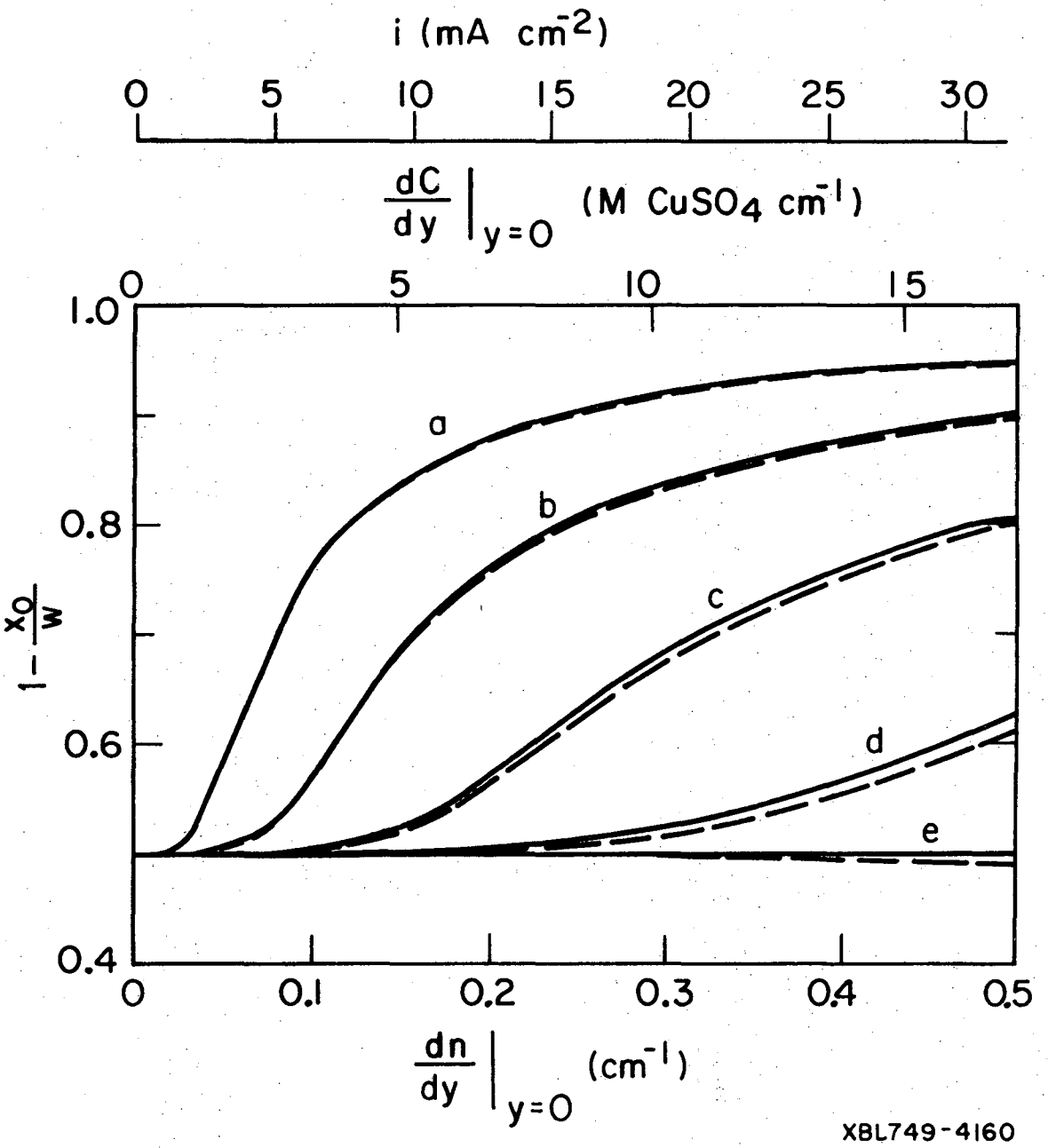
i (mA cm⁻²)
0
5
10
15
20
25
30
dC/dy |y=0 (M CuSO4 cm⁻¹)
0
5
10
15
1.0
0.8
0.6
0.4
1 − x0/w
a
b
c
d
e
0
0.1
0.2
0.3
0.4
0.5
dn/dy |y=0 (cm⁻¹)
XBL749-4160

Fig. 4

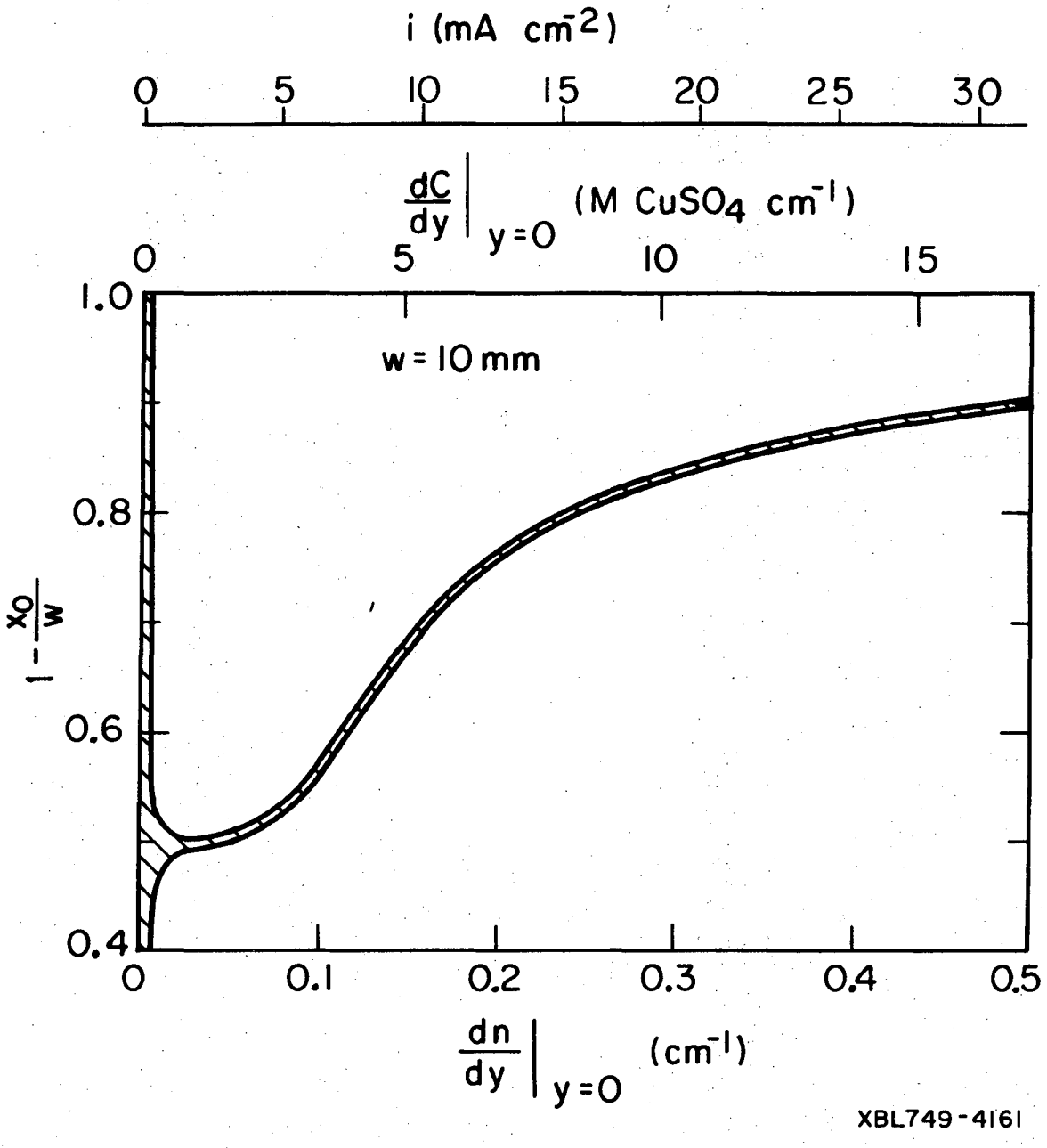

Fig. 5

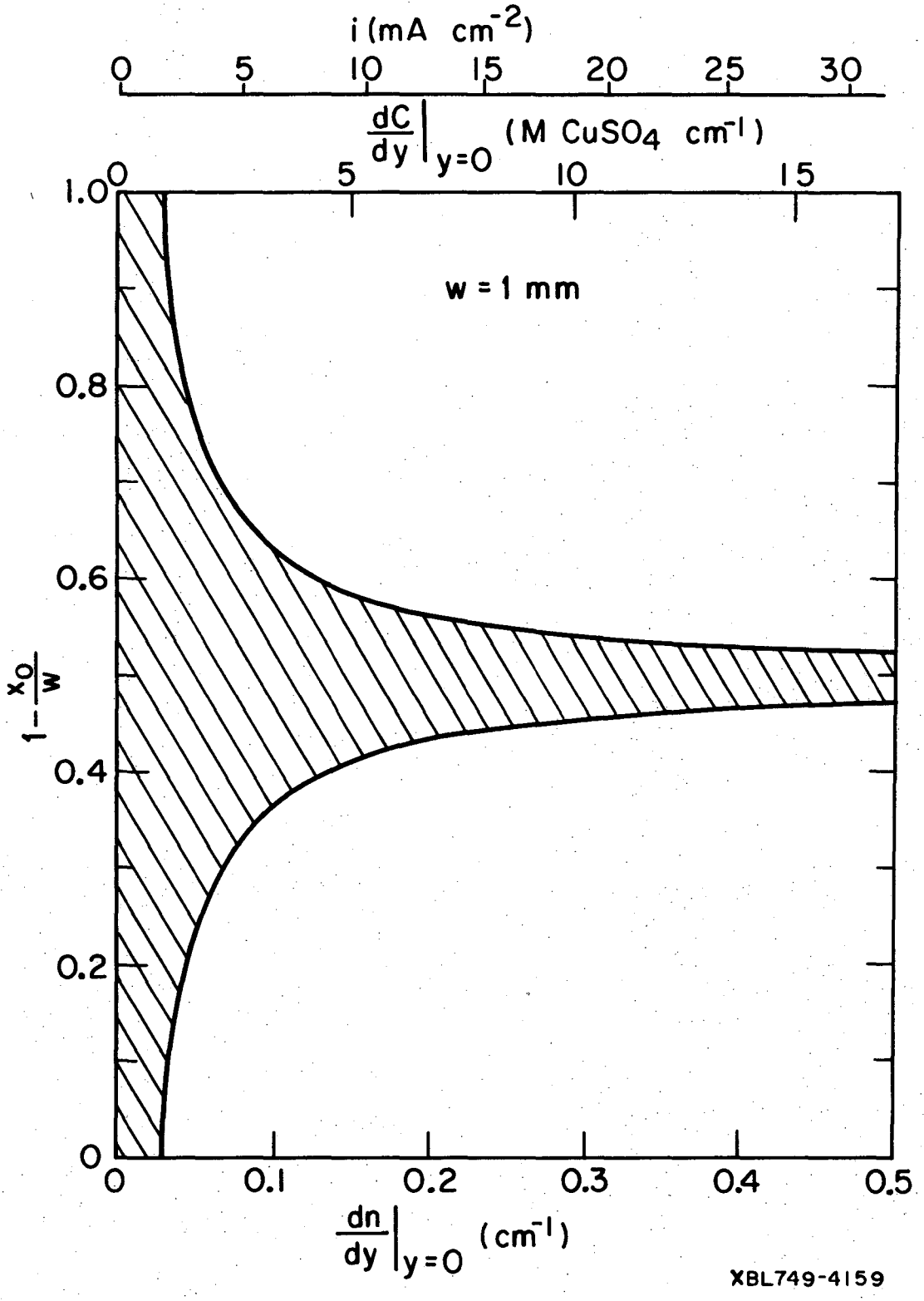
i (mA cm^{-2})
0
5
10
15
20
25
30
$\left.\frac{dC}{dy}\right|_{y=0}$ (M CuSO$_4$ cm^{-1})
0
5
10
15
w = 1 mm
1.0
0.8
0.6
0.4
0.2
0
$1-\frac{x_o}{w}$
0
0.1
0.2
0.3
0.4
0.5
$\left.\frac{dn}{dy}\right|_{y=0}$ (cm^{-1})
XBL749-4159

Fig. 6

2.2. Light-Deflection Errors in the Interferometry of Electrochemical Mass Transfer Boundary Layers

This part is identical to LBL-2240 Rev., which is reproduced in Appendix V.

2.3 Derivation of One-Dimensional Refractive-Index Profiles from Interferograms

Introduction

Conventional interpretation of interferograms assumes that light propagates along a straight line through a specimen. Local refractive-index variations within the specimen are then calculated from the local phase change (fringe shifts) in the interferogram. However, because refractive-index variations normal to the beam direction deflect the beam as it traverses the refractive-index field, conventional interpretation of the resulting interferogram can lead to large errors.[1,2] This section presents a method for the derivation of one-dimensional refractive-index profiles from interferograms which may be distorted by light-deflection effects.

A numerical solution to the equation of light deflection has permitted computation[1] of the interferogram associated with any given refractive-index field. For the reverse problem, an iterative technique must be used to calculate the refractive-index field associated with a given interferogram because no direct computational method exists. Closed-form solutions to the equation of light-deflection have now been derived for a polynomial-type refractive-index field and are used in the iterative method presented in this section.

Light-Deflection in a Refractive-Index Field

Figure 1 schematically illustrates the trajectory of a light ray within a refractive-index field. The field in this case is a boundary layer, which is a transparent medium of variable refractive-index near an opaque surface (the plane identified by $y = 0$ in Fig. 1). The refractive-index increases continuously from its minimum value

n_s at $y = 0$ to its maximum value n_b at $y = \delta$, the edge of the boundary layer; and the refractive-index has a constant value n_b for $y \geq \delta$. Such boundary layers are encountered in heat and mass transfer between two phases. Local variations in temperature or concentration result in corresponding refractive-index variations near the interface. The trajectory $y(x)$ of light beam AB is calculated by solving the light-deflection equation for this coordinate system:[1,3]

$$\frac{d^2y}{dx^2} = \frac{1}{n}\left[1 + \left(\frac{dy}{dx}\right)^2\right]\left[\frac{\partial n}{\partial y} - \left(\frac{dy}{dx}\right)\frac{\partial n}{\partial x}\right] \qquad (1)$$

where $n = n(x,y)$ is the refractive-index within the field. Concurrently, the optical path length p of the beam must be calculated in order to determine the phase difference between various rays traversing the specimen:

$$p(x) = \int_0^x n(x,y)\sqrt{1 + \left(\frac{dy}{dx}\right)^2}\, dx \qquad (2)$$

Solution of the Light-Deflection Equations

In the analysis of one-dimensional boundary layers, the refractive-index is a function of y only ($n = n(y)$) and the last term on the right-hand side of Eq. (1) vanishes. Equation (1) may now be integrated directly:

$$\frac{dy}{dx} = \sqrt{\left(\frac{n}{n_e}\right)^2 - 1} \tag{3}$$

$$x = \int_{y_e}^{y} \frac{dy}{\sqrt{\left(\frac{n}{n_e}\right)^2 - 1}} \tag{4}$$

where y_e is the position where a particular light ray enters the specimen (parallel to the plane $y = 0$) and n_e is the medium refractive-index at $x = 0$ and $y = y_e$. The tractability of Eq. (4) depends upon the form of the refractive-index function $n = n(y)$. Solutions for a constant refractive-index gradient of unlimited extent ($n \propto y$) have been obtained previously.[4]

Solutions for more general refractive-index profiles can be obtained if the light-deflection equation [Eq. (4)] is simplified. If we define $\varepsilon = \frac{n}{n_e} - 1$, we see that ε is a small number for many interferometric systems. For example, the maximum value of ε likely to be encountered in the interferometry of aqueous $CuSO_4$ systems[2] is about 0.01. We can then approximate $(n/n_e)^2 - 1 = 2\varepsilon + \varepsilon^2 \approx 2\varepsilon$ to within about 0.5%.

The light-deflection equations [Eqs. (2) to (4)] now simplify to

$$\frac{dy}{dx} = \sqrt{2\,\frac{n - n_e}{n_e}} \tag{5}$$

$$x = \int_{y_e}^{y} \frac{dy}{\sqrt{2\,\frac{n - n_e}{n_e}}} \tag{6}$$

$$p(x) = n_e \cdot x + 2 \int_0^x (n - n_e)dx \qquad (7)$$

Use of these approximate equations is justified in Appendix A for the interferometric analysis of a particular refractive-index field. Note that as $n \to n_e$, the refractive-index variations vanish and Eq. (7) becomes $p(x) = n_e \cdot x$, which corresponds to conventional interferogram interpretation.

Two-Parameter Refractive-Index Profile

A closed-form solution of both Eqns. (4) and (6) can be obtained (see Appendix B) for a parabolic refractive-index profile

$$\theta = \frac{n - n_s}{n_b - n_s} = 1 - (1 - Y)^2 = 2Y - Y^2 \ , \quad 0 \leq Y \leq 1 \qquad (8)$$

$$\theta = 1 \ , \quad Y \geq 1$$

where Y is a reduced distance in the boundary layer $Y = y/\delta$. The parabolic profile has only two degrees of freedom, n_s and δ: the parameter n_s permits stretching along the refractive-index axis (e.g., the abscissa in Fig. 4) and the parameter δ allows stretching along the distance axis (e.g., the ordinate in Fig. 4).

Three-Parameter Refractive-Index Profile

A polynomial refractive-index function can be formulated as

$$\theta = 1 - (1 - kY)^2(1 - Y)^2 \ , \ -0.268 < k \leq 1 \ , \ 0 \leq Y \leq 1 \qquad (9)$$

$$\theta = 1 \ , \ Y \geq 1$$

where the limits on the parameter k insure that the function $\theta(Y)$ suffers no inflection or extremum points for $0 < Y < 1$. This relatively simple functionality offers two advantages: (a) it permits a closed-form solution to the equations of light-deflection [Eqs. (5) to (7)], and (b) it is flexible enough to approximate closely typical refractive-index fields encountered in heat and mass transfer. Note that the parabolic boundary layer profile Eq. (8) is a special case of Eq. (9) for $k = 0$.

There are three variable parameters in Eq. (9): n_s, δ and k. In addition to the two stretching parameters n_s and δ, the curve shape parameter k provides additional flexibility to fit data. The polynomial function Eq. (9) is plotted in Fig. 2 for several values of k.

We can obtain a closed-form solution to Eq. (6) for the polynomial boundary layer profile by first defining the following variables and parameters:

$$u(Y) = (1 - kY)(1 - Y) \qquad (10)$$

$$U = \frac{u}{u_e} = \frac{u(Y)}{u(Y_e)} \qquad (11)$$

$$m = \frac{1}{2}\left[1 + \frac{(1 - k)^2}{4k\ u_e}\right] \qquad (12)$$

$$h = 2\,\frac{n_b - n_e}{n_e} \tag{13}$$

$$x_m = \delta\sqrt{\frac{u_e}{2kh}} \tag{14}$$

U is a transformation variable related to dimensionless distance Y by

$$Y = \frac{1 + k}{2k} - \sqrt{\frac{u_e}{k}\,(2m - 1 + U)} \tag{15}$$

Using the new variable of integration U , Eq. (6) transforms into:

$$x = \frac{x_m}{\sqrt{2}} \int_U^1 \frac{dU}{\sqrt{(1 - U)(U + 1)(U - 1 + 2m)}} \tag{16}$$

for which the solution is:[5]

$$x = x_m \cdot sn^{-1}\left(\sqrt{\frac{1 - U}{2m}}\ ,\ m\right) \tag{17}$$

where m (defined by Eq. (12)) is the parameter of the elliptic integral of the first kind sn^{-1} . Equation (17) can be inverted to a function of the Jacobian elliptic function sn :

$$U = 1 - 2m \cdot sn^2\left(\frac{x}{x_m}\ ,\ m\right) \tag{18}$$

The phase integration formula Eq. (7) becomes:

$$p(x) = n_e\left[x + h\left(x - \int_0^x U^2 dx\right)\right] \tag{19}$$

which can be easily integrated by standard formulae (e.g., Gauss-Legendre Quadrature). Formulae similar to Eqs. (17) - (19) can be derived[6] for $k < 0$. For $k = 0$, the parabolic boundary layer formulae (see Appendix B) apply.

Calculation of Ray Trajectories and Optical Paths

Equation (18) may be used to calculate the trajectory of a light ray through a boundary layer. Figure 3 illustrates two types of ray trajectories to consider: Type I, represented by line ABC, in which the ray remains within the boundary layer for $0 \leq x \leq w$, and Type II, represented by line DEF, in which the ray leaves the boundary layer before entering the glass wall at $x = w$. Since the ray would leave the boundary layer by definition when the ray reaches the edge of the boundary layer $Y = 1$ (or $U = 0$), we can easily determine the type trajectory (I or II) of a ray by using Eq. (17) for $U = 0$ to calculate the abscissa location x_b where the ray leaves the boundary layer:

$$x_b = x_m \cdot sn^{-1}\left(\sqrt{\frac{1}{2m}}, m\right) \tag{20}$$

Type I $x_b > w$: the ray remains within the boundary layer for $0 \leq x \leq w$. Integration of Eq. (19) provides the optical path length of the beam:

$$p(w) = n_e\left[w + h\left(w - \int_0^w U^2 dx\right)\right] \tag{21}$$

The integral in Eq. (21) can be accurately evaluated by 3-point Gauss-Legendre Quadrature,[7] where Eq. (18) supplies the functional values $U^2(x)$. The accuracy of the 3-point quadrature is discussed in Appendix A. Eq. (18) and Eq. (15) provide the location $Y(w)$ (see Fig. 1) of the ray as it leaves the medium to enter the glass wall. Equation (9) gives the medium refractive-index and Eq. (5) gives the slope of the ray at this plane.

Type II $x_b < w$: the ray leaves the boundary layer before entering the glass sidewall. For $x > x_b$, the ray travels along a straight line since above the edge of the boundary layer there is no refractive-index gradient. Inspection of Eqs. (5) and (13) shows that the ray has a slope $\frac{dy}{dx} = \sqrt{h}$ for $x_b \leq x \leq w$, so the location of the ray at the plane where it leaves the medium to enter the glass wall is

$$Y(w) = 1 + \sqrt{h}\ (w - x_b) \tag{22}$$

The optical path length of the ray can be calculated from Eq. (2) and Eq. (19):

$$p(w) = n_e\left[x_b + h\left(x_b - \int_0^{x_b} U^2 dx\right)\right] + n_b \cdot (w - x_b)\sqrt{1 + h} \tag{23}$$

Calculation of Interferograms from Known Refractive-Index Fields

The formulae derived in the previous section provide the trajectory $y(x)$ and the optical path length $p(x)$ of a light ray as it traverses the medium $0 \leq x \leq w$. The ray then passes through the glass wall $w \leq x \leq w + d$ and propagates to the imaging objective lens of the interferometer. If the real plane of focus (optically conjugate to the film plane of the interferometer) lies at some plane $x = x_f$, we can calculate[1] the location of the virtual plane of focus GM (Fig.1) (relative to the plane of light-exit $x = w + d$ from the specimen):

$$F = \frac{w - x_f}{n_b} + \frac{d}{n_g} \tag{24}$$

The distance F is shown on Fig. 1 for focus at $x_f = 0$, $n_b = 1.33$ and $n_g = 1.5$. All rays, provided they are accepted by the objective lens, appear to emanate from the virtual plane of focus GM. The deflected ray ABC thus appears to come from its virtual origin M, and its location on the interferogram can be calculated by considering refraction in the glass wall and the distance $S = F \cdot \tan \phi_a$ shown in Fig. 1

$$y_i = y(w) + d \cdot \tan \phi_g - F \cdot \tan \phi_a \tag{25}$$

The angles ϕ_g in the glass wall and ϕ_a in the surrounding medium (e.g., air) are easily determined by Snell's Law.

Phase on the interferogram is calculated from the optical path length difference between the deflected ray ABC (Fig. 1) and a hypothetical undeflected ray LMN passing through the virtual origin M. The exit points C and N of each ray lie on an equiphase arc CN centered on the virtual origin M. Beyond points C and N the imaging optics introduce no phase difference between the rays ABC and LMN. The optical path p_o of the hypothetical undeflected ray is calculated by considering the distance $T = F\cdot\left(\sqrt{1 + \tan^2 \phi_a} - 1\right)$ on Fig. 1:

$$p_o = n_b\cdot w + n_g\cdot d + F\cdot\left(\sqrt{1 + \tan^2 \phi_a} - 1\right) \tag{26}$$

where the surrounding medium is assumed to be air. The phase is given by

$$\Delta p = p(w) + n_g\cdot d\cdot \sqrt{1 + \tan^2 \phi_g} - p_o \tag{27}$$

and is related to the number of fringe shifts on the interferogram by

$$N = \left|\frac{\Delta p}{\lambda}\right| \tag{28}$$

Using a large number (e.g., 50) of rays entering the plane $x = 0$ at different positions (y_e values) an interferometric phase vs distance relationship, i.e. an interferogram, can be constructed by application of the above formulae.

Derivation of Refractive-Index Profiles from Interferograms

Although the interferogram associated with a given polynomial refractive-index field can now be derived in closed form, the reverse is not possible. Rather,an iterative technique is required to find the refractive-index profile associated with a given (i.e., experimental) interferogram. The three variable parameters of the polynomial function Eq. (9) can be estimated by a conventional analysis of the interferogram. These parameters are then varied in a systematic fashion, and a new interferogram is calculated each time a single parameter is changed until the best fit between the experimental and computed interferograms is found.

The following parameter variation technique has been used to find the refractive-index profile associated with a given interferogram by minimizing the deviations between the given and calculated interferograms:

1. Vary the interfacial refractive-index n_s until the average deviation between computed and given interferograms is zero (or less than some arbitrary small value).
2. Change the orientation parameter k and calculate the new n_s value by repeating step #1.
3. Repeat step #2 until a minimum in standard deviation between calculated and given interferograms is found.
4. Change the boundary layer thickness δ and calculate the new k and n_s values by repeating step #3.

5. Repeat step #4 until a minimum in standard deviation between calculated and given interferograms is found.

Details of this iterative technique are given elsewhere.[6]

Accuracy of Polynomial Representation of Refractive-Index Fields

Results of sample interferogram analyses are shown in Fig. 4. On the abscissa of this figure the interference order (fringe shifts) is linearly related to refractive-index (concentration). This relation corresponds to conventional interpretation $\Delta p = w(n - n_b)$. The true refractive-index fields correspond to concentration profiles (boundary layers) formed by the electrodeposition of Cu from aqueous 0.1 M $CuSO_4$ electrolyte. These profiles are depicted by the filled circles on Fig. 4 and correspond to the following functional relationships:

$$\text{a:}\quad \theta = 1 + \pi^{1/2} Y(1 - \text{erf}Y) - e^{-Y^2} \tag{29a}$$

$$\text{b:}\quad \theta = \text{erf}Y \tag{29b}$$

$$\text{c:}\quad \theta = 2Y - 2Y^3 + Y^4 \ . \tag{29c}$$

Equations (29a) and (29b) describe the concentration profiles[2] formed by diffusion-controlled electrodeposition at (a) constant current[9] (constant interfacial refractive-index gradient) and (b) constant potential[10] (constant interfacial refractive-index). Equation (29c) is a Pohlhausen-type field[11] that approximates the concentration profile

one might expect[12] for forced convection-controlled electrodeposition. The open circles shown on Figure 4 are the "data" - the interferogram to be analyzed. These points were calculated by numerical integration[1,8] of the light-deflection equation (Eq. (1)) for the refractive-index fields Eq. (29) for real plane of focus $x_f = 0$. The solid and dashed curves are the derived polynomial concentration profile and its associated computed interferogram, respectively. 40-90 iterations are usually required to find the minimum standard deviation between computed (dashed curve) and given (open circles) interferograms, consuming about 1 sec of computer[13] time. About 20 seconds of computer time would be required to perform a similar analysis using a numerical solution[1,8] of the light-deflection equation.

Figure 4 shows that the refractive-index field derived from a given interferogram by the technique presented in this section does approximate the "true" field. A serious question arises, however, about the uniqueness of the derived refractive-index profile. In Fig. 4b and 4c the form of the derived profile closely approximates the form of the true profile, but careful inspection shows that the slopes dC/dy at $y = 0$ do not match. Figures 5 and 6 present a series of computations that illustrate this problem. Figure 5 depicts the ratio R_g of the derived interfacial refractive-index gradient to the true interfacial refractive-index gradient as a function of the true gradient. The calculations were performed for the three model refractive-index profiles Eq. (29) for a real plane of focus $x_f = 0$. The filled symbols on Fig. 5 represent conventional interpretation of the (computed) interferograms while the open symbols illustrate

interpretation as previously described in Fig. 4. Figure 6 shows similar calculations for the ratio R_n of derived refractive-index differences (bulk less interfacial) to the true refractive-index difference.

The open points in Figs. 5 and 6 show that while the technique presented here is likely to find the interfacial refractive-index to within 5%, serious (up to 30%) errors can result in the determination of the interfacial refractive-index gradient. These errors are related to the insufficient flexibility of the polynomial refractive-index function Eq. (9); it can accurately represent the model profile Eq. (29a), but it cannot adequately describe the profiles Eqns. (29b) and (29c).

Although one's immediate reaction might be to suggest another refractive-index functionality more general than Eq. (9), careful inspection of Fig. 4 indicates a problem in the uniqueness of the refractive-index field derived from the interferogram. Note that the end point of the computed interferogram (dashed line) matches the end point of the given interferogram (lowest open circle) only in Fig. 4a. In Fig. 4b and 4c, there are 0.023 mm and 0.017 mm discrepancies between the end points. This misfit is the only apparent signal that the best match between computed and given (experimental) interferograms has not been found. In practice, there is considerable difficulty[14] in reading the exact location of the interface on an experimental interferogram, so it is unlikely that this small difference between the computed and given interferograms could be detected. In other words, there are two different refractive-index fields (e.g. the

solid curve and filled circles in Fig. 4b) associated with practically indistinguishable interferograms (e.g., the dashed curve and open circles in Fig. 4b). Thus, while the technique presented in this section can indeed approximate both the form of the refractive-index field and the interfacial refractive-index associated with a given interferogram, it is not able to find either the unique refractive-index profile functionality or the exact interfacial refractive-index gradient.

Under certain circumstances, however, it may be possible to determine the true refractive-index profile functionality directly from the (distorted) interferogram. The solid curves in Fig. 7 depict two specific forms of the polynomial refractive-index function Eq. (9): the parabolic profile $k = 0$ and the quartic profile $k = 1$. The computed interferograms associated with the parabolic and quartic profiles are indicated by the dashed curves. Note that the dashed curves correspond to dimensionless plots of the distorted interferograms (conventional interpretation). The close agreement between the form of the parabolic profile and its associated interferogram suggests that the true refractive-index functionality may be determined directly from the distorted interferogram if the true profile is not too different from parabolic. For example, the Pohlhausen profile Eq. (29c) would be of this type. However, the mismatch between the quartic profile and its associated interferogram suggests the refractive-index functionality cannot be determined directly from the distorted interferogram. This is the case for the refractive-index functionality Eq. (29a).

The filled symbols in Figs. 5 and 6 show that except for small refractive-index gradients, conventional interpretation of interferograms can lead to large (up to 60-85%) errors in the determination of the interfacial composition and gradient of refractive-index. Reference (2) discusses the effect of specimen sizes and refractive-index differences on such light-deflection errors. While the technique presented in this section obviously has its limitations, it is certainly preferable to conventional interferogram interpretation when the refractive-index gradients are large.

Determination of the unique refractive-index field associated with a given interferogram is possible only if at least one of the following conditions is met:

(1) If the refractive-index gradients are so small that light-deflection effects are negligible.

(2) If the light-deflection equation can be inverted and the refractive-index field directly determined from the interferogram.

(3) If the form of the refractive-index function is known beforehand,[15] numerical integration of the light-deflection equation coupled with a suitable iteration technique can be used to determine quantities such as interfacial refractive-index, etc.

(4) If, for example, the interfacial refractive-index gradient is known beforehand,[16] numerical integration of the light-deflection equation can be performed for various types of refractive-index profiles until the derived gradients match the known gradients.

(5) If the refractive-index functionality is not unlike the parabolic profile $k = 0$, the functionality may be determined directly from the interferogram.

Appendix A

Validity of Approximations

The interferogram associated with two boundary layers can be computed by several methods to estimate the accuracy of the two approximations made in the derivation of closed-form solutions of the light-deflection equations. Two parabolic boundary layers are chosen to represent an electrochemical system[2,6,8] where the refractive-index field corresponds to aqueous $CuSO_4$ electrolyte depleted in $CuSO_4$ concentration near an electrode surface. For each case, the concentration difference between the bulk ($y \geq \delta$) solution and interface ($y = 0$) is 0.1 M $CuSO_4$, corresponding to refractive-index values[2] $n_b = 1.3340$ and $n_s = 1.3311$ at $\lambda = 632.8$ nm.

Type I: $\delta = 0.70$ mm, and no rays are deflected out of the boundary layer.

Type II: $\delta = 0.35$ mm, and all rays are deflected out of the boundary layer.

The various computation schemes are analyzed by calculating the interferograms of Type I and Type II boundary layers, using the formulae derived in Appendix B. Two characteristics of the computed interferograms are given in Table I: y_{sf} , the position on the interferogram of a ray entering the specimen at $y_e = 0$; and ΔN , the total number of fringe shifts seen on the interferogram. The calculations are performed for $w = 10.0$ mm , $d = 12.7$ mm , and $\lambda = 632.8$ nm (see Ref. 2 for the dependence of light-deflection errors on w , d and $n_b - n_s$).

The accuracy of the phase integration by 3-point Gauss-Legendre Quadrature can be checked by comparing computations #3 and 4 of Table 1. Both computations have been carried out for the simplified version of the light-deflection equation [Eq. (6)], but the calculation scheme #4 uses the Gauss-Legendre Quadrature while #3 uses the closed-form solution for the phase integration, Eq. (37).

The accuracy of approximating Eqs. (4) and (2) with Eqs. (6) and (7) can be checked by comparing scheme #4 with scheme #2. Note that the approximation is good to within 0.1%.

The accuracy of the numerical integration[1,8] of the light-deflection equation can be checked by comparing schemes #5-9 with #2. Note that about 500 intervals (step size 0.02 mm) are required to approach the closed-form solution to within 0.001 mm (y_{sf}) and 0.1 fringe (ΔN) .

Table 1

Validity of Approximations and Convergence of Numerical Solutions

Computation Scheme #			Type I boundary layer δ = 0.70 mm		Type II boundary layer δ = 0.35 mm	
			y_{fs} (mm)	ΔN (fringes)	y_{fs} (mm)	ΔN (fringes)
1	Conventional analysis Eq. 29		0	45.83	0	45.83
2	Eqs. 33 - 35*		-0.2466	53.26	-0.2027	38.51
3	Eqs. 36 - 37		-0.2464	53.25	-0.2025	38.50
4	Eq. 36*		-0.2464	53.25	-0.2025	38.50
	Numerical Integration[1,8]					
	Intervals	Mesh Size (mm)				
5	10	1.0	-0.2824	57.20	-0.2663	47.42
6	100	0.1	-0.2502	53.66	-0.2086	39.00
7	500	0.02	-0.2474	53.35	-0.2039	38.68
8	1000	0.01	-0.2469	53.29	-0.2035	38.62
9	10000	0.001	-0.2467	53.26	-0.2030	38.54

*3-point Gauss-Legendre Quadrature used for phase integration

Appendix B

Parabolic Boundary Layers

The solution to the complete equation of light-deflection [Eq. (4)] can be obtained for a parabolic refractive-index profile Eq. (8) by use of the following transformation:

$$H = \frac{n}{n_e} \quad \text{and} \quad H_{max} = \frac{n_b}{n_e} \tag{30}$$

In addition, a scaling factor x_p is defined as

$$x_p = \delta \sqrt{\frac{n_e}{(n_b - n_s)(1 + H_{max})}} \tag{31}$$

Eq. (4) then transforms into

$$x = \frac{\delta}{2} \sqrt{\frac{n_e}{n_b - n_s}} \int_1^H \frac{dH}{\sqrt{(H_{max} - H)(H - 1)(H + 1)}} \tag{32}$$

for which the solution is[5]

$$x = x_p \cdot sn^{-1}\left(\sqrt{\frac{1}{m}\frac{H - 1}{H + 1}}\ ,\ m\right) \tag{33}$$

Here, m is the parameter for the elliptic integral of the first kind sn^{-1} and is defined as $m = (n_b - n_e)/(n_b + n_e)$ for this solution. Equation (33) may be inverted:

$$H = \frac{1 + m \cdot sn^2\left(\frac{x}{x_p}, m\right)}{1 - m \cdot sn^2\left(\frac{x}{x_p}, m\right)} \tag{34}$$

where sn is the Jacobian elliptic function, and the phase integration equation [Eq. (2)] becomes:

$$p(x) = n_e \cdot \int_0^x H^2 dx \tag{35}$$

which may be integrated by standard formulae (e.g., Gauss-Legendre Quadrature).

The simplified form of the light-deflection equations [Eqs. (6) and (7)] can be integrated directly for a parabolic boundary layer profile:

$$\frac{Y - 1}{Y_e - 1} = \cos \frac{x}{x_0} \tag{36}$$

$$p(x) = n_b \cdot x - (n_b - n_e) \cdot x_0 \cdot \sin \frac{x}{x_0} \cdot \cos \frac{x}{x_0} \tag{37}$$

where

$$x_0 = \delta \sqrt{\frac{n_e}{2(n_b - n_s)}} \tag{38}$$

Equation (37) is a closed-form solution of the phase integration equation and can be used to estimate the accuracy of Gauss-Legendre

quadrature as applied to Eqs. (35) and (37). Equation (36) permits a simple determination of the location x_b where all rays leave the boundary layer:

$$x_b = \frac{\pi}{2} x_0 \, . \tag{39}$$

REFERENCES

1. K. W. Beach, R. H. Muller and C. W. Tobias, J. Opt. Soc. Am. 63, 559 (1973).

2. F. R. McLarnon, R. H. Muller and C. W. Tobias, J. Electrochem. Soc. 122, 59 (1975). See also section 2.2.

3. F. P. Kapron, J. Opt. Soc. Am. 60, 1433 (1970).

4. R. H. Muller, in Advances in Electrochemistry and Electrochemical Engineering, R. H. Muller, ed., (Wiley-Interscience, New York, 1973) Vol. 9, pp. 326-353.

5. M. Abramowitz and I. Stegun, eds., Handbook of Mathematical Functions, Washington, National Bureau of Standards, 1964, pp. 569-607.

6. See Appendix I.

7. L. Lapidus, Digital Computation for Chemical Engineers, (McGraw-Hill, New York, 1962) p. 60.

8. K. W. Beach, Ph.D. Thesis, UCRL-20324, Dept. of Chemical Engineering, University of California, Berkeley (Univ. Microfilms, Ann Arbor, Michigan, order no. 72-13269).

9. H. J. S. Sand, Phil. Mag. (6) 1, p. 45 (1901).

10. F. G. Cottrell, Z. Physikal. Chem. 42, 385 (1903).

11. H. Schlichting, Boundary Layer Theory, (McGraw-Hill, New York, 1968) p. 291.

12. J. S. Newman, Ind. and Eng. Chem. 60, 12 (1968).

13. Control Data Corporation 7600 computer.

14. A 0.1° misalignment of the test beam corresponds to a 0.02 mm uncertainty in the location of a 10 mm wide surface.

15. This is the case for diffusion-controlled electrodeposition. See Ref. (2).

16. In many electrochemical systems, the local interfacial refractive index gradient is directly related to local current density, which can often be measured independently.

NOMENCLATURE

C	electrolyte concentration (M $CuSO_4$)
d	glass wall width (mm)
F	location of virtual plane of focus (mm)
h	parameter Eq. (13)
H, H_{max}	transformation variable Eq. (30)
i	current density (mA cm^{-2})
k	parameter Eq. (9)
m	parameter of the elliptic integral of the first kind Eq. (12) or Eq. (33)
n	refractive-index
n_b	bulk refractive-index ($y \geq \delta$)
n_e	refractive-index at $x = 0$, $y = y_e$
n_s	interfacial refractive-index ($y = 0$)
N	interference order Eq. (28)
p	optical path length (mm)
p_o	optical path length of undeflected ray (mm)
R_g	ratio of the derived interfacial refractive-index gradient to the true gradient
R_n	ratio of the derived refractive-index difference $n_b - n_s$ to the true difference
u	transformation variable Eq. (10)
u_e	$u(y_e)$
U	u/u_e
w	cell width (mm)
x	horizontal distance (mm)

x_b location where ray leaves boundary layer (mm) (Eqs. (20), (39))

x_m parameter (mm) Eq. (14)

x_0 parameter (mm) Eq. (38)

x_p parameter (mm) Eq. (31)

y vertical distance (mm) Fig. 1

y_e position of light entrance into specimen (mm) Fig. 1

y_i distance on interferogram (mm)

y_{sf} interfacial location on interferogram (mm)

Y dimensionless distance $Y = y/\delta$

Y_e y_e/δ

δ boundary layer thickness (mm)

ΔN number of fringe shifts on an interferogram

Δp phase (mm)

ε $(n - n_e)/n_e$

θ dimensionless refractive-index Eq. (8), (9), or (29)

λ wavelength of light (nm)

ϕ_a ray angle in air (rad)

ϕ_g ray angle in glass (rad)

FIGURE CAPTIONS

Fig. 1. Schematic illustration of a light ray trajectory.

ABC Ray trajectory

LMN Hypothetical undeflected ray

GM Virtual plane of focus

CN Equiphase arc centered on virtual origin M

PQ Edge of the boundary layer

x Horizontal distance

y Vertical distance

y_e Position of light ray entrance into specimen

d Glass wall thickness, refractive-index n_g

w Cell thickness, medium refractive-index $n(x,y)$

F,S,T See text

δ Boundary layer thickness

Fig. 2. Polynomial boundary layer refractive-index profiles.

Ordinate: dimensionless distance $Y = y/\delta$

Abscissa: dimensionless refractive-index $\theta = (n-n_s)/(n_b-n_s)$

a $k = -0.268$

b $k = 0$

c $k = 0.5$

d $k = 1.0$

Fig. 3. Schematic illustration of different ray trajectories.

ABC Trajectory of a ray that remains inside the boundary layer (Type I)

DEF Trajectory of a ray that is deflected out of the boundary layer (Type II)

GH Edge of the boundary layer

Fig. 4. Interpretation of interferograms.

Abscissa: local concentration (M $CuSO_4$) or phase change N (fringes).

Ordinate: distance y(mm).

o o o Interferogram (phase vs distance relationship) to be analyzed. (Computed from the refractive-index fields (Eq. (29)) by numerical methods[1,8].) Plane of focus $x_f = 0$, w = 10.0 mm and d = 12.7 mm .

——— Polynomial concentration profile (refractive-index field) derived from the above interferogram.

- - - Interference fringe associated with the above concentration profile.

•••• True concentration profile (refractive-index field Eq. 29). $C_s = 0$ and $C_b = 0.1$ M $CuSO_4$ ($n_s = 1.3311$ and $n_b = 1.3340$ for $\lambda = 632.8$ nm).

a Refractive-index field described by Eq. (29a). Derived concentration profile: $\delta = 0.535$ mm, $k = 0.800$, $C_s = -0.0004$ M $CuSO_4$. Standard deviation 1.97×10^{-4} M $CuSO_4$ per data point.

b Refractive-index field described by Eq. (29b). Derived concentration profile: $\delta = 0.408$ mm, $k = 0.454$, $C_s = -0.0053$ M. Standard deviation 2.43×10^{-4} M/point.

c Refractive-index field described by Eq. (29c). Derived concentration profile: δ = 0.272 mm, k = 0.068, C_s = -0.0020 M. Standard deviation 1.37 X 10^{-4} M/point.

Fig. 5. Measurement of interfacial refractive-index gradients.

Abscissa: true interfacial refractive-index gradient (cm^{-1}).

Ordinate: R_g = derived interfacial refractive-index gradient divided by true gradient.

● ▼ ■ Apparent refractive-index gradient derived by conventional interpretation of the (computed) interferograms.

○ ▽ □ Refractive-index gradient derived by interpretation of interferograms as shown in Fig. 4.

○ ● Refractive-index field described by Eq. (29a).

▽ ▼ Refractive-index field described by Eq. (29b).

□ ■ Refractive-index field described by Eq. (29c).

Fig. 6. Measurement of interfacial refractive-index.

Abscissa: true interfacial refractive-index gradient (cm^{-1}).

Ordinate: R_n = derived refractive-index difference ($n_b - n_s$) divided by true refractive-index difference.

● ▼ ■ Apparent interfacial refractive-index derived by conventional interpretation of the (computed) interferograms.

○ ▽ □ Interfacial refractive-index derived by interpretation of interferograms as shown in Fig. 4.

Other designations as in Fig. 5.

Fig. 7. Parabolic and Quartic refractive-index fields and corresponding interferograms.
Ordinate: dimensionless distance

Abscissa: dimensionless refractive-index

———— True refractive-index field (parabolic $k = 0$ and quartic $k = 1$).

- - - - - Computed interferogram associated with the true refractive-index field. Corresponds to interfacial refractive-index gradient $\left.\frac{dn}{dy}\right|_{y=0} = 0.3\ cm^{-1}$.

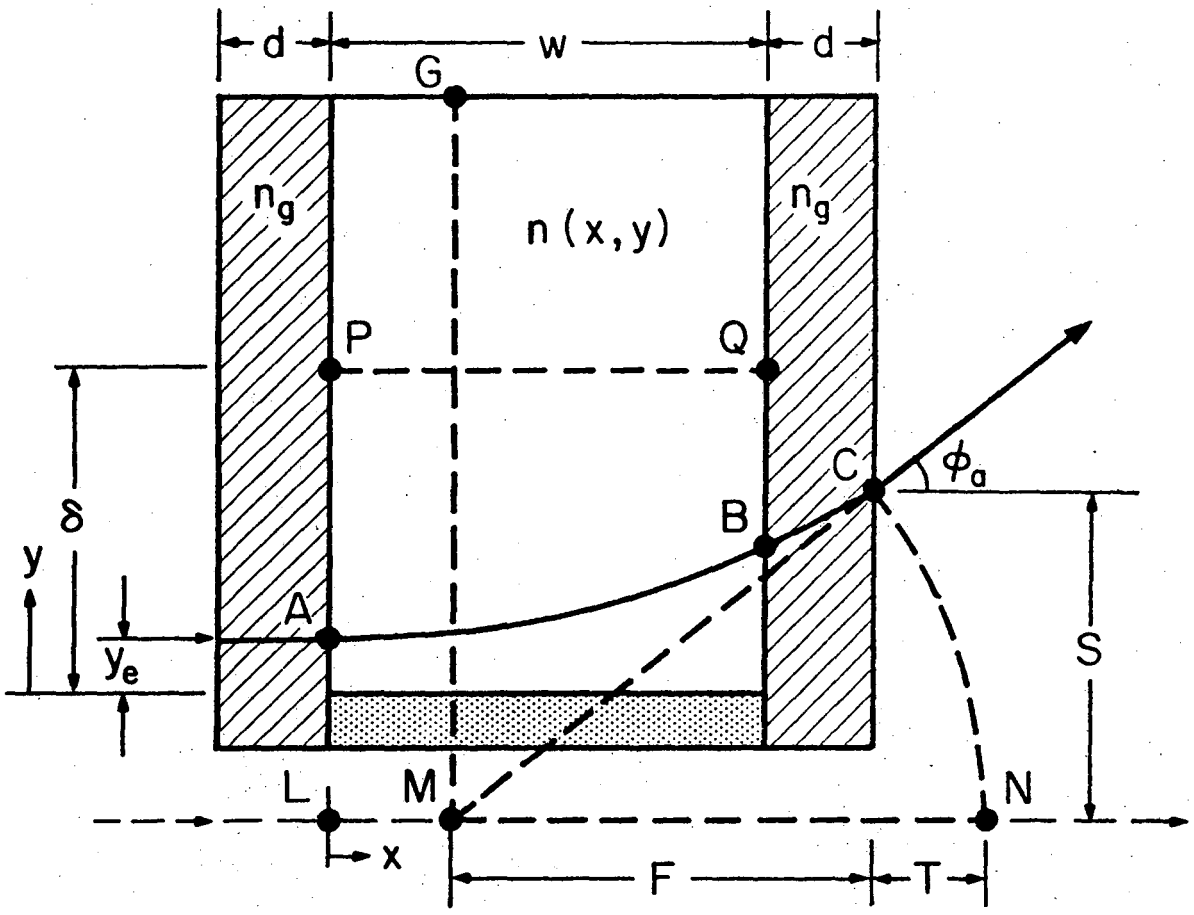

XBL 747-3705

Fig. 1

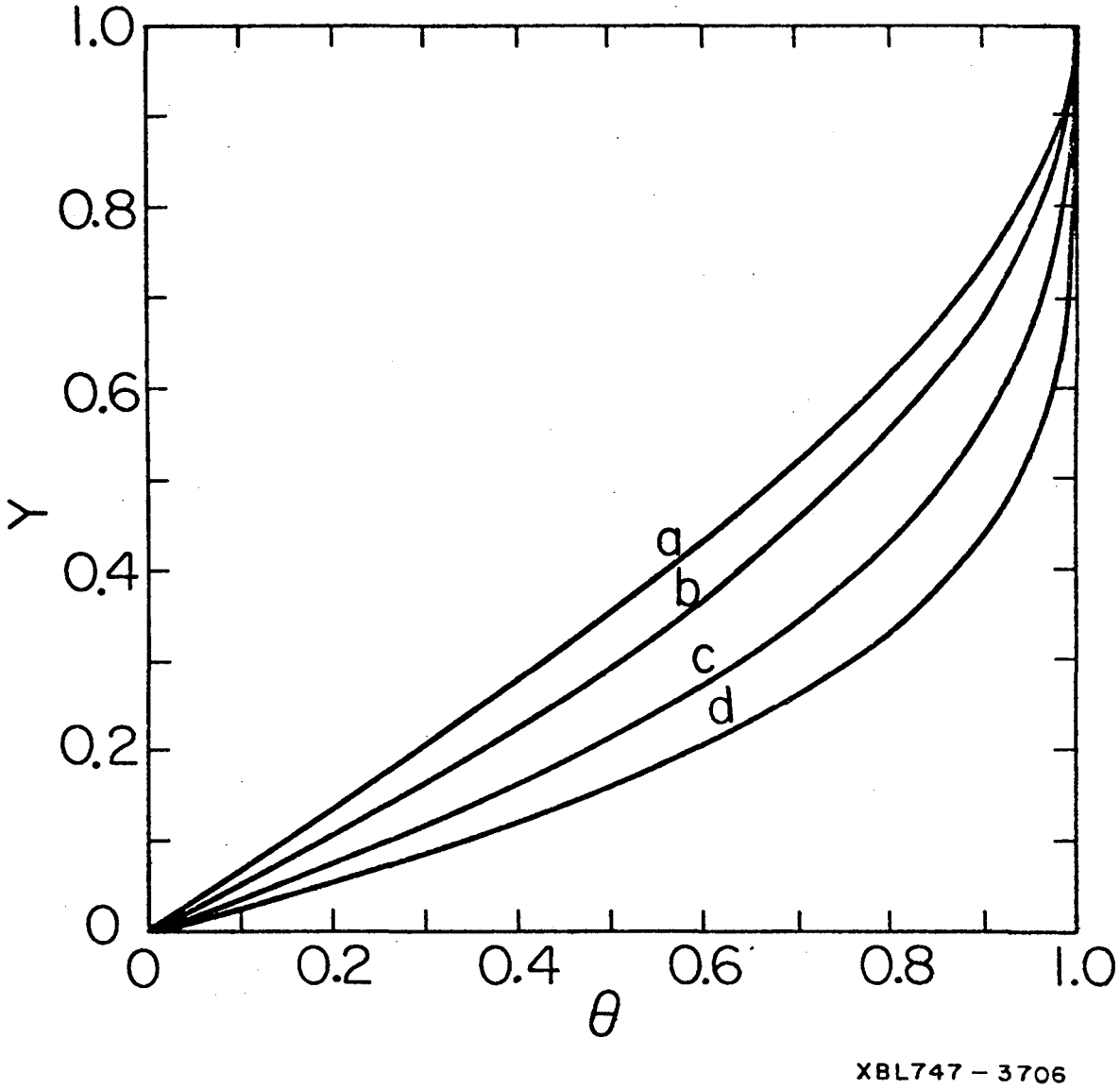

Fig. 2

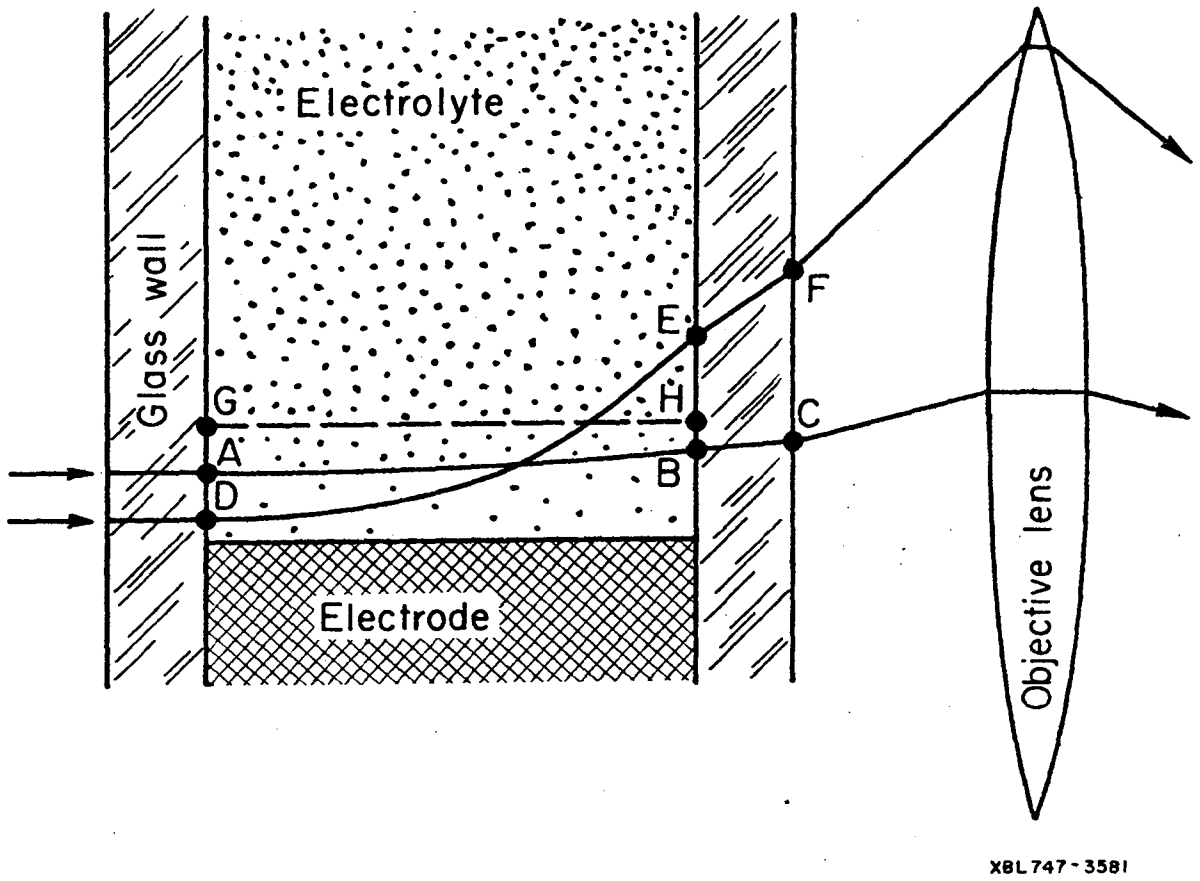
Electrolyte
Glass wall
Electrode
Objective lens
A
B
C
D
E
F
G
H
XBL747-3581

Fig. 3

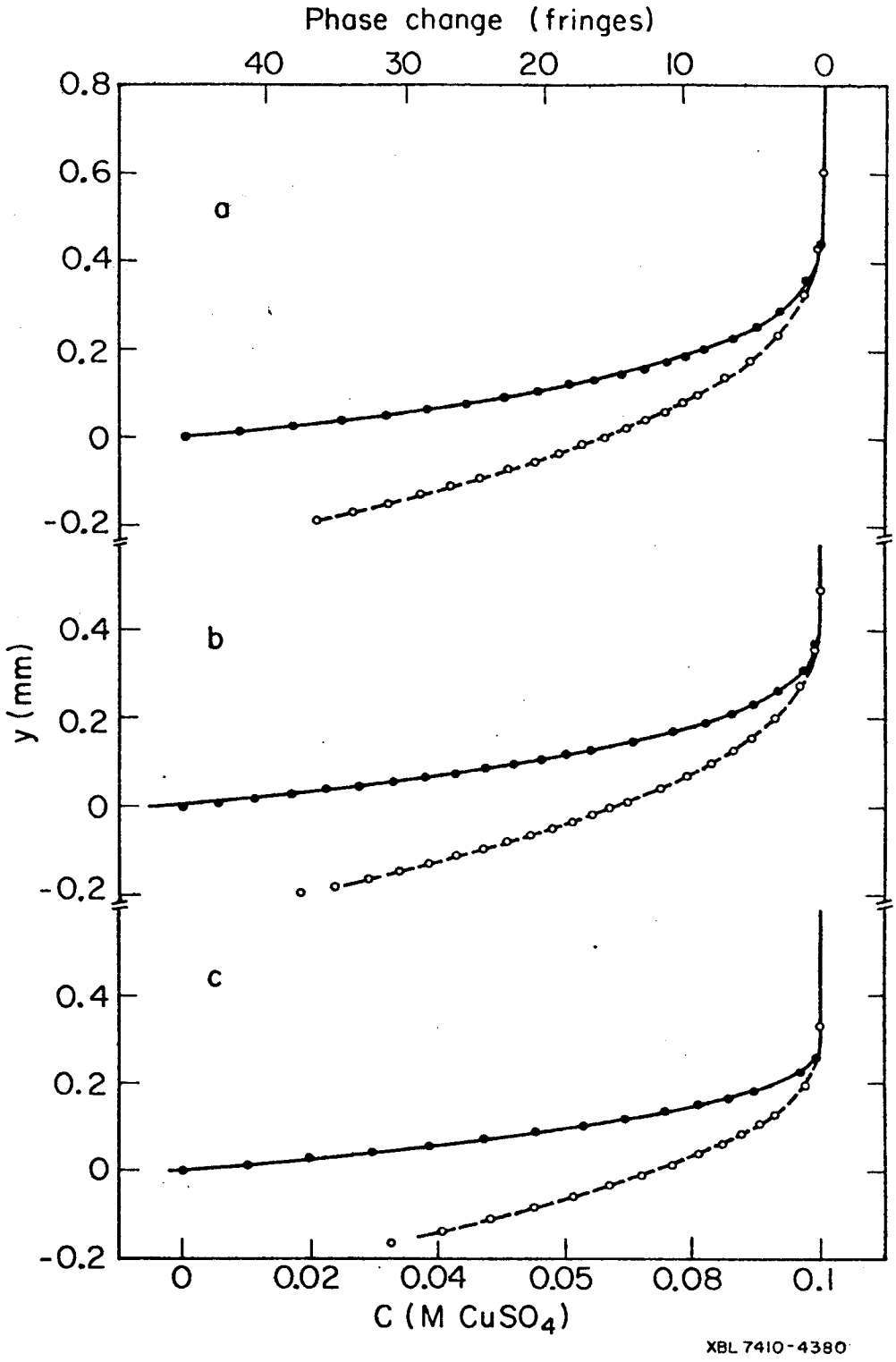
Phase change (fringes)
40
30
20
10
0
0.8
0.6
0.4
0.2
0
-0.2
a
b
c
y (mm)
0.02
0.04
0.05
0.08
0.1
C (M CuSO4)
XBL 7410-4380

Fig. 4

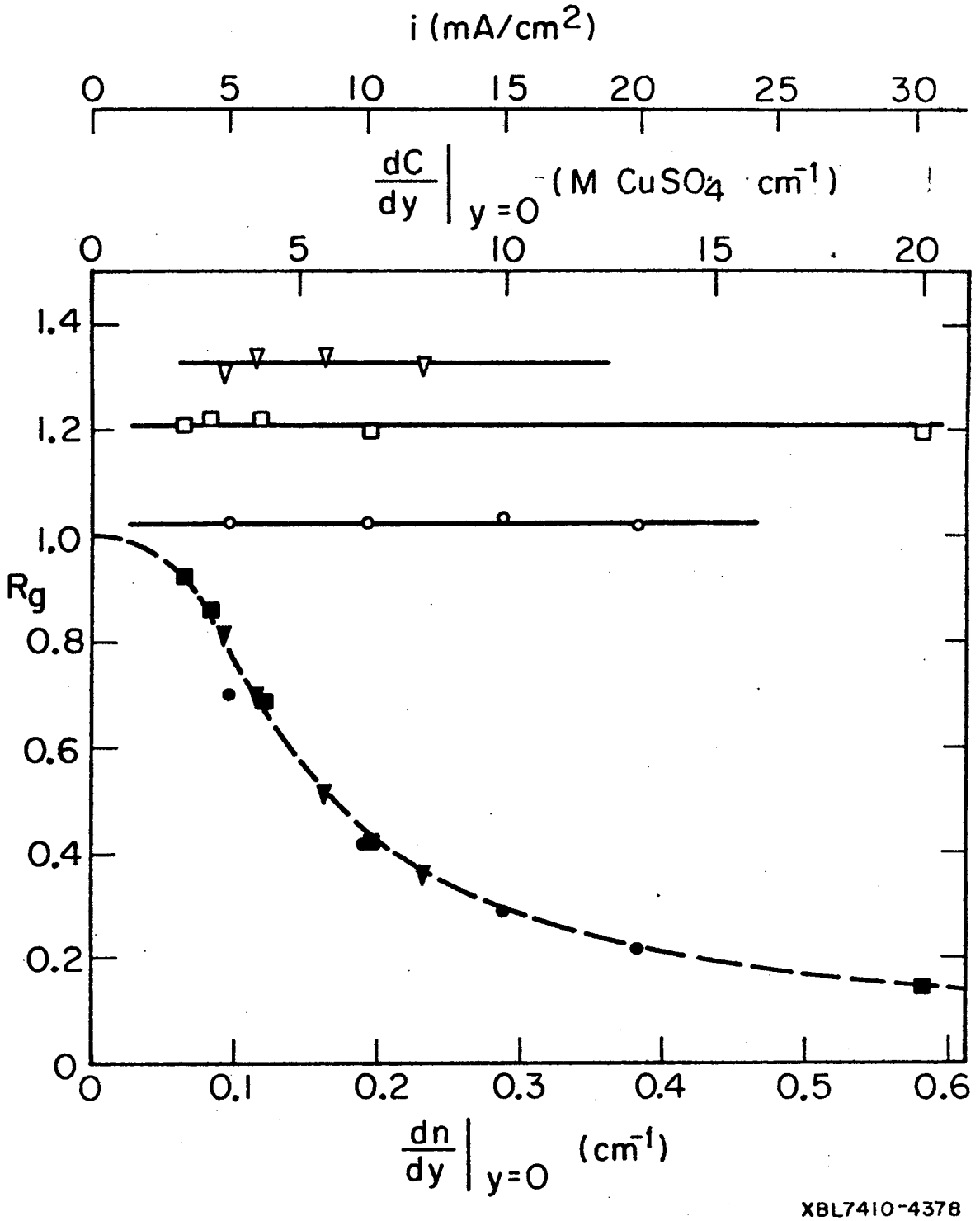

Fig. 5

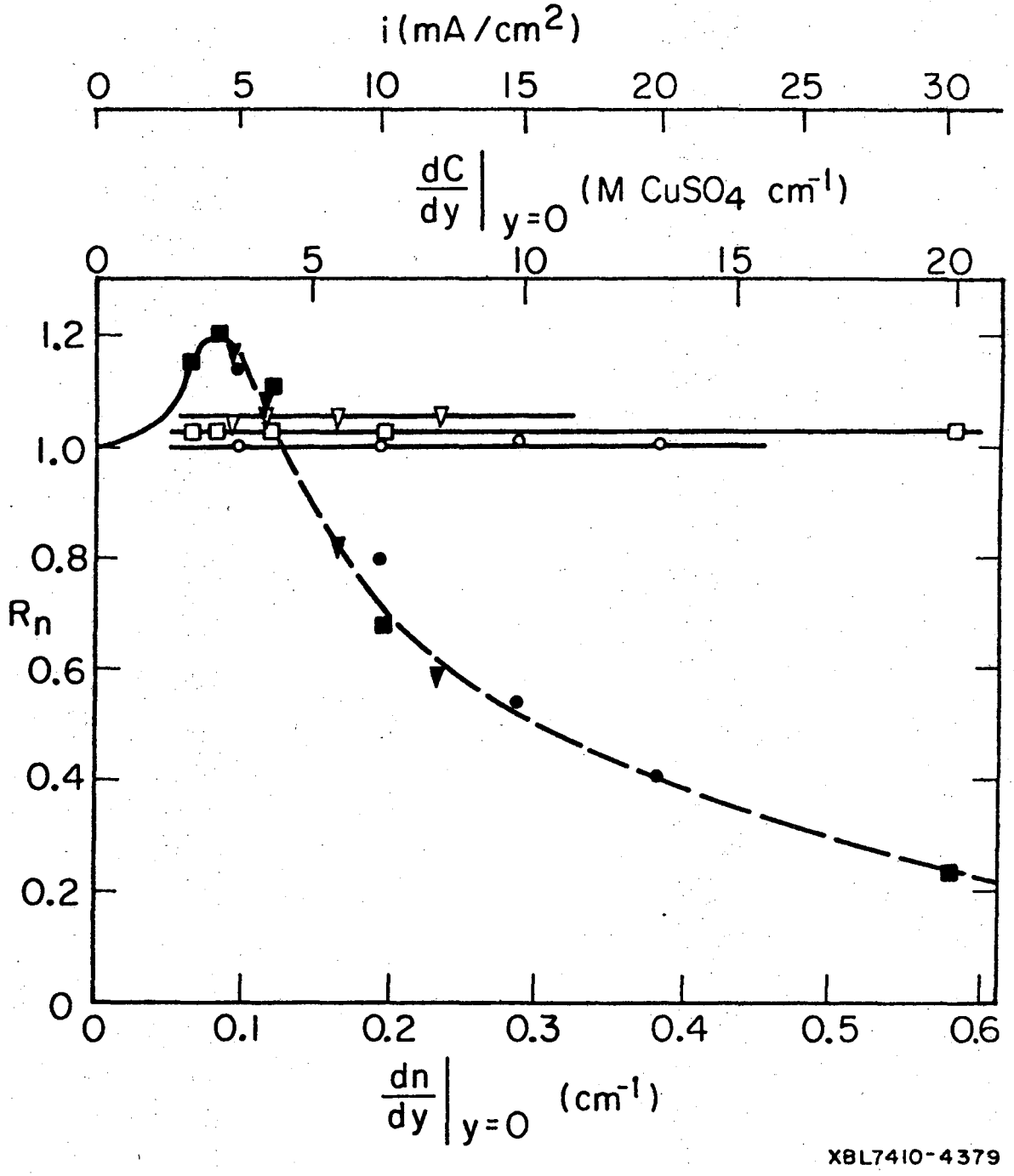

Fig. 6

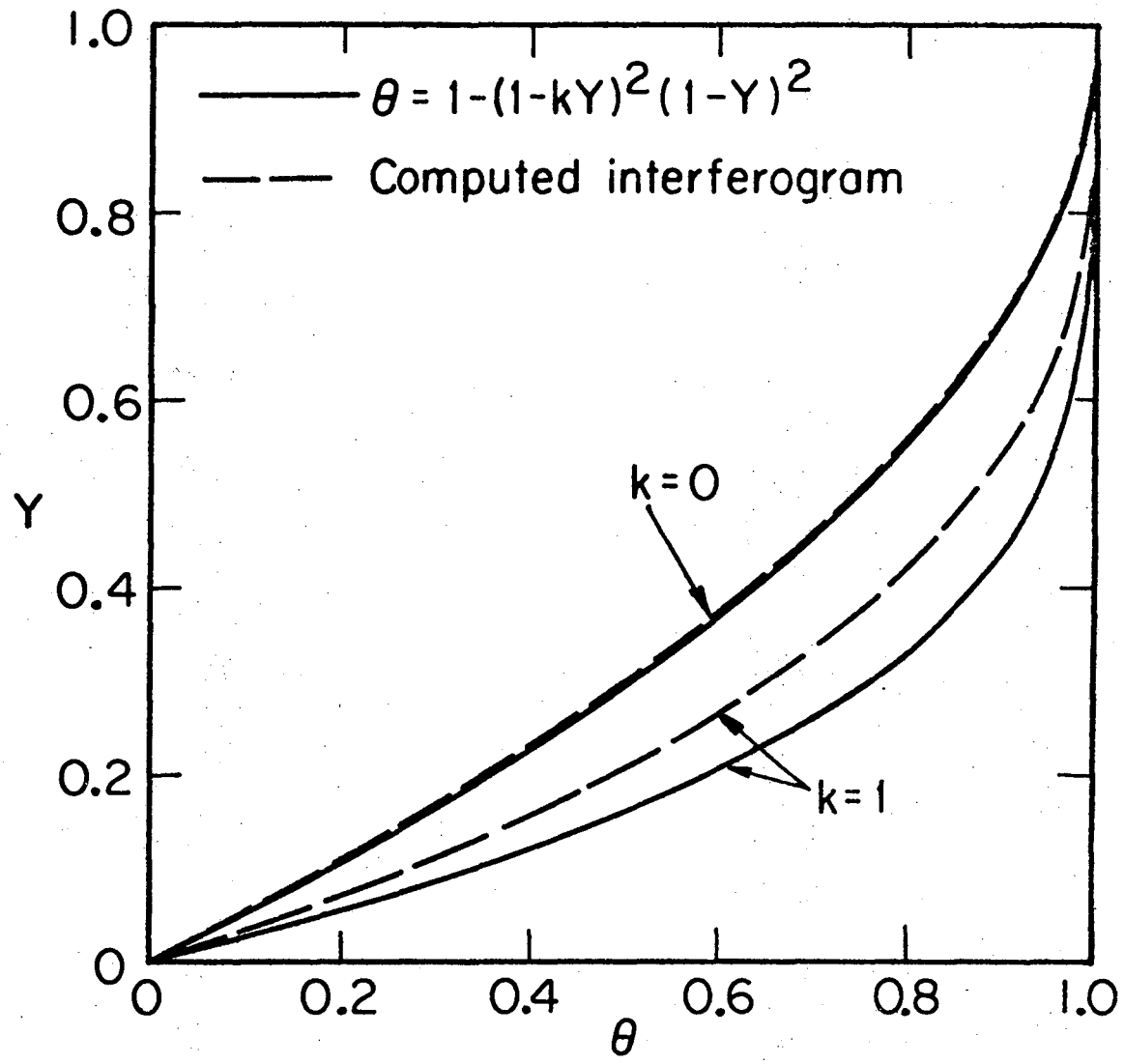
1.0
0.8
0.6
0.4
0.2
0
Y
0
0.2
0.4
0.6
0.8
1.0
θ
θ = 1-(1-kY)²(1-Y)²
Computed interferogram
k=0
k=1
XBL7411-4574

Fig. 7

3. SURFACE REFLECTION EFFECTS IN INTERFEROMETRY

Introduction

Interferometry has been frequently used for the observation of refractive-index variations in fluids near solid surfaces.[1-3] When no refractive-index gradients are present in the interfacial region, i.e., the fluid has everywhere a constant refractive-index, the resulting interference fringes are expected to be uniformly straight, and the solid-fluid interface is expected to coincide with the shadow of the solid on the interferogram. However, spurious fringe displacements in the interferograms of solid-fluid phase boundaries are often observed. We have now identified reflection as the chief cause of these distortions; the interference fringes bend as if a refractive-index gradient existed near the interface. Another limitation in the optical observation of such phase boundaries is diffraction, which will not be considered here.

Because reflected rays will traverse the fluid along broken lines (unreflected rays traverse a homogeneous fluid along straight lines), two types of distortions result in the interferogram: (a) Geometrical distortion due to displacement of the beam normal to its original propagation direction. This effect falsifies conventional interpretation of distance on the interferogram and causes displacement of the apparent interfacial location. (b) Phase distortion due to increased geometrical path length. The magnitude and character of each of these abberations depend strongly[4] on the choice of the plane of focus of the imaging objective lens.

It is the purpose of this chapter to present sample calculations of interferogram distortions caused by reflection from the slightly rounded leading edge of an otherwise planar surface and compare them with the corresponding experimental results. We will also recommend two simple methods for minimizing reflection effects.

Reflection from the Rounded Edge of a Planar Surface

Figure 1 schematically illustrates the reflection of an ray ABC from the rounded edge of a plane surface at point B. According to the Law of Reflection, the angle of reflection CBE, with respect to the surface tangent plane DBE, equals the angle of incidence ABD with respect to the same plane. Other rays that enter the specimen at higher locations $y \geqslant 0$ will not reflect from the surface and will traverse the specimen along straight lines parallel to the plane $y = 0$.

Figure 2 illustrates the trajectory of a reflected ray ABCD as it traverses a specimen consisting of a homogeneous fluid layer above a solid, both bounded by parallel flat glass sidewalls. The light ray is incident perpendicular to the glass walls and parallel to the planar region $y = 0$ of the solid surface.

Application of the Law of Reflection at point B in Fig. 2 provides the angle ϕ_f of the reflected ray $x_B \leqslant x \leqslant w$. Note that if $y_B \geqslant 0$, the incident ray misses the solid surface and $\phi_f = 0$. The ray angle in the glass wall $w \leqslant x \leqslant w + d$ is easily calculated from Snell's Law

$$n_f \cdot \sin\phi_f = n_g \cdot \sin\phi_g \tag{1}$$

and geometrical considerations show that the ray leaves the specimen at

$$y_D = y_B + (w - x_B)\cdot\tan\phi_f + d\cdot\tan\phi_g \qquad (2)$$

The beam has thus been displaced from its original location $y = y_B$ at $x = 0$ to $y = y_D$ at $x = w + d$. At the latter plane the ray enters the surrounding medium (e.g., air) and propagates to the interferometer imaging optics at an angle ϕ_a, easily calculated by Snell's Law. The optical path p_r of reflected ray ABCD is given by

$$p_r = n_f\cdot x_B + n_f\cdot(w - x_B)\sqrt{1 + \tan^2\phi_f} + n_g\cdot d\sqrt{1 + \tan^2\phi_g} \qquad (3)$$

All rays, provided they are accepted by the objective lens of the interferometer, appear to emanate from the virtual plane of focus of the objective lens. The virtual plane of focus is calculated[4] from the real plane of focus (which is optically conjugate to the interferometer film plane) as follows: If the real plane of focus lies at some plane $x = x_f$, the virtual plane of focus lies at the plane $x = w + d - F$, where

$$F = \frac{w - x_f}{n_f} + \frac{d}{n_g} \qquad . \qquad (4)$$

F is depicted on Fig. 2 as the horizontal distance between the plane of light-exit from the specimen and the virtual plane of focus RQ.

The reflected ray ABCD on Fig. 2 appears to emanate from its virtual origin Q, which is a vertical distance $S = F\cdot\tan\phi_a$ below the location Y_D where the reflected ray leaves the specimen. Therefore, the reflected ray ABCD appears on the interferogram at a position

$$y_i = y_D - F\cdot\tan\phi_a \qquad (5)$$

The phase on the interferogram is calculated by comparing the optical path of the reflected ray Eq. (3) with that of a hypothetical unreflected ray GQE passing through the virtual origin Q. The exit points D and E of each ray lie on an equiphase arc DE centered on the virtual origin Q. Beyond points D and E the interferometer introduces no phase difference between the rays ABCD and GQE. The optical path p_o of the hypothetical unreflected ray GQE is calculated by considering the length $T = F(\sqrt{1 + \tan^2\phi_a} - 1)$:

$$p_o = n_f \cdot w + n_g \cdot d + n_a \cdot F \cdot (\sqrt{1 + \tan^2\phi_a} - 1) \qquad (6)$$

The phase on the interferogram is given in fringe shifts as

$$N = \frac{p_r - p_o}{\lambda} \qquad (7)$$

Calculation of Interferograms for Reflection from the Edge of a Planar Surface

The present work arises from the interferometric study[4-6] of concentration profiles in aqueous $CuSO_4$ electrolyte near planar copper surfaces. The copper electrodes are w = 10.0 mm wide and fully occupy the space between the d = 12.7 mm wide parallel optically flat glass sidewalls (as in Fig. 2). The modified Mach Zehnder interferometer has been described elsewhere.[5] The objective lens of this interferometer can accept light emanating from the specimen at angles up to 7.0°.

The electrode surfaces were carefully polished with progressively finer (up to #600) grades of carbide paper using kerosene as a carrier for the chromium oxide (initial) and 1 μm diamond paste (final) abrasives. Electrode surface profiles[7] are illustrated in Fig. 3, curve a, and

Fig. 4. Figure 3, curve a, represents a typical surface profile for a long (100 cm) electrode, Fig. 4, curve a, shows the flattest smooth surface that could be obtained for a short (5 cm) electrode, and Fig. 4, curve b, indicates a surface with a deliberately rounded edge. The actual surface roughnesses, not shown on the surface profiles, are about 1.0 μm peak-to-peak. The central (1 mm < x < 9 mm) regions of the surfaces are flat to within 1.0 μm.

The rounded edge shown in Fig. 3, curve a, has been approximated by a hyperbolic curve

$$y = -0.00125/x \tag{8}$$

for ease of computation (curve b in Fig. 3).

In the calculations that follow, all incident light rays are assumed to enter the specimen parallel to the planar solid surface y = 0. If the beam entered at a negative angle with respect to the plane y = 0, i.e., impinging on the planar region of the surface, the interferogram distortions due to a reflection would be more pronounced. If the incident rays entered at a positive angle, i.e., shielded from the planar surface by the edge of the surface, the distortions would be less pronounced.

The light wavelength used in the calculations was λ = 632.8 nm, corresponding to the HeNe laser light source used in our experiments. The fluid refractive-indices were set n_f = 1.0 and 1.334, corresponding to air and 0.1 M $CuSO_4$, respectively. The 12.7 mm wide glass sidewalls had a refractive-index n_g = 1.5231. Refraction in the glass walls has a negligible effect[2] on the computed interferogram. The refractive-index of the surrounding medium was set n_a = 1.0 (air).

Calculation of the trajectories and optical paths of several (e.g., 10) reflected rays for different planes of focus allows construction of the interferograms--phase vs distance relationships--associated with reflection from the electrode edge. The following stipulation applies to the calculations: a reflected ray must be accepted by the aperture of the objective lens in order to contribute to the interferogram. Rays emanating from the specimen at angles higher than 7.0° are, therefore, not considered in the construction of the interferogram.

Computed interference fringes are shown in Fig. 5 for different planes of focus. The shape of the curves is seen to depend strongly on the choice of plane of focus and only weakly on the fluid refractive-index. The extent of the curves depend on the maximum angle of acceptance of the objective lens. The end point of each curve (e.g., $y = -0.03$ mm and $N = -3$ fringes for focus B) is determined by this maximum angle (here 7.0°). For a large acceptance angle the curves would extend more, i.e., to lower y-values for focus A and B and to higher y-values for focus C and D. For focus at $x \leq 0$ the interface will thus appear receded from its true location $y = 0$, and spurious fringe shifts will appear near the apparent interface. These spurious fringes create the false impression that a region of lower refractive-index exists near the apparent interface.

For focus at $x > 0$ the calculations suggest a double value of phase in the interferogram and no distortion in the apparent interfacial location. Therefore, the true interface can be found on the interferogram by creating a plane of focus $x_f > 0$.

Observed Interferograms

Figure 6 shows experimental interferograms of the interface between homogeneous 0.1 M $CuSO_4$ electrolyte (fluid phase refractive-index corresponds to the dashed lines in Fig. 5) and the electrode surface curve a in Fig. 3. Note that there are no concentration or temperature gradients in the electrolyte. For focus at $x \leq 0$ the experimental interferograms show substantial agreement with the interference fringes predicted (Fig. 5) for the hyperbolic surface approximation Eq. (8). For focus at $x > 0$ the apparent interface does indeed coincide with the true surface $y = 0$, but a double value of phase cannot easily be identified on the interferogram. Instead, diffraction fringes, caused by defocusing of the "edge" of the electrode surface, appear to be more prominent.

Figure 7 illustrates the interferograms of the interfaces between air and the two copper surfaces shown in Fig. 4. At a given plane of focus, the interferogram of the purposely rounded surface (b) shows more distortion than the interferogram of the flatter surface (a).

Figure 8 compares the interferograms of the phase boundary between 0.1 M $CuSO_4$ and the copper surface Fig. 3, curve a, for full (7.0°) objective lens aperture and restricted (0.5°) aperture. Restricting the lens aperture reduces the interferogram distortion.

Discussion

Figure 6 demonstrates that reflected rays from the only slightly rounded edge of an otherwise planar surface can cause a large discrepancy between the true location of the interface and the apparent location (shadow) in the interferogram. There are two simple methods for finding the true interface when reflection effects are present:

(a) Variation of the plane of focus by moving the camera parallel to the electrode surface until a constant interfacial location is observed--i.e., until the location does not change with further change in the plane of focus; (b) Restriction of the objective lens aperture so that no off-axis reflected rays are accepted by the lens; as in Fig. 8.

Although these techniques will locate the true planar surface on the interferogram, a word of caution is in order: The two methods should not be used to find the true interface when refractive-index gradients are present in the fluid. Rays deflected[4,6] by the refractive-index field must be accepted by the objective lens; this contribution is necessary to construct a valid interferogram. Restriction of the objective lens aperture would correspond to a loss of information on the interferogram. Since variations of the plane of focus can have large effects on interferograms, a fixed plane of focus is recommended.[4]

The effect of edge curvature on the interferograms shown in Fig. 7 suggests that reflection from macroscopically curved surfaces, i.e., spheres and cylinders, would also distort interferograms. Failure to account for reflection effects in the interferometric study of fluid-phase refractive-index variations near <u>any</u> extended surface can lead to significant errors in the determination of the interfacial location and interfacial refractive-index. For example, this would result in deriving erroneous interfacial concentrations and boundary layer thicknesses in the interferometry of concentration fields.

REFERENCES

1. W. Hauf and U. Grigull in Advances in Heat Transfer, J. P. Hartnett and T. F. Irvine, eds. (Academic Press, N. Y., 1970), Vol. 6, pp. 133-366.

2. R. H. Muller in Advances in Electrochemistry and Electrochemical Engineering, R. H. Muller, ed. (Wiley-Interscience, N. Y., 1973), Vol. 9, pp. 326-353.

3. R. B. Kennard, J. Res. Natl. Bur. Stand. (U. S.) 8, 787 (1932).

4. K. W. Beach, R. H. Muller and C. W. Tobias, J. Opt. Soc. Am. 63 559 (1973).

5. K. W. Beach, R. H. Muller and C. W. Tobias, Rev. Sci. Instr. 40, 1248 (1969).

6. See Section 2.2.

7. Surfanalyzer Model 150 System, Clevite Corp. Cleveland, Ohio.

NOMENCLATURE

d	glass wall width (mm)
F	location of virtual plane of focus (mm)
n_a	refractive-index of medium surrounding specimen (e.g., air)
n_f	refractive-index of fluid
n_g	refractive-index of glass walls
N	interferometric phase change (fringes)
p_r	optical path of a reflected ray (mm)
p_o	optical path of hypothetical unreflected ray (mm)
w	solid surface width (mm)
x	horizontal distance (mm)
x_f	location of plane of focus (mm)
x_B, y_B	position where a ray is reflected (mm)
y	vertical distance (mm)
y_D	position where a reflected ray leaves specimen (mm)
y_i	distance on an interferogram (mm)
λ	wavelength (nm)
ϕ_a	angle of reflected ray in surrounding medium (rad)
ϕ_f	angle of reflected ray in fluid (rad)
ϕ_g	angle of reflected ray in glass wall (rad)

FIGURE CAPTIONS

Fig. 1. Reflection from the rounded edge of a planar surface.

- ABC incident ray reflected at point B
- DBE surface tangent plane at point B

Fig. 2. Reflected ray trajectory.

- ABCD reflected ray
- GQE hypothetical unreflected ray
- RQ virtual plane of focus
- Q virtual origin of ray ABCD
- DE equiphase arc centered on virtual origin Q
- d glass wall thickness
- w solid surface width
- x_B position where ray is reflected
- ϕ_a ray angle in surrounding medium
- ϕ_f ray angle in fluid
- ϕ_g ray angle in glass
- F,S,T see text

Fig. 3. Electrode surface profiles.

- a measured profile
- b hyperbolic approximation $y = 0.00125/x$

Fig. 4. Electrode surface profiles.

- a sharpest edge obtainable
- b purposely rounded edge

Fig. 5. Calculated interferograms associated with reflection from the hyperbolic surface profile approximation Fig. 3b.

——— n_f = 1.0000 (air)

- - - - n_f = 1.3340 (0.1 M $CuSO_4$)

A location of real plane of focus x_f = -0.5 mm

B x_f = 0

C x_f = 0.5 mm

D x_f = 1.0 mm

Fig. 6. Experimental interferograms of the interface between 0.1 M $CuSO_4$ and the electrode surface profile 3a. Designations as in in Fig. 5.

Fig. 7. Effect of surface edge curvature on experimental interferograms. Interface between air and the electrode surfaces shown in Fig. 4.

A x_f = 0, surface 4a

B x_f = 0, surface 4b

C x_f = 0.5 mm, surface 4a

D x_f = 0.5 mm, surface 4b

Fig. 8. Effect of aperture restriction on experimental interferograms. Interface between 0.1 M $CuSO_4$ and surface 3a.

A full (7.0°) aperture

B restricted (0.5°) aperture

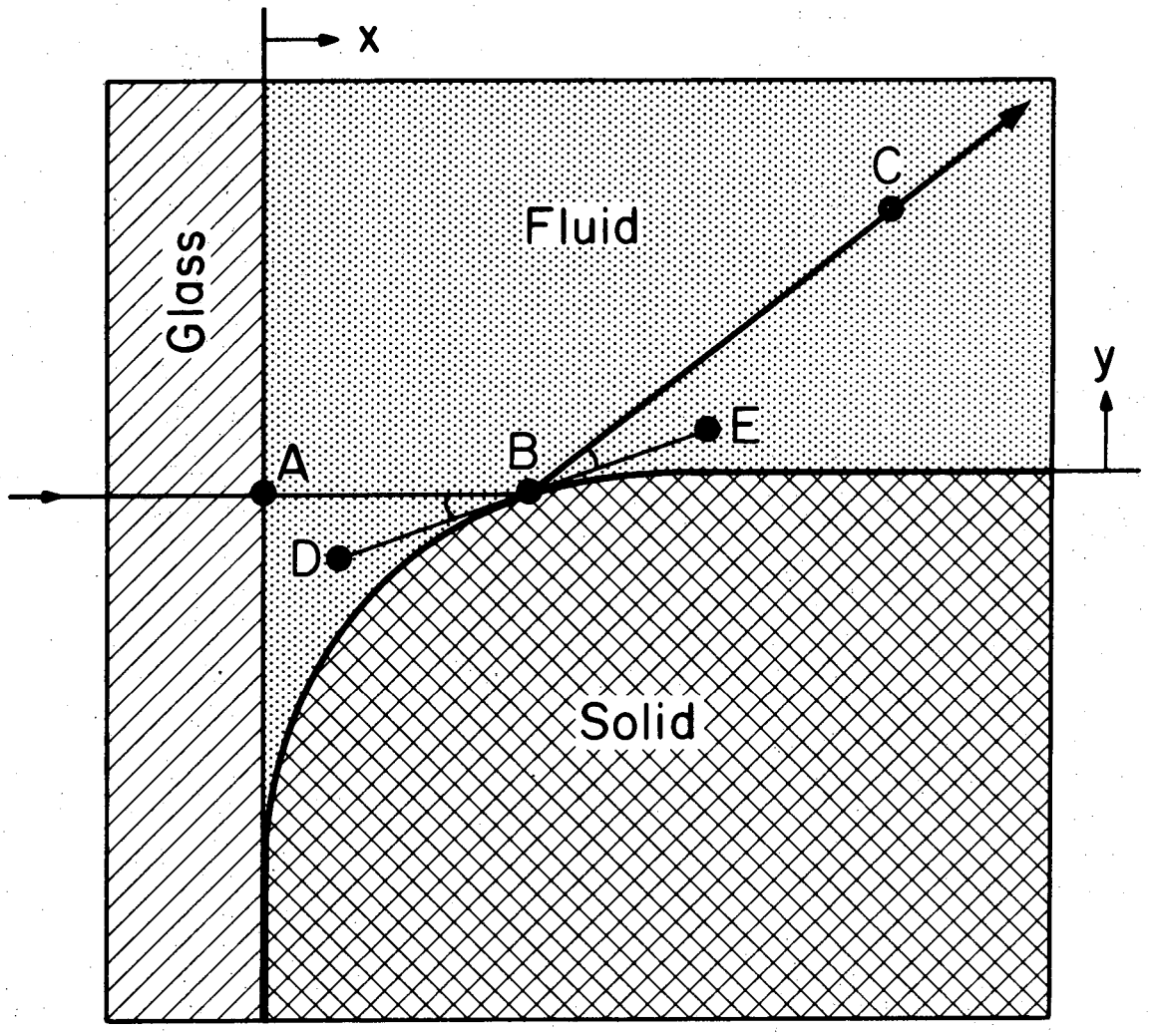

XBL7311-4556

Fig. 1

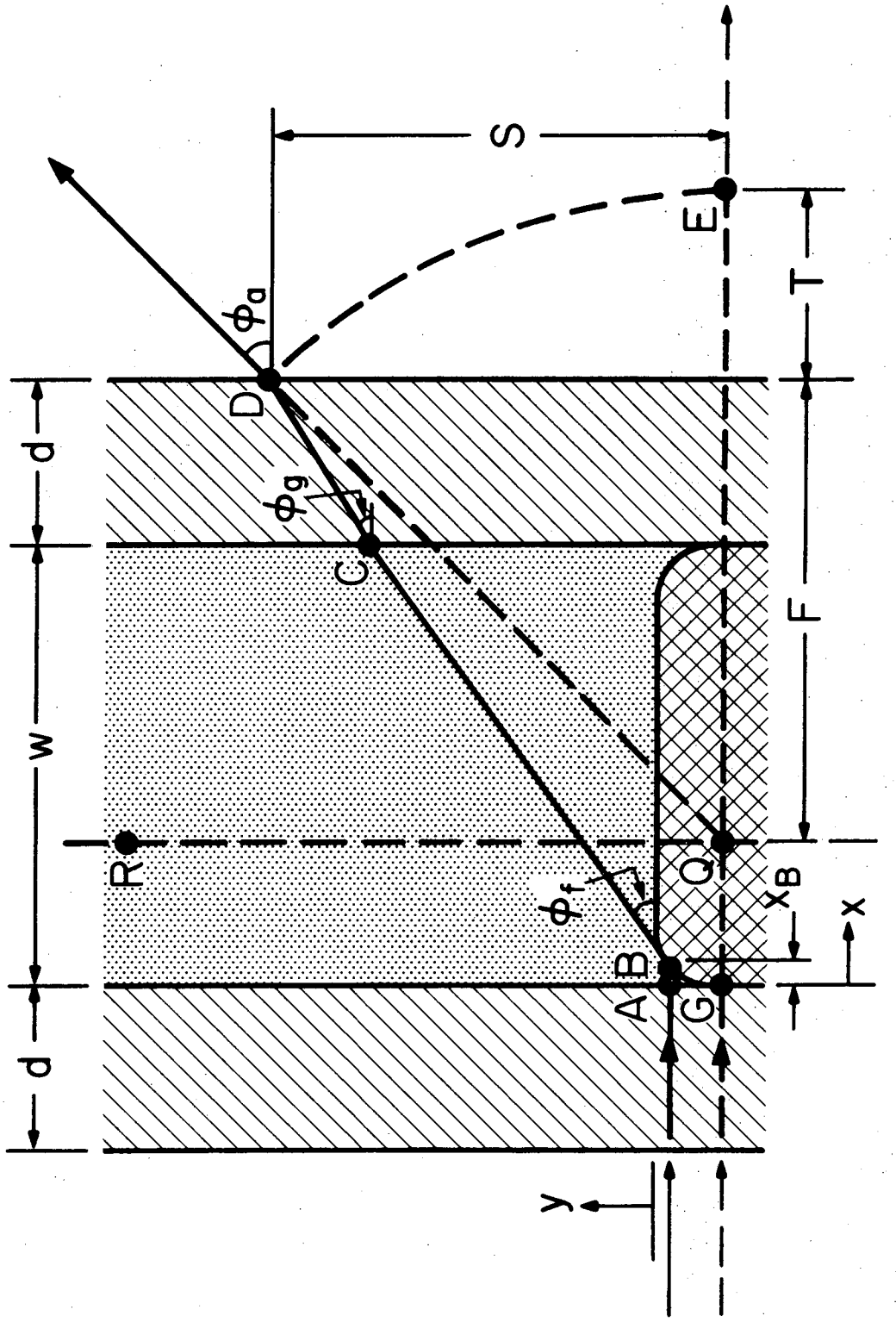

XBL748-4044

Fig. 2

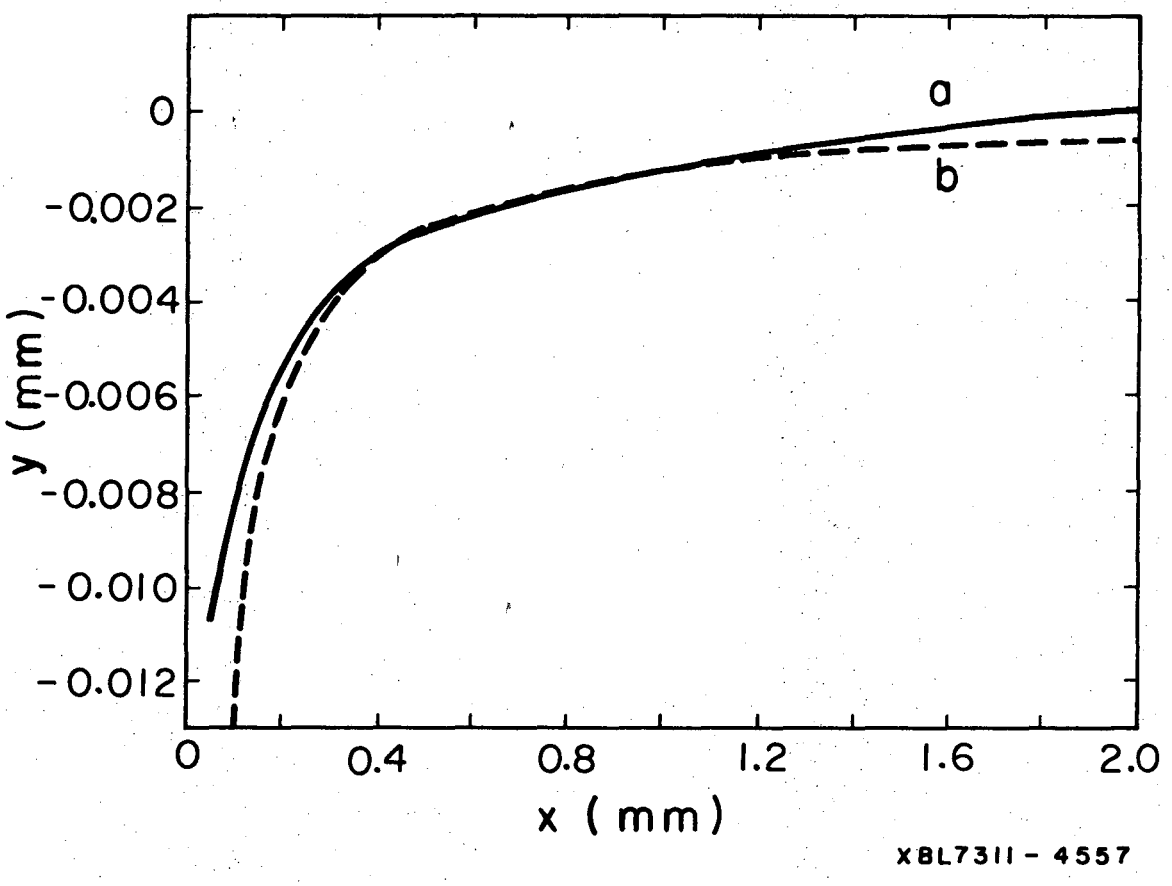

Fig. 3

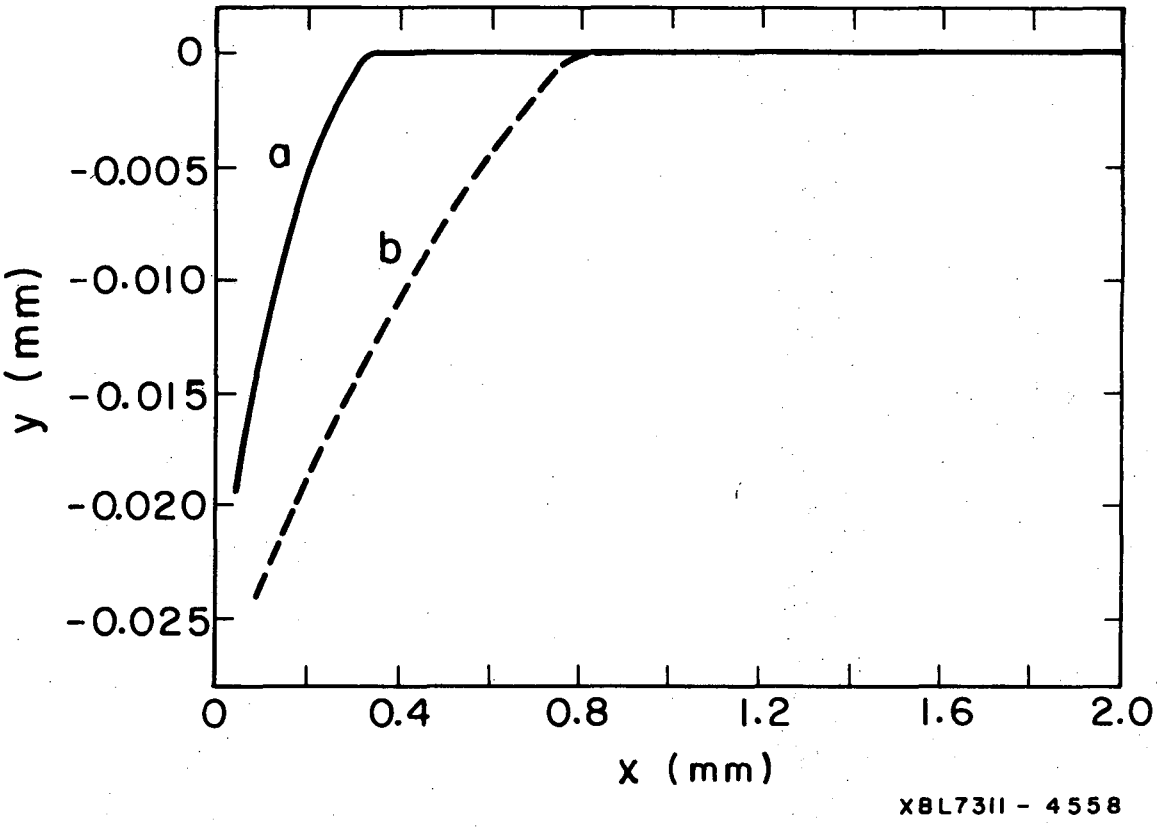
0
-0.005
-0.010
-0.015
-0.020
-0.025
y (mm)
a
b
0
0.4
0.8
1.2
1.6
2.0
x (mm)
XBL7311 - 4558

Fig. 4

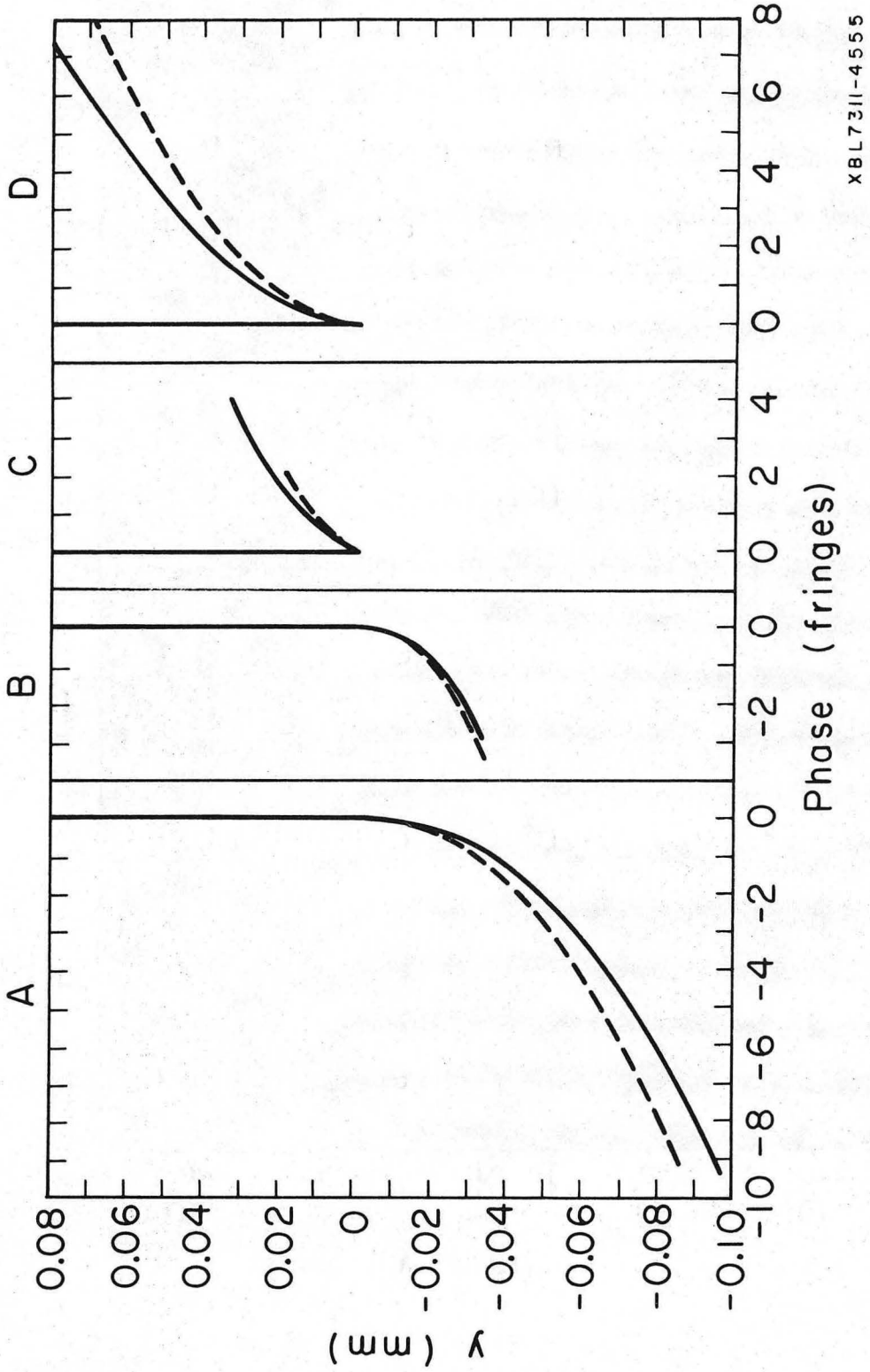

Fig. 5

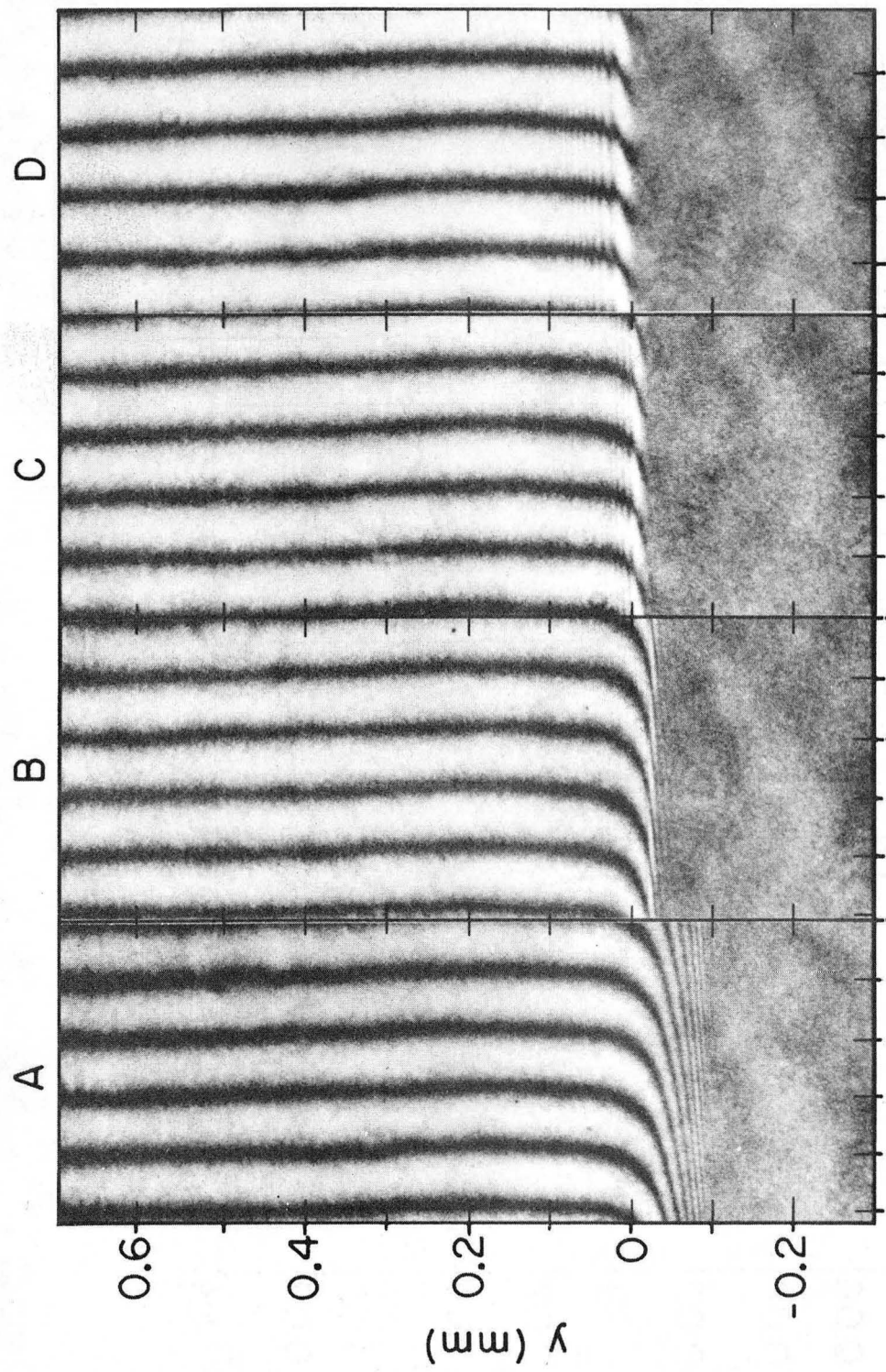

XBB 7311-7012

Fig. 6

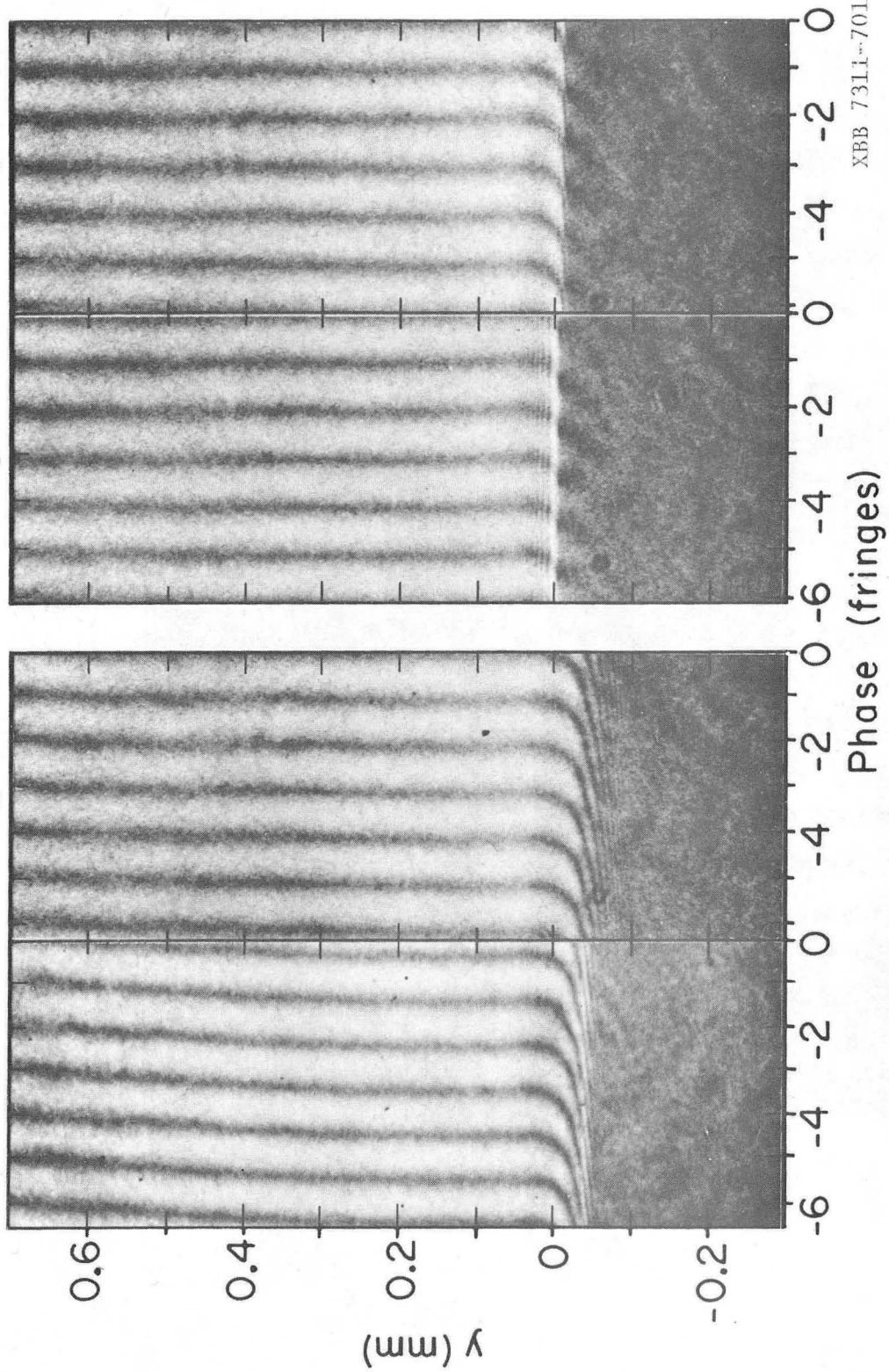

Fig. 7

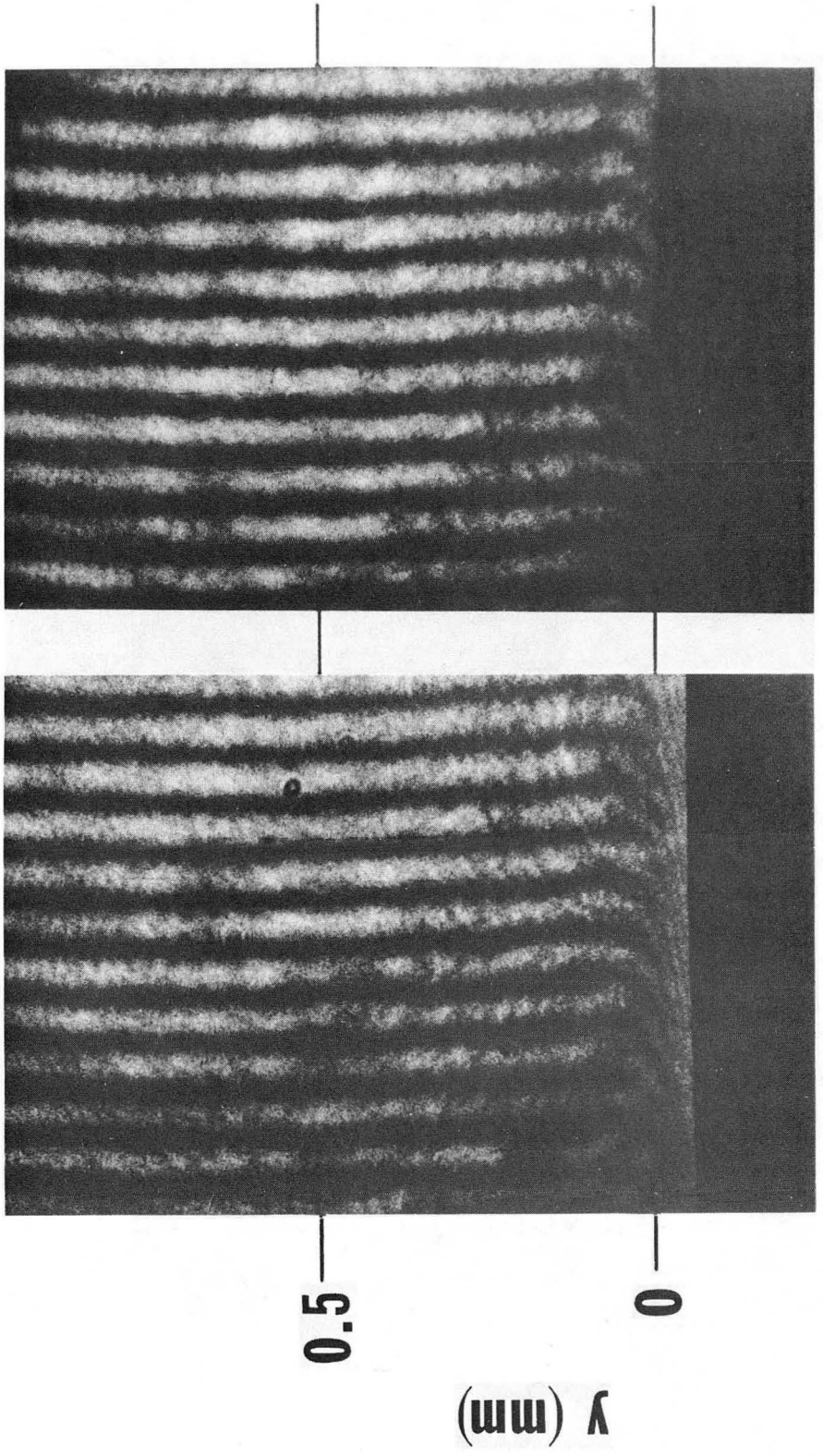

XBB 7411-8120

Fig. 8

4. INTERFEROMETRIC STUDY OF TRANSIENT DIFFUSION LAYERS

Concentration changes in the electrolyte contained between working electrodes are often confined to a thin boundary layer region near the electrode surface. Measurement of the electrolyte concentration profiles in these layers can be useful in the study of transport phenomena in electrochemical systems.[1] Double-beam interferometry[2] offers the following advantages for such measurements: (a) possibility of high resolution of concentration changes (10^{-5} M) and of distance (10^{-3} mm), (b) continuous observation of small (1 mm^2) regimes at the surface, (c) no restriction of the applied current level and (d) no interference with the electrolyte flow or alteration of the electrode surface. However, interferometry is suitable for the determination of concentration profiles only in binary systems, i.e., when the local refractive-index depends only on the concentration of a single solute. For this reason the method is not applicable when a supporting electrolyte (e.g., H_2SO_4 in the case of copper deposition) is also present.

Previous interferometric studies[3-6] of concentration changes in electrochemical systems have been based on the conventional interpretation of interferograms, in which local phase change in the interferogram is directly related to local refractive-index variation in the object. Such interpretation assumes that all light rays travel along straight paths as they traverse the specimen. We have shown, however, that: (a) Deflection (refraction, Schlieren effect) of the beam as it passes through the refractive-index field can lead to large errors[8] if interferograms are interpreted in the conventional manner.

(b) Reflection[9] of light rays from the even slightly rounded edge of an otherwise planar electrode surface can likewise lead to large errors. These optical distortions must be taken into account if reliable information regarding interfacial concentration, concentration gradient and boundary layer thickness is to be obtained from experimental interferograms.

It is the purpose of this chapter to present concentration profiles derived by the interferometric study of the diffusion layer formed by constant-current electrodeposition and compare them with those predicted by the appropriate solution of the one-dimenional equation of unsteady diffusion. This also supports the validity of the the optical analysis.[8,9]

Experimental

A cross-sectional sketch of the interferometer and electrochemical cell is presented in Fig. 1. The electrodes are 1.00 m long, and the cell is the heart of a 3.00 m long flow channel. The regions upstream and downstream of the electrodes were sealed off by lucite blocks during the diffusion experiments. The electrolyte temperature was 20°C ± 1°C.

One side of each electrode was polished flat to within 0.03° and 0.3 μm (peak-to-peak) roughness using progressively finer (to #200) carbide paper with chromium oxide (initial) and 1.0 μm diamond paste (final) abrasives (kerosene was used as a lubricant). Each electrode working surface was then polished in a similar manner using a right-angle polishing jig that travelled flush to both the previously polished side

(non-abrasive contact) and the working surface (abrasive contact). The resulting electrode working surface was flat to within 1.0 μm (over 80% of its width) and 1.0 μm (peak-to-peak) roughness. This procedure caused the electrode working surfaces to be slightly rounded such that the edges were 0.01 mm lower than the center of the surface. The actual surface profiles were measured with a profileometer[10] and are shown elsewhere.[9,11]

This polishing technique permitted alignment of the test beam with the electrode by reflecting the beam from the polished side of the electrode such that it retraced its path. This procedure guaranteed that the incident light rays would traverse the cell parallel to the electrode working surface to within 0.1°. The effect of beam misalignment on interferograms is discussed elsewhere.[7]

The modified Mach-Zehnder interferometer was mounted on a lathe bed to permit travel of the instrument along the length of the electrodes. (Details of the interferometer and the flow channel are given elsewhere.[12,13]) The channel was oriented with the electrode working surfaces perpendicular to the gravitational field. The cathode was observed in two orientations: facing up and facing down. Constant current at preset values of 5.0 and 10.0 mA/cm^2 was passed through the cell. The interferograms of the resulting transient diffusion layers were recorded by a Bolex Paillard 16 mm motion picture camera on Kodak Plus-X film at 20 frames/sec. The camera was positioned such that the plane of focus (optically conjugate to the camera film plane) was located on the inside of the glass wall farthest from the camera. This is the recommended[7] plane of focus for interferometric observation of cathodic boundary layers. The film was later developed and analyzed

by projecting it onto a table and extracting the phase vs distance information.

Theory of Transport

The convection-free electrodeposition of a metal cation from a stagnant aqueous binary salt electrolyte is described by the unsteady diffusion equation in one dimension:

$$\frac{\partial C}{\partial t} = \frac{\partial}{\partial x}\left(D \frac{\partial C}{\partial x}\right) \tag{1}$$

Equation (1) can account for variation of the diffusion coefficient D with electrolyte concentration C and represents a simplification* of the complete diffusion equation, which is given on page 225 of Ref. 1.

Current density is related to the interfacial concentration gradient by:

$$i = \frac{zFD}{1 - t_+} \left.\frac{\partial C}{\partial x}\right|_{x=0} \tag{2}$$

For galvanostatic electrodeposition, the boundary conditions to Eq. (1) are:

$$\frac{\partial C}{\partial x} = \frac{i(1 - t_+)}{zFD} \quad \text{at} \quad x = 0 \;, \quad t > 0 \tag{3}$$

$$C = C_b \quad \text{at} \quad t \leqslant 0 \;, \quad \text{all } x \tag{4}$$

$$C = C_b \quad \text{as} \quad x \to \infty \tag{5}$$

If the diffusion coefficient D and cation transference number t_+ are assumed invarient with concentration, the solution to the above equations is the well-known Sand equation.[8,18]

*Variations of the cation transference number t_+ are not accounted for in Eq. (1).

The actual variation of the $CuSO_4$ diffusion coefficient over the range 0-0.1 M $CuSO_4$ is illustrated in Fig. 2. Smoothed data of Eversole, Kindsvater and Peterson,[16] corrected to 20°C, are indicated by the solid curve. We can approximate the physical property variations as linear functions of electrolyte concentration:

$$\frac{D}{D_o} = 1 - \alpha\theta \tag{6}$$

$$\frac{1 - t_+}{(1 - t_+)_o} = 1 + \gamma\theta \tag{7}$$

The subscripted properties correspond to zero electrolyte concentration, and θ is a dimensionless concentration C/C_b. Two linear approximation curves are shown on Fig. 2, each indicating the proper value of diffusion coefficient at C = 0.1 M $CuSO_4$. The curve for $\alpha = 0.0869$ accurately represents the data for $0.04\ M \leq C \leq 0.10\ M$, while the curve for $\alpha = 0.141$ approximates the data over the entire range $0 \leq C \leq 0.1$ M. The variation of cupric ion transference number measured by Fritz and Fuget[17] can be represented by $(1 - t_+)_o = 0.597$ and $\gamma = 0.0648$ over the range $0 \leq C \leq 0.1$ M $CuSO_4$.

The appropriate equations of unsteady diffusion can now be derived (using Eqs. (1) through (7)):

$$\frac{\partial\theta}{\partial t} = D_o\left[(1 - \alpha\theta)\ \frac{\partial^2\theta}{\partial x^2} - \alpha\left(\frac{\partial\theta}{\partial x}\right)^2\right] \tag{8}$$

$$\theta = 1 \quad \text{at} \quad t \leq 0 \quad , \quad \text{all } x \tag{9}$$

$$\theta = 1 \quad \text{as} \quad x \to \infty \tag{10}$$

$$\frac{\partial\theta}{\partial x} = \frac{i(1 - t_+)_o}{ZFD_oC_b}\ \frac{1 + \gamma\theta}{1 - \alpha\theta} \quad \text{at } x = 0,\ t > 0 \tag{11}$$

These equations can be solved by standard numerical techniques. Casting the equations into Crank-Nicholson finite difference representation[14] and solving the resulting system of nonlinear algebraic equations by the Thomas method[15] determines the theoretical concentration profiles to within about 0.0002 M $CuSO_4$ (see below). Details are given in Appendix III.

Concentration profiles were calculated from Eqs. (8) through (11) using the above-mentioned numerical techniques. For $\alpha = \gamma = 0$, the numerical solution matches the closed-form solution (Sand equation[8,18]) to within 0.0002 M $CuSO_4$ for step sizes of 0.001 mm and 0.1 sec.

Interpretation of Interferograms

Figure 3 illustrates the analysis of a single interferogram recorded at a downward facing cathode after 30 sec of electrolysis at 10.0 mA/cm^2. The ordinate denotes distance from the true (undistorted by refraction or reflection) image of the electrode surface. The abscissa relates electrolyte concentration to interferometric phase change (in fringes) according to the conventional interpretation of interferograms. The location of the true interface $x = 0$ on the experimental interferogram is estimated by the method of focal plane variation outlined in Ref. 9. This technique locates the interface to within about 0.01 mm when no refractive-index gradients are present in the electrolyte (i.e., before switching on the current) by reducing the phase and distance distortion caused by reflection from the slightly rounded electrode edge. Now that the interface $x = 0$ is defined, the phase vs distance information obtained from analysis of the developed film can be plotted as the experimental interferogram depicted by the open circles on Fig. 3.

The experimental interferogram is now interpreted by a method[19] that accounts for light-deflection (only) in the refractive-index field. This iterative technique determines the concentration profile (dashed line in Fig. 3) associated with a computed interferogram (solid line in Fig. 3) that best matches the experimental interferogram. The good agreement can be seen by comparing the computed and experimental interferograms in Fig. 3.

At this juncture, the shape of the computed interferogram may well agree with the shape of the experimental interferogram. However, the computed fringe could suggest an apparent (i.e., on the interferogram) interfacial location B different than that indicated by the experimental interferogram A (neither of which corresponds to the true interfacial location $x = 0$). Small (0.01 mm) errors in the original determination of the true interfacial location can have a comparable (0.02 mm) effect on this difference between experimental (A) and computed (B) end points.

Reflection from the edge of the electrode surface when refractive-index gradients are present in the electrolyte can have an effect much like reflection when no gradients are present: the apparent interfacial location can be different from the location expected considering light-deflection alone. Reflection thus causes two sources of error: (a) an 0.01 mm uncertainty in the determination of the true interfacial location without refractive-index gradients present in the electrolyte and (b) 0.02 mm uncertainty in measurement of the apparent interfacial location when refractive-index gradients are present.

Results

For all experiments performed, the estimated error in the interferometrically derived current density was about ±10%. The derived current densities are compared to the applied currents on Fig. 4. The interferometrically derived transient interfacial concentrations for an experiment at 10 mA/cm^2 are shown in Fig. 5. Also shown are the theoretical interfacial concentrations for $\alpha = 0$ (Sand equation) and for $\alpha = 0.0869$ and $\alpha = 0.141$. While the uncertainty in derived interfacial concentrations precludes assigning a particular value of α as best representing the actual variation of diffusion coefficient with concentration, the results do suggest better experimental agreement with numerical solutions for variable physical properties than with the Sand equation. The cell potential is also plotted, illustrating a rise in potential difference between anode and cathode due to a rapid change in concentration overpotential at the cathode when zero concentration is approached at the cathode surface.

Figure 6 compares the interferometrically derived transient interfacial concentrations for two different current densities with those predicted by the numerical solution using $\alpha = 0.0869$. The theoretical (solid) curves are bounded by dashed curves corresponding to numerical solutions for $D_o = 5.4 \times 10^{-6}$ cm^2/sec ± 10%, representing a possible uncertainty in electrolyte diffusion coefficient. The accuracy of the interferometric technique used in this study is evidently comparable to the uncertainty in diffusion coefficient.

This is in contrast to the apparent $CuSO_4$ diffusion coefficient $D = 3.2\times10^{-5}$ cm^2/s derived by Tvarusko and Watkins[6] from experimental interferograms of transient $CuSO_4$ diffusion layers. Their analysis failed to account for light-deflection effects, so the interfacial concentration gradient derived by the conventional interpretation of their interferograms was smaller than the actual gradient. The cause of this phenomenon is explained in Ref. 8 and is illustrated in Fig. 3: the interfacial concentration gradient depicted by the experimental interferogram is smaller than that of the true concentration profile. Inspection of Eq. (2) reveals why the diffusion coefficient D derived by Tvarusko and Watkins was too high: their measured interfacial concentration gradient was anomalously low. The magnitude of the error can be estimated from Fig. 10 in Ref. 8 to be approximately a factor of five, which accounts for the magnitude of the false value of $D = 3\times10^{-5}$. O'Brien's interferometric study[5] of the $CuSO_4$ diffusion layer also failed to consider light-deflection effects. The interferometrically derived current densities presented in Fig. 4 of Ref. 5 are 30-80% of the level of applied current, an anomoly which can be directly attributed to light-deflection effects.

On the other hand, the interferometrically derived concentration profiles presented by Hsueh and Newman[20] are substantially free of light-deflection errors. Their long (40 min) electrolysis times at constant potential resulted in a small interfacial concentration gradient (= 0.1 M $CuSO_4$ cm^{-1}) and negligible light-deflection effects.

The concentration profiles obtained here by interferometry can be analyzed to provide a measure of the cation transference number t_+ in

0.1 M $CuSO_4$ electrolyte. The total charge passed during constant-current electrolysis can be related to the electrolyte depletion within the diffusion layer as follows:

$$i\,t(1 - t_+) = zF\int_0^\infty (C_b - C)\,dx \quad . \tag{12}$$

Table 1 lists the cation transference numbers computed from both the corrected and uncorrected interferograms using Eq. (12). The values derived from the corrected interferograms are 5-24% higher than those given by Fritz and Fuget[17] (t_+ = 0.36 and 0.40 at C = 0.1 M $CuSO_4$ and C = 0, respectively), while those derived from the uncorrected interferograms show a wide variation with time and current density.

For short galvanostatic deposition times, results for the cathode facing upward matched those for the cathode facing down to within the above-mentioned accuracy. At times greater than 13 (or 18) sec for i = 10 (or 5) mA/cm^2, onset of natural convection became apparent as indicated clearly by irregular distortions of fringes above the surface.

Conclusions

The agreement between the interferometrically derived concentration profiles and those predicted by the numerical solution to the one-dimensional unsteady diffusion equation justifies the use of the new techniques[9,19] developed in this laboratory for interpretation of interferograms. We have shown that we can competently generate

Table 1

Cation Transference Numbers

i (mA/cm^2)	t(s)	Derived from uncorrected interferograms	Derived from corrected interferograms
		t_+	t_+
5	10	0.212	0.377
5	30	0.062	0.388
5	50	0.070	0.415
10	10	0.439	0.414
10	20	0.357	0.448
10	30	0.289	0.429
10	40	0.261	0.431

one-dimensional concentration profiles from interferograms. This opens the way for interferometric investigation of concentration fields formed by convection-controlled electrodeposition, where theoretical solutions for the concentration profiles are not available.

REFERENCES

1. J. S. Newman, Electrochemical Systems (Prentice-Hall, Inc., Englewood Cliffs, N. J., 1973).

2. R. H. Muller in Advances in Electrochemistry and Electrochemical Engineering, R. H. Muller, ed. (Wiley-Interscience, N. Y., 1973), Vol. 9, pp. 326-353.

3. C. S. Lin, R. W. Multon and G. L. Putnam, Ind. Eng. Chem. 45, 640 (1953).

4. N. Ibl and R. H. Muller, Z. Elektrochem. 59, 671 (1955).

5. R. N. O'Brien, J. Electrochem. Soc. 113, 389 (1966).

6. A. Tvarusko and L. S. Watkins, Electrochimica Acta 14, 1109 (1969).

7. K. W. Beach, R. H. Muller and C. W. Tobias, J. Opt. Soc. Am. 63, 559 (1973).

8. See part 2.2.

9. See Chapter 3.

10. Surfanalyzer Model 150 System, Clevite Corp., Cleveland, Ohio.

11. See part 1.2.

12. K. W. Beach, R. H. Muller and C. W. Tobias, Rev. Sci. Instr. 40, 1248 (1969).

13. K. W. Beach, Optical Methods for the Study of Convective Mass Transfer Boundary Layers on Extended Electrodes (Ph. D. Thesis), UCRL-20324, July 1971.

14. L. Lapidus, Digital Computation for Chemical Engineers (McGraw-Hill, N. Y., 1962), p. 162.

15. Ibid, p. 254-255.

16. W. G. Eversole, H. M. Kindsvater and J. D. Peterson, J. Phys. Chem. 46, 370 (1942).

17. J. J. Fritz and C. R. Fuget, J. Phys. Chem. 62, 303 (1958).

18. H. J. S. Sand, Phil. Mag. 1(6), 45 (1901).

19. See part 2.3.

20. L. Hsueh and J. Newman, Electrochimica Acta 16, 479 (1971).

NOMENCLATURE

C	electrolyte concentration (M $CuSO_4$)
C_b	bulk electrolyte concentration (M $CuSO_4$)
D	diffusion coefficient (cm^2/sec)
D_o	diffusion coefficient at C = 0 (cm^2/sec)
F	faraday constant (coul/eq)
i	current density (mA/cm^2)
t	time after current switch-on (sec)
t_+	cation transference number
x	distance from electrode surface (mm)
z	cation valence
α	constant (Eq. (6))
γ	constant (Eq. (7))
θ	dimensionless concentration C/C_b

FIGURE CAPTIONS

Fig. 1. Interferometer and electrochemical cell cross section.

————	Light path
- - - -	Off-axis rays demonstrating point-to-point relationship between plane of focus and film plane
A	Copper anode
C	Copper cathode
E	0.1 M $CuSO_4$ electrolyte
F	Film plane
G	Glass sidewalls
L	Lens. The test lens (focal length 87 mm) is 115 mm from the center of the cell. The focal length of the reference lens is 81 mm.
M	Mirror
S	Light source (HeNe laser)
U	Beam uniter
d	12.7 mm
h	25.4 mm
w	10.0 mm

Fig. 2. $CuSO_4$ diffusion coefficient.

———— Smoothed data of Eversole et al.,[16] corrected to 20°

— — — — Linear approximations to diffusion coefficient variation

- — -

Fig. 3. Interferogram interpretation.

ordinate: distance from electrode surface (mm)

abscissa: electrolyte concentration (M $CuSO_4$) or interferometric phase change (fringes)

o o o o experimental interferogram, i = 10.0 mA/cm^2, C_b = 0.1 M $CuSO_4$, t = 30 sec, cathode faces down.

- - - - concentration profile derived from experimental interferogram

_____ computed interferogram associated with derived concentration profile

. . . . theoretical concentration profile computed by numerical techniques for α = 0.0869

A apparent interfacial location on the experimental interferogram

B apparent interfacial location on the computed interferogram

Fig. 4. Derived current densities.

△ ▲ Conventional analysis of the experimental interferograms

○ ● Complete interferogram analysis (considering light-deflection and edge reflection)

—▲—● Applied current = 5.0 mA/cm^2

—△—○ Applied Current = 10.0 mA/cm^2

Fig. 5. Transient interfacial concentrations. $i = 10.0\ mA/cm^2$.

ordinate: interfacial concentration C_s (M $CuSO_4$) or cell voltage (volts)

abscissa: time after current switch-on (sec)

— — — numerical solution for $\alpha = 0$ (corresponds to the Sand equation)

——— numerical solution for $\alpha = 0.0869$, $D_o = 5.41\times10^{-6}\ cm^2/s$

— - — - numerical solution for $\alpha = 0.141$, $D_o = 5.75\times10^{-6}\ cm^2/s$

• interferometrically determined interfacial concentrations

Fig. 6. Transient interfacial concentrations, $i = 5.0$ and $10.0\ mA/cm^2$.

——— numerical solution for $\alpha=0.0869$, $D_o = 5.41\times10^{6}\ cm^2/sec$

_ _ _ _ ±10% uncertainty in diffusion coefficient D_o

• interferometrically determined interfacial concentrations

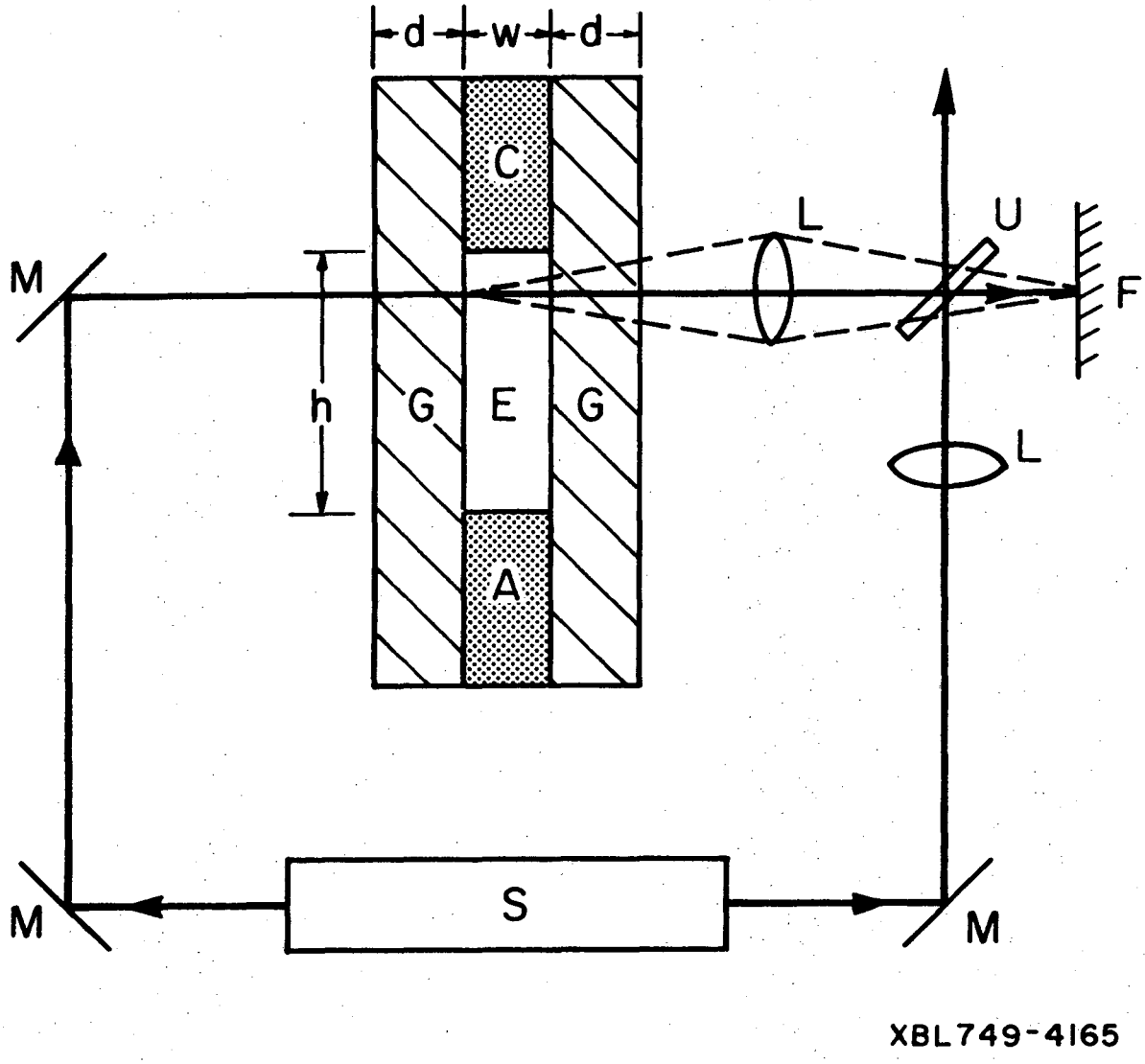

Fig. 1

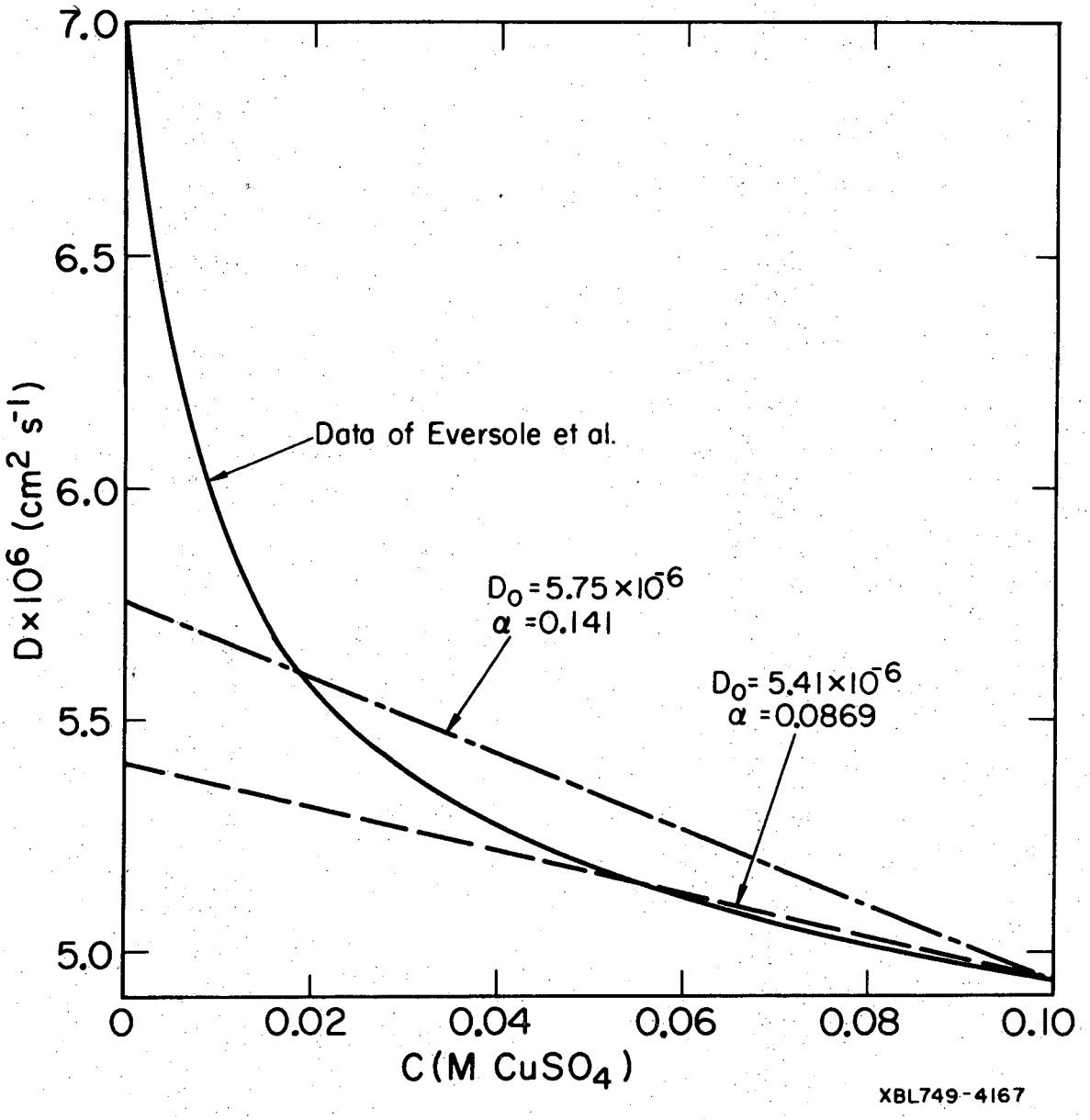

Fig. 2

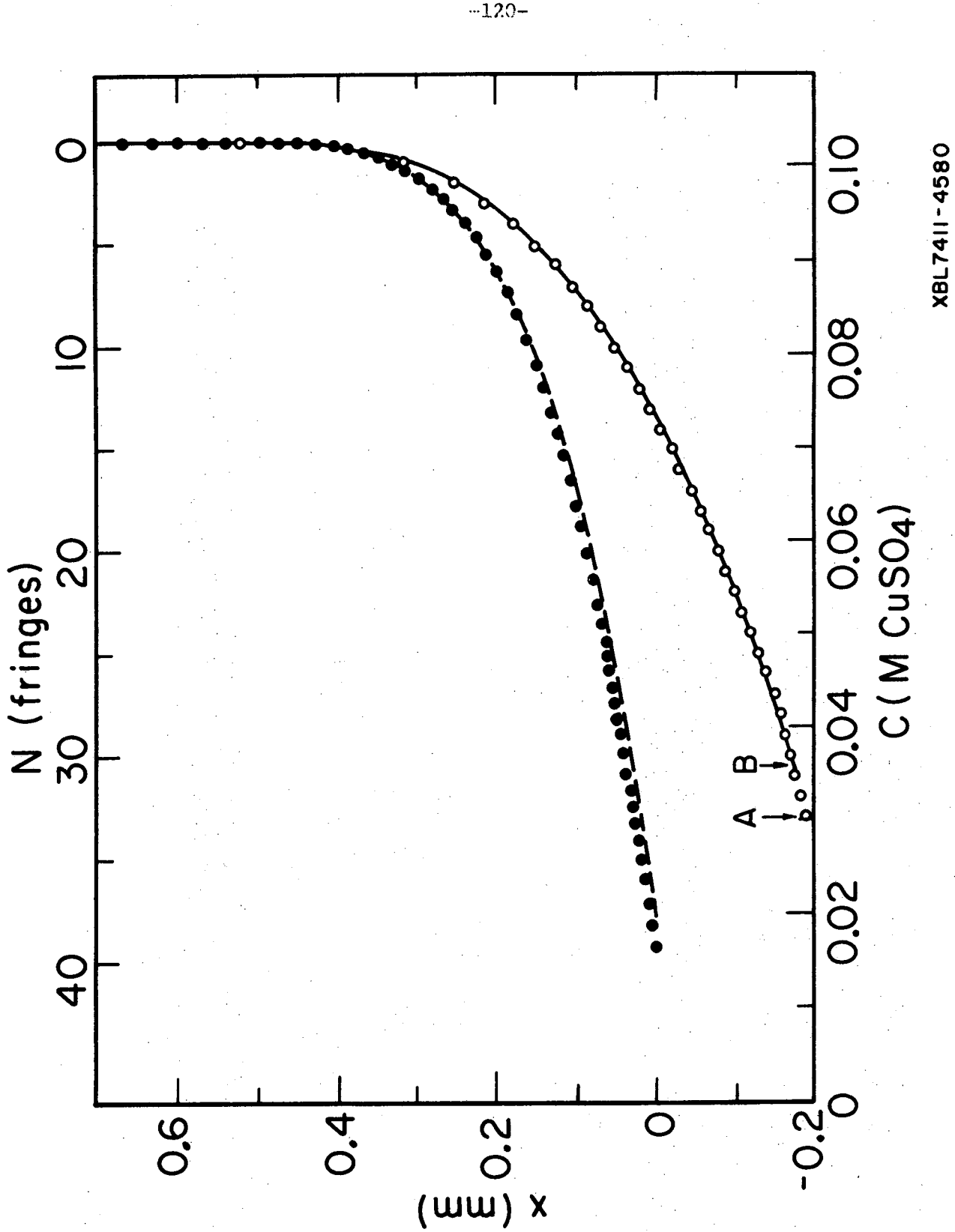
N (fringes)
0
10
20
30
40
x (mm)
0.6
0.4
0.2
0
-0.2
C (M CuSO4)
0
0.02
0.04
0.06
0.08
0.10
A
B
XBL7411-4580

Fig. 3

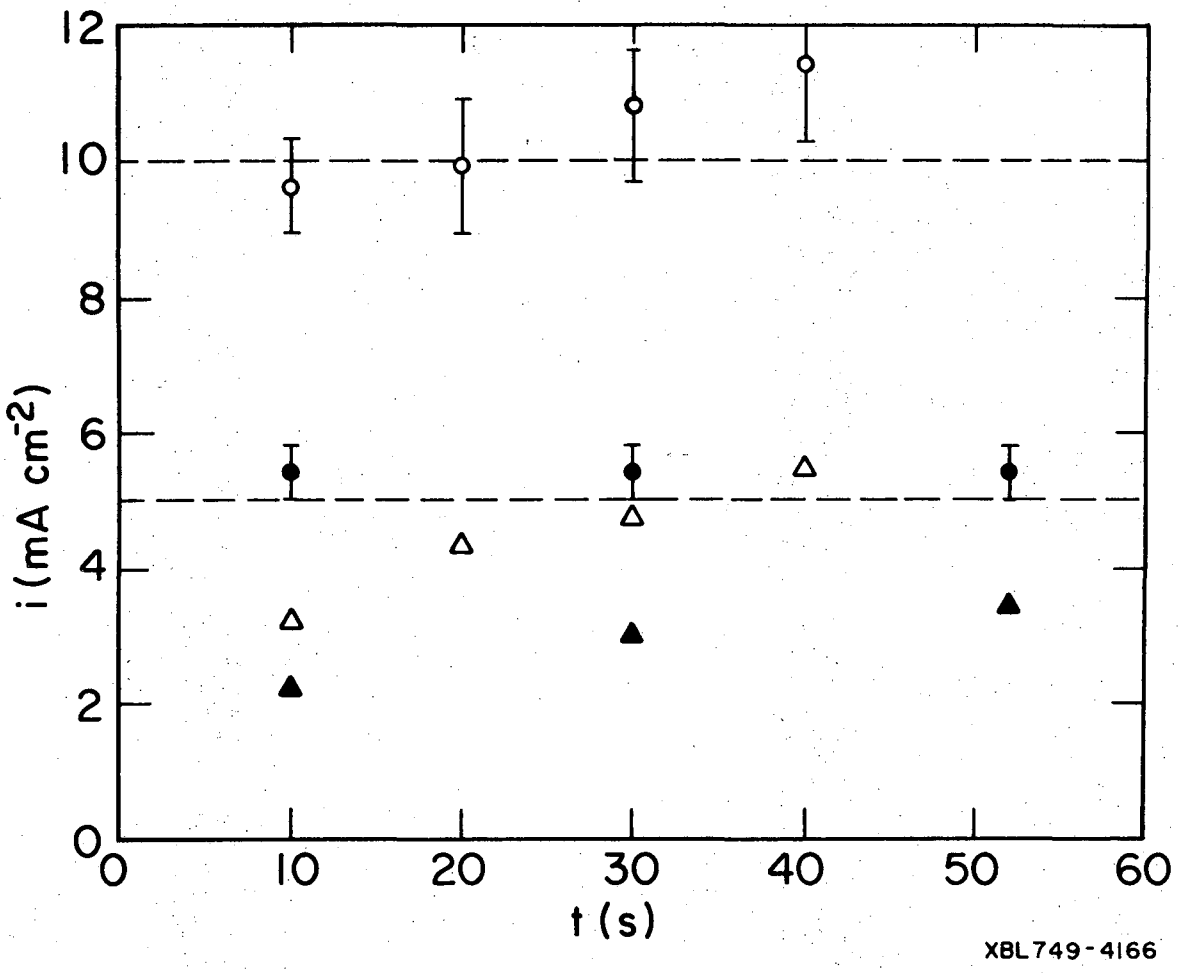

Fig. 4

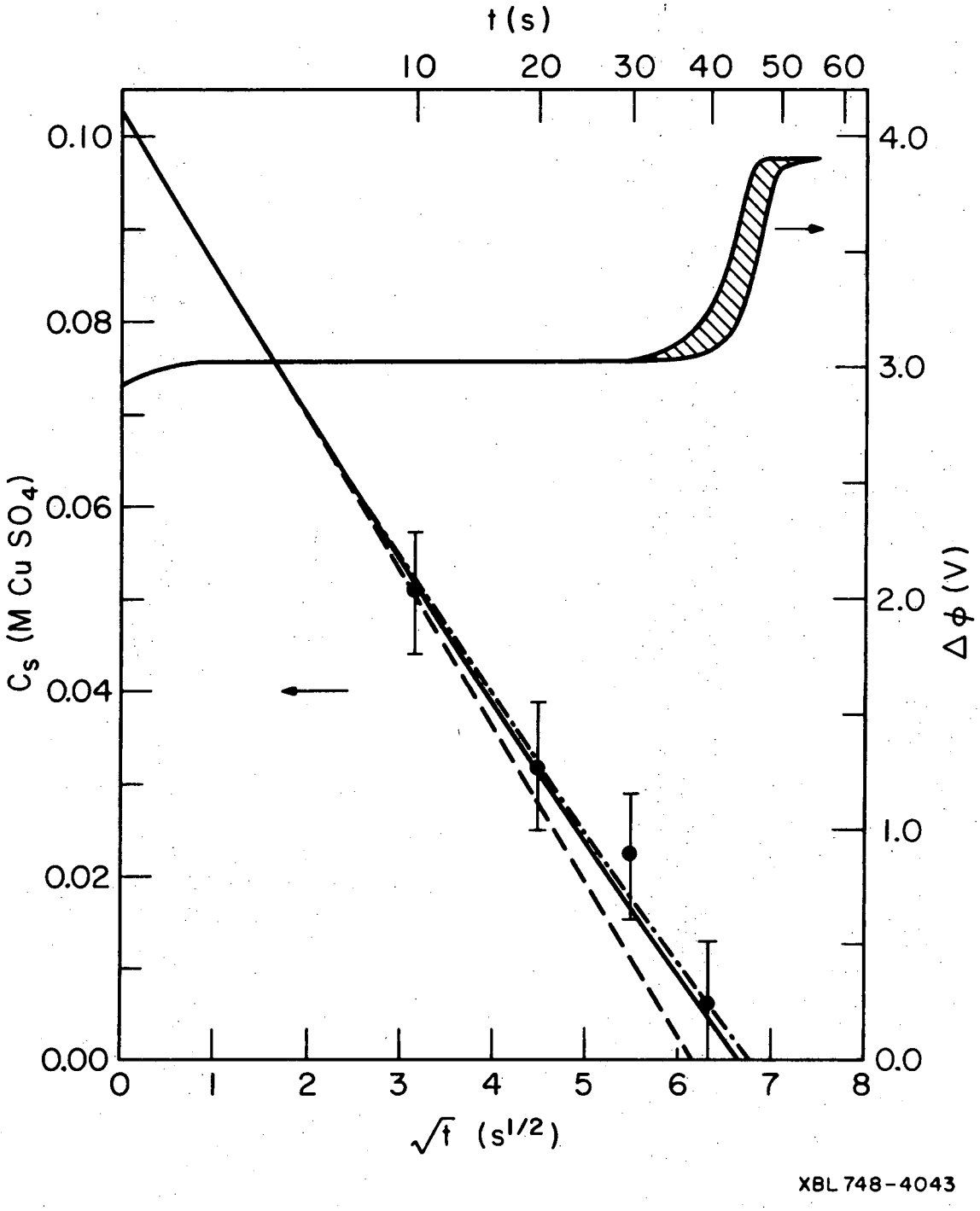
t (s)
10
20
30
40
50
60
0.10
0.08
0.06
0.04
0.02
0.00
C_s (M Cu SO_4)
4.0
3.0
2.0
1.0
0.0
$\Delta\phi$ (V)
0
1
2
3
4
5
6
7
8
$\sqrt{t}$ ($s^{1/2}$)
XBL 748-4043

Fig. 5

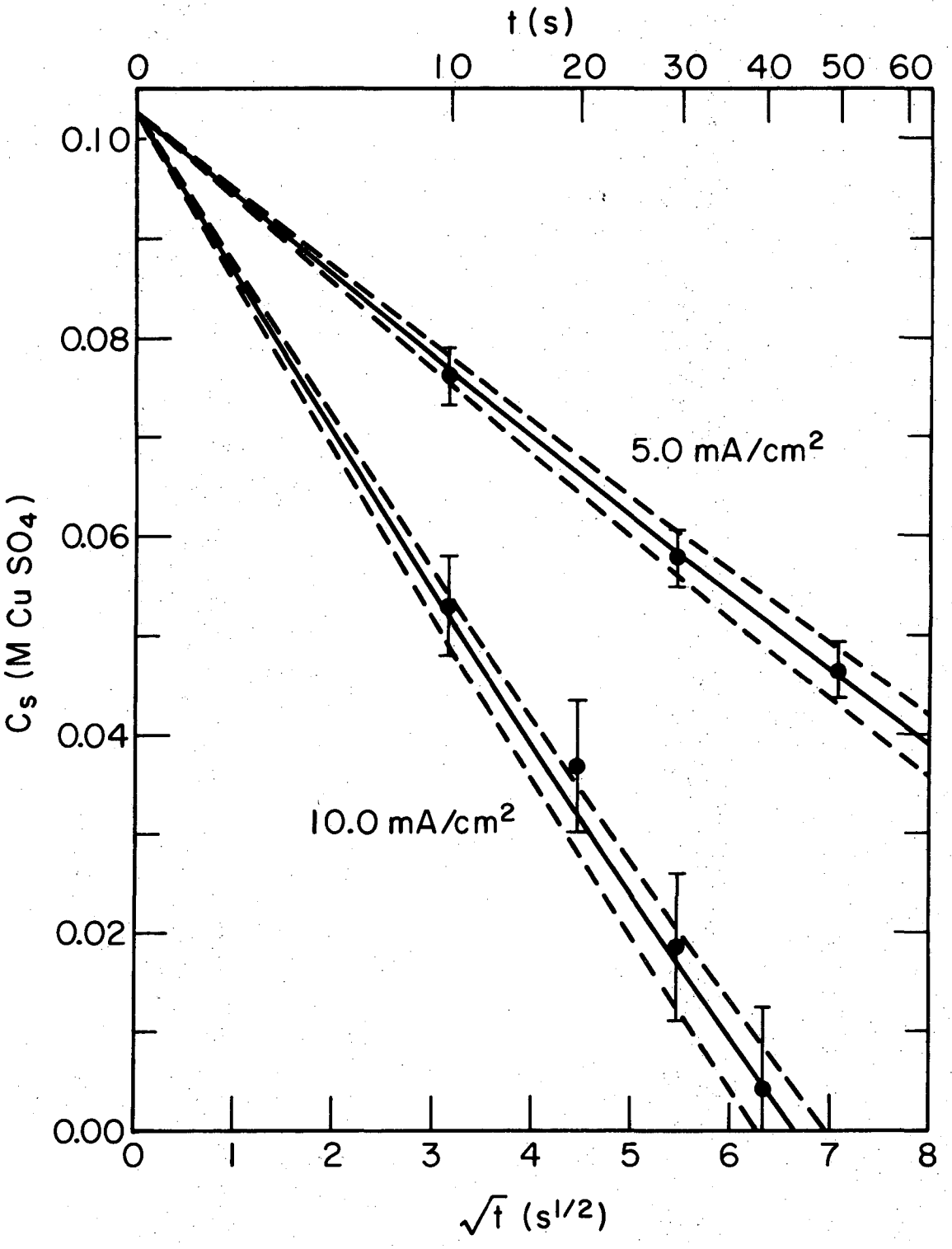

Fig. 6

5. INTERFEROMETRIC STUDY OF CONVECTIVE BOUNDARY LAYERS

The interferometric study described in the previous chapter served to verify particular portions of the optical analysis presented in Chapter 2 of this work. Here, the study is extended to areas of more practical significance: the observation of various convective mass transfer boundary layers.

This chapter is divided into three parts. Parts 5.1 and 5.2 describe an interferometric study of the laminar mass transfer boundary layers formed by the electrodeposition of Cu onto horizontal cathodes from flowing $CuSO_4$ electrolyte. In part 5.1, the cathode is studied in the downward-facing orientation: a depleted layer of relatively low density electrolyte flows above the higher density bulk electrolyte, so there is no density driving force for natural convection. The mass transfer process is, therefore, controlled by forced convection. In part 5.2, the cathode is studied in the upward-facing orientation: the depleted layer flows below the bulk electrolyte, and there is the possibility of free convection superimposed on forced convection. Part 5.3 presents the results of a brief comparative study of turbulent mass transfer boundary layers. The effect of turbulence induced by small promoters (obstacles) attached to the cathode surface is compared to that due to simply increasing the electrolyte flowrate.

5.1. Interferometric Study of Laminar Forced Convection Mass Transfer Boundary Layers

Ionic mass transport by forced convection in channel flow has been a subject of investigation in this laboratory since the early 1960's. Previous investigations by Hickman,[1] Selman,[2] Acosta[3] and Landau[4]

employed the limiting current technique to investigate mass transfer limitations and current distributions along sectioned horizontal electrodes embedded in the walls of rectangular ducts.

The interferometric technique described in this work is an alternative to the limiting current method . Table 1 presents a brief comparison of the two methods.

The Convective-Diffusion Problem

Figure 1 illustrates a semi-scale drawing of the flow channel described in part 1.1. The equation of convective diffusion[5] for this rectangular coordinate system is

$$\frac{\partial C}{\partial t} + v \frac{\partial C}{\partial z} = D\left[\frac{\partial^2 C}{\partial x^2} + \frac{\partial^2 C}{\partial y^2} + \frac{\partial^2 C}{\partial z^2}\right] \quad , \tag{1}$$

where C is the single-salt electrolyte concentration, D is the electrolyte diffusion coefficient and v is the electrolyte velocity (for laminar channel flow, the only nonzero velocity component is along the z-direction). Due to the thinness of the diffusion layer compared to the region of variation of electrolyte velocity (high Schmidt Number), the derivative $\partial^2 C/\partial y^2$ will be the dominant term on the right-hand side of Eq. (1).

For steady-state laminar flow between two parallel plates, the convective-diffusion equation becomes

$$v \frac{\partial C}{\partial z} = D \frac{\partial^2 C}{\partial y^2} \quad , \tag{2}$$

$$C = C_b \text{ at } z = 0 \tag{3a}$$

$$C = C_b \text{ as } y \to \infty \tag{3b}$$

$$\frac{\partial C}{\partial y} = \gamma \text{ at } y = 0 \quad , \tag{3c}$$

Table 1. Comparison of the interferometric and limiting current techniques.

	Interferometry	Limiting Current
Spatial resolution	high	usually low
Level of current density	any	restricted to limiting current
Provides quantitative information with supporting electrolyte present	no	yes
Can determine boundary layer structure	yes	no
Straightforward analysis of experimental results	no	yes
Electrode sectioning required	no	yes
Continuous visualization of the boundary layer	yes	no

where γ is a constant. Boundary condition (Eq. (3c)) corresponds to uniform current distribution along the electrode surface (see below). The solution to Eqs. (2) and (3) is derived in Appendix VI and may be approximated by the well-known solution[5] for constant interfacial concentration:*

$$Nu(z) = 1.2325 \left(Re\ Sc\ \frac{d_e}{z} \right)^{1/3} \quad . \tag{4}$$

Nu(z) is the local Nusselt Number for mass transfer

$$Nu(z) = \frac{i d_e (1 - t_+)}{mFD\Delta C} = \frac{d_e}{\delta_N} \quad , \tag{5}$$

and local current density i is related to the Nernst boundary layer thickness δ_N and total concentration change ΔC by

$$i = \frac{mFD}{(1 - t_+)} \left. \frac{\partial C}{\partial y} \right|_{y=0} = \frac{mFD}{(1 - t_+)} \frac{\Delta C}{\delta_N} \quad . \tag{6}$$

The solution Eq. (4) strictly applies to laminar flow between infinitely wide parallel plates. The electrodes instead fully occupy the space between the glass sidewalls, as illustrated in Fig. 1. Therefore, the electrolyte velocity will also vary in the x-direction; the glass walls will slow the electrolyte in the region x = 0 and x = w. This effect is accounted for in the computations presented in Appendix VI. Figure 2 schematically illustrates the variation of the interfacial velocity gradient $(dv/dy)_{y=0}$ and concentration boundary layer thickness in the x-direction.

---

*Boundary condition (Eq. (3c)) would be $c = c_s$ at $y = 0$.

slow the electrolyte in the region x = 0 and x = w. Figure 2 schematically illustrates the variation of the interfacial velocity gradient $(dv/dy)_{y=0}$ and concentration boundary layer thickness in the x-direction.

The variation of boundary layer thickness in the x-direction can be estimated by first computing the interfacial velocity gradient $(dv/dy)_{y=0}$ for various positions across the width w of the electrode. Beach[6] performed such calculations for a rectantular duct of the exact dimensions shown in Fig. 1, using the formulae of Happel and Brenner.[7] In laminar flow, the interfacial velocity gradient is proportional to Reynolds Number Re, and inspection of Eqs. (4) and (5) reveals that the local boundary layer thickness $\delta_N(x)$ should then vary in proportion to the interfacial velocity gradient raised to the minus one-third power. Details of computations for the variation of boundary layer thickness are given in Appendix II.

The entire equation of convective diffusion Eq. (1) must be solved in order to find <u>transient</u> concentration profiles. Rather than deal with the mathematical difficulties involved in such a solution, it might be preferable to find asymptotic solutions. For sufficiently short times after current switch-on, the concentration variations will be confined to a relatively thin (e.g., one-tenth of the steady-state boundary layer thickness) layer right at the electrode surface. The local concentration gradient $(\partial C/\partial y)$ will depend only upon the local current density because there will have been insufficient time for upstream regions of depleted electrolyte to flow downstream and affect the concentration variations there. Since the current is expected to be distributed quite uniformly along the length of the electrode (see below),

the concentration variations should, therefore, be independent of the local z along the electrode. The term $(\partial C/\partial z)$ in Eq. (1) can then be neglected, and the convective diffusion equation reduces to

$$\frac{\partial C}{\partial t} = D \frac{\partial^2 C}{\partial y^2} \tag{7}$$

which can be solved as in Chapter 4. The mass transfer process is, therefore, controlled by diffusion for short times after current switch-on. Selman[2] has presented transition times for the transient current response to a step concentration change at the wall in laminar flow between parallel plates.

Current Distribution

The primary current distribution is governed by the electric field between anode and cathode. This distribution was calculated[5] for the specific electrode lengths and spacing illustrated in Fig. 1 and is depicted in Fig. 3 as the ratio of local current density to average current density. The primary distribution is uniform (to within 1% over 98% of the electrode surface) because the electrodes are 100 cm long and separated by only 2.54 cm. Kinetic limitations to the electrode reaction would prevent the infinite primary current density indicated at $z = 0$ and $z = L$, so the current distribution limited by ohmic and kinetic effects would then be even more uniform than the primary distribution indicated in Fig. 3. So long as the interfacial electrolyte concentration does not approach zero, the effects of concentration polarization will be negligible compared to the ohmic and kinetic effects; practically uniform current distribution will prevail. On the

other hand, if the interfacial concentration was zero everywhere along the electrode, concentration polarization effects would dominate over ohmic and kinetic effects; the current distribution would be limited by diffusion and convection. This tertiary distribution can be calculated[5] from Eq. (4) and is shown in Fig. 3.

Variation of Steady-State Boundary Layer Thickness and Interfacial Concentration

For uniform current distribution along the length of the electrode, the local Nernst boundary layer thickness δ_N and the local concentration difference ΔC can be calculated from Eqs. (4) and (5). The value of electrolyte kinematic viscosity ν used in the computation of Reynolds Number $Re = vd_e/\nu$ and Schmidt Number $Sc = \nu/D$ was taken from the compilation of Chapman and Newman[8] and assumed invariant with electrolyte concentration (valid to within 5.6% for $0 \leq C \leq 0.1$ M $CuSO_4$). On the other hand, the diffusion coefficient D and cation transference number t_+ vary significantly with electrolyte concentration. The linear variation approximations for D and t_+ used in Chapter 4 are also used here in the computations for the expected variations of δ_N and ΔC. A simple iterative procedure was used to find the local interfacial concentration that satisfied Eqs. (4), (5) and (6) and the uniform current conditions. The horizontal curves in Figs. 4 and 5 and all curves in Figs. 11 through 13 were computed in this manner.

Transient Boundary Layer Growth Experimental Results

Four separate experiments were performed to determine the effects of (a) electrolyte flowrate, (b) level of applied current density and (c) position z downstream from the cathode leading edge on the

transient growth of forced convection mass transfer boundary layers. The interferograms were analyzed as outlined in part 2.3 and Appendix I: the one-dimensional polynomial boundary layer profile

$$\theta = 1 - (1 - kY)^2 (1 - Y)^2 \tag{8}$$

was used to describe the concentration field. This procedure computes local values of current density, boundary layer thickness and interfacial concentration from experimental interferograms without considering effects of the glass sidewalls on the flow profile. The average (i.e., averaged in the x-direction) values determined in this fashion are very similar to those derived considering such alteration of the flow profile, as discussed later.

Interferometrically derived concentration differences are plotted in Figs. 4 and 5 as a function of square root of time after current switch-on. The solid curves are the asymptotic solutions to the convective diffusion equation (Eq. (1)): The short time solution (sloped line) corresponds to the solution of the unsteady, one-dimensional diffusion equation (Eq. (7)), which is the sand equation,[9] presented in part 2.2. The long time, steady-state solution Eqs. (4) and (5) to Eq. (1) are represented by the horizontal lines. The dashed curves correspond to ±10% uncertainty in the value of the diffusion coefficient.

The interferometrically derived transient interfacial concentrations show good agreement with those predicted by combining the asymptotic solutions. The character of the results can be explained in terms of a restricted diffusion model. A dimensionless group[10]

$$\tau = \frac{Dt}{\delta_N^2} \tag{9}$$

would represent a characteristic dimensionless time for the solution of the one-dimensional unsteady diffusion equation (Eq. (7)) within the confines of a region of dimension δ_N. The minimum transition time t to steady-state corresponds to the joint between the two asymptotic solutions (solid lines) on Figs. 4 and 5. Using this value for t and the steady-state Nernst boundary layer thickness computed from Eqs. (4) and (5) we can calculate the dimensionless transition times τ shown in Table 2.

The characteristic diffusion time τ can also be computed by eliminating δ_N, i and ΔC between Eqs. (6) and (9) in this chapter and Eq. (14) in part 2.2. For a constant diffusion coefficient $D = 4.94\times10^{-6}$ cm^2/s (see Chapter 4), $\tau = \pi/4 = 0.785$. The deviations (below $\tau = \pi/4$) seen in Table 2 are due to the variations in physical properties that have been incorporated in the computations for the steady-state concentration differences, but are not considered in this second calculation of τ.

Table 3 shows that τ is relatively insensitive to changes in electrolyte flowrate, applied current density or position z along the electrode surface. The form of Eq. (9) suggests that the transition time t should (a) be independent of the level of applied current density and (b) increase with increasing boundary layer thickness.

Comparing the curves in Fig. 4 illustrates this lack of dependence of transition time t on the level of applied current at a given flow rate and position (constant boundary layer thickness). The shorter transition time indicated in Fig. 5 by the curve for Re = 1500, z = 79.5 cm (as compared to that for Re = 590, z = 79.5 cm, Fig. 4) is due to the

Table 2. Dimensionless transition times.

Re	i (mA/cm^2)	z (cm)	t (min)	τ
590	1.5	79.5	4.6	0.78
590	3.0	79.5	3.8	0.65
1500	2.5	79.5	2.2	0.68
1500	5.0	5.0	0.36	0.72

Table 3. Derived transient current densities and curve shape parameters.

	Re = 590 z = 79.5 cm i = 1.5 mA/cm^2		Re = 590 z = 79.5 cm i = 3.0 mA/cm^2		Re = 1500 z = 79.5 cm i = 2.5 mA/cm^2		Re = 1500 z = 5.0 cm i = 5.0 mA/cm^2	
t(min)	i	k	i	k	i	k	i	k
0.17	1.2	1.00	1.9	0.90	2.5	0.79	4.1	1.00
0.5	1.4	0.60	2.4	0.82	2.1	0.46	5.6	0.42
1.0	1.5	0.81	3.0	1.00	2.4	0.84	6.6	0.42
2.0	1.4	0.43	3.0	1.00	2.6	0.30	---	----
5.0	1.7	0.18	3.6	0.31	3.1	0.24	---	----
10.0	1.8	0.19	3.4	0.22	3.3	0.27	---	----
20.0	1.9	0.28	3.6	0.24	3.1	0.22	6.6	0.48
30.0	1.9	0.20	3.6	0.25	3.1	0.23	5.9	0.34

thinner boundary layer at Re = 1500. Figure 5 also illustrates an even shorter transition time at z = 5 cm, where the steady-state boundary layer is thinner than at z = 79.5 cm (see Fig. 6 in this chapter).

Table 3 lists the interferometrically derived transient current densities and curve shape parameters for the previously mentioned experiments (Table 2). Note that the derived currents show general agreement with the applied currents only for shorter times. (The concentration variation is very small for very short times, which can lead to relatively large errors in reading the experimental interferogram. Thus, derived quantities for t = 0.17 min should be given less weight than others.) At longer times, the derived currents are consistently high. This is an indication that the polynomial function Eq. (8) is successfully fitting the actual concentration profiles at shorter times but not at longer times. The derived curve shape parameter k is also listed in Table 3. For short times k is closer to unity, while for long times k is closer to zero. This corresponds to a change in the functionality of the concentration field from approximately a quartic profile k = 1 (Eq. (8)) to approximately a parabolic profile k = 0 as steady-state conditions are approached. The success of the polynomial function Eq. (8) in describing the short-time concentration profiles should be expected: The mass transfer process is diffusion controlled, and the polynomial function proved quite adequate in the analysis of transient diffusion layers (see Chapter 4). However, Eq. (8) apparently does not describe well the steady-state concentration profiles. This will be discussed more fully later on. Nevertheless, the interfacial concentrations (Figs. 4 and 5) derived using Eq. (8) are expected to be accurate (see part 2.3, Fig. 6).

Analysis of Steady-State Boundary Layers

Figure 6 shows experimental interferograms of steady-state mass transfer boundary layers at three different positions downstream from the cathode leading edge. These interferograms show significant distortions due to light-deflection effects--in no case does the location of the apparent (i.e., on the interferogram) electrode/electrolyte interface agree with the true* interface, identified by "0" on the ordinate scale. However, pertinent qualitative information can be gleaned by comparing the interferograms. (a) Note that the slope of the fringe contours at the apparent interface is quite similar for the three positions. This suggests that the current distribution is uniform along the cathode surface. (b) The edge of the boundary layer is about 0.3 mm from the true electrode surface at z = 5 cm and about 0.8 mm from the surface at z = 80 cm; the boundary layer does grow thicker with increasing distance from the cathode leading edge. (c) There are 18 fringe shifts between the edge of the boundary layer and the apparent interface at z = 5 cm and 46 such shifts at z = 80 cm. This corresponds to $\Delta C = 0.04$ M $CuSO_4$ at z = 5 cm and $\Delta C = 0.10$ M $CuSO_4$ at z = 80 cm, according to convectional interferogram interpretation (part 1.4). In conformity with theoretical expectations, the interfacial concentration decreases with increasing z.

*The image of the electrode surface in the absence of optical aberrations.

Preliminary attempts at quantitative interpretation of such interferograms employed the polynomial function Eq. (8) to describe the concentration field. Although it was possible to find computed (Appendix I) interferograms showing excellent agreement with all experimental interferograms, the derived current densities were consistently 20-30% higher than the applied current densities. This is in marked contrast to the similar analysis applied to interferograms obtained from the study of transient diffusion layers (Chapter 4), where derived current densities agreed with the applied currents to within 10%.

Figures 4 and 5 in part 2.3 suggest that the discrepancy between derived and applied currents is caused by insufficient flexibility of the polynomial fitting function Eq. (8); a search for a better fitting function is indicated. Table 3 shows that the interferometric analysis of steady-state boundary layers gives a derived value of the curve shape parameter $k \sim 0.2$ (the concentration boundary layer functionality is, therefore, close to parabolic, $k = 0$). As suggested in part 2.3 it may be possible to determine the actual refractive-index functionality directly from the experimental interferograms. Figure 7 illustrates such an attempt; it depicts a dimensionless plot of 28 interferograms from four laminar forced convection experiments (Table 3). The solid curve shown in Fig. 7 is a Pohlhausen[11] boundary layer profile:

$$\theta = 2Y - 2Y^3 + Y^4 \qquad (10)$$

and the dashed curve is the polynomial function Eq. (8), for $k = 0.2$. There is no obvious preference for a particular profile Eq. (9) or (10) on the basis of uncorrected interferogram shapes.

Now, preference between specific boundary layer profiles (e.g., Eq. (8) or (10)) can be decided only on the basis of a mass balance: The interferometrically derived current densities must agree with the applied currents. A generalized Pohlhausen-type boundary layer profile

$$\theta = KY + (4 - 3K)\ Y^3 + (2K - 3)\ Y^4$$
$$4/3 \leqslant K \leqslant 2 \qquad (11)$$

can be used as a fitting function. The limits on the curve shape parameter K insure that the function Eq. (11) demonstrates no extremum or inflection points in the range $0 < Y < 1$. Note that the Pohlhausen profile Eq. (10) is a special case of Eq. (11) for $K = 2$.

Table 4 compares two different analyses of interferograms recorded at $z = 79.5$ cm during laminar flow. The one-dimensional analysis is similar to that described in part 2.3 and Appendix I, except that the function Eq. (11) is used instead of the polynomial function Eq. (8). Numerical integration of the light-deflection equation is required, as outlined in part 2.1. The two-dimensional analysis accounts for the effect of the glass sidewalls on the electrolyte flow profile by permitting both the local boundary layer thickness and local interfacial concentration to vary in the x-direction (cross-channel). These variations allow (a) the local boundary layer thickness to vary in proportion to the minus one-third power of the local interfacial velocity gradient, as outlined earlier in this chapter and in Appendix II, and (b) the local interfacial concentration to vary in such a manner to give a uniform current distribution in the x-direction considering both the local boundary layer thickness variation and concentration-dependent

Table 4. Interferogram analysis using one- and two-dimensional Pohlhausen-type boundary layer profiles. Interferograms of steady-state mass transfer boundary layers recorded at z = 79.5 cm.

		$i(mA/cm^2)$	K	ΔC (M $CuSO_4$)	δ_N (mm)
Re = 590	*	1.51	2.06	0.039	0.415
i = 1.5	**	1.56	2.04	0.040	0.405
Re = 590	*	2.73	2.02	0.067	0.407
i = 3.0	**	2.81	2.00	0.067	0.404
Re = 1500	*	2.41	2.00	0.044	0.296
i = 2.5	**	2.43	1.76	0.044	0.296
Re = 1500	*	4.54	1.98	0.078	0.290
i = 5.0	**	4.73	1.88	0.089	0.289

*One-dimensional concentration field; analysis described in Appendix I, except Pohlhausen-type boundary layer profile (Eq. (11)) is used.

**Two-dimensional concentration field; analysis described in Appendix II.

transport properties D and t_+. In no case is the interfacial concentration permitted to drop below zero. Note that the form of the boundary layer profile Eq. (11) does not vary in the x-direction. Complete details of this two-dimensional boundary layer profile are given in Appendix II.

Table 4 shows little difference between values of i, K, ΔC and δ_N derived from the experimental interferograms by the two different methods. There is, however, a difference between the interferograms computed by the two techniques, as illustrated in Fig. 8. Figure 8a shows a one-dimensional analysis of the experimental interferogram of the steady-state concentration boundary layer at z = 79.5 cm for Re = 590 and i = 1.5 mA/cm^2. The computed interferogram, identified by the solid curve, passes below the three uppermost data points (fringe shifts on the experimental interferogram) (the uppermost point is at y = 0.85 mm). Figure 8b depicts the two-dimensional analysis of the same interferogram; the computed fringe passes above only the uppermost point. These small deviations are also characteristic of the other experiments listed in Table 4 and can be explained in terms of the thicker than average mass transfer boundary layer right at the glass sidewall. The one-dimensional analysis Fig. 8a cannot account for this effect, so the edge of the boundary layer (three uppermost data points) appears to extend somewhat higher than the computed (average) boundary layer edge. The two-dimensional analysis can account for this effect, but the observed boundary layer edge (uppermost data point in Fig. 8b) appears somewhat lower than the computed edge. This is an indication that the boundary layer x-direction variation (see Fig. 1 in Appendix II) is too

strong. This should be expected, however, in light of the simplification from Eq. (1) to Eq. (2). The cross-channel diffusion term ($\partial^2 C/\partial x^2$) was neglected, and it is such diffusion that would prevent a very large boundary layer thickness right at the glass sidewalls.

Figures 9 and 10 compare interferometrically derived current densities with applied currents for the four experiments. The filled symbols represent conventional interpretation of the experimental interferograms, as described in part 1.4. The open symbols correspond to interferogram analysis using the two-dimensional Pohlhausen-type boundary layer profile Eq. (11), as outlined in Appendix II. At lower current densities (i.e., less than 2 mA/cm^2) conventional analysis of the experimental interferograms gives results not unlike those from the detailed analysis. At higher current densities, however, conventional analysis would lead to erroneous conclusions. For example, the closed triangles in Fig. 10 would indicate (a) local currents 20-60% lower than the applied current $i = 5\ mA/cm^2$ and (b) local current densities increasing in the direction of flow. The low current densities violate mass balance considerations, and the apparent current distribution is contrary to both the primary and tertiary current distributions shown in Fig. 3.

The anomalous current distribution derived by simple analysis of the experimental interferograms could have been predicted by the light-deflection error correlation Fig. 10 in part 2.2. That correlation shows that the interfacial refractive-index gradient (current density) derived from an interferogram in the conventional way is likely to be lower

than the true gradient. Moreover, the derived current density will be lower (i.e., the light-deflection error is more severe) for smaller concentration difference ΔC, and vice-versa. This latter effect is the cause of the apparent false current distribution; the apparent current density is lower near the cathode leading edge where ΔC is smaller and higher near the cathode trailing edge where ΔC is larger.

The preceding paragraph points out an important concept in the design of interferometric experiments. To avoid distortions due to light-deflection effects, one must consider refractive-index gradients, specimen size and refractive-index differences. For instance, a small interfacial refractive-index gradient ($i \approx 1$ mA/cm^2) does not guarantee negligible light-deflection errors. The interferometric study of forced convection boundary layers by Lin, Moulton and Putnam[12] is a case in point. This work employed a Mach-Zehnder interferometer (Hg arc light source, $\lambda = 546$ nm) to observe the mass transfer boundary layer formed by the electrodeposition of Cd from 0.01 M $CdSO_4$ electrolyte in a 3.17 cm wide flow channel. Table 5 lists the results of a conventional analysis of three different interferograms presented in the Ph. D. dissertation of C. S. Lin.[13] This computation of current densities from the experimental interferograms required knowledge of the relation between changes in electrolyte concentration and changes in refractive-index; the value $dn/dC = 0.029$ M^{-1} (see part 1.3) for $CuSO_4$ was used for this purpose. Durou, Giraudou and Moutou[14] measured the refractive-indices of aqueous solutions of $CuSO_4$, $ZnSO_4$ and other electrolytes, and their results indicate that $dn/dC = 0.029 \pm 0.001$ for either $CuSO_4$ or $ZnSO_4$, $0 \leq C \leq 0.1$ M. Therefore, it is not unreasonable to use this same value for dilute $CdSO_4$

Table 5. Conventional analysis of Lin's[13] experimental interferograms

Experiment Number	Total Number of Fringe Shifts (Proportional to ΔC)	Applied Current Density	Derived Current Density
69	3.24	1.0	0.54
71	3.23	0.44	0.35
79	6.96	0.96	0.97

electrolyte. Current densities were computed from the interferometrically derived concentration gradients using Eq. (6) and the values $D = 7.9\times10^{-6}$ cm^2/s and $t_+ = 0.40$ for 10^{-2} M $CdSO_4$ given in the compilation of Chapman and Newman.[8] These values correspond to an effective diffusion coefficient

$$D_{eff} = D/(1 - t_+) = 1.3\times10^{-5} \text{ cm}^2/\text{s} \qquad (12)$$

which is 30% higher than that used by Lin et al.,[12] $D_{eff} = 10^{-5}$ cm^2/s.

Table 5 shows that the apparent current density is smaller than the applied current for experiments 69 and 71, and the current densities show good agreement for experiment 79. These observations are consistent with the light-deflection errors predicted in part 2.2: the error is more severe for higher current densities and smaller concentration differences. Even though small current densities were used, the wide (3.17 cm) cell and small concentration differences (<0.01M) resulted in significant light-deflection errors.

Figures 11-13 show that the average boundary layer thicknesses and concentration changes derived using the two-dimensional Pohlhausen-type boundary layer profile Eq. (11) (see Appendix II) agree with those predicted by Eqs. (4) and (5). The discrepancy between derived and predicted ΔC at $z = 0.5$ cm seen in Figs. 12 and 13 is caused by the higher than average current density near the cathode leading edge $z = 0$ (primary current distribution, Fig. 3). The general agreement serves as an optical check on the laminar forced convection results of previous workers in this laboratory[1-4] and the original laminar heat transfer correlation of Norris and Streid[15] (identical to Eq. (4)).

Table 6. Derived values of the curve shape parameter K for the Pohlhausen-type boundary layer profile (Eq. (11)). Analysis described in Appendix II.

z(cm)	Re = 590 $i = 1.5\ mA/cm^2$	Re = 590 i = 3.0	Re = 1500 i = 2.5	Re = 1500 i = 5.0
0.5	2.46	2.02	2.04	2.07
5.0	1.97	2.04	2.13	2.28
9.5	2.01	2.01	2.05	2.04
19.5	2.01	2.02	1.80	2.08
49.5	2.06	1.90	2.34	1.81
49.5	2.02	2.00	2.06	1.99
79.5	2.04	2.00	1.76	1.88

Table 6 catalogues derived values of the curve shape parameter K (see Eq. (11)) associated with the interferometric results presented in Figs. 9 through 13. The derived values cluster about K = 2.0, which corresponds to the Pohlhausen profile Eq. (10). Equation (10) is plotted as the dashed curve in Fig. 14 and can be compared to the solid curve shown on the same figure:

$$\theta = 0.893 \int_0^y e^{-\zeta^3} \, d\zeta \quad . \tag{13}$$

Equation (13) was suggested by Newman[5] and Rousar et al.[16] to describe the concentration profile in laminar boundary layers for uniform interfacial concentration $C_s = 0$. Equation (13) approximates closely the concentration profile derived in Appendix VI (the solution to Eqs. (2) and (3)). While there may be no strict theoretical basis to expect the tabulated[17] function Eq. (13) to describe the concentration profiles for uniform current distribution, the close approximation between the (successful) Pohlhausen profile Eq. (10) and the function Eq. (13) indicates that either profile adequately represents the concentration profiles associated with the experimental interferograms. The dotted curve in the same figure depicts the (unsuccessful) polynomial function Eq. (8) for k = 0.2.

5.2. Combined Free and Forced Convection Boundary Layers

The interferometric study is now extended to the mass transfer boundary layers formed by electrodeposition of Cu from flowing $CuSO_4$ electrolyte onto an upward-facing cathode. The experimental arrangement is identical to that described in the previous section. There is now the possibility of hydrodynamic flow caused by density gradients in the

electrolyte adjacent to the cathode, and free convection can be superimposed on forced convection. This work parallels the investigation of Hickman[1] in which the limiting current technique was employed.

Some qualitative information about the mechanism of combined free and forced convection can be obtained directly from the experimental interferograms shown in Fig. 15. Both the upper and lower halves of Fig. 15 depict the transient growth of the laminar concentration boundary layers formed by galvanostatic (current step from i = 0 to i = 10 mA/cm^2 at t = 0) electrodeposition of Cu from 0.10 M $CuSO_4$ 10 cm from the cathode leading edge. The cathode is facing down in the upper half of Fig. 15, and the mass transfer process is controlled by laminar forced convection; the boundary layer will grow until a stationary state is reached. The cathode is facing up in the lower half of Fig. 15, and natural convection effects are visible at $t \geqslant 20$ s.

The similarity between the two interferograms (cathode facing up and cathode facing down) at t = 10 s indicates that the respective concentration profiles are the same. The density driving force within the electrolyte near the upward-facing cathode (the deviation from straight interference fringes indicates a lower $CuSO_4$ concentration--consequently a lower density) is not large enough to induce natural convection. The mass transfer process is, therefore, controlled by forced convection at both the upward- and downward-facing cathodes. At t = 20 s, however, there is a visible difference between the two interferograms. The kink in the interference fringes about 0.5 mm above the upward-facing cathode represents a minor disturbance in the concentration field and is caused by natural convection effects. The disturbance is called minor because it does not significantly reduce the boundary layer

thickness; the edge (i.e., where the fringes first appear perpendicular to the apparent cathode surface) of the boundary layer is about 0.4 mm from both the upward- and downward-facing cathode surfaces. This kink becomes a major disturbance at t = 30 s. The edge of the boundary layer is only about 0.25 mm from the upward-facing cathode surface and about 0.5 mm from the downward-facing cathode surface. The major disturbance effectively thins the mass transfer boundary layer.

Motion picture studies of these disturbances have led to the following generalizations:

(1) The kinks always appear to indicate electrolyte regions of lower concentration; all of the kinks bend approximately 1 to 2 fringes in the same direction. However, they correspond to refractive-index changes (disturbances) averaged across the width of the cell, so the apparent phase difference depicted by the kink does not necessarily represent a region of lower concentration electrolyte extended across the entire cell.

(2) The kinks oscillate up and down over distances 0.2 to 1.0 mm from the electrode surface over periods of at least 1 sec. Some disturbances are quite steady, and the interferogram can depict the same fringe contour for periods of 1 min or more.

(3) The distrubances can extend for several centimeters in the flow direction, remaining parallel to the electrode surface, and many different kinks are visible along the 100 cm length of the electrode surface.

(4) Minor distrubances can appear within 1 cm of the electrode leading edge, even though a major disturbance does not manifest itself until z = 5 cm or more. This effect is particularly evident at higher current densities.

The longitudinal extent and size of the disturbances conform to the roll cells (lengthwise vorticies) suggested by Tobias and Hickman[18] to describe the flow patterns during combined natural and forced convection-controlled ionic mass transport to planar electrodes.

Quantitative interpretation of the experimental interferograms was attempted using the polynomial boundary layer profile Eq. (8) in part 5.1, as outlined in Appendix I. While it was possible to find a computed interferogram that agreed well with every experimental interferogram analyzed, the derived current densities were often only half of the level of applied current. Only when there were no disturbances, minor or major, in the experimental interferograms did the derived currents show agreement with applied currents. This is an indication that the polynomial boundary layer profile cannot completely describe the actual concentration variations when natural convection is superimposed on forced convection. Another attempt at quantitative interpretation employed the Pohlhausen-type boundary layer profile Eq. (11) in part 5.1; the results were quite similar to those using the polynomial profile. The failure of smoothly-varying functions to describe perfectly the concentration fields, however, is not unexpected considering the form of the experimental interferograms depicted in Fig. 15.

Figure 16 presents a comparison of the Nernst boundary layer thicknesses derived from various experimental interferograms obtained during laminar flow Re = 500. The interferograms were interpreted assuming a one-dimensional Pohlhausen boundary layer profile:

$$\theta = 2Y - 2Y^3 + Y^4 \qquad (14)$$

The analysis procedure was similar to that outlined in Appendix I, but there were two significant modifications: (a) there was no variation of curve shape parameter k because the profile functionality was set according to Eq. (14) and (b) numerical integration of the light-deflection equation was employed, described in part 2.1. The profile Eq. (14) was used because of its success in approximating the forced convection boundary layer concentration profiles.

The open circles in Fig. 16 represent the Nernst thicknesses derived from experimental interferograms of the forced convection boundary layer at a downward-facing cathode. These points show the expected agreement with the Norris and Streid correlation, depicted by the straight line in Fig. 16. The filled symbols represent the boundary layer thicknesses derived from the interferograms recorded at an upward-facing cathode for three different levels of applied current density. These data indicate two separate regimes of mass transfer control: (a) Near the cathode leading edge, the points generally follow the straight line, and the mass transfer process is dominated by forced convection. (b) Far downstream, the boundary layer thickness is relatively uniform, $\delta_N = 0.14 \pm 0.03$ mm, and the process is controlled by combined natural and forced convection. These results show considerably more scatter than those for the downward-facing cathode; this is a consequence of the above-mentioned inadequacy of smoothly-varying fitting functions. Similar results are shown in Fig. 17 for Re = 1500. The downstream boundary layer thickness is slightly thinner: $\delta_N = 0.10 \pm 0.02$ mm.

The location z_c downstream from the cathode leading edge where the transition from forced convection control to combined free and forced convection control occurs can be determined either directly from the experimental interferograms or from plots such as Figs. 16 and 17. Table 7 lists these positions for various flowrates and current densities. Also listed are the Rayleigh Numbers:

$$Ra = Gr\ Sc = \frac{g \cdot \delta_c^3 \cdot \Delta\rho}{\nu^2 \cdot \rho} \frac{\nu}{D} = \frac{g \cdot \delta_c^3 \cdot \alpha \cdot \Delta C}{\mu \cdot D} \quad , \qquad (15)$$

where δ_c is a characteristic distance over which the density difference $\Delta\rho$ is manifest and α is a proportionality constant relating density differences to concentration changes. The variation of density with concentration presented in part 1.3 indicates the appropriate value of α is:

$$\alpha = 0.155\ \text{gm cm}^{-3}\ (\text{M CuSO}_4)^{-1}$$

over the range $0 \leq C \leq 0.1$ M $CuSO_4$. The Rayleigh Numbers listed in Table 7 were computed from Eqs. (4) and (5) in part 5.1 <u>for the transition locations</u> z_c. In other words, the computed Rayleigh Number corresponds to that for a downward-facing cathode at the location z_c. Proper choice of the value of δ_c for use in Eq. (15) is not obvious. The value used for the Rayleigh Number computations presented in Table 7 corresponds to the 90% boundary layer edge ($\theta = 0.90$) of the Pohlhausen profile Eq. (14). This thickness is indicated by the open circle in Fig. 18 and closely corresponds to the edge of an "equivalent" boundary layer[19] depicted by the dashed line in Fig. 18. Other plausible values of δ_c would be the 99% boundary layer edge, indicated by the filled

Table 7. Onset of natural convection.

Re	i (mA/cm^2)	z_c (cm)	Uncertainty ± (cm)	Ra	Uncertainty ±
500	2.0	8.0	1.0	1100	190
500	3.0	6.0	1.0	1120	250
500	3.8	5.0	1.0	1110	310
500	6.1	4.0	1.0	1310	450
500	10.0	3.0	1.0	1450	680
1000	3.0	12.0	1.0	1120	125
1000	4.0	14.0	4.0	1820	660
1000	5.8	8.5	1.0	1360	215
1000	10.0	5.0	1.0	1140	310
1500	3.0	20.0	5.0	1290	440
1500	4.0	14.0	4.0	1070	420
1500	10.0	8.5	1.0	1320	210

circle in Fig. [18], and the edge of the Nernst layer, also shown in Fig. 18. Use of these other boundary layer thicknesses would of course result in different numerical values for computed Rayleigh Numbers.

All but one of the computed Rayleigh numbers falls into the range Ra = 1270 ± 200, which indicates a relatively narrow range for the observed onset of natural convection effects. These interferometric observations provide optical confirmation of certain experimental results obtained by Hickman,[1] reproduced in Fig. 19. The upturn of the dashed curves in Fig. 19 corresponds to the onset of natural convection effects at the upward-facing electrode. The transitions shown for Re = 650 and 1400 in Fig. 19 shown good agreement with those in Table 7 for i = 10 mA/cm^2 at Re = 500 and 1500.

5.3. Comparative Study of Turbulent Boundary Layers

This section presents the results of an interferometric study of mass transfer boundary layers formed in turbulent flow. The turbulence induced by increasing the electrolyte flowrate permits high rates of mass transfer because the boundary layer is thin. However, the increased pumping costs required to maintain turbulent flow can more than offset the economic advantage of higher mass transfer rates.[3] Inserting small turbulence promoters in the flow channel is an alternate method of thinning the mass transfer boundary layer. The interferometric results presented here indicate that judicious choice of promoter shape and spacing can give high rates of mass transfer for pumping costs lower than those required by the equivalent bulk turbulent flow.

Bulk Turbulent Flow

Some qualitative information about turbulent flow can be derived directly from the experimental interferograms shown in Fig. 20. These interferograms were obtained using the same experimental set-up described in part 5.1. The cathode is facing down in all cases, so the mass transfer process is controlled by forced convection. The two interferograms on the left-hand side of Fig. 20 illustrate the relatively thick mass transfer boundary layers formed in laminar flow; the layer at Re = 1500 is somewhat thinner than that at Re = 500. There are 45 fringe shifts visible in the interferogram at Re = 500 and 40 shifts in that at Re = 1500, which conventionally indicates a total concentration change ΔC larger at Re = 500 than at Re = 1500. Also, there are obvious light-deflection distortions in these two interferograms: the apparent electrode/electrolyte interface deviates significantly from the true cathode surface, identified by "0" in Fig. 20.

The two interferograms on the right-hand side of Fig. 20 depict the relatively thin mass transfer boundary layers formed in turbulent flow; the layer at Re = 10,000 is thinner than that at Re = 5,000. There are 10 fringe shifts visible in the interferogram at Re = 5,000 and only three in that at 10,000, which conventionally indicates that ΔC at Re=5000 is larger than at Re = 10,000. This does not imply, however, that ΔC at Re = 5,000 is smaller than ΔC at Re = 1500. The current density in the right-hand side of Fig. 20 is five times larger than in the left-hand side, and the light-deflection effects depend strongly on current density. Note that the apparent current density depicted by all four interferograms is similar: the slope of the fringe contour at the apparent interface

does not change appreciably as the current is increased five-fold. This is a light-deflection effect caused by light-ray curvature out of the boundary layer at higher current densities, as discussed in part 2.2. The apparent electrode/electrolyte interface approximates the true cathode surface location more closely at Re = 5,000 and 10,000 than at Re = 500 and 1,500. This effect could have been predicted by inspection of the light-deflection error correlation Fig. 8 in part 2.2. The figure demonstrates that the relative error in boundary layer thickness (directly related to interfacial distortion) does not vary significantly in the range $5 \leq i \leq 25$ mA/cm^2 for $\Delta C \leq 0.1$ M $CuSO_4$. Therefore, there is less distortion of the interfacial location on the interferogram during turbulent flow because the absolute dimension of the boundary layer is smaller.

Direct observation of the interferograms of turbulent boundary layers revealed rapid fluctuations of the fringe contours; the apparent electrode/electrolyte interface moves up and down over time periods shorter than 0.03 sec.

Attempts at quantitative interpretation of the experimental interferograms were identical to those outlined in part 5.2. The derived current densities showed unexpected large fluctuations (faster than 0.05 s), ranging between 10% and 100% of the level of applied current. This is an indication that the smoothly varying one-dimensional boundary layer profiles cannot account for the expected random perturbations of local concentrations within the boundary layer (the interferogram represents an integrated average of the local concentrations). A new optical analysis would be necessary to account for such fluctuations.

Figure 21 illustrates the Nernst boundary layer thicknesses for three experiments: at Re = 5,000, i = 15 and 25 mA/cm^2 and at Re = 10,000, i = 25 mA/cm^2. The symbols represent the Nernst thickness derived from the experimental interferograms using the method outlined in Appendix I. The error bars reflect the uncertainty due to the above-mentioned fluctuations in the experimental interferograms. The solid line indicates the average Nernst thickness derived using Eq. (5) in part 5.1, where the average Nusselt Number was calculated using the Chilton-Colburn analogy:[20]

$$Nu_{avg} = \frac{f}{2} \, Re \, Sc^{1/3} \qquad (16)$$

Here, f is the Fanning friction factor: Ref. 21 gives f = 0.00938 at Re = 5,000 and f = 0.00773 at Re = 10,000. The dashed lines represent a ±10% uncertainty in diffusion coefficient. The interferometrically derived boundary layer thicknesses show fair agreement with those predicted using the Chilton-Colburn analogy, except very near the cathode leading edge where the mass transfer boundary layer is not yet fully developed.

Turbulent Flow Induced by Obstacles in a Laminar Stream

Laminar flow experiments were performed with five different turbulence promoters placed in the flow channel. Figure 22 schematically illustrates the relative sizes, shapes and locations of the obstacles in the channel (see Fig. 1 in part 5.1 for an oblique view of the channel). The large obstacle represents a circular glass cylinder of diameter 12.7 mm and length 10.0 mm sandwiched between the two glass

sidewalls midway between the cathode (facing down) and anode (facing up). This object, therefore, occupies one-half of the channel cross-section available for flow of electrode; it creates turbulence by increasing the electrolyte flow velocity nearby.

The remaining four objects were machined from plastic and glued to the cathode surface. The three larger obstacles all (a) extend 0.76 mm from the cathode surface, (b) cover the entire 10.0 mm width of the cathode, and (c) occupy only 3% of the channel cross-section. The smallest object extends 0.28 mm from the cathode surface. These smaller obstacles create turbulence by disrupting the electrolyte laminar flow pattern right near the cathode surface.

The two experiments were preformed at Re = 500, i = 2.0 mA/cm^2, and Re = 1500, i = 2.5 mA/cm^2. Figures 23-26 show experimental interferograms of the four smaller obstacles (a) with no current (b) Re = 500, i = 2.0 mA/cm^2, and (c) Re = 1500, i = 2.5 mA/cm^2. Figures 27 and 28 depict the experimental interferograms at the following locations near the triangular parallelopiped: (a) 0.5 cm upstream, (b) right at the obstacle, (c) 0.5 cm downstream, (d) 2.5 cm downstream and (e) 12.5 cm downstream.

The following generalizations can be drawn from qualitative interpretation of Figs. 23-28 :

(1) Significant turbulence is induced by the larger obstacles at Re = 1500, and all four obstacles have a relatively small effect at Re = 500.

(2) The turbulence induced by the triangular parallelopiped effectively thins the mass transfer boundary layer for several centimeters downstream of the object at Re = 1500.

(3) The smaller half-cylinder has little effect at either flow velocity Re = 500 or Re = 1500.

Figure 22 also illustrates the edges of the mass transfer boundary layers at Re = 500 and Re = 1500. Note that the boundary layer dimension is (a) always larger than that of the smaller half-cylinder, (b) about the same size of the three larger obstacles at Re = 500, and (c) smaller than the same three obstacles at Re = 1500. The above generalizations can now be condensed to the following: the turbulence induced by small flow obstacles significantly thins the local mass transfer boundary only when the dimension of the object is larger than that of the undisturbed boundary layer.

Quantitative interpretation of the experimental interferograms employed the Pohlhausen boundary layer profile, Eq. (14) in part 5.2, to describe the concentration field. This profile was chosen because of its success in the quantitative interpretation of the interferograms of laminar forced convection boundary layers, as outlined in part 5.1. Figures 29 and 30 compare the derived Nernst boundary layer thicknesses with those predicted by the Norris and Streid correlation[15] for laminar forced convection boundary layers (see part 5.1). For each flow velocity, Re = 500 and Re = 1500, the derived boundary layer thicknesses show the expected agreement with the above correlation for locations upstream of the first promoter (z = 22 cm). The downstream results for

Re = 500 indicate significant thinning of the mass transfer boundary layer only in the vicinity of the large detached circular cylinder, while the results for Re = 1500 indicate substantial turbulence effects just downstream of the three larger attached promoters. These results concur with the previous generalizations derived by qualitative interpretation of the experimental interferograms Figs. 23-28 .

Figures 28 and 25(c) show that the laminar boundary layer at Re = 1500 substantially thinned for several centimeters downstream of the trianglular parallelopiped. In particular, the Nernst thickness is reduced from about 0.25 mm just upstream of the obstacle to about 0.08 mm 1.5 cm downstream from the obstacle. The flow velocity required for a 0.08 mm Nernst thickness can be computed from Eq. (16) in this section and Eq. (4) in part 5.1; turbulent flow Re = 2790 is required. The pressure drop dP/dz (directly related to pumping cost) required to maintain a given average flow velocity v is given by:

$$\frac{dP}{dz} = 2\rho v^2 \frac{f}{d_e} \tag{17}$$

Since the friction factor f varies only slightly[21] from $1500 \leqslant Re \leqslant 2790$ and the flow velocity v is proportional to the Reynolds Number Re, the ratio of the pressure drops is:

$$\frac{(dP/dz)_{Re=2790}}{(dP/dz)_{Re=1500}} = \left(\frac{2790}{1500}\right)^2 = 3.5 \tag{18}$$

In other words, reduction of the Nernst thickness from 0.25 mm to 0.08 mm by increasing the electrolyte flowrate from Re = 1500 to Re = 2790 requires a 3 1/2-fold increase in pumping power.

Leitz et al.[22] have obtained the following correlation for the increased pressure drop caused by the presence of triangular parallelopipeds attached to an electrode:

$$f = \frac{a}{Re} + 0.175 \cdot n_p \cdot d_e \cdot \frac{1 - \beta^2}{\beta^2} \qquad (19)$$

a is a specific channel dimension parameter, n_p is the number of promoters per centimeter along the length of the channel, and β is the ratio of the open area perpendicular to the flow at the obstacle to the cross-sectional area of the channel without the obstacle. For the triangular obstacle and the given flow channel dimensions (Fig. 1 in part 5.1) the parameters are a = 16.6 and β = 0.97. If triangular turbulence promoters were spaced two centimeters apart along the length of the cathode (n_p = 0.5 cm^{-1}), the friction factor f computed from Eq. (19) would only increase by a factor of 1.7 over that for a smooth electrode. While the rectangular turbulence promoter appears to be as effective as the triangular promoter, the associated increase in pressure drop is about four times larger[22] than that for the triangular promoter. The half-cylinder appears to be less effective than either the triangular or rectangular promoters.

The interferometric study outlined in this section has shown that spaced triangular turbulence promoters can thin the mass transfer boundary layer three-fold for a 72% increase in pumping power, whereas the equivalent alternate route of increasing the electrolyte flow velocity would require a 3 1/2-fold increase in pumping power. While this brief investigation by no means represents a thorough evaluation of turbulence promoters, it does demonstrate the ability of interferometry to provide qualitative and quantitative insight to a complex domain.

REFERENCES

1. R. G. Hickman, The Effect of Buoyancy Forces on Forced Convection Ionic Mass Transfer at Horizontal Planar Electrodes (Ph. D. Thesis), Department of Chemical Engineering, University of California, Berkeley, 1963.

2. J. R. Selman, Measurement and Interpretation of Limiting Currents (Ph. D. Thesis), UCRL-20557, June 1971.

3. R. E. Acosta, Transport Processes in High Rate Electrolysis (Ph. D. Thesis), LBL-2242, May 1974.

4. U. Landau, in progress.

5. J. S. Newman, Electrochemical Systems (Prentice-Hall, Inc., Englewood Cliffs, N. J., 1973).

6. K. W. Beach, Optical Methods for the Study of Convective Mass Transfer Boundary Layers on Extended Electrodes (Ph. D. Thesis), UCRL-20324, July 1971.

7. J. Happel and H. Brenner, Low Reynolds Number Hydrodynamics (Prentice-Hall, Englewood Cliffs, N. J., 1963).

8. T. W. Chapman and J. S. Newman, A Compilation of Selected Thermodynamics and Transport Properties of Binary Electrolytes in Aqueous Solution, UCRL-17767 (1968).

9. H. J. S. Sand, Phil. Mag. 1(6), 45 (1901).

10. R. B. Bird, W. E. Stewart and E. L. Lightfoot, Transport Phenomena (Wiley, New York, 1960), p. 354.

11. H. Schlichting, Boundary Layer Theory (McGraw-Hill, N. Y., 1968), p. 291.

12. C. S. Lin, R. W. Moulton and G. L. Putnam, Ind. Eng. Chem. 45, 640 (1953).

13. C. S. Lin, Mass Transfer between Solid Wall and Fluid Streams (Ph. D. Thesis), Department of Chemical Engineering, University of Washington, 1952.

14. C. Durou, J. C. Giraudou and C. Moutou, J. Chem. Eng. Data 18, 289 (1973).

15. R. H. Norris and D. D. Streid, Trans. ASME 62, 525 (1940).

16. I. Rousar, J. Hostomsky and V. Cezner, J. Electrochem. Soc. 118, 881 (1971).

17. M. Abramowitz and I. Stegun, eds, Handbook of Mathematical Functions, National Bureau of Standards, Washington, 1964, p. 320.

18. C. W. Tobias and R. G. Hickman, Z. Physik. Chem. 229, 145 (1965).

19. As shown in Fig. 18, the "equivalent" boundary layer is a linear variation of concentration with distance having the same integrated concentration change

$$\int_0^1 (C_b - C)\, dY$$

as the Pohlhausen profile.

20. D. W. Hubbard and E. N. Lightfoot, Ind. Eng. Chem. Fund. 5, 370 (1966).

21. W. L. McCabe and J. C. Smith, Unit Operations of Chemical Engineering (McGraw-Hill, N. Y., 1967), p. 102.

22. F. Leitz, L. Marincic, P. Johnson and J. Liston, Effect of Turbulence Promoters on Local Mass Transfer (Ionics, Inc., Watertown, Mass., 1974).

NOMENCLATURE

C	electrolyte concentration (mole/liter)
C_b	bulk electrolyte concentration (mole/liter)
C_s	interfacial electrolyte concentration (mole/liter)
d_e	equivalent duct diameter (mm)
D	electrolyte diffusion coefficient (cm^2/s)
D_{eff}	effective diffusion coefficient, includes effect of ionic migration (cm^2/s)
f	fanning friction factor
F	Faraday constant (coul/eq)
g	gravitational acceleration (cm/s^2)
Gr	Grashof number
h	electrode separation (mm)
i	current density (A/cm^2)
k	curve shape parameter for the polynomial profile, Eq. (8)
K	curve shape parameter for the Pohlhausen-type profile, Eq. (11)
L	electrode length (cm)
m	cation valence
n_p	promoter spacing (cm^{-1})
Nu	Nusselt number for mass transfer
Ra	Rayleigh number
Re	Reynolds number
Sc	Schmidt number
t	time (s)
t_+	cation transference number
v	electrolyte flow velocity (cm/s)
w	electrode width (mm)

x,y,z	coordinates defined in Fig. 1 (all mm)
Y	reduced distance normal to the cathode surface, y/δ
α	proportionality constant relating density differences to changes in electrolyte concentration (gm $cm^{-3}M^{-1}$)
β	ratio of open area perpendicular to flow at an obstacle to the cross-sectional area of the duct without the obstacle
γ	constant (mole $liter^{-1}cm^{-1}$)
δ	total mass transfer boundary layer thickness (mm)
δ_C	equivalent[19] mass transfer boundary layer thickness (mm)
δ_N	Nernst (linear) mass transfer boundary layer thickness (mm)
ΔC	$C_b - C_s$ (mole/liter)
θ	dimensionless concentration $(C - C_s)/(C_b - C_s)$
μ	electrolyte viscosity (gm $cm^{-1}s^{-1}$)
ν	kinematic viscosity (cm^2/s)
ρ	electrolyte density (cm/cm^3)
τ	dimensionless time, Eq. (9)

FIGURE CAPTIONS

Fig. 1. Semi-scale drawing of the flow channel. w = 10.0 mm, h = 25.4 mm and L = 100.0 cm.

Fig. 2. Boundary layer variation in the cross-channel direction.

Velocity gradients. v = 0 at the glass wall and electrode surface.

Concentration profiles. The concentration boundary layer is thicker at the glass wall and thinner near the center of the electrode.

Fig. 3. Current distributions along the electrode surfaces shown in Fig. 1.

Ordinate: local current density divided by average current density

Abscissa: reduced distance z/L

The primary current distribution is limited by ohmic drop, and the tertiary current distribution is limited by convection and diffusion.

Fig. 4. Transient concentration changes. Re = 590, z = 79.5 cm.

Ordinate: concentration difference bulk less interfacial ($M\ CuSO_4$)

Abscissa: square root of time after current switch-on ($min^{1/2}$)

Interfacial concentrations predicted by asymptotic solutions to the convective diffusion equation. Horizontal solid lines account for variation of diffusion coefficient D and cation transference number t_+ with electrolyte concentration; linear approximations for D and t_+ variations described in Chapter 4 are used ($D_o = 5.41 \times 10^{-6}\ cm^2/s$ and $\alpha = 0.0869$).

- - - - - ±10% uncertainty in value of diffusion coefficient D_o

O $i = 1.5$ mA/cm^2 } interferometrically measured

● $i = 3.0$ mA/cm^2 }

Fig. 5. Transient concentration changes. Re = 1500.

O $i = 5.0$ mA/cm^2, $z = 5.0$ cm

● $i = 2.5$ mA/cm^2, $z = 79.5$ cm

Other designations as in Fig. 4.

Fig. 6. Experimental interferograms showing the growth of the boundary layer in the flow direction.

Ordinate: vertical distance, measured downward from the true electrode/electrolyte interface identified by "0".

The cathode is represented by the black area and is facing down.

Actual current density $i = 4.5$ mA/cm^2.

Fig. 7. Comparison of dimensionless experimental interferograms with dimensionless concentration profiles of steady-state laminar boundary layers.

Ordinate: dimensionless distance $Y = y/\delta$, where δ corresponds here to the total apparent boundary layer thickness seen on the interferogram and y is measured from the apparent interface.

Abscissa: dimensionless refractive-index change depicted by conventional analysis of the experimental interferogram. Computed as the number of fringes crossed by a vertical line extending from the apparent electrode/electrolyte interface to the edge of the boundary layer, divided by the total number of fringes crossed by such a line. See Fig. 9 in Chapter 1.

..... The points correspond to the conventional analysis, as described above, of the experimental interferograms of steady-state concentration boundary layers at 7 different positions along the cathode surface during 4 separate experiments (those described in Figs. 4 and 5).

_____ Pohlhausen boundary layer profile, Eq. (10)

- - - - - Polynomial boundary layer profile, Eq. (8), k = 0.2.

Fig. 8. Interferogram analysis showing the effect of considering boundary layer variation across the channel.

Ordinate: distance y from electrode surface (mm)

Abscissa: electrolyte concentration (M $CuSO_4$) or phase change (fringes). The two abscissa scales are linearly related according to conventional interpretation of interferograms (part 1.4).

o o o o Experimental interferogram, Re = 590, i = 1.5 mA/cm^2 and z = 79.5 cm.

_____ Computed interferogram. Figure 8a shows the interferogram computed using a one-dimensional concentration field and Fig. 8b shows the computed using a two-dimensional field.

- - - - Concentration profile associated with the computed interferogram.

Fig. 9. Derived current densities. Re = 590.

_____ Level of applied current density

- - - - Represents ±10% uncertainty in diffusion coefficient

●▼ Derived by conventional analysis of the experimental interferograms

○▽ Derived using a two-dimensional Pohlhausen-type boundary layer profile, as described in Appendix II.

○● $i = 1.5$ mA/cm^2

▽▼ $i = 3.0$ mA/cm^2

Fig. 10. Derived current densities. Re = 1500.

○● $i = 2.5$ mA/cm^2

▽▼ $i = 5.0$ mA/cm^2

Other designations as in Fig. 9.

Fig. 11. Derived laminar boundary layer thicknesses.

Ordinate: Nernst boundary layer thickness (mm)

Abscissa: Reduced distance from cathode leading edge

_____ Boundary layer thickness computed using Eqs. (4) and (5)

- - - - - Represents ±10% uncertainty in diffusion coefficient. The symbols represent boundary layer thicknesses derived using a two-dimensional Pohlhausen-type boundary layer profile, as described in Appendix II:

○ $i = 1.5$ mA/cm^2 (Re = 590) or $i = 2.5$ mA/cm^2 (Re = 1500)

▽ $i = 3.0$ mA/cm^2 (Re = 590) or $i = 5.0$ mA/cm^2 (Re = 1500)

Fig. 12. Derived laminar concentration changes. Re = 590.

Ordinate: Concentration change ΔC (M $CuSO_4$)

Abscissa: Reduced distance from cathode leading edge

_____ ΔC computed using Eqs. (4), (5) and (6).

- - - - represents ±10% uncertainty in diffusion coefficient

Other designations as in Fig. 11.

Fig. 13. Derived laminar concentration changes. Re = 1500. Designations as in Fig. 12.

Fig. 14. Concentration profiles.

Ordinate: Vertical distance y (arbitrary units) or reduced vertical distance $Y = y/\delta$.

Abscissa: Dimensionless concentration

_____ $\theta = 0.893 \int_0^y e^{-\zeta^3} d\zeta$

- - - - $\theta = 2Y - 2Y^3 + Y^4$ (Pohlhausen profile, $\delta = 1.7$)

..... $\theta = 1 - (1 - 0.2Y)^2(1 - Y)^2$ (Polynomial profile, $k = 0.2$, $\delta = 1.7$)

Fig. 15. Experimental interferograms showing transient boundary layer growth.

Ordinate: vertical distance from cathode cathode surface (mm). The true cathode surface is identified by "0".

The cathode faces down in the four interferograms in the upper half. It faces up in the lower half of this figure.

Fig. 16. Variation of boundary layer thickness, Re = 500.

Ordinate: Nernst boundary layer thickness (mm).

Abscissa: Reduced distance from cathode leading edge.

Open Symbols: Derived from experimental interferograms, cathode faces down.

Filled Symbols: Derived from experimental interferograms, cathode faces up.

○ ● $i = 2.0$ mA/cm^2

▼ $i = 3.8$

■ $i = 6.1$

_____ Norris and Streid correlation.[15]

- - - - Boundary layer thinned by superimposed natural convection.

Fig. 17. Variation of boundary layer thickness, Re = 1500.

● $i = 3.0$ mA/cm^2

▼ $i = 4.0$

■ $i = 10.0$

Other designations as in Fig. 2.

Fig. 18. Pohlhausen profile.

Ordinate: Reduced distance.

Abscissa: Dimensionless concentration.

_____ Pohlhausen profile Eq. (10).

__ - __ "Equivalent" boundary layer[19]

- - - - Nernst boundary layer

○ 90% boundary layer edge

● 99% boundary layer edge

Fig. 19. Smoothed limiting current results of Hickman.[1] C_b = 0.11 M $CuSO_4$.

Fig. 20. Experimental interferograms showing the effect of electrolyte flow velocity on steady-state boundary layer thickness.

Ordinate: distance from the cathode surface (mm).

Fig. 21. Turbulent boundary layer thicknesses.

Ordinate: Nernst boundary layer thickness (mm).

Abscissa: Distance from cathode leading edge (cm).

———— Thickness computed from Eqs. (5) and (16)

- - - - Represents ±10% uncertainty in diffusion coefficient.

O Derived from experimental interferograms, Re = 5000, i = 15.0 mA/cm^2.

Δ Re = 5000, i = 25.0

□ Re = 10,000, i = 25.0

Fig. 22. Flow obstacles.

Ordinate: distance from cathode surface (mm).

Abscissa: distance from cathode leading edge (cm).

The smaller half-cylinder is attached to the cathode surface surface at z = 22 cm, the larger half-cylinder at 32 cm, the triangular parallelopiped at 47 cm, the rectangular parallelopiped at 62 cm, and the large circular cylinder is wedged between the two glass sidewalls at z = 82 cm.

- - - - Mass transfer boundary layer edge

Fig. 23. Experimental interferograms of the smaller half-cylinder. The electrolyte flow is from left to right.

left: $i = 0$

center: $Re = 500$, $i = 2.0$ mA/cm^2

right: $Re = 1500$, $i = 2.5$ mA/cm^2

Fig. 24. Experimental interferograms of the larger half-cylinder. Designations as in Fig. 23.

Fig. 25. Experimental interferograms of the triangular parallelopiped. Designations as in Fig. 23.

Fig. 26. Experimental interferograms of the rectangular parallelopiped. Designations as in Fig. 23.

Fig. 27. Experimental interferograms of the region near the triangular parallelopiped. $Re = 500$, $i = 2.0$ mA/cm^2. The electrolyte flow is from left to right.

a $z = 46.5$ cm

b 47.0

c 47.5

d 49.5

e 59.5

Fig. 28. Experimental interferograms of the region near the triangular parallelopiped. $Re = 1500$, $i = 2.5$ mA/cm^2. Designations as in Fig. 27.

Fig. 29. Boundary layer thicknesses at Re = 500.

Ordinate: Nernst boundary layer thickness (mm).

Abscissa: reduced distance from cathode leading edge.

● derived from experimental interferograms.

_____ Norris and Streid correlation.[15]

— — — reduced boundary layer thicknesses near obstacles.

a z = 22 cm, location of smaller half-cylinder

b z = 32 cm, larger half-cylinder.

c z = 47 cm, triangular parallelopiped

d z = 62 cm, rectangular parallelopiped

e z = 82 cm, large circular cylinder

Fig. 30. Boundary layer thicknesses at Re = 1500. Designations as in Fig. 10.

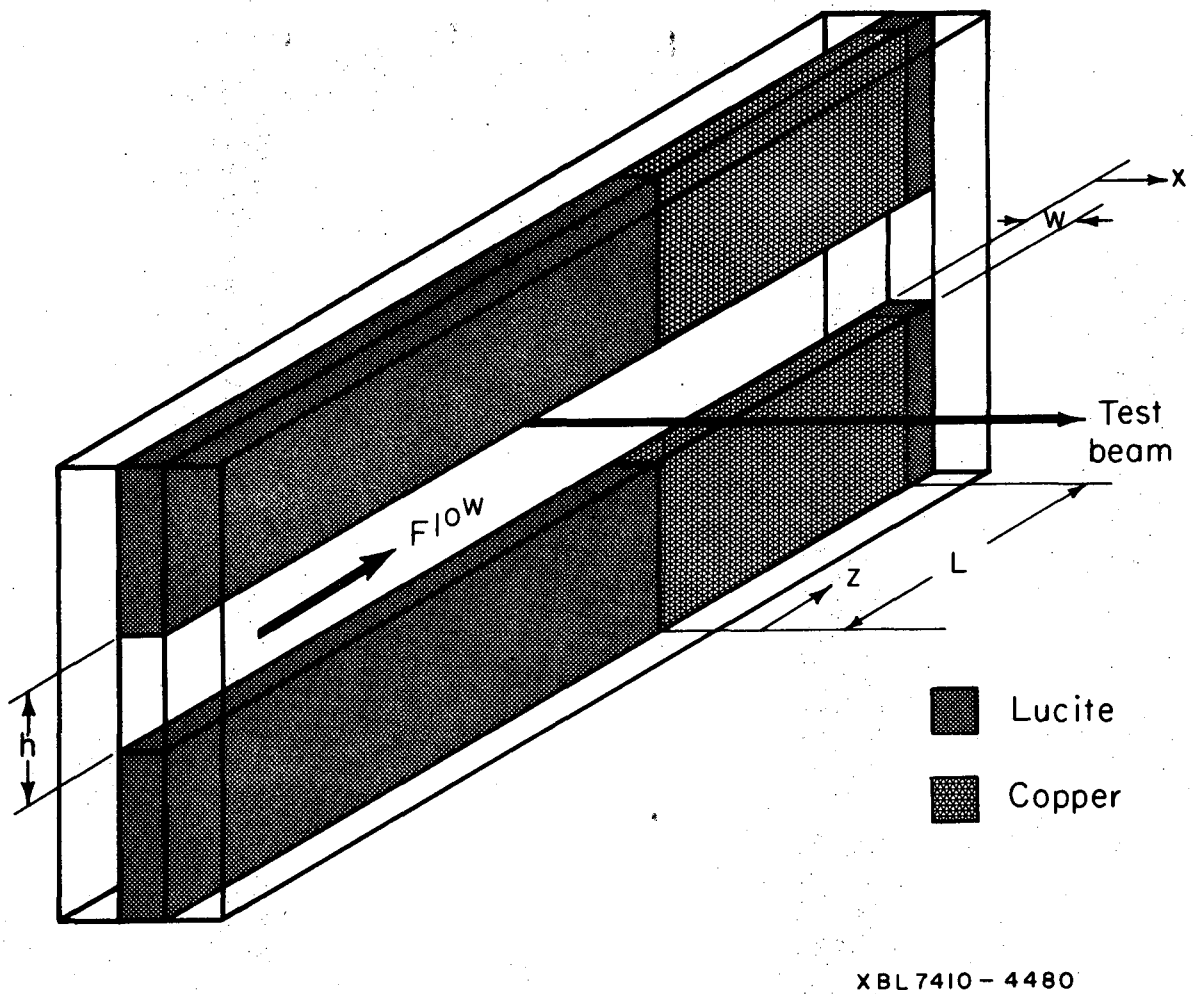

XBL 7410 - 4480

Fig. 1

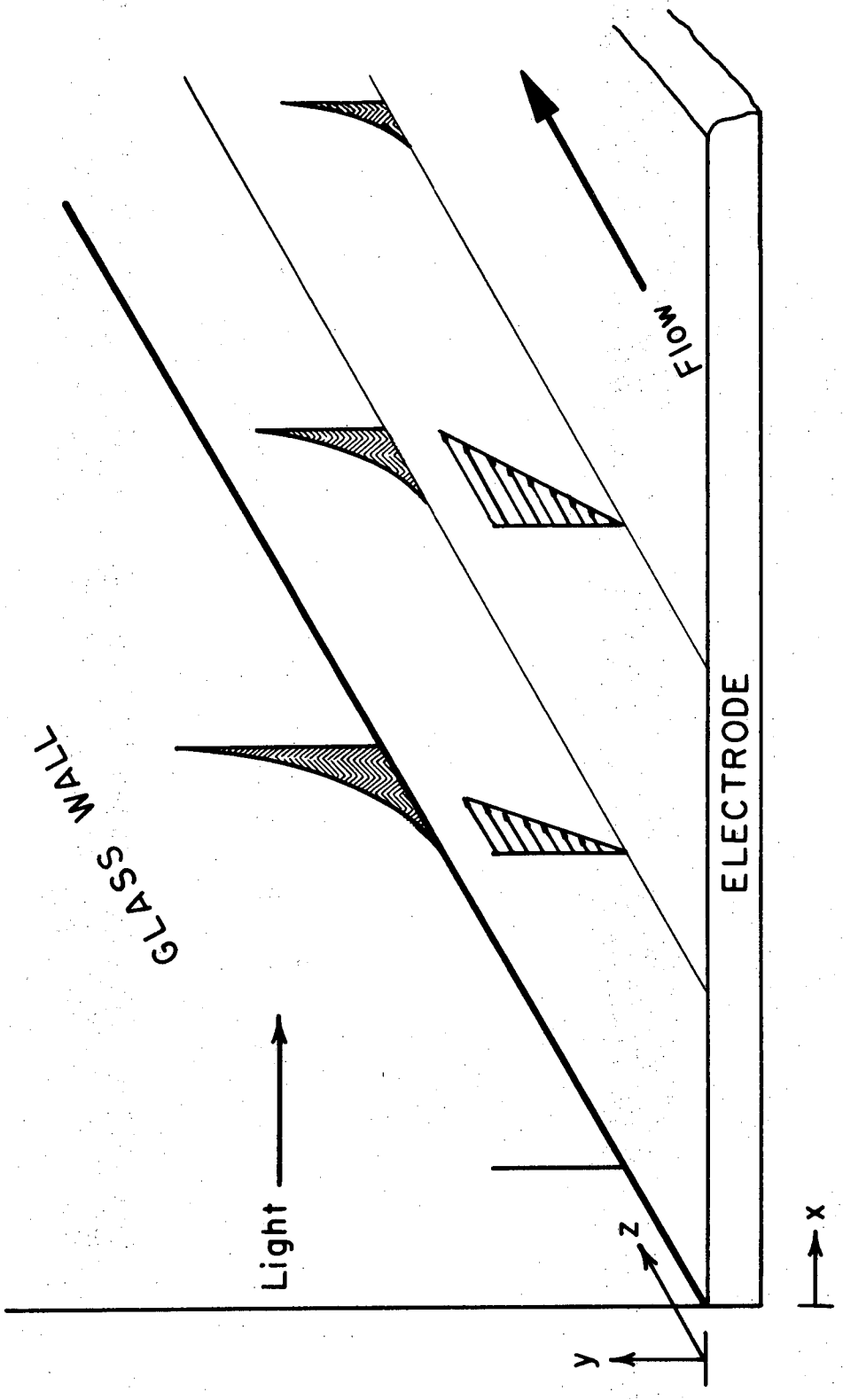

Fig. 2

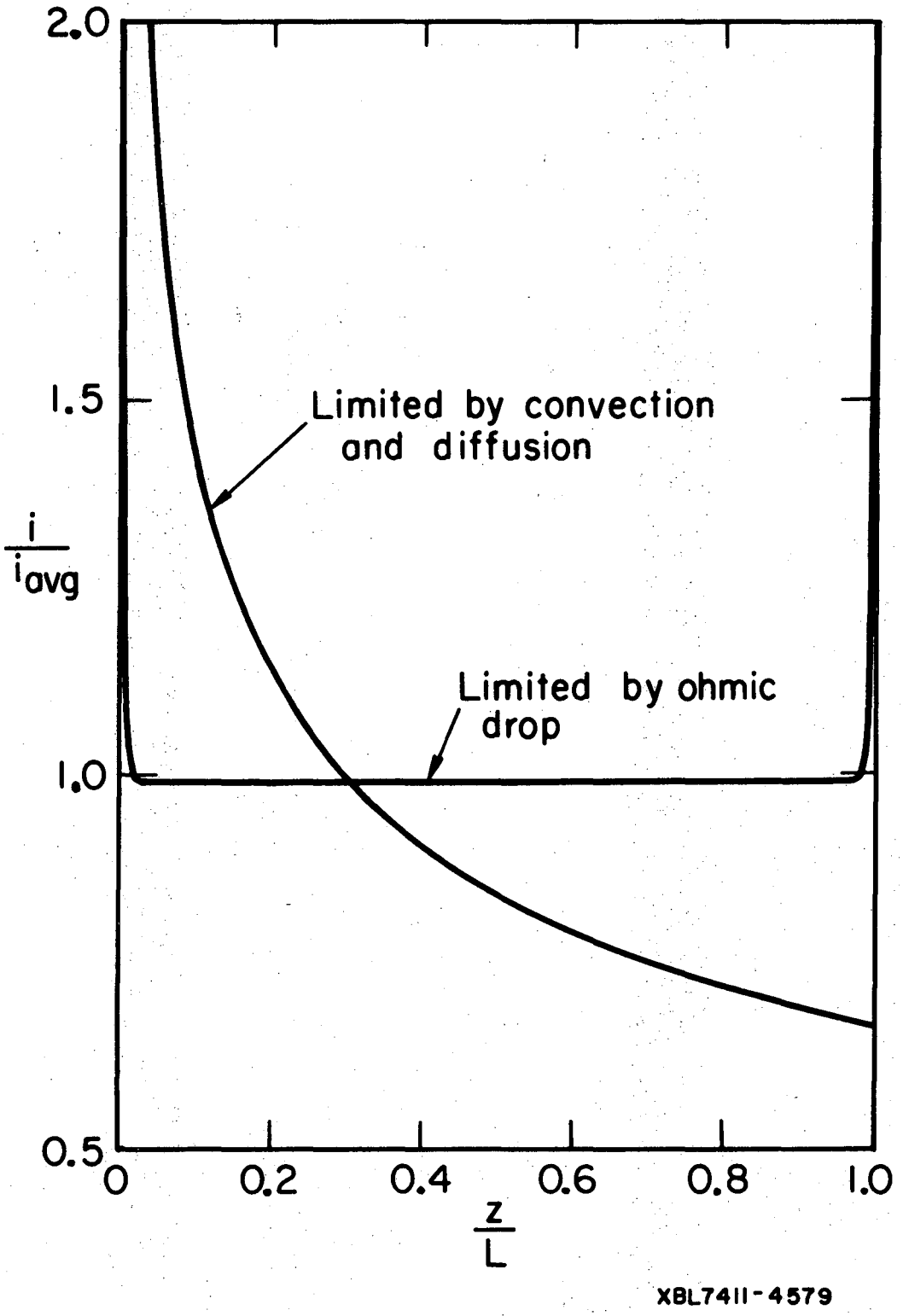

Fig. 3

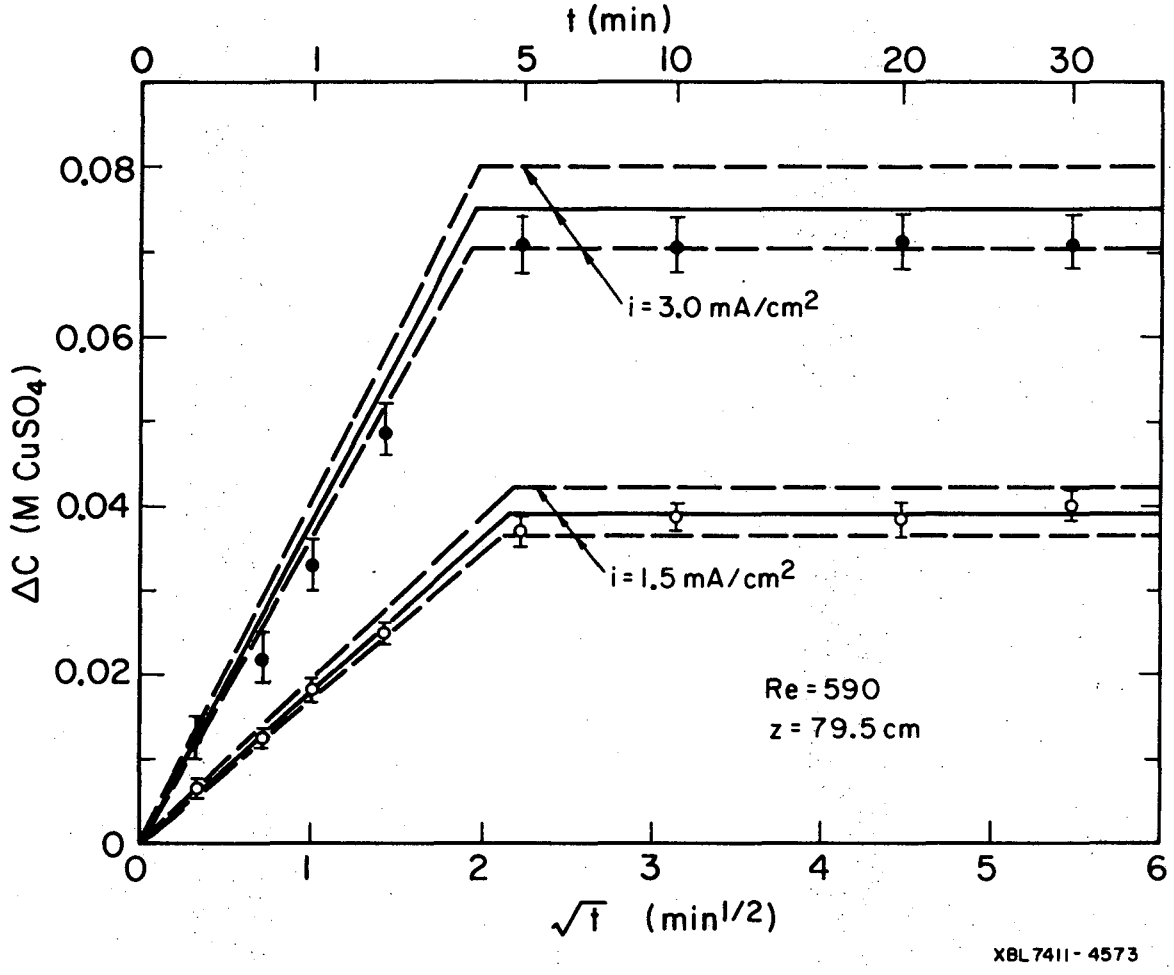
t (min)
0
1
5
10
20
30
0.08
0.06
0.04
0.02
0
ΔC (M CuSO4)
i = 3.0 mA/cm2
i = 1.5 mA/cm2
Re = 590
z = 79.5 cm
0
1
2
3
4
5
6
√t (min1/2)
XBL7411-4573

Fig. 4

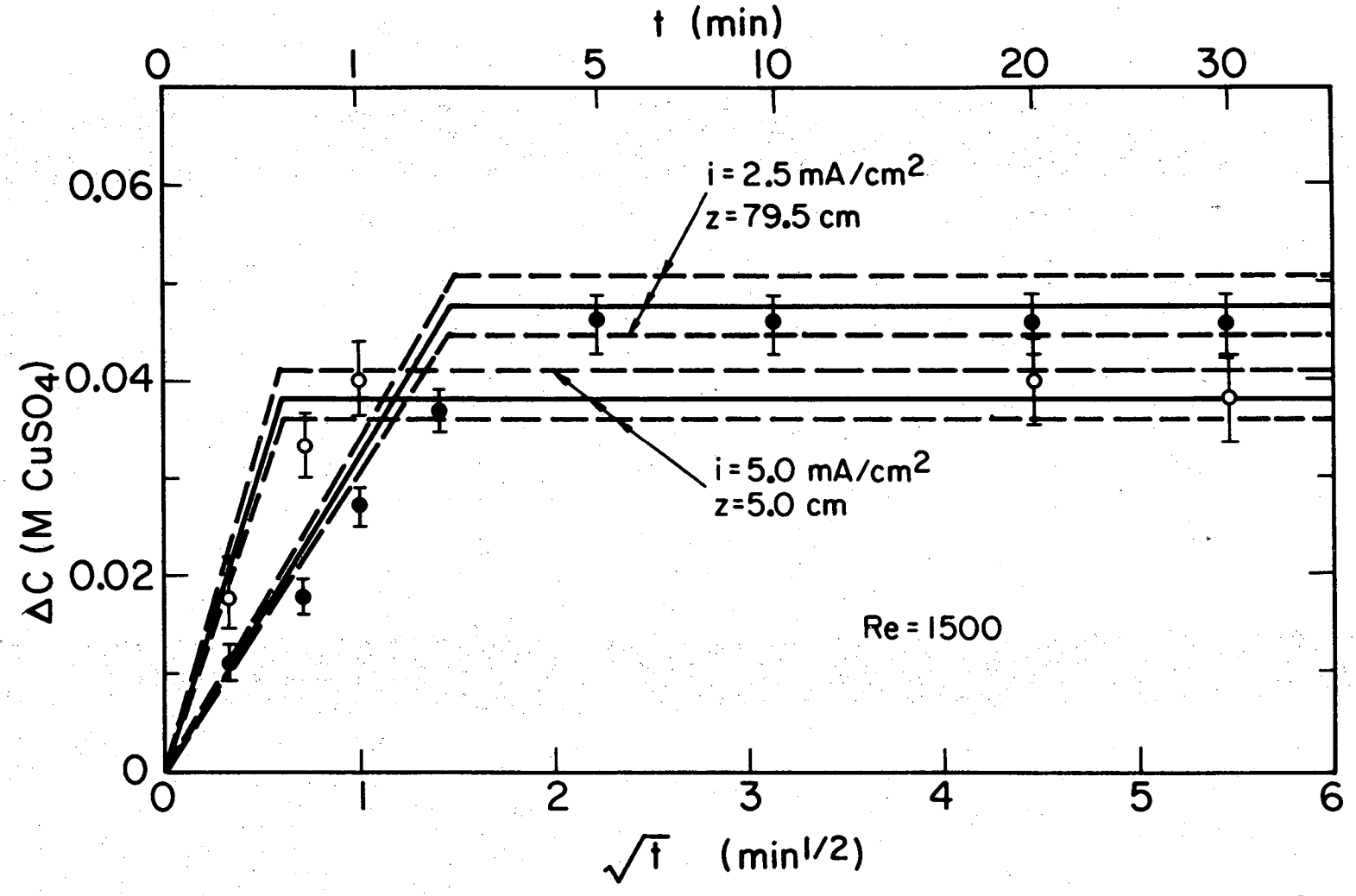

Fig. 5

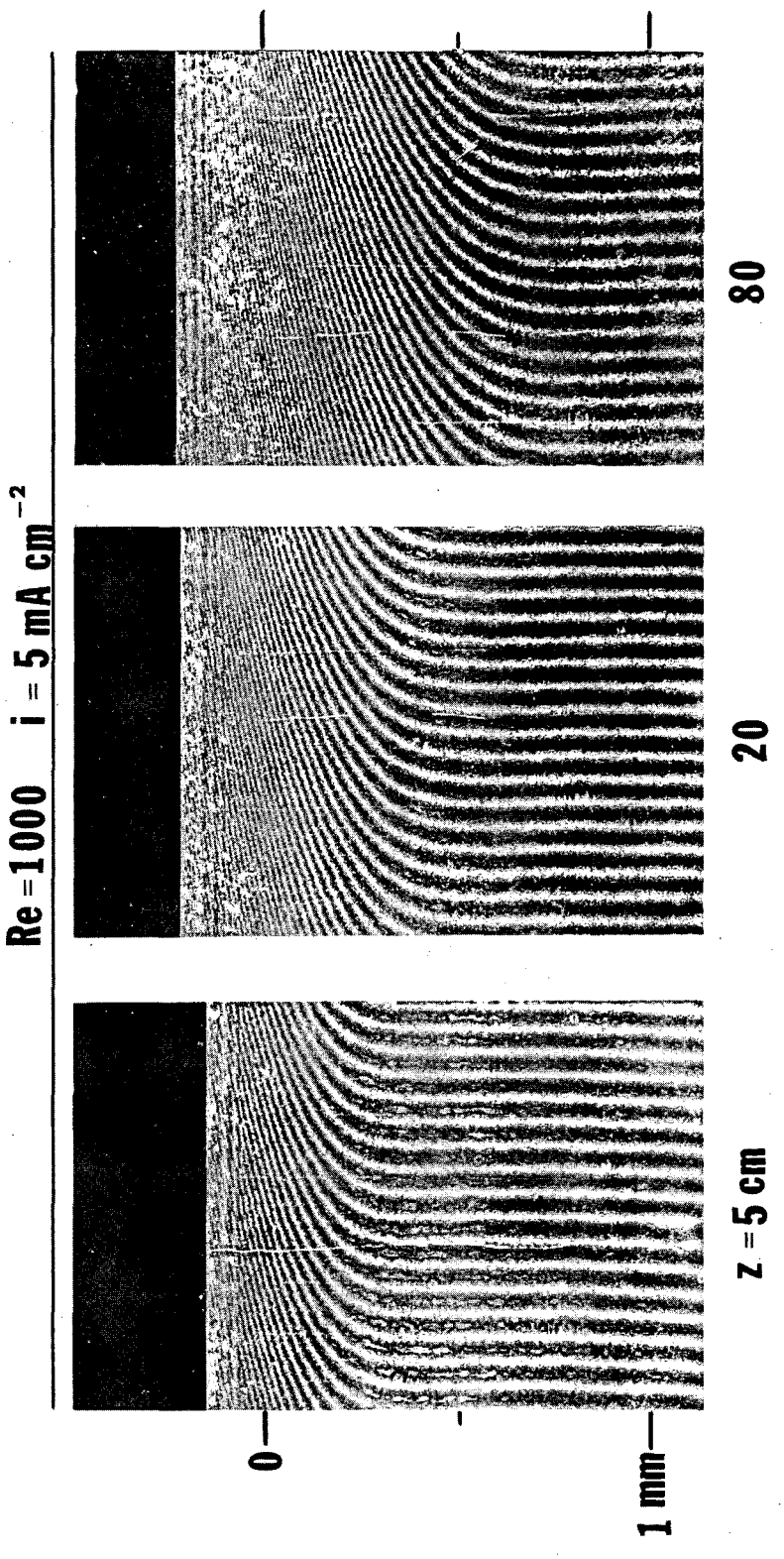

XBB 748-5797

Fig. 6

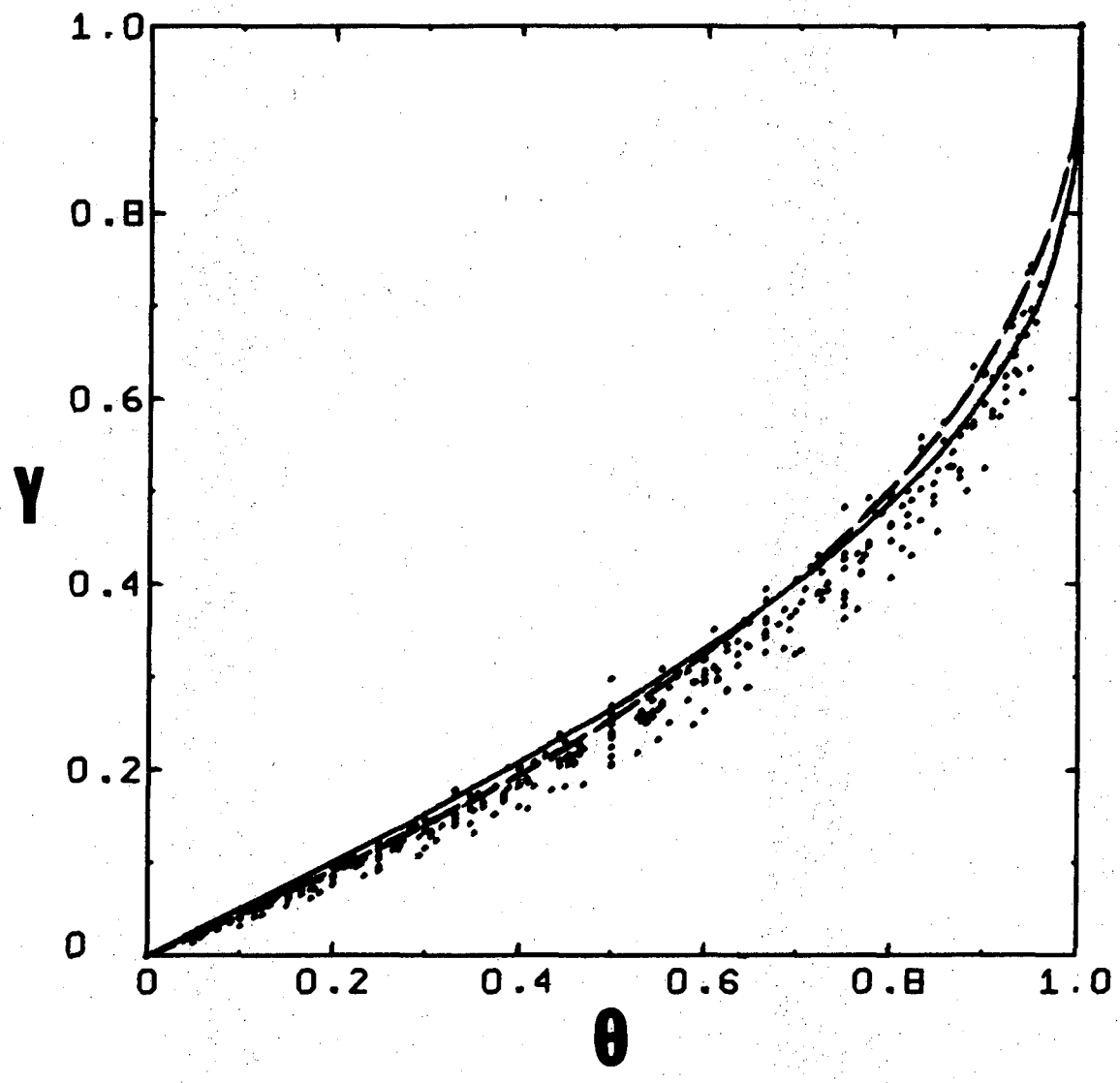

XBL 7411-7560

Fig. 7

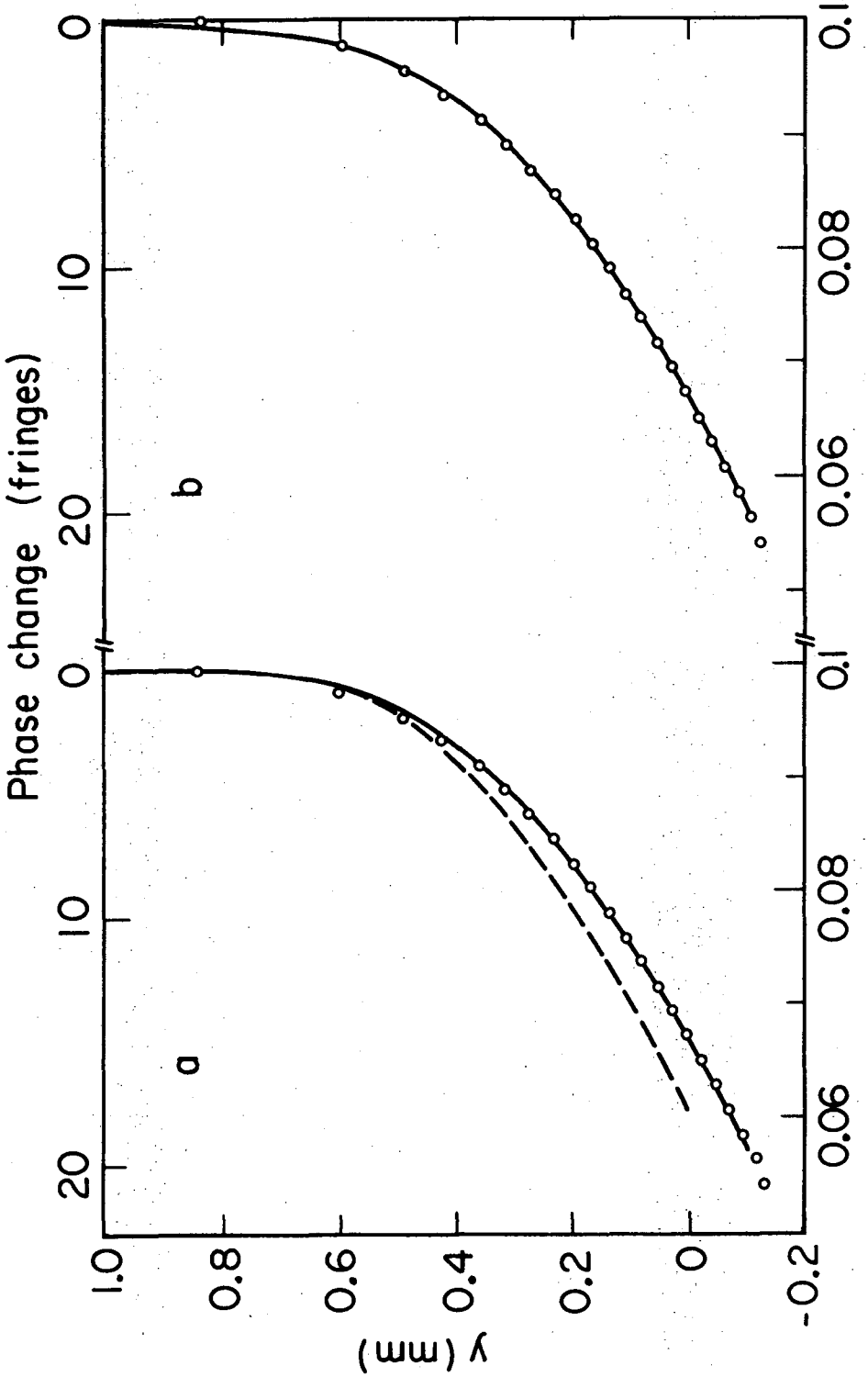
Phase change (fringes)
0
10
20
0
10
20
a
b
1.0
0.8
0.6
0.4
0.2
0
-0.2
y (mm)
0.1
0.08
0.06
0.1
0.08
0.06
C (M CuSO4)
XBL7410-4381

Fig. 8

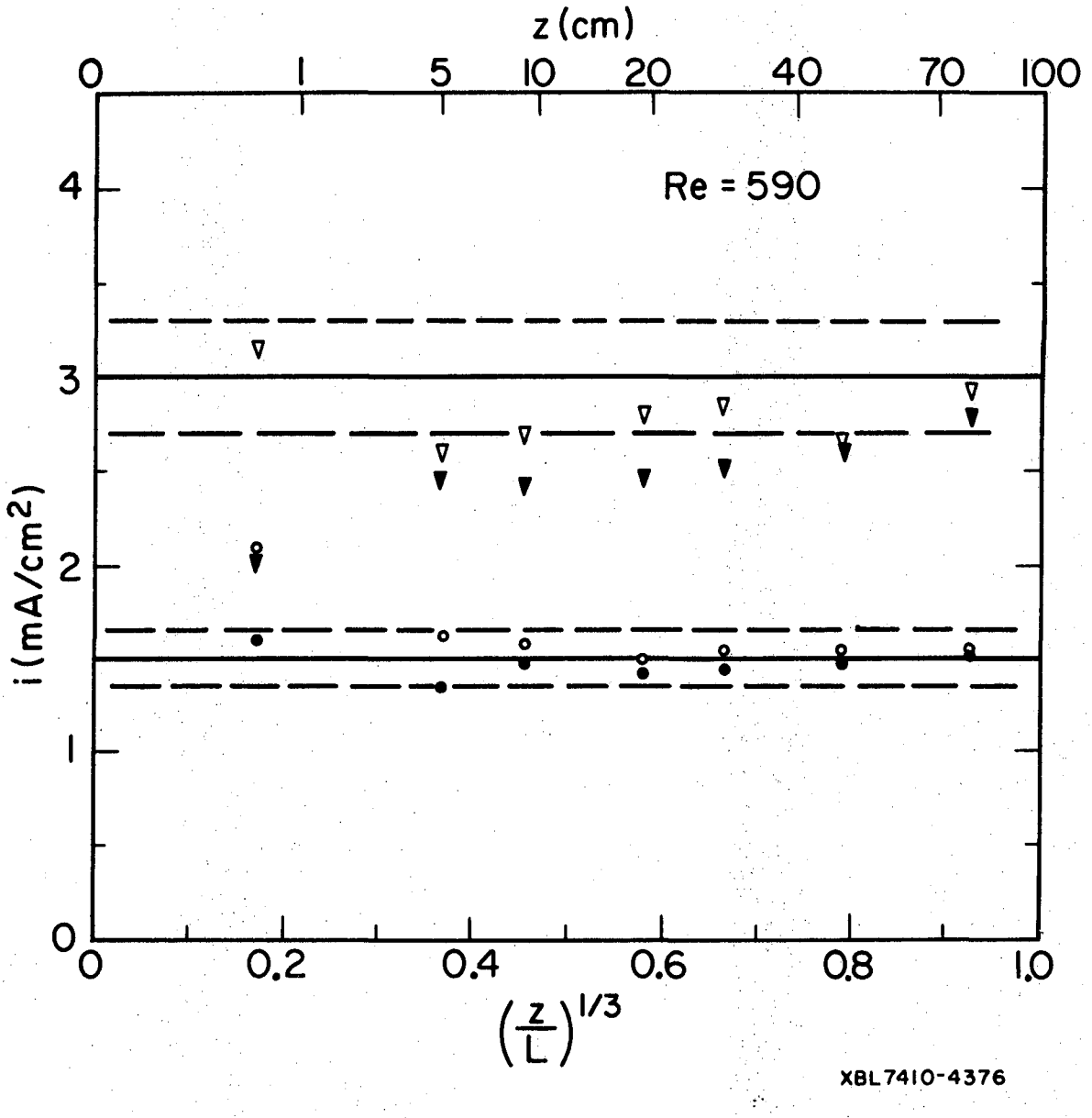

Fig. 9

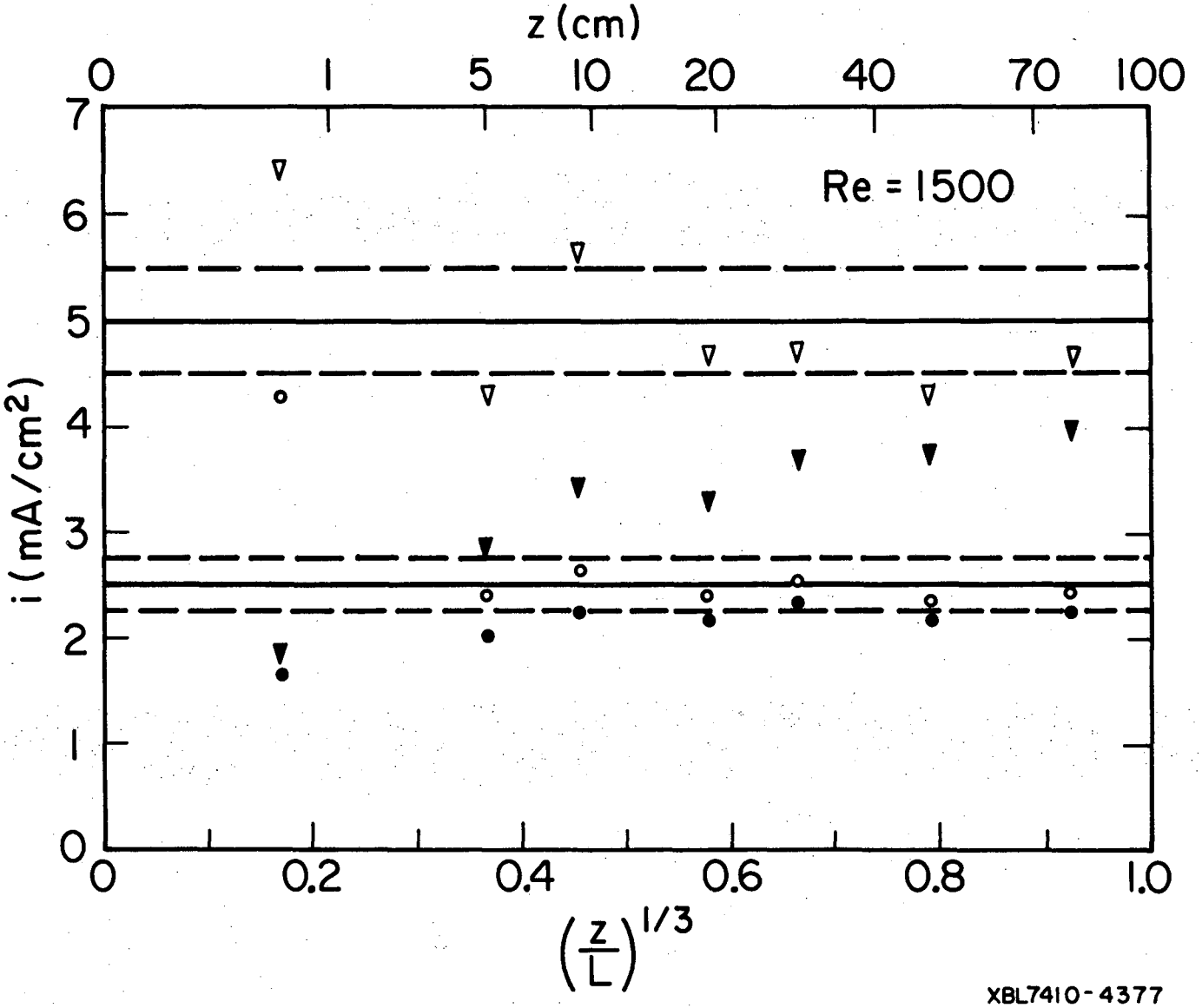
z (cm)
0
1
5
10
20
40
70
100
Re = 1500
i (mA/cm²)
0
1
2
3
4
5
6
7
0
0.2
0.4
0.6
0.8
1.0
(z/L)^1/3
XBL7410-4377

Fig. 10

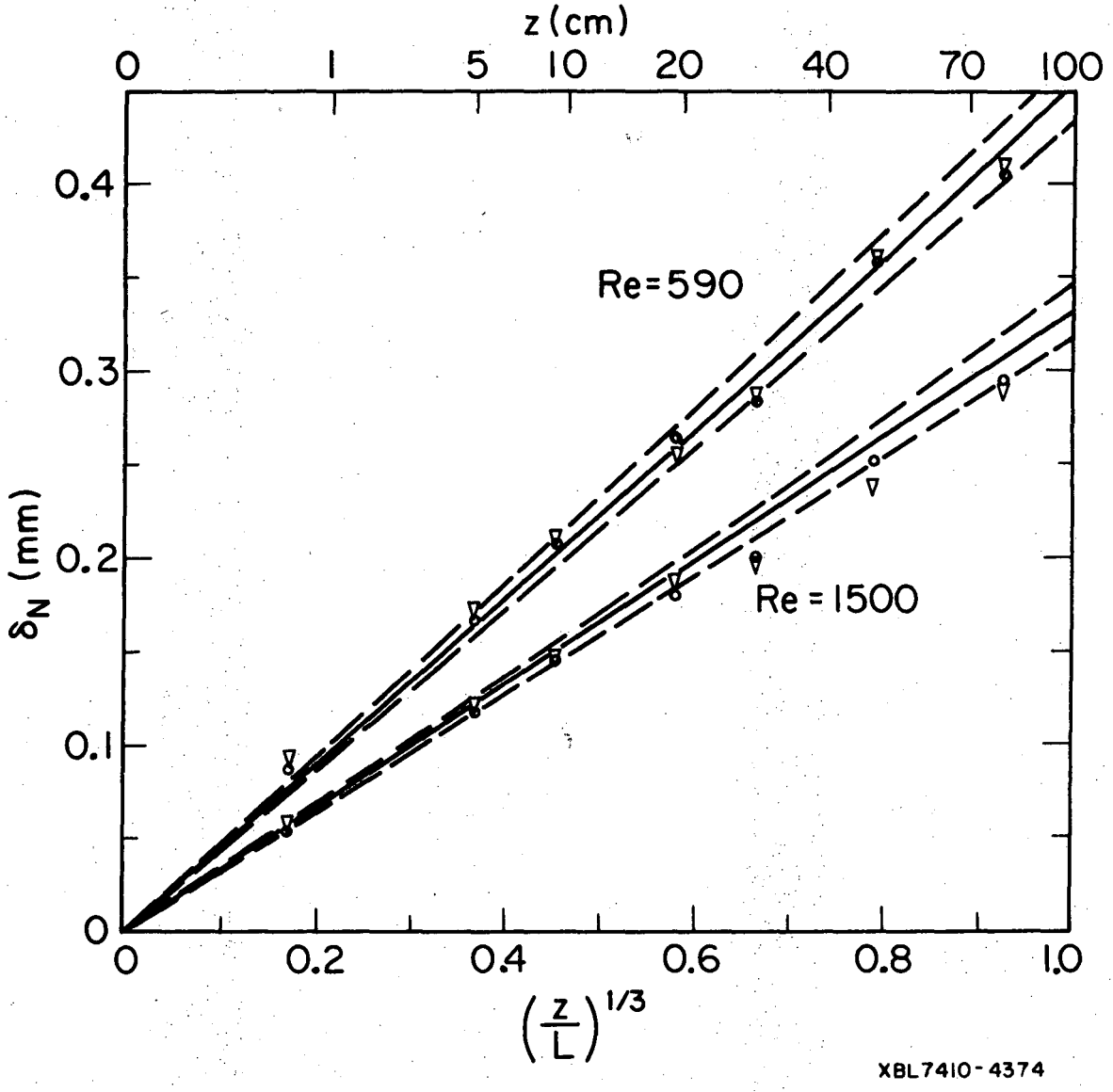

Fig. 11

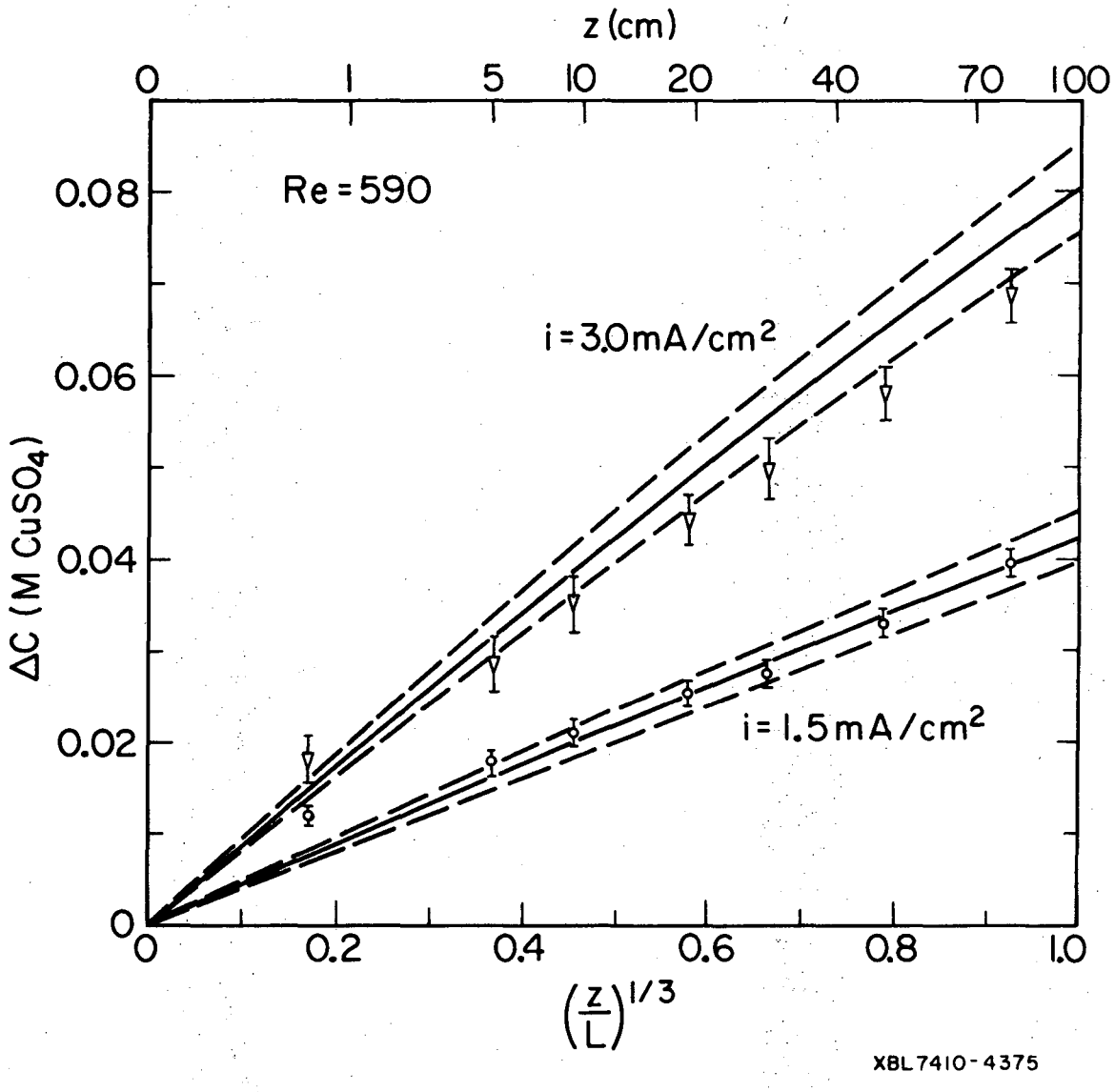
z (cm)
0
1
5
10
20
40
70
100
Re = 590
i = 3.0 mA/cm²
i = 1.5 mA/cm²
ΔC (M CuSO4)
0.08
0.06
0.04
0.02
0
0.2
0.4
0.6
0.8
1.0
(z/L)^1/3
XBL7410-4375

Fig. 12

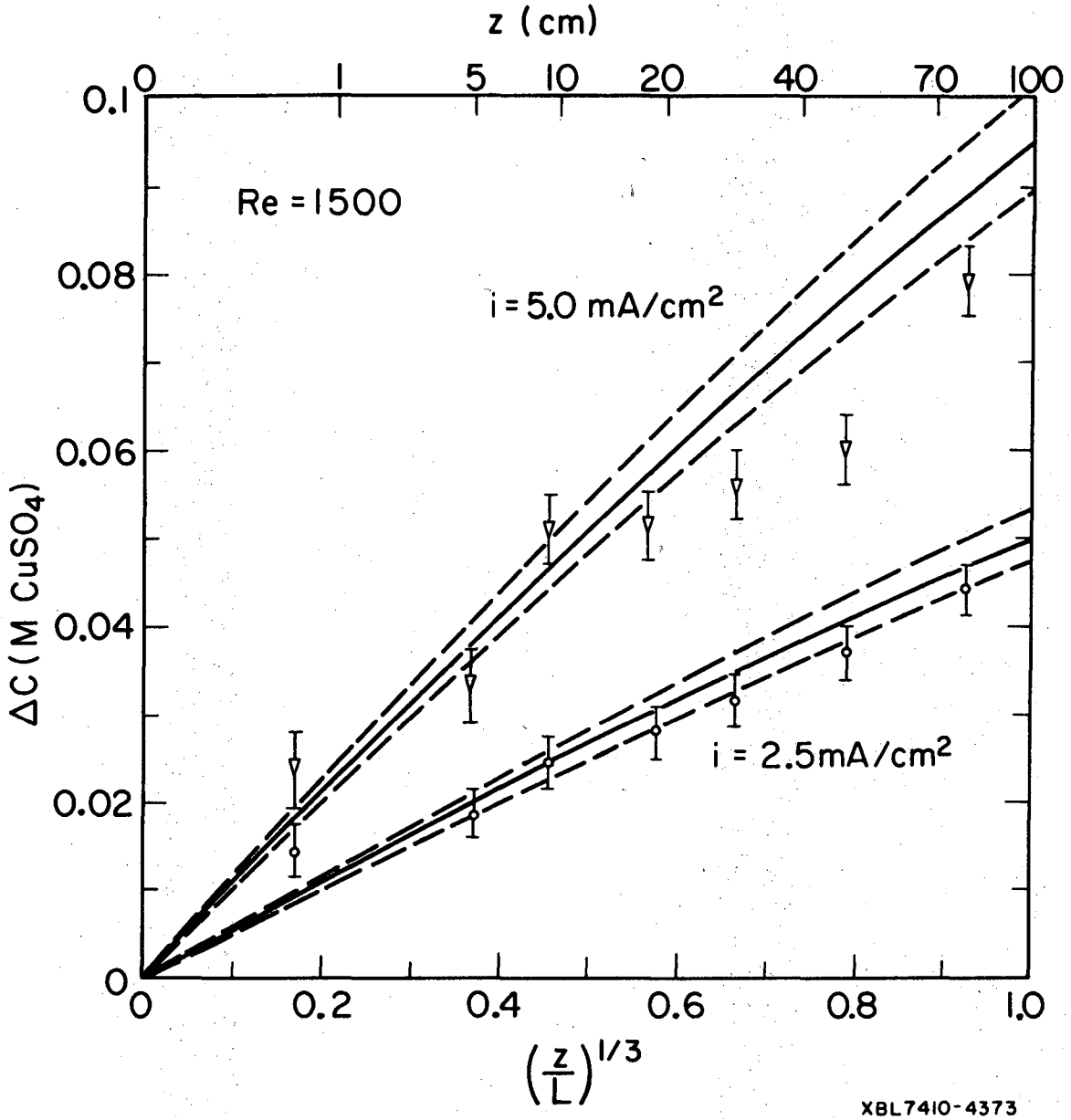

Fig. 13

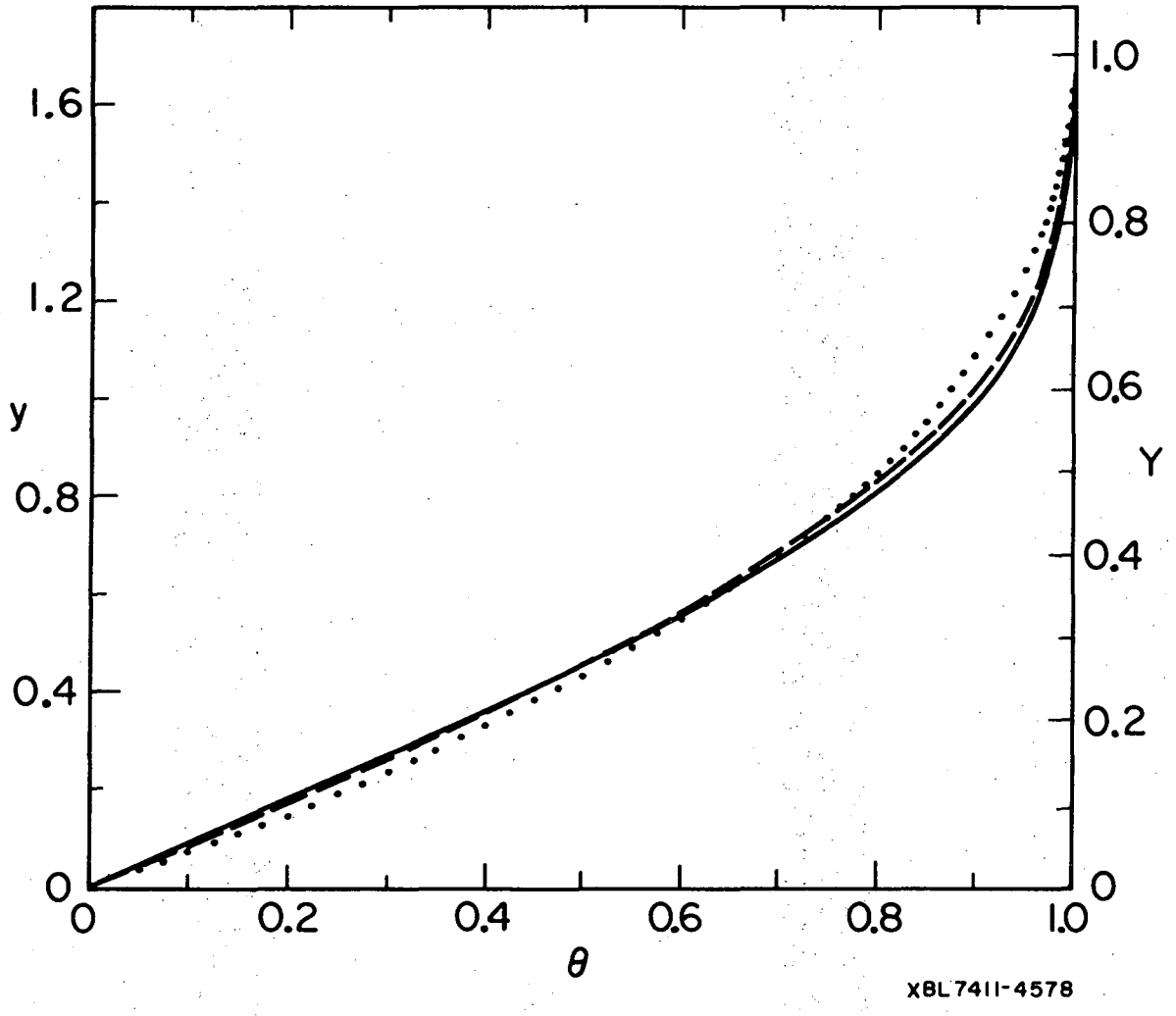

Fig. 14

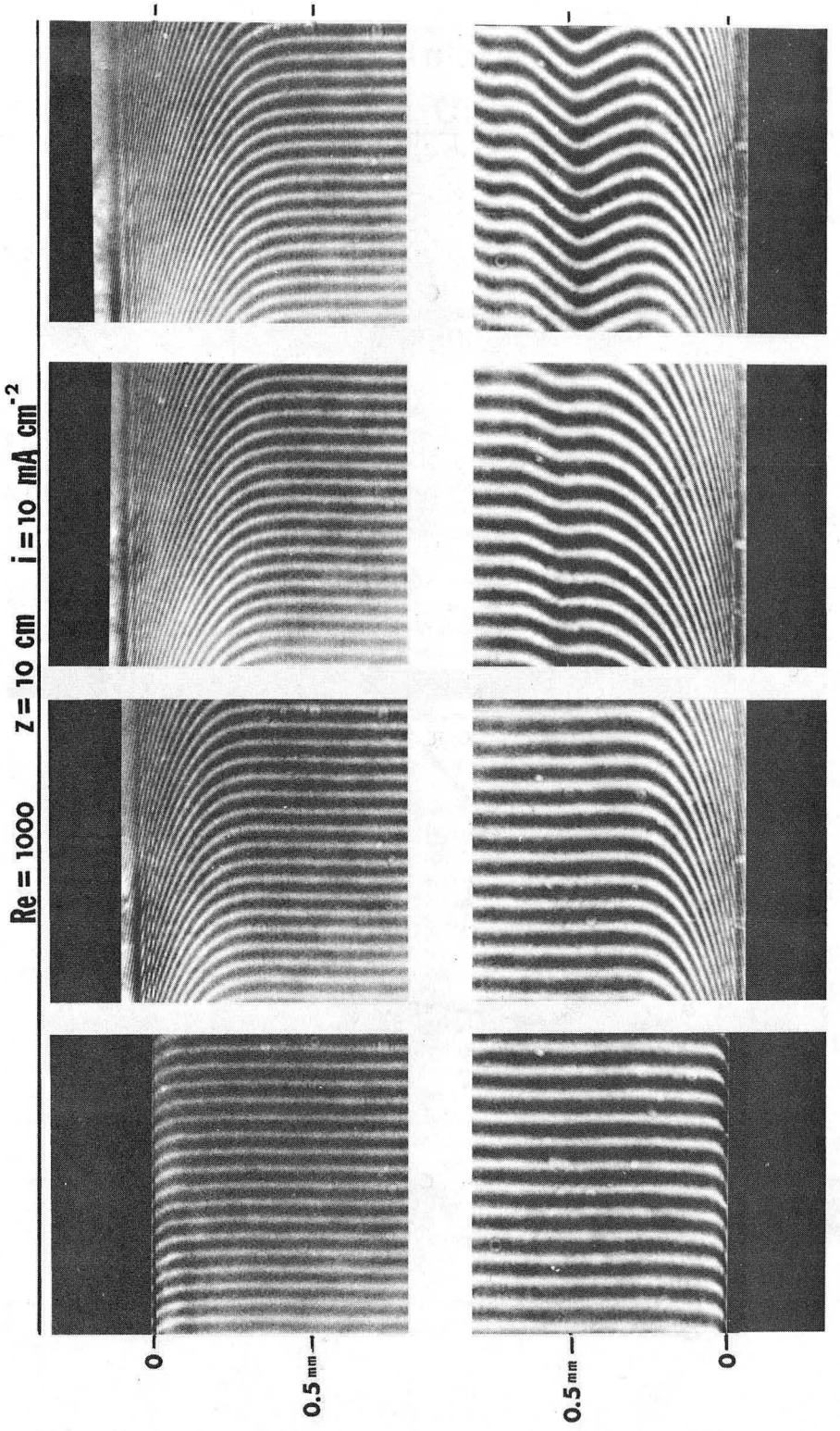

XBB 748-5799

Fig. 15

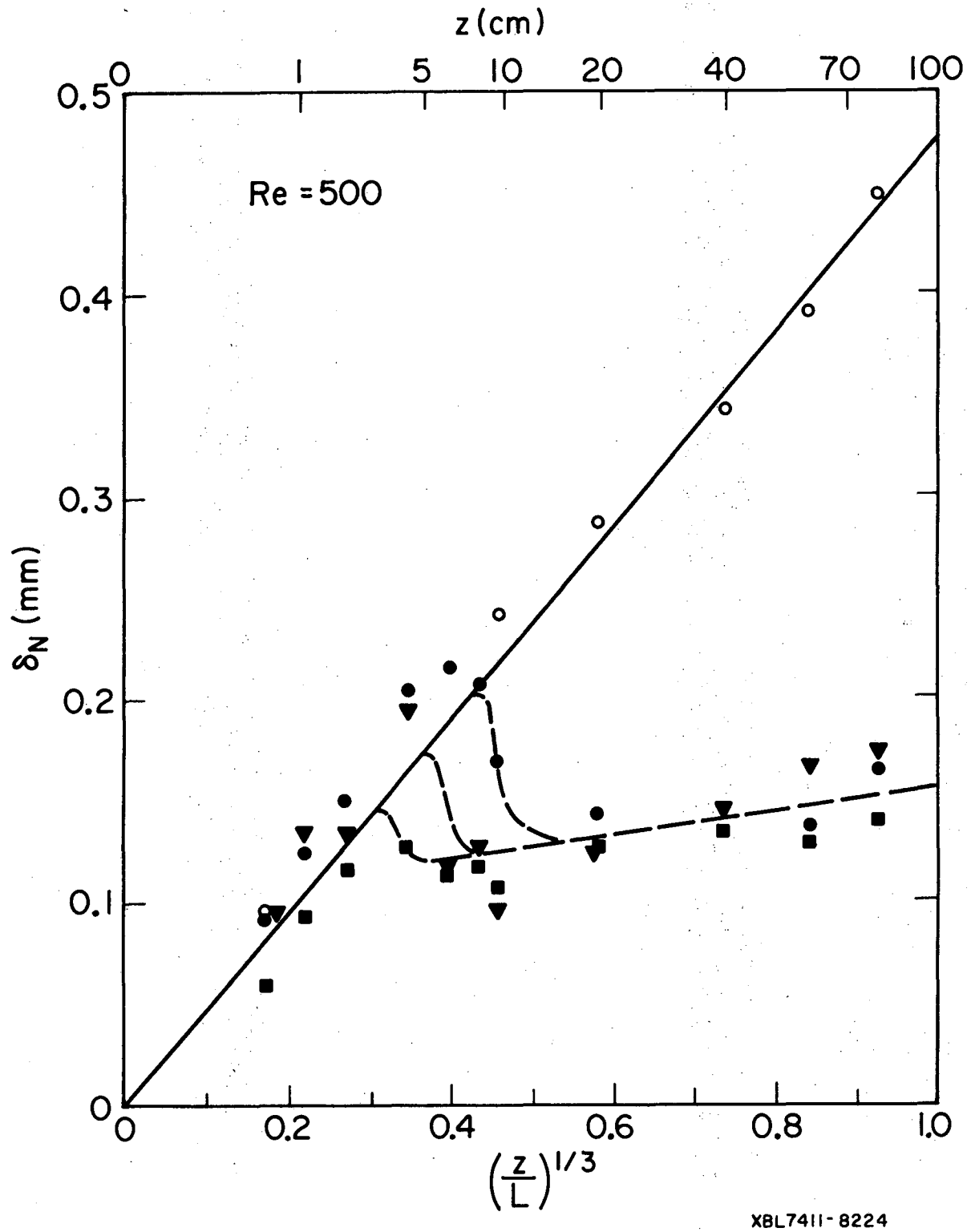
z (cm)
0
1
5
10
20
40
70
100
Re = 500
δ_N (mm)
0.5
0.4
0.3
0.2
0.1
0
0.2
0.4
0.6
0.8
1.0
$\left(\frac{z}{L}\right)^{1/3}$
XBL7411-8224

Fig. 16

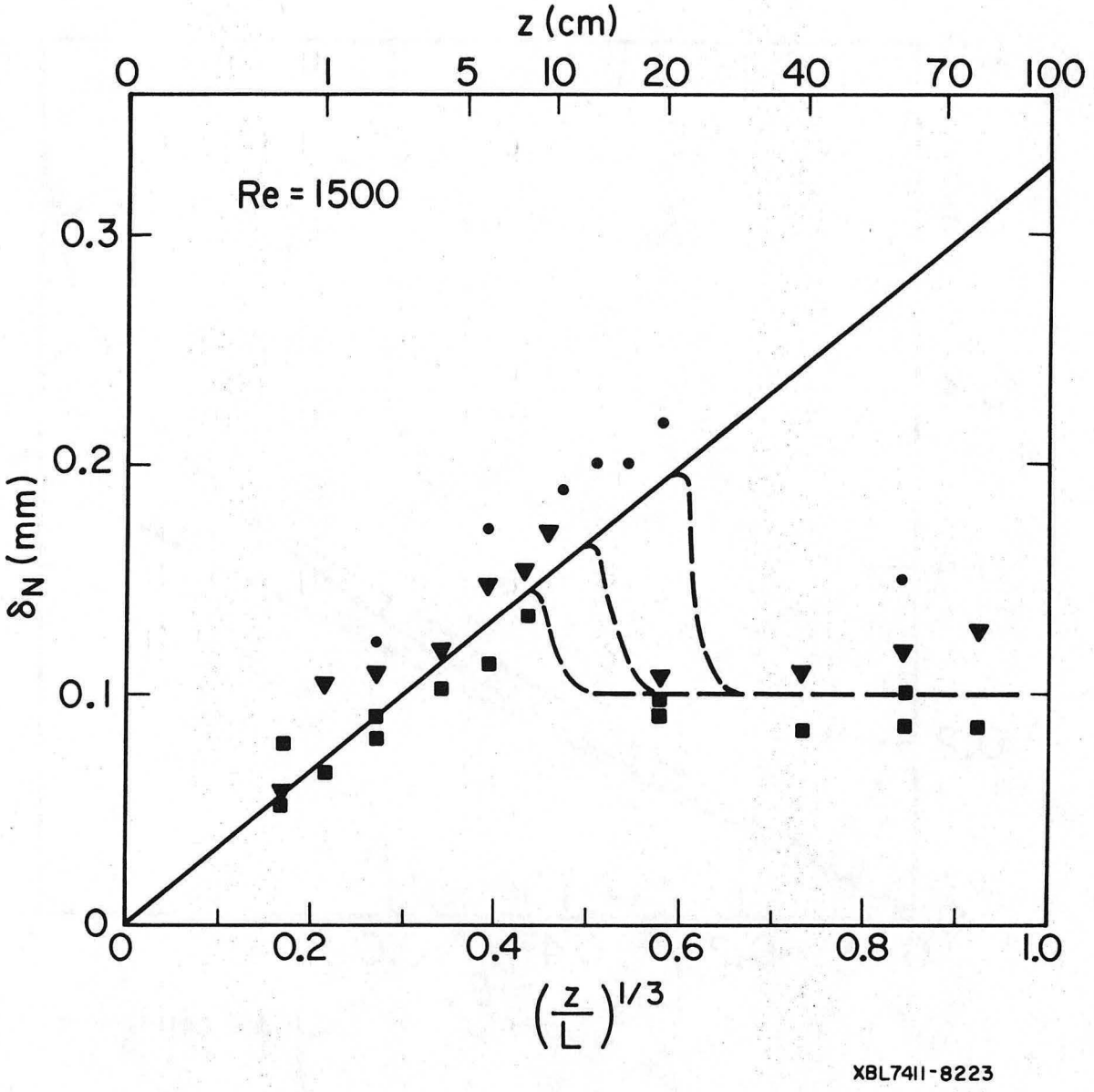

Fig. 17

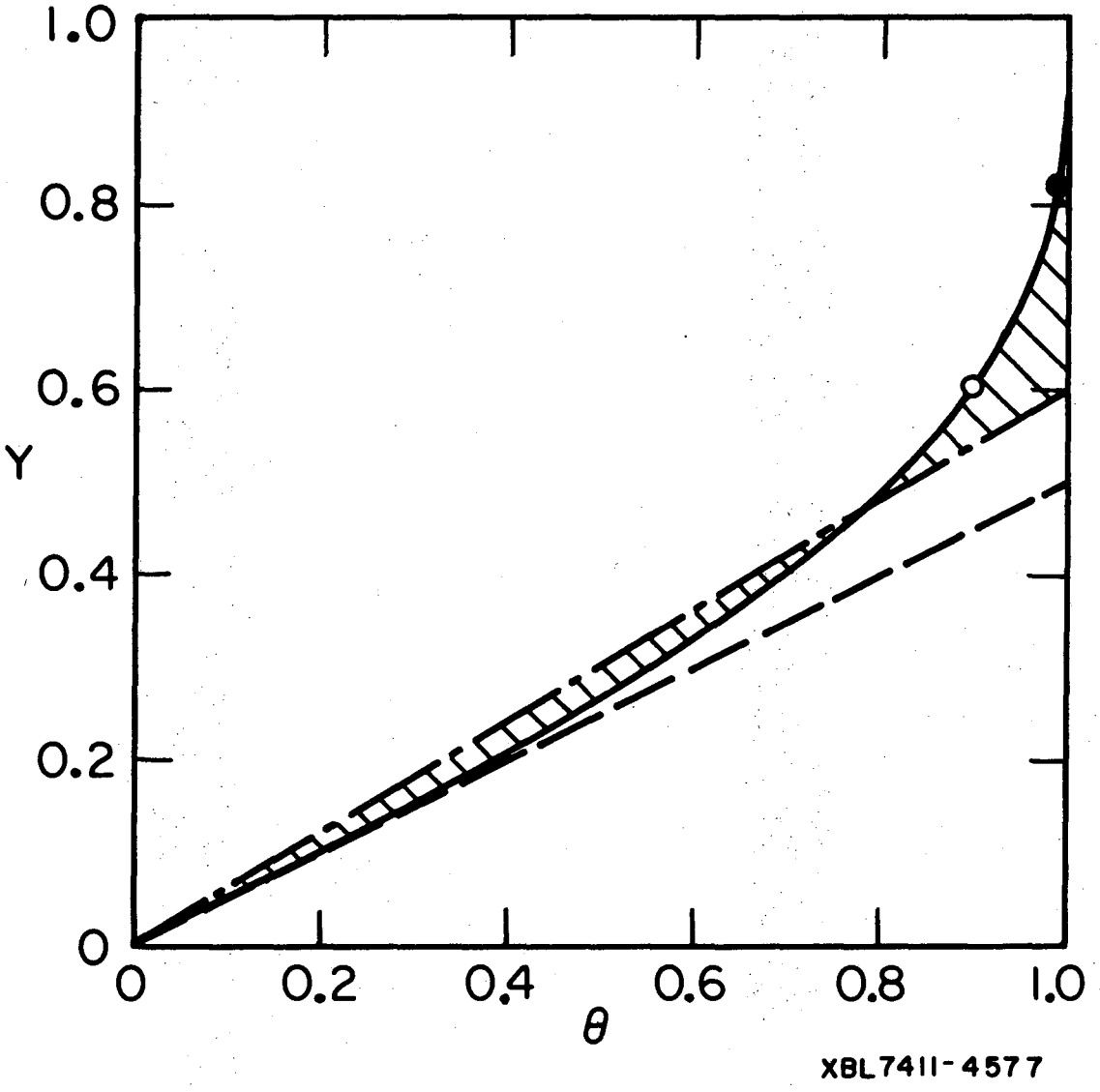

Fig. 18

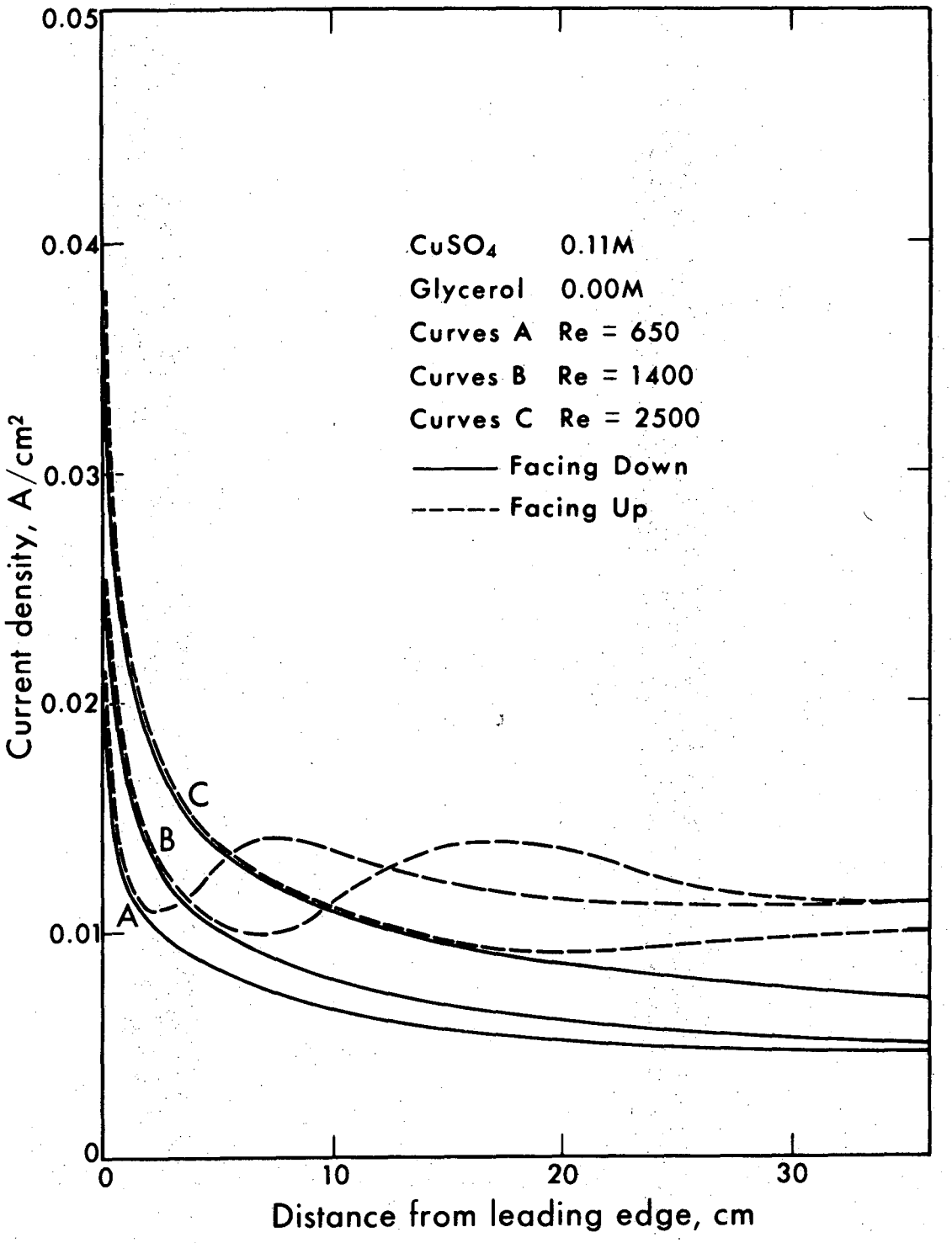

XBL 7411-8618

Fig. 19

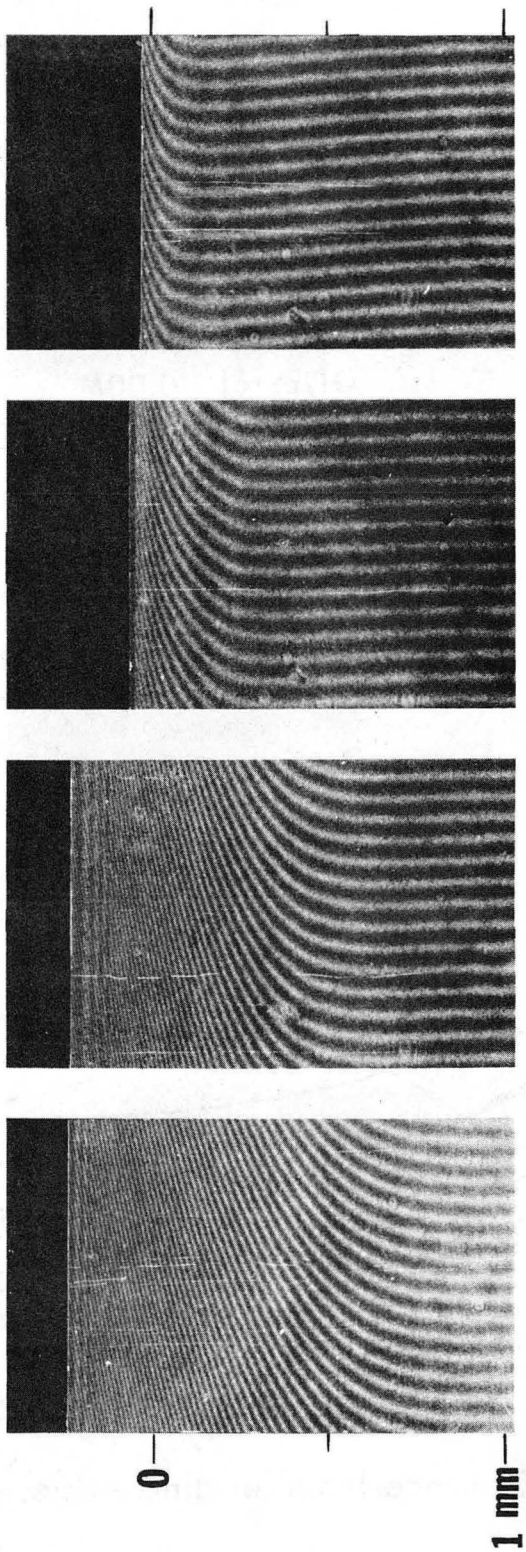

XBB 748-5798

Fig. 20

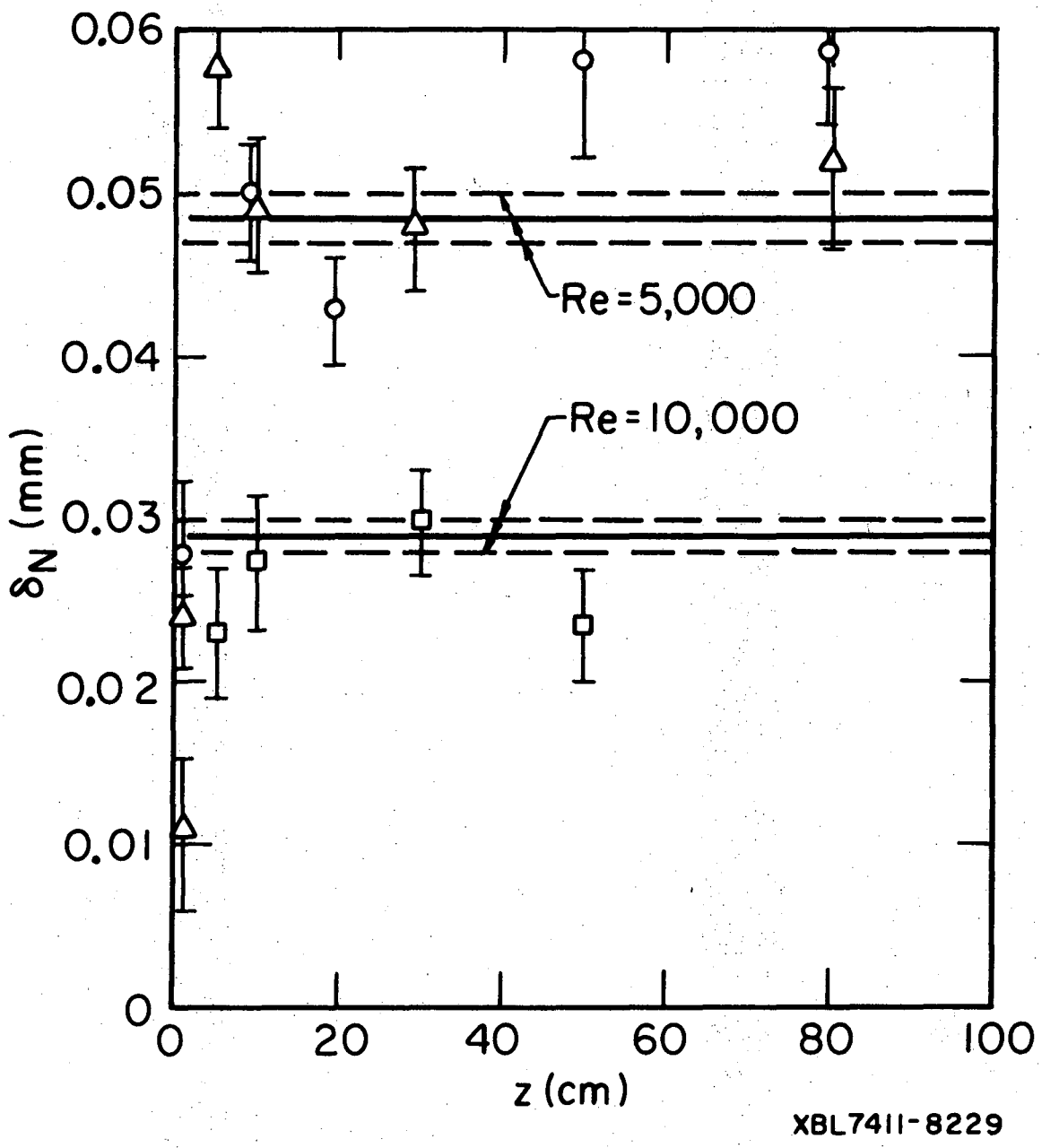

Fig. 21

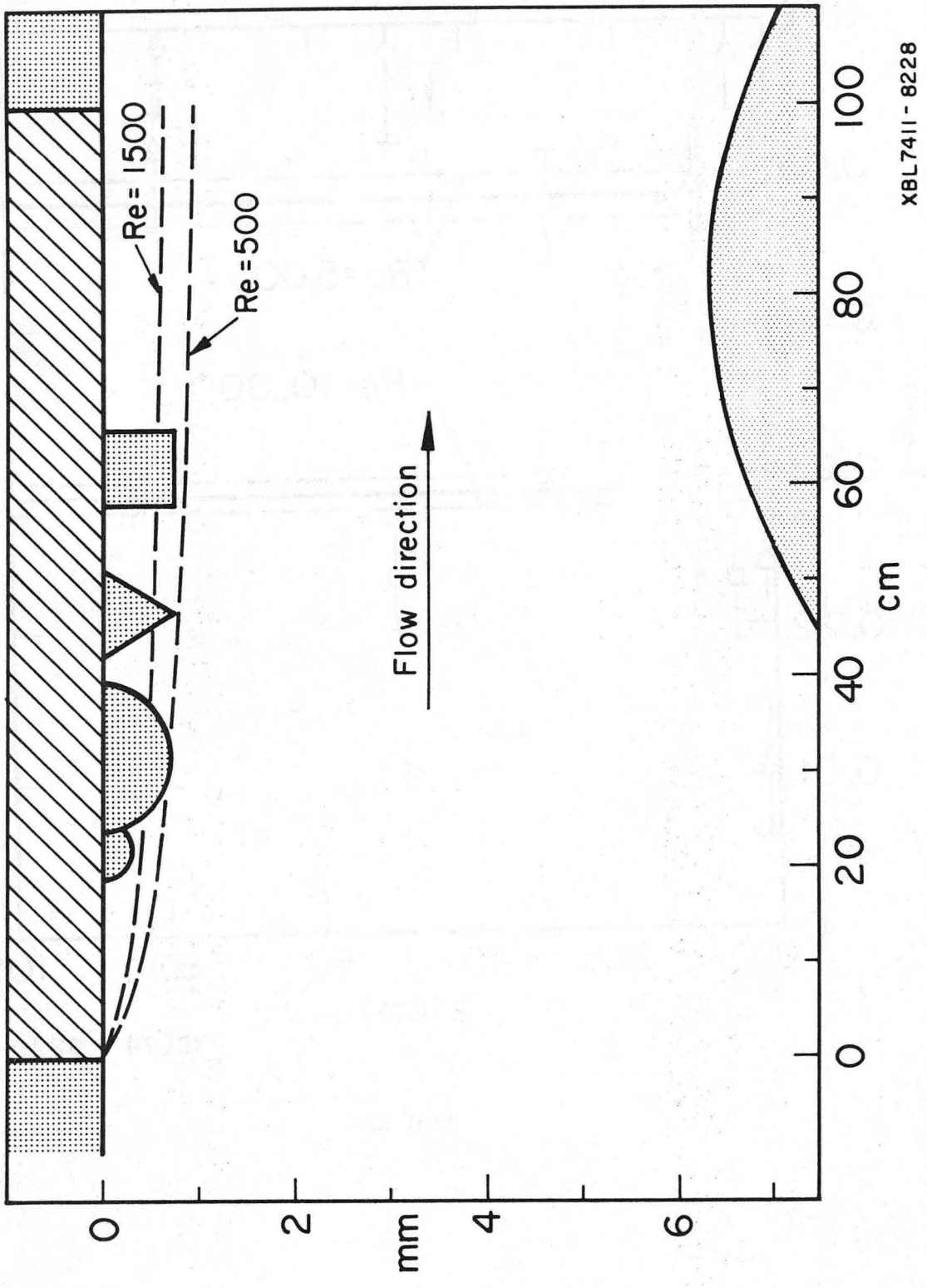
Re= 1500
Re=500
Flow direction
0
2
4
6
mm
0
20
40
60
80
100
cm
XBL7411-8228

Fig. 22

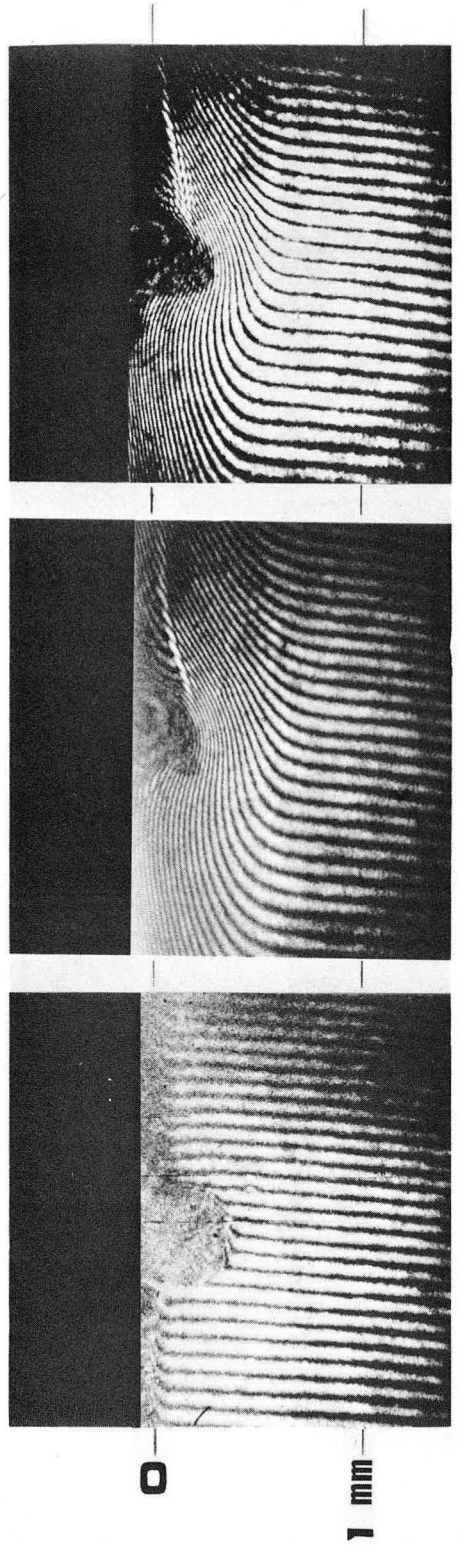

XBB 7411-8122

Fig. 23

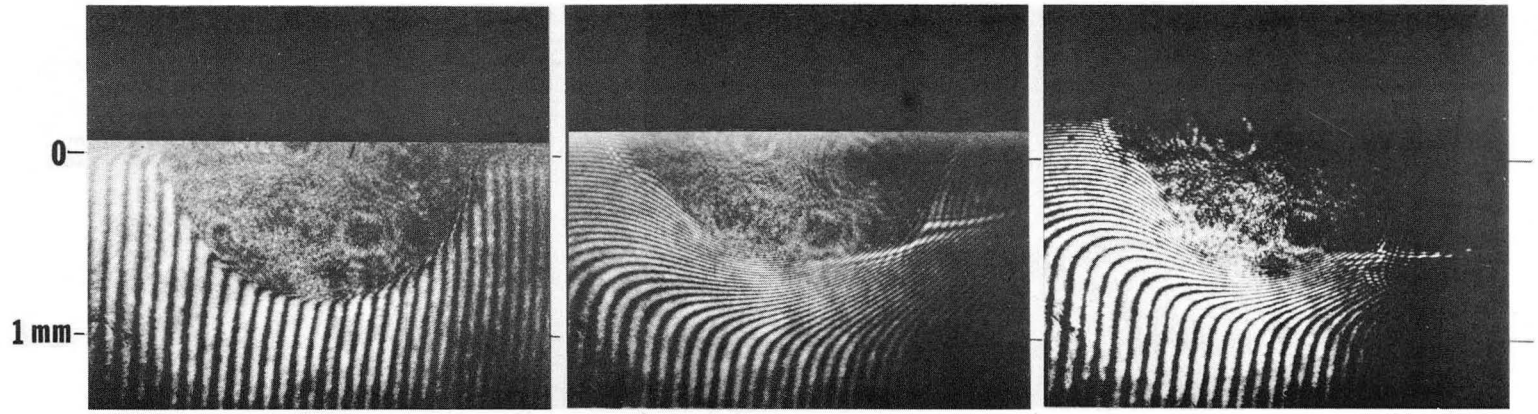

XBB 7411-8121

Fig. 24

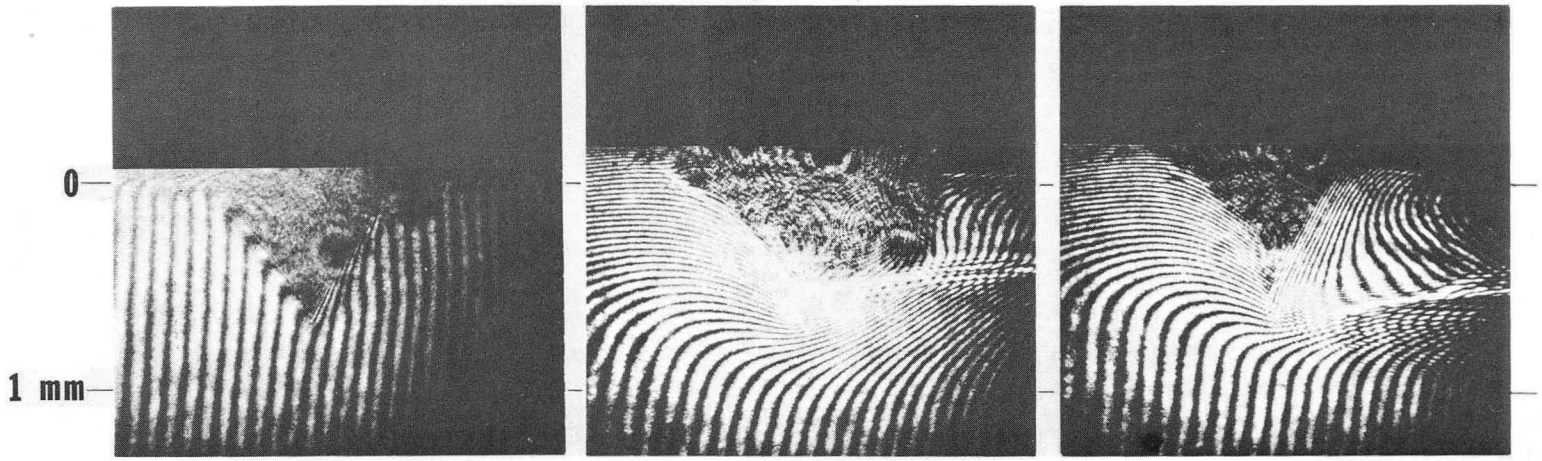

XBB 7411-8123

Fig. 25

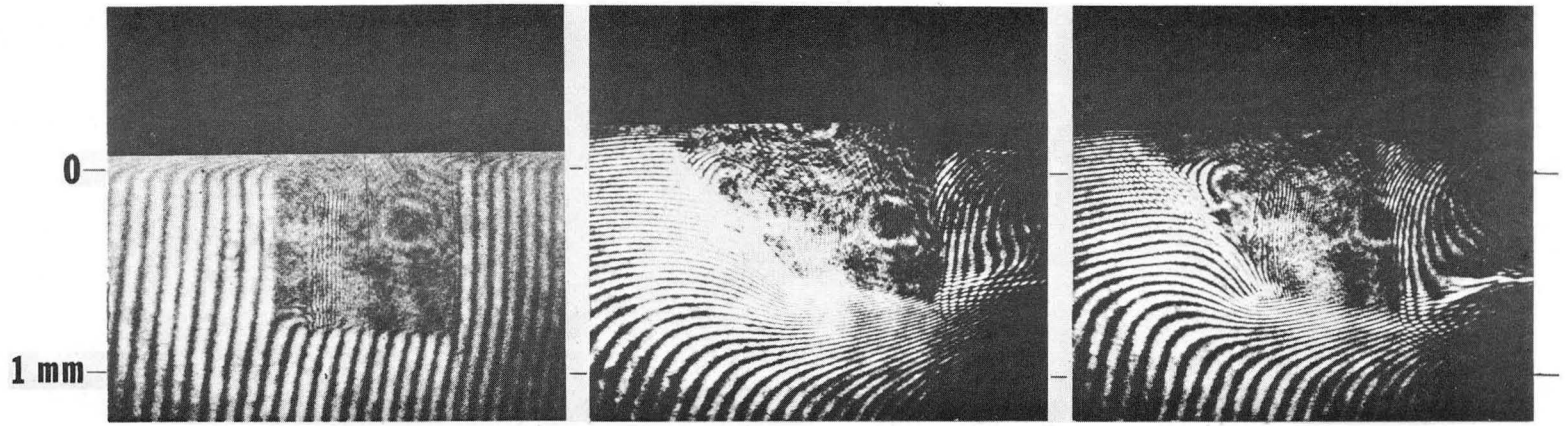

XBB 7411-8124

Fig. 26

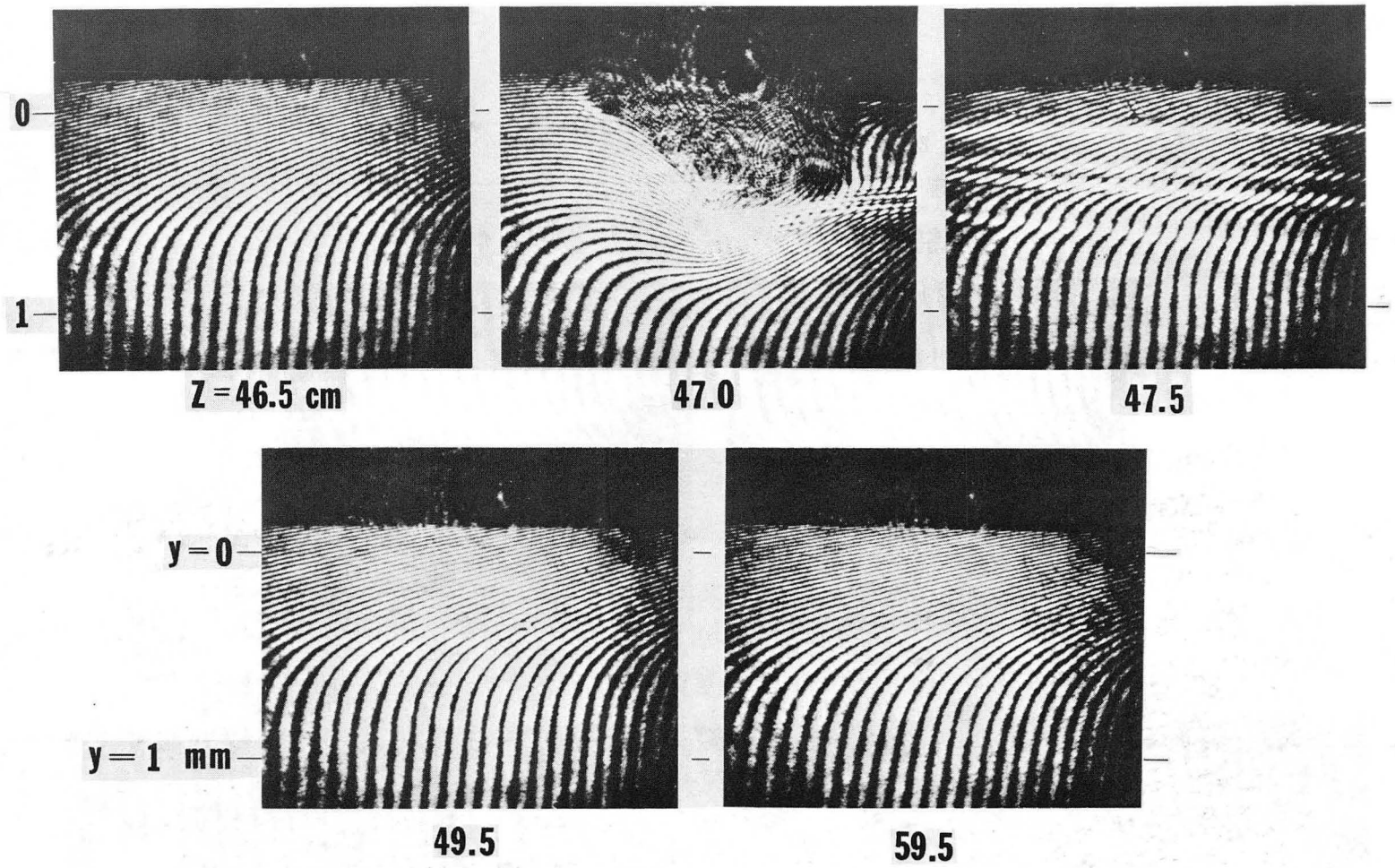

XBB 7411-8125

Fig. 27

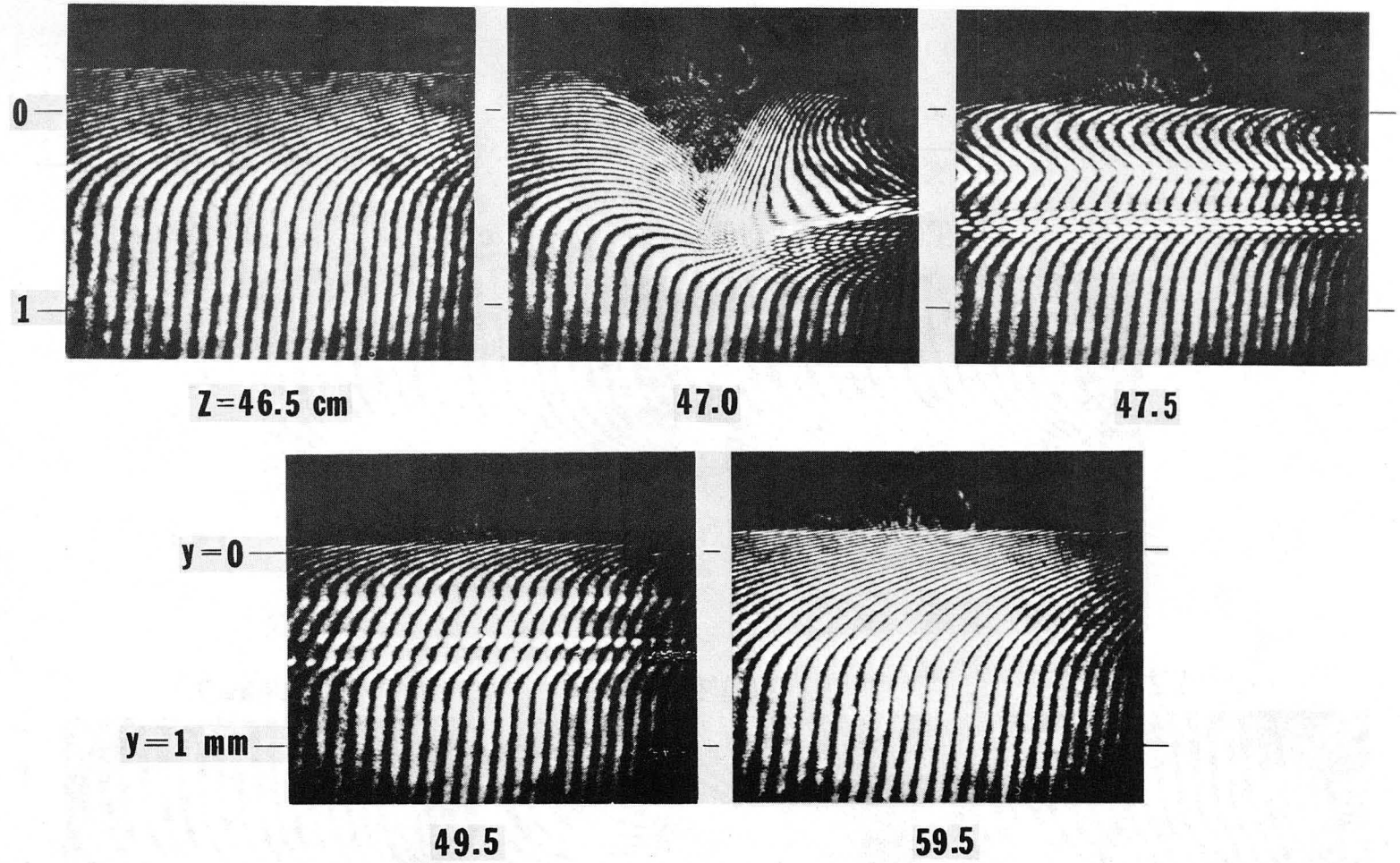
0
1
Z=46.5 cm
47.0
47.5
y=0
y=1 mm
49.5
59.5
Re=1500
i=2.5 mA/cm²
XBB 7411-8126

Fig. 28

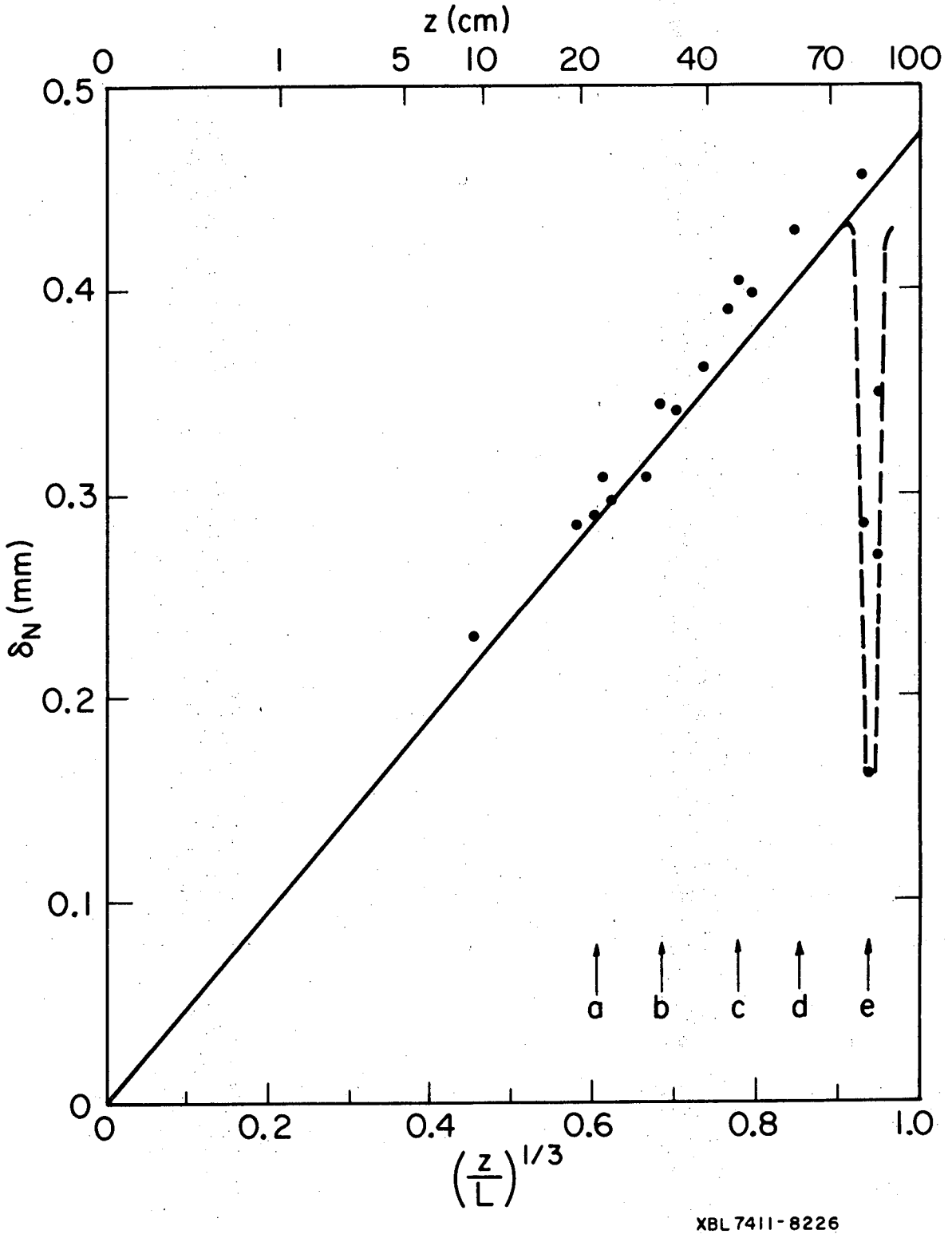

Fig. 29

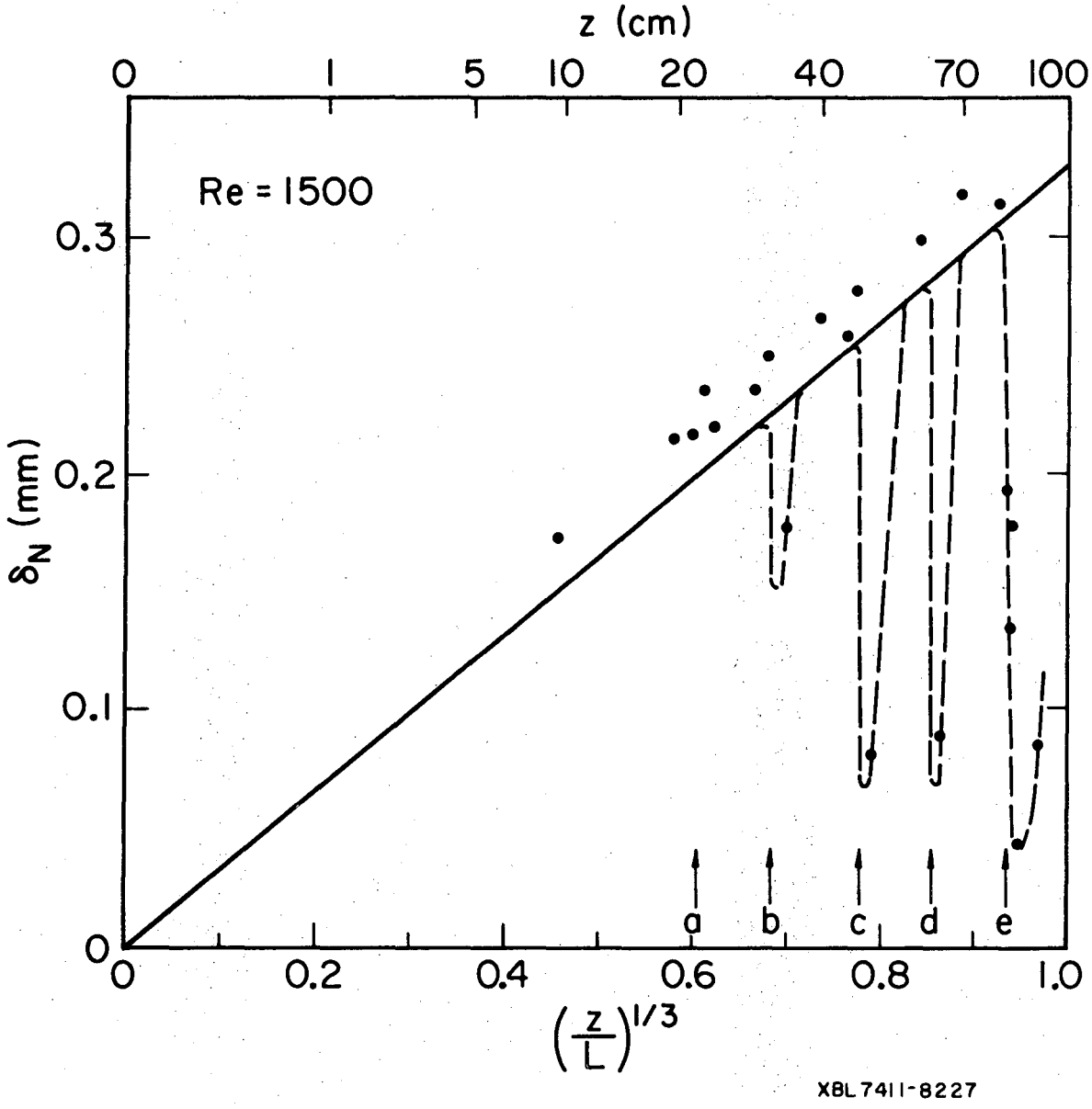
z (cm)
0
1
5
10
20
40
70
100
Re = 1500
0.3
0.2
0.1
0
δ_N (mm)
a
b
c
d
e
0
0.2
0.4
0.6
0.8
1.0
$\left(\frac{z}{L}\right)^{1/3}$
XBL7411-8227

Fig. 30

CONCLUSIONS

When this experimental program was first conceived, the travelling double-beam interferometer was expected to measure directly the concentration profiles in electrochemical mass transfer boundary layers of technical importance, i.e., current densities larger than 10^{-3} A/cm^2 and electrodes wider than a few millimeters. Following the initial observations of K. Beach,* this work has conclusively demonstrated that quantitative interpretation of the experimental interferometric fringe patterns requires careful consideration of unavoidable optical observations. Chapter 2 outlines the corrections needed to account for light-deflection within the boundary layer, and Chapter 3 describes the distortions caused by reflection from an even slightly rounded electrode edge.

The study of transient diffusion layers outlined in Chapter 4 served as both a calibration of the interferometer and a check on some of the light-deflection computations presented in Chapter 2.

The interferometric observations of laminar forced convection boundary layers presented in part 5.1 concur with a specific implication of the light-deflection analysis given in part 2.3: the loss of (optical) information caused by light curvature within the concentration boundary layer renders determination of the exact shape of the concentration profile practically impossible by interferometry alone. However, mass balance information provided in the form of current density measurement has demonstrated that a Pohlhausen-type boundary layer profile closely describes the concentration profile.

---

*K. W. Beach, Optical Methods for the Study of Convective Mass Transfer Boundary Layers on Extended Electrodes (Ph. D. Thesis), UCRL-20324, July 1971.

Part 5.2 presents studies of electrochemical mass transfer by combined free and forced convection. Onset of natural convection effects is correlated with a constant value of Rayleigh Number for a variety of current densities and electrolyte flow velocities.

The comparative study of turbulent boundary layers outlined in part 5.3 indicates the practical utility of small obstacles to promote turbulence in an otherwise laminar stream. This analysis demonstrates the ability of interferometry to provide both qualitative and quantitative information about complex phenomena in electrochemical systems.

ACKNOWLEDGEMENTS

I express my gratitude to Dr. Rolf Muller and Professor Charles Tobias for their energies and patience in guiding me throughout this work, and I thank Professor John Newman and Professor Kurt Spiegler for reviewing this manuscript.

I give my special thanks to Mr. Walter Giba for his invaluable help in preparing the electrodes and flow obstacles used in the experimental work. Credits for preparation of this manuscript go to Mrs. Shirley Ashley, Ms. Linda Betters, Ms. Alice Ramirez and Ms. Jean Wolslegel.

During the course of this work I have had the help and support of many other people, whom I thank without mentioning their names.

Financial support was provided by the Atomic Energy Commission, through the Inorganic Materials Research Division of the Lawrence Berkeley Laboratory, and the National Aeronautics and Space Administration, through a predoctoral traineeship.

APPENDIX I. COMPUTATIONAL METHOD FOR INTERPRETATION OF INTERFEROGRAMS OF ONE-DIMENSIONAL REFRACTIVE-INDEX FIELDS

Program POBOL utilizes closed-form solutions to the light-deflection equation (part 2.3 of Chapter 2) to compute the polynomial boundary layer refractive-index profile associated with a given (experimental) interferogram. A listing of both the program and its output for the analysis of a single interferogram* is presented, followed by a key that discusses the meaning of every term used in POBOL.

The closed-form solutions were derived for values of the curve shape parameter "k" $0 \leqslant k \leqslant 1$ (see Eq. (9) in part 2.3). For $k < 0$, the solutions take a slightly different form, which becomes apparent by comparison of the two sections: "K·LT·0" and "K·GT·0".

The input to program POBOL is indicated by the two "READ" commands at statement #1 and the line just above statement #5. Format #100 is used to input the following four numbers: experiment number (NE), number of data points (NP), location downstream from the electrode leading edge (Z), and time after current switch-on (T). Format #110 is used to input the locations of the data points from the experimental interferogram (YT).

The output of program POBOL first lists NE, Z and T, followed by a tabulation of the data points. The current density (I), concentration difference (DELC) and Nernst boundary layer thickness (DELN) derived by conventional interpretation of the interferogram are then given, followed by a listing of the intermediate parameter values computed during the iterative procedure. Each line corresponds to one iteration. The best set of parameters is given by the numbers in the last line of a block of intermediate values, followed by the corresponding correction

(YIC) in interfacial location and other derived quantities (I, DELC, etc.). Each successive block of computed intermediate parameter values is followed by the corresponding YIC value. Finally, the derived concentration profile (Y,C) and computed interferogram (YF,CF) is given in both tabular and graphical output.

Note that POBOL can be easily modified to use boundary layer refractive-index profiles other than the polynomial function Eq. (9) in part 2.3 of Chapter 2. In general, a numerical integration routine would replace the main iterative loop in POBOL (headed by the statement "DO 50 I = 1,50", 4 lines below statement #15). The elliptic functions EI and SN would be replaced by the chosen refractive-index function and its derivative. Such a modification is made in program POBOLN, which is presented in Appendix II.

---

*The experimental interferogram is from a series of experiments to measure the transient diffusion concentration profiles formed by galvanostatic electrodeposition of Cu from aqueous $CuSO_4$ electrolyte. Chapter 4 describes these experiments, one of which is E 135 ($i = 10$ mA/cm^2).

```
      PROGRAM POBOL(INPUT,OUTPUT,TAPE98,PLOT,TAPE99=PLOT)

C     THIS PROGRAM FINDS THE POLYNOMIAL BOUNDARY LAYER CONCENTRATION PROFILE
C     ASSOCIATED WITH A GIVEN INTERFEROGRAM BY SEEKING THE MINIMUM STANDARD
C     DEVIATION BETWEEN GIVEN(YP,NP) AND COMPUTED(YF,CF) INTERFEROGRAMS.
C     MODIFIED FOR ANALYSIS OF TRANSIENT, ONE-DIMENSIONAL BOUNDARY LAYERS

      COMMON/E/EM,M,MU,N,NM,A(10),B(10),C(10)
      COMMON/CCFACT/FACTOR
      COMMON/CCPOOL/XMIN,XMAX,YMIN,YMAX,CCXMIN,CCXMAX,CCYMIN,CCYMAX
      DIMENSION YE(50),CE(50),YF(50),CF(50),YP(50),CP(50),THETA(50)
      DIMENSION X(3),US(3),YT(50)
      REAL K,M

      DATA XMIN,XMAX,YMIN,YMAX/0.0,0.12,-0.02,0.08/
      DATA W,WG,EG,EW,BETA,A(1)/1.0,1.27,1.5231,1.3311,0.029,1.0/
      DATA ALFA,GAMMA,FC,DO,TMO/0.0869,0.0648,96487.0,0.00000541,0.597/
      DATA CB/0.1026/

  100 FORMAT(2I5,2F10.5)
  105 FORMAT(///*CONVENTIONAL INTERPRETATION*,/,*I =*,F5.2,5X,*DELC =*,F
     17.4,5X,*DELN =*,F7.4,//)
  110 FORMAT(F6.4)
  120 FORMAT(31X,2F10.4)
  125 FORMAT(//,*INCOMPLETE ITERATION*)
  130 FORMAT(10X,2F12.4,15X,2F12.4)
  140 FORMAT(17X,F7.4,F10.3,F10.4,2F13.6)
  150 FORMAT(///,*EXPERIMENT*,I5,9X,*Z =*,F5.1,* CM*,5X,*T =*,F4.1,* S*)
  160 FORMAT(///38X,*DATA POINTS*/38X,*YP*,8X,*CP*)
  170 FORMAT(///19X,*Y*,11X,*C*,26X,*YF*,10X,*CF*)
  180 FORMAT(//,34X,*INTERMEDIATE VALUES*,/,19X,*DELTA*,8X,*K*,8X,*CS*,1
     10X,*SD*,11X,*AD*)
  190 FORMAT(//,*YIC =*,F7.4,5X,*DYS =*,F7.4,10X,*I =*,F5.2,5X,*DELC =*,
     1F7.4,5X,*DELN =*,F7.4,5X,*DEL90 =*,F7.4,5X,*DEL99 =*,F7.4)
  200 FORMAT(*EXP*,I5,/,*Z =*,F5.1,/,*T =*,F5.1)

      CALL CCBGN
      CCXMIN=200. $ CCXMAX=1100. $ CCYMIN=250. $ CCYMAX=888.
      EB=EW+BETA*CB $ F=W/EB+WG/EG $ CDM=2.0*FC*DO/TMO $ DYM=-0.67

C  DATA INPUT

    1 READ 100,NE,NP,Z,T
      IF(NE.EQ.0) GO TO 99
      PRINT 150,NE,Z,T $ PRINT 160
      DO 5 I=1,NP
      READ 110,YT(I) $ CP(I)=CB-0.002182*(NP-I)
    5 PRINT 120,YT(I),CP(I)

C     CONVENTIONAL INTERPRETATION

      N=3 $ IF(NP.GT.12) N=4 $ IF(NP.GT.20) N=5
      IF(NP.GT.25) N=6 $ IF(NP.GT.30) N=7
      IA=1 $ IF(NP.LT.8) IA=0
      SX=0.0 $ SY=0.0 $ SXY=0.0 $ SXX=0.0
      DO 6 I=1,N
      J=I+IA
      SX=SX+YT(J) $ SY=SY+CP(J)
      SXY=SXY+YT(J)*CP(J)
    6 SXX=SXX+YT(J)*YT(J)
      DCDY=(N*SXY-SX*SY)/(N*SXX-SX*SX)
```

```
      CD=COM*(CB-ALFA*CP(2))*DCDY/(CB+GAMMA*CP(2))
      DELC=CB-CP(2) $ DELN=DELC/DCDY
      PRINT 105,CD,DELC,DELN

C     PARAMETER SPECIFICATION

      CS=CP(1) $ DYS=1.0 $ YIC=0.0 $ K=0.0
      CSP=CS $ CST=CS $ CSM=3.0
    7 ADP=0.0 $ DYSP=DYS
      DO 8 I=1,NP
    8 YP(I)=YT(I)+YIC
      DELTA=YP(NP)
      SDD=1.0 $ DD=-0.1*DELTA $ DKD=0.2
      NI=0 $ DK=0.1 $ PRINT 180
   10 SDK=1.0
      YM=0.025*DELTA $ IF(YM.LT.0.001) YM=0.001
   15 NI=NI+1 $ IF(NI.GT.100) GO TO 90
      IF(K.GT.1.0) K=1.0 $ IF(K.LT.-0.268) K=-0.268
      IA=0 $ IF(CS.GE.CB) CS=0.9*CB
      ES=EW+BETA*CS $ DELC=CB-CS $ DELE=EB-ES
      DO 50 I=1,50
      YE(I)=YM*(IA+I-1) $ YER=YE(I)/DELTA
      IF(YER.GE.0.999) GO TO 52
      UE=(1.0-K*YER)*(1.0-YER)
      THETA(I)=1.0-UE*UE
      EE=ES+DELE*THETA(I)
      H=2.0*(EB/EE-1.0)
      IF(K.LE.0.001) GO TO 30

C     POLYNOMIAL BOUNDARY LAYER, K.GT.0

      M=0.5*(1.0+0.25*(1.0-K)**2/(K*UE))
      XM=DELTA*SQRT(0.5*UE/(K*H))
      XL=XM*EI(1.0/SQRT(2.0*M))
      IF(XL.GT.W) XL=W $ XR=XL/XM
      IF(XL.LT.W) GO TO 20
      U=1.0-2.0*M*(SN(XR))**2
      E=ES+DELE*(1.0-(UE*U)**2)
      Y=DELTA*(0.5*(1.0+K)/K-SQRT(UE*(2.0*M-1.0+U)/K))
      S=SQRT(2.0*(E/EE-1.0))
      GO TO 25
   20 S=SQRT(H) $ Y=DELTA+S*(W-XL) $ E=EB
   25 X(1)=0.1127016654*XR $ X(2)=0.5*XR $ X(3)=0.8872983346*XR
      DO 28 J=1,3
      U=1.0-2.0*M*(SN(X(J)))**2
   28 US(J)=U*U
      GO TO 38
   30 CONTINUE
      IF(K.GT.-0.001) GO TO 40

C     POLYNOMIAL BOUNDARY LAYER, K.LT.0

      M=2.0/(1.0-0.25*((1.0-K)**2)/(K*UE))
      XM=DELTA*SQRT(0.5*M*UE/(-K*H))
      XL=XM*EI(1.0/SQRT(2.0-M))
      IF(XL.GE.W) XL=W $ XR=XL/XM
      IF(XL.LT.W) GO TO 32
      U=(SN(XR))**2 $ U=((2.0-M)*U-1.0)/(M*U-1.0)
      E=ES+DELE*(1.0-(UE*U)**2)
      Y=DELTA*(0.5*(1.0+K)/K+SQRT(-UE*((2.0-M)/M-U)/K))
      S=SQRT(2.0*(E/EE-1.0))
      GO TO 34
```

```
   32 S=SQRT(H) $ Y=DELTA+S*(W-XL) $ E=EB
   34 X(1)=0.1127016654*XR $ X(2)=0.5*XR $ X(3)=0.8872983346*XR
      DO 36 J=1,3
      U=(SN(X(J)))**2 $ U=((2.0-M)*U-1.0)/(M*U-1.0)
   36 US(J)=U*U
   38 P=XL*(5.0*US(1)+8.0*US(2)+5.0*US(3))/18.0
      P=EE*(XL+H*(XL-P))+EB*(W-XL)*SQRT(1.0+H)
      GO TO 45

C  PARABOLIC BOUNDARY LAYER

   40 XM=DELTA*SQRT(0.5*EE/DELE)
      XL=1.57079632*XM
      IF(XL.GE.W) XL=W $ XR=XL/XM
      IF(XL.LT.W) GO TO 42
      YR=1.0-(1.0-YER)*COS(XR)
      E=ES+DELE*YR*(2.0-YR)
      Y=YR*DELTA
      S=SQRT(2.0*(E/EE-1.0))
      GO TO 43
   42 S=SQRT(H) $ Y=DELTA+S*(W-XL) $ E=EB
   43 P=EB*XL-(EB-EE)*(XM*SIN(XR)*COS(XR))+EB*(W-XL)*SQRT(1.0+H)
   45 SG=TAN(ASIN(E*SIN(ATAN(S))/EG))
      SA=TAN(ASIN(EG*SIN(ATAN(SG))))
      YF(I)=Y+WG*SG-F*SA
      P=W*EB-P+WG*EG*(1.0-SQRT(1.0+SG*SG))-F*(1.0-SQRT(1.0+SA*SA))
      CE(I)=CS+DELC*THETA(I) $ CF(I)=CB-P/(W*BETA)
      IF(THETA(I).GE.0.85) IA=IA+1 $ IF(THETA(I).GE.0.90) IA=IA+1
      IF(THETA(I).GE.0.95) IA=IA+1 $ IF(THETA(I).GE.0.98) IA=IA+1
   50 CONTINUE
   52 NR=I+1 $ CE(I)=CB $ CE(NR)=CB $ CF(I)=CB $ CF(NR)=CB
      YE(NR)=YE(I)+0.006 $ YF(I)=YE(I) $ YF(NR)=YE(NR)

C  STANDARD DEVIATION CALCULATION

      SD=0.0 $ AD=0.0 $ L=1
      DO 60 I=1,NP
      DO 56 J=L,NR
      IF(YP(I).LT.YF(J)) GO TO 58
   56 CONTINUE
   58 L=J
      IF(J.EQ.1) L=2 $ LM=L-1
      DC=CF(L)-(YF(L)-YP(I))*(CF(L)-CF(LM))/(YF(L)-YF(LM))-CP(I)
      AD=AD+DC
   60 SD=SD+DC*DC
      AD=AD/NP $ SD=SQRT(SD/NP)
      PRINT 140,DELTA,K,CS,SD,AD

C  CS VARIATION

      IF(ABS(AD).LE.0.0C001.OR.ABS((AD-ADP)/AD).LE.0.01) GO TO 65
      IF(ABS(ADP).GE.1.0E-10) CSM=(CS-CST)/(AD-ADP)
      CST=CS $ ADP=AD $ CS=CS-CSM*AD $ GO TO 15
   65 DELCS=CS-CSP $ CSP=CS $ ADP=0.0

C  K VARIATION

      IF(SDK.LE.0.0) GO TO 80 $ IF(SD.GE.SDK) GO TO 75
      IF(K.GE.1.0) GO TO 80 $ IF(K.LE.-0.268) GO TO 80
      SDKK=SDK $ SDK=SD $ K=K+DK
      IF(K.LE.1.0) GO TO 68
      G=(1.0-(K-DK))/DK $ K=1.0 $ GO TO 70
```

```
   68 G=1.0
      IF(K.GE.-0.268) GO TO 70
      G=-(0.268+(K-DK))/DK $ K=-0.268
   70 CONTINUE
      IF(SDKK.LT.1.0) GO TO 72 $ GO TO 15
   72 CS=CS+DELCS $ GO TO 15
   75 CONTINUE
      IF(SDKK.LT.1.0) GO TO 77
      K=K-2.0*DK $ DK=-DK $ SDKK=SD $ CSP=CS-DELCS $ CS=CSP-DELCS
      GO TO 15
   77 DSD=0.5*((G*G*SDKK-(1.0+G)**2*SDK+(1.0+2.0*G)*SD)/(G*SDKK-(1.0+G)*
     1SDK+SD))
      SDK=-1.0 $ K=K-DK*DSD $ CS=CS-DELCS*DSD $ GO TO 15

C  DELTA VARIATION

   80 CONTINUE
      IF(SDD.LE.0.0) GO TO 90
      RSDD=ABS((SD-SDD)/SD) $ IF(RSDD.LT.0.01) GO TO 89
      IF(SD.GE.SDD) GO TO 85
      SDDD=SDD $ SDD=SD $ DELTA=DELTA+DD
      K=K-DKD
      GO TO 10
   85 CONTINUE
      IF(SDDD.LT.1.0) GO TO 88
      DELTA=DELTA-2.0*DD $ DD=-DD $ SDDD=SD
      K=K+2.0*DKD $ DKD=-DKD
      GO TO 10
   88 DSD=0.5+(SD-SDD)/(SDDD-2.0*SDD+SD)
      SDD=-1.0 $ DELTA=DELTA-DD*DSD
      K=K+DSD*DKD
      GO TO 10
   89 SDD=-1.0 $ DELTA=DELTA-0.5*DD $ GO TO 10
   90 DYS=YP(1)-YF(1) $ IF(NI.GT.100) PRINT 125
      DELN=0.5*DELTA/(1.0+K)
      DEL90=0.5*DELTA*(1.0+K-SQRT(1.0-0.7350888*K+K*K))/K
      DEL99=0.5*DELTA*(1.0+K-SQRT(1.0-1.6*K+K*K))/K
      CD=COM*DELC*(CB-ALFA*CS)/(DELN*(CR+GAMMA*CS))
      PRINT 190,YIC,DYS,CD,DELC,DELN,DEL90,DEL99

C   INTERFACIAL LOCATION VARIATION

      DI=DYS+0.0015 $ IF(ABS(DI).LE.0.0005) GO TO 97
      IF(DYSP.LT.1.0) DYM=(YICP-YIC)/(DYS-DYSP)
      YICP=YIC $ YIC=YIC+DYM*DI $ GO TO 7
   97 PRINT 170
      DO 98 I=1,NR
   98 PRINT 130,YE(I),CE(I),YF(I),CF(I)

C   GRAPHICAL OUTPUT

      CALL CCGRID(1,12,1,6HNOLBLS,1,10,1)
      CALL FIXLBL(6,5,2,-2,-2)
      CALL CCLTR(580.,170.,0,2,11HC (M CUSO4),11)
      CALL CCLTR(100.,530.,1,2,6HY (CM),6)
      WRITE(98,200) NE,Z,T
      CALL CCLTR(250.,800.,0,2)
      CALL CCPLOT(CP,YP,NP,6HNOJOIN,6,1)
      CALL CCPLOT(CF,YF,NR)
      CALL CCPLOT(CE,YE,NR,4HJOIN,1,1)
      CALL CCNEXT
      GO TO 1
```

```
99 CONTINUE
   CALL CCEND
   STOP
   END
```

```
      FUNCTION EI(X)
C  CALCULATES THE ELLIPTIC INTEGRAL OF THE FIRST KIND, ARGUMENT X, PARAMETER M
      COMMON/E/EM,M,MU,N,NM,A(10),B(10),C(10)
      REAL M,MU
  100 FORMAT(*ARGUMENT GREATER THAN UNITY       X =*,F6.4,*       M =*,F
     16.4,*          Y =*,F6.4)
  110 FORMAT(* A.G.M.  ITERATION NOT CONVERGING.........C =*,F9.7)
  120 FORMAT(10X,*ELLIPTIC INTEGRAL INFINITE*)
      IF(M.LE.1.0) GO TO 10
      MU=1.0/M $ C(1)=SQRT(MU) $ EM=C(1) $ GO TO 20
   10 MU=M $ C(1)=SQRT(MU) $ EM=1.0
   20 Y=X/EM
      B(1)=SQRT(1.0-MU)
      IF(Y.LE.1.0) GO TO 30
      PRINT 100,X,M,Y
      Y=1.0
   30 PHI=ASIN(Y)
      IF(MU.GT.0.999) GO TO 70
      DO 40 I=2,10
      J=I-1
      A(I)=0.5*(A(J)+B(J))
      B(I)=SQRT(A(J)*B(J))
      C(I)=0.5*(A(J)-B(J))
      IF(C(I).LT.0.000001) GO TO 50
   40 CONTINUE
      PRINT 110,C(10)
   50 N=I $ NM=J
      IF(PHI.GE.1.57079632) GO TO 65
      DO 60 J=1,NM
      P=PHI
      IF(PHI.GT.1.57079633) P=PHI-3.14159265
      TP=TAN(P)
   60 PHI=PHI+PHI-ATAN((A(J)-B(J))*TP/(A(J)+B(J)*TP*TP))
      EI=EM*PHI/(A(N)*2.0**NM) $ GO TO 90
   65 EI=1.57079633*EM/A(N) $ GO TO 90
   70 ALFA=ASIN(C(1)) $ EI=EM
      IF(MU.LT.0.99999999) GO TO 75 $ IF(PHI.LT.1.57079632) GO TO 75
      EI=1.0E10 $ PRINT 120 $ GO TO 90
   75 SA=SIN(ALFA)
      ALFA=ACOS((1.0-SA)/(1.0+SA))
      PHI=0.5*(PHI+ASIN(SA*SIN(PHI)))
      EI=EI*2.0/(1.0+SA)
      IF(SA.GE.0.99999999) GO TO 80
      GO TO 75
   80 EI=EI*ALOG(TAN(0.78539816+0.5*PHI))
   90 CONTINUE
      RETURN
      END
```

```
      FUNCTION SN(X)

C  CALCULATES THE JACOBIAN ELLIPTIC FUNCTION SN, ARGUMENT X, PARAMETER M

      COMMON/E/EM,M,MU,N,NM,A(10),B(10),C(10)
      REAL M,MU
      DIMENSION PHI(10)
      Y=X/EM
      IF(MU.GT.0.999) GO TO 20
      PHI(N)=Y*A(N)*2.0**NM
      DO 10 I=1,NM
      J=N-I $ JP=J+1
   10 PHI(J)=0.5*(PHI(JP)+ASIN(C(JP)*SIN(PHI(JP))/A(JP)))
      SN=EM*SIN(PHI(1)) $ GO TO 30
   20 TY=TANH(Y)
      SN=EM*(TY+0.25*(1.0-MU)*(TY-4.0*Y/(EXP(Y)+EXP(-Y))**2))
   30 CONTINUE
      RETURN
      END
```

Sample Output

EXPERIMENT 135 Z = 50.0 CM T =30.0 S

DATA POINTS

YP	CP
-.0185	.0306
-.0178	.0328
-.0171	.0350
-.0166	.0371
-.0160	.0393
-.0153	.0415
-.0145	.0437
-.0135	.0459
-.0125	.0480
-.0114	.0502
-.0104	.0524
-.0095	.0546
-.0085	.0568
-.0074	.0590
-.0064	.0611
-.0053	.0633
-.0043	.0655
-.0030	.0677
-.0017	.0699
-.0002	.0721
.0010	.0742
.0024	.0764
.0039	.0786
.0057	.0808
.0074	.0830
.0089	.0851
.0109	.0873
.0130	.0895
.0157	.0917
.0183	.0939
.0221	.0961
.0258	.0982
.0322	.1004
.0524	.1026

CONVENTIONAL INTERPRETATION
I = 5.19 DELC = .0698 DELN = .0224

INTERMEDIATE VALUES

DELTA	K	CS	SD	AD
.0524	0.000	.0306	.009546	-.009144
.0524	0.000	.0580	.006836	.002904
.0524	0.000	.0514	.004845	-.000373
.0524	0.000	.0522	.004972	-.000014
.0524	0.000	.0522	.004978	.000000
.0524	.100	.0522	.004966	.001093
.0524	.100	.0499	.004428	.000072

.0524	.100	.0497	.004399	.000001
.0524	.200	.0473	.003901	.000128
.0524	.200	.0470	.003852	.000013
.0524	.200	.0470	.003847	.000000
.0524	.300	.0442	.003363	.000128
.0524	.300	.0439	.003312	.000011
.0524	.300	.0439	.003308	.000000
.0524	.400	.0407	.002830	.000121
.0524	.400	.0404	.002782	.000011
.0524	.400	.0404	.002777	.000000
.0524	.500	.0369	.002298	.000123
.0524	.500	.0365	.002248	.000011
.0524	.500	.0365	.002243	.000000
.0524	.600	.0326	.001762	.000110
.0524	.600	.0322	.001717	.000010
.0524	.700	.0280	.001237	.000125
.0524	.700	.0276	.001188	.000021
.0524	.700	.0275	.001179	.000000
.0524	.800	.0228	.000716	.000092
.0524	.800	.0224	.000683	.000008
.0524	.900	.0173	.000491	.000101
.0524	.900	.0169	.000493	.000016
.0524	.900	.0168	.000496	.000000
.0524	1.000	.0112	.000891	.000054
.0524	1.000	.0110	.000913	.000004
.0524	.881	.0179	.000474	.000002
.0472	.681	.0179	.000498	.000072
.0472	.681	.0176	.000502	-.000000
.0472	.781	.0176	.001310	.001197
.0472	.781	.0120	.000847	.000063
.0472	.781	.0116	.000873	.000001
.0472	.581	.0236	.000745	.000079
.0472	.581	.0232	.000714	-.000012
.0472	.581	.0232	.000717	-.000000
.0472	.668	.0183	.000495	-.000005
.0576	1.000	.0183	.000930	-.000758
.0576	1.000	.0216	.000629	-.000021
.0576	1.000	.0217	.000634	.000000
.0504	.723	.0217	.000651	-.000163
.0504	.723	.0224	.000675	.000003
.0504	.623	.0224	.001506	-.001281
.0504	.623	.0281	.001225	.000121
.0504	.623	.0276	.001168	-.000003
.0504	.823	.0172	.000497	.000092
.0504	.823	.0169	.000502	.000013
.0504	.823	.0168	.000504	.000000
.0504	.923	.0112	.000899	.000058
.0504	.923	.0109	.000923	.000004
.0504	.802	.0180	.000482	.000007

YIC = 0.0000 DYS = -.0010 I =10.30 DELC = .0846 DELN = .0140

INTERMEDIATE VALUES

DELTA	K	CS	SD	AD
.0521	.802	.0180	.001545	-.001389
.0521	.802	.0246	.000724	.000126
.0521	.802	.0241	.000672	-.000003
.0521	.902	.0241	.001357	.001168
.0521	.902	.0190	.000505	.000050
.0521	.902	.0188	.000510	.000001

.0521	1.000	.0135	.000899	.000036
.0521	1.000	.0133	.000914	.000003
.0521	.880	.0199	.000487	-.000028
.0521	.880	.0200	.000485	-.000000
.0468	.680	.0200	.000507	.000064
.0468	.680	.0197	.000511	.000001
.0468	.780	.0197	.001294	.001175
.0468	.780	.0144	.000838	.000076
.0468	.780	.0140	.000868	.000001
.0468	.580	.0254	.000750	.000080
.0468	.580	.0250	.000719	-.000012
.0468	.580	.0251	.000722	-.000000
.0468	.667	.0204	.000505	-.000004
.0573	1.000	.0204	.000910	-.000729
.0573	1.000	.0235	.000633	-.000020
.0573	1.000	.0235	.000638	.000000
.0501	.723	.0235	.000653	-.000162
.0501	.723	.0242	.000677	.000002
.0501	.623	.0242	.001485	-.001254
.0501	.623	.0297	.001217	.000116
.0501	.623	.0292	.001163	-.000002
.0501	.823	.0193	.000505	.000085
.0501	.823	.0189	.000510	.000012
.0501	.823	.0189	.000512	.000000
.0501	.923	.0135	.000899	.000059
.0501	.923	.0133	.000923	.000004
.0501	.802	.0201	.000491	.000007

YIC = -.0003 DYS = -.0015 I =10.08 DELC = .0825 DELN = .
.013

Y	C	YF	CF
0.0000	.0201	-.0174	.0359
.0013	.0273	-.0157	.0405
.0025	.0340	-.0140	.0448
.0038	.0402	-.0122	.0490
.0050	.0461	-.0105	.0530
.0063	.0515	-.0088	.0568
.0075	.0565	-.0070	.0605
.0088	.0611	-.0053	.0640
.0100	.0654	-.0035	.0673
.0113	.0693	-.0017	.0704
.0125	.0729	.0001	.0734
.0138	.0762	.0019	.0762
.0150	.0793	.0037	.0789
.0163	.0820	.0056	.0814
.0175	.0846	.0074	.0837
.0188	.0868	.0092	.0859
.0200	.0889	.0111	.0879
.0213	.0907	.0129	.0897
.0238	.0939	.0166	.0930
.0263	.0964	.0203	.0956
.0300	.0990	.0256	.0986
.0350	.1012	.0325	.1010
.0413	.1023	.0404	.1023
.0475	.1026	.0474	.1026
.0538	.1026	.0538	.1026
.0598	.1026	.0598	.1026

Sample Graphical Output

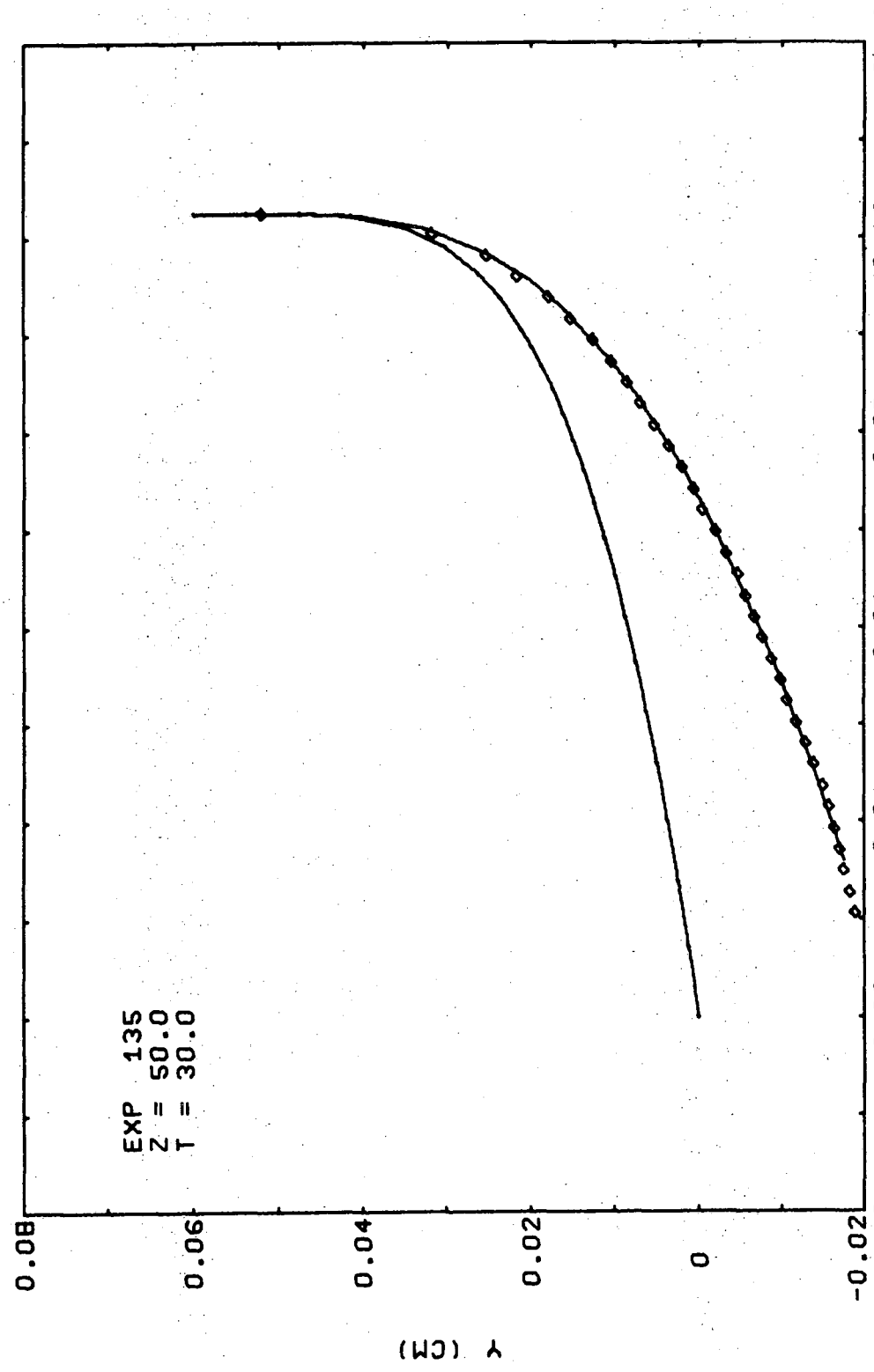

XBL 7410-7958

Key to Program POBOL

Symbol	Use	Units
A	Computation of elliptic functions.	
AD	Average deviation between computed and experimental interferograms.	mole/liter
ADP	Average deviation for the previous iteration.	mole/liter
ALFA	Correlation coefficient for variation of diffusion coefficient with electrolyte concentration. α in Chapter 4.	
B	Computation of elliptic functions.	
BETA	Correlation coefficient relating refractive-index variations to concentration variations.	liter/mole
C	Computation of elliptic functions.	
	-or-	
	Concentration (output)	mole/liter
CB	Bulk electrolyte concentration.	mole/liter
CCXMAX CCXMIN CCYMAX CCYMIN	Graphical output parameters.	
CD	Current density.	mA/cm^2
CDM	Multiplication factor for computation of current density.	$A\text{-}cm^2/mole$
CE	Local electrolyte concentration.	mole/liter
CF	Concentration depicted by a computed interference fringe (linearly related to phase according to conventional interferogram interpretation).	mole/liter
CP	Concentration depicted by an experimental interferogram (related to phase as above).	mole/liter
CS	interfacial concentration.	mole/liter

Symbol	Use	Units
CSM	Relates changes in interfacial concentration CS to changes in average deviation AD. Used as a multiplication factor to find the CS value corresponding to AD $\leq 10^{-5}$ M.	
CSP	Interfacial concentration for the last iteration in which the parameter K was changed.	mole/liter
CST	Interfacial concentration for the previous iteration in which only CS was changed.	mole/liter
DC	Concentration difference between a point on a computed interference fringe and that on the experimental fringe. Linear interpolation is employed to find the concentration depicted on the computed fringe that corresponds to the same point (YP value of the data point) on the experimental fringe. Used to calculate SD and AD.	mole/liter
DCDY	Apparent interfacial concentration gradient depicted by the experimental interference fringe. Calculated by a least squares fit through the data points nearest to the apparent interface.	mole-liter^{-1}-cm^{-1}
DD	Incremental change in boundary layer thickness.	cm
DELC	Total concentration difference CB - CS.	mole/liter
	-or-	
	Apparent concentration difference determined from the experimental interferogram CB - CP(2). The lowest data point CP(1) is not used here in order to account for spurious "extra" fringe shifts due to reflection effects (Chapter 3). (See below statement #6.)	mole/liter
DELCS	Difference in interfacial concentration CS between interations in which the parameter K was changed.	mole/liter
DELE	Refractive-index difference EB - ES.	
DELN	Nernst (effective) boundary layer thickness.	cm

Symbol	Use	Units
DELTA	Boundary layer thickness. Equation (9) in part 2.3.	cm
DEL90	90% boundary layer edge.	cm
DEL99	99% boundary layer edge.	cm
DI	DYS + 0.0015 cm. If DI = 0, there will be an 0.0015 cm discrepancy between the computed and experimental interfacial locations, YF(1) and YP(1). This approximates the estimated effect of reflection from the slightly rounded electrode edge (see Chapter 3).	cm
DK	Incremental change in parameter K.	
DKD	Incremental change in parameter K when the boundary layer thickness DELTA is changed.	
DSD	Fractional change of a parameter (either DELTA or K) that gives a minimum in standard deviation SD. Effectively fits a parabola to three successive (K,SD) or (DELTA,SD) pairs to find the minimum SD. See discussion of parameter G.	
DYM	Multiplication factor to relate changes in YIC to changes in DYS.	
DYS	Difference between experimental interfacial location YP(1) and computed interfacial location YF(1). Related to errors in the original determination of the true interfacial location y = 0 on the experimental interferogram. Also related to uncertainty in the determination of the apparent interfacial location YT(1) on the interferogram due to reflection effects. A strong function of YIC.	cm
DYSP	Previous DYS value (associated with a previous value of YIC).	cm
DO	Correlation coefficient for variation of diffusion coefficient. Corresponds to the value of the diffusion coefficient at zero electrolyte concentration.	cm^2/s

Symbol	Use	Units
E	Electrolyte refractive-index at the plane where a deflected ray leaves the electrolyte to enter the glass sidewall nearer to the camera.	
EB	Refractive-index of the bulk electrolyte.	
EE	Refractive-index of the electrolyte at the plane where a light ray enters the electrolyte from the glass sidewall farther from the camera.	
EG	Refractive-index of the glass sidewalls.	
ES	Interfacial electrolyte refractive-index.	
EW	Correlation coefficient relating refractive-index variations to concentration variations. Corresponds to the refractive-index of water (electrolyte concentration = 0).	
F	Location of virtual plane of focus relative to the outside plane of the glass sidewall nearest to the camera. See part 2.1 of Chapter 2.	cm
FC	Faraday constant.	coul/eq
G	A number that is equal to unity unless an attempt is made to increase or decrease the parameter K beyond its limits (see part 2.3 of Chapter 2). If the local minimum in standard deviation corresponds to a value of K within its acceptable limits, the number G is adjusted so that when the number DSD is calculated, it can account for possible unequal increments in the K values. This is reflected in the different calculational forms for DSD. DSD is computed at statement #77 in a form that can account for unequal increments of K. Statement #88 computes DSD in a form suited for equal increments of the parameter DELTA. If the local minimum standard deviation corresponds to a value of K outside its acceptable limits, K is set equal to the limit and the search ended. The computation sequence then proceeds to the "DELTA variation" section.	

Symbol	Use	Units
GAMMA	Correlation coefficient for variation of anion transport number ($1 - t_+$) with electrolyte concentration. γ in Chapter 4.	
H	Parameter; "h" in part 2.3 of Chapter 2.	
I	Variable integer. -or- Current density (output)	 mA/cm^2
IA	Provides larger spacing between locations (YE values) of light rays when the concentration changes more slowly with YE. See statements directly above statement #50 and 5 lines below statement #15. -or- Permits the lowest data point (CP(1)) to be discarded when the slope DCDY of the experimental interference fringe is computed, unless there are only a small number (8) of data points. This point is likely to be in error because of reflection effects. (See below statement #6.)	
J	Variable integer.	
K	Parameter in the polynomial function relating dimensionless concentration to dimensionless distance. See part 2.3 of Chapter 2.	
L	Variable integer used in AD, SD calculation.	
LM	L - 1	
M	Parameter for elliptic functions. See part 2.3 of Chapter 2.	
N	Number of data points (CP,YT) used in calculation of DCDY.	
NE	Experiment number.	
NI	Iteration number.	
NP	Number of data points.	
NR	Number of light rays used in construction of the computed interferogram CF,YF.	

Symbol	Use	Units
P	Optical path difference between a deflected ray and a hypothetical undeflected ray. Also used as an intermediate value (the optical path length of a deflected ray in the electrolyte) in the computation of the optical path difference.	mole/liter
RSDD	Relative difference between the minimum standard deviations computed for successive DELTA values. If this number is less than 0.01, the search for a smaller standard deviation is halted after computation of the best K and CS values for a new DELTA midway between the two successive values.	
S	Slope of the deflected light ray as it leaves the electrolyte to enter the glass sidewall nearer to the camera.	
SA	Slope of the deflected light ray as it leaves the glass sidewall and enters air.	
SD	Standard deviation between computed and experimental interference fringes.	mole/liter
SDD	Minimum standard deviation calculated for the previous DELTA value.	mole/liter
SDDD	Minimum standard deviation calculated for the DELTA value previous to the above value.	mole/liter
SDK	Minimum standard deviation calculated for the previous K value.	mole/liter
SDKK	Minimum standard deviation calculated for the K value previous to the above value.	mole/liter
SG	Slope of the deflected light ray as it traverses the glass sidewall nearer to the camera.	
SX	Used in the least squares computation for DCDY.	cm
SXX	Used in the least squares computation for DCDY.	cm^2

Symbol	Use	Units
SXY	Used in the least squares computation for DCDY.	cm-mole/liter
SY	Used in the least squares computation for DCDY.	mole/liter
T	Time after current switch-on	s
THETA	Dimensionless concentrations (CE-CS)/(CB-CS).	
TMO	Correlation coefficient for variation of anion transport number ($1-t_+$) with concentration. Corresponds to $1-t_+$ at zero concentration.	
U	Transformation variable. Corresponds to "U" part 2.3 of Chapter 2.	
UE	Corresponds to u_e in part 2.3 of Chapter 2.	
US	U^2	
W	Electrode width.	cm
WG	Glass sidewall width.	cm
X	Reduced horizontal distance, O<X<XR. Statement #25 indicates the three X values used in 3-point Gauss-Legendre quadrature for phase integration for the case K>0. Also used in statement #34 for phase integration when K<0.	
XL	Horizontal location where a deflected light ray leaves the boundary layer. If XL>W, the ray leaves the electrolyte to enter the glass wall from a vertical location Y<DELTA, i.e., from within the boundary layer. This condition corresponds to the Type I ray discussed in part 2.3 of Chapter 2. (XL corresponds to x_b in that section.) If XL<W, the ray leaves the boundary layer before entering the glass wall. This corresponds to the Type II ray discussed in part 2.3 of Chapter 2.	

Symbol	Use	Units
XM	Scale factor. Corresponds to x_m in part 2.3 of Chapter 2.	cm
XMAX, XMIN	Graphical output parameters.	mole/liter
XR	Scaling factor to facilitate the phase integration by Gauss-Legendre quadrature. XR = W when XL $\geq$ W (Type I) and the phase integration is performed by the quadrature method for 0<X<W. XR = XL when XL<W (Type II) and the phase integration is performed only for 0<X<XL. The remaining phase integration XL$\leq$X<W can be calculated directly because the ray travels along a straight line through electrolyte of uniform refractive-index EB.	cm
Y	Vertical distance, corresponds to "y" in part 2.3 of Chapter 2.	cm
YE	Location where a light ray enters the electrolyte from the glass wall farther from the camera. y_e in part 2.3 of Chapter 2.	cm
YER	YE/DELTA. Y_e in part 2.3 of Chapter 2.	cm
YF	Vertical distance on the computed interference fringe.	cm
YIC	Correction term for the true interfacial location y = 0. Introduces small corrections to the original data points YT (measured relative to the interfacial location y = 0 originally determined from the 16 mm film). See discussion on DYS, DI, YP and YT.	cm
YICP	Previous YIC value.	cm
YM	Scale factor for YE values. Determines spacing between incident light rays.	cm
YMAX, YMIN	Graphical output parameters.	cm
YP	Vertical distance on the corrected experimental interferogram. YP = YT + YIC. The effect of YIC is to shift all of the original data points (YT) up or down.	cm

Symbol	Use	Units
YR	Y/DELTA	
YT	Vertical distance on the original experimental interferogram.	cm
Z	Experiment location downstream from electrode leading edge.	cm

Key to Functions EI and SN

Function EI(x,m) calculates the elliptic integral of the first kind, argument x, parameter m. Function SN(x,m) calculates the Jacobian Elliptic function, argument x, parameter m. These functions are tabulated in Abramowitz,* Chapters 16 and 17. The Process of the Arithmetic-Geometric Mean described by Abramowitz was used to compute the functions. The symbols A, B, C, PHI, ALFA and M used in functions EI and SN correspond to a, b, c, ϕ, α and m used by Abramowitz. MU, EM, TP, P, J, JP, Y, SA and TY are intermediate variables used to facilitate programming.

Functions EI and SN were tested and found to reproduce the tabulated values to within one or two digits in the 8^{th} decimal.

*M. Abramowitz and I. Stegun, eds., Handbook of Mathematical Functions (National Bureau of Standards, Washington, 1964), Chapters 16 and 17.

APPENDIX II. COMPUTATIONAL METHOD FOR INTERPRETATION OF INTERFEROGRAMS OF TWO-DIMENSIONAL REFRACTIVE-INDEX FIELDS

Program POBOLN uses a numerical solution to the light-deflection equation (part 2.1 of Chapter 2) to compute the refractive-index profile associated with a given (experimental) interferogram. A listing of both the program and its output (for the analysis of a single interferogram) are presented, followed by a key. Since this program is actually a modification of program POBOL (described in Appendix I), a large fraction of the terms used in POBOLN are also used to POBOL. Therefore, the key to program POBOLN lists only those terms that are used differently than in POBOL.

This program was written specifically for the analysis of the interferograms of two-dimensional concentration boundary layers formed by the constant-current electrodeposition of Cu from aqueous $CuSO_4$ electrolyte during laminar flow. A Pohlhausen-type boundary layer profile (Eq. (11) in part 5.1) is used to describe the concentration field. Also, the variations of local boundary layer thickness DEL (see Fig. 1) and local concentration difference DELC in the x-direction (direction of beam propagation) are quite specific to this problem. For instance, such variations would not apply to the study of the laminar forced convection boundary layer in a flow channel of cross-section different from the one considered here (described in part 1.1 of Chapter 1). However, the equations represented in part 2.1 of Chapter 2 as applied in this program would be applicable for any two-dimensional boundary layer $n = n(x,y)$.

The input to program POBOLN is indicated by the three "READ" commands at statement #3, just below statement #5 and two lines above statement #8. Format #100 is used to input the following five numbers: experiment number (NE), number of data points (NP), location downstream from the electrode leading edge (Z), time after current switch-on (T) and the location of the interface on the experimental inteyferogram (YC). This latter number serves to fix the origin of the data point locations (YT) read just below statement #5. Program POBOL can supply the values of the parameters YIC, DELTA, K and CS read two lines above statement #8.

The output of program POBOLN first provides a listing of the Q and QA functions--see Fig. 1. Next, NE, Z and T are printed, followed by a tabulation of the data points. The current density, concentration difference and Nernst boundary layer thickness derived by conventional interpretation of the experimental interferogram are given, followed by the intermediate parameter values computed during the iterative procedure. The best set of parameters is given by the numbers in the last line of the block of intermediate values, followed by a listing of local I and DELC values, which correspond to the XA values given at the beginning of the output. Finally, the derived quantities (I,DELC, etc) are tabulated, followed by a graphical output of the computed and experimental interferograms.

Function THETA represents a Pohlhausen-type boundary layer profile, as given in Eq. (11) of part 5.1. Function GRAD computes the dimensionless refractive-index gradient $d\theta/dY$ where θ and Y are defined in part 2.3.

```
      PROGRAM POBOLN(INPUT,OUTPUT,TAPE98,PLOT,TAPE99=PLOT)
C     THIS PROGRAM FINDS THE POLYNOMIAL BOUNDARY LAYER CONCENTRATION PROFILE
C     ASSOCIATED WITH A GIVEN INTERFEROGRAM BY SEEKING THE MINIMUM STANDARD
      DEVIATION BETWEEN GIVEN(YP,NP) AND COMPUTED(YF,CF) INTERFEROGRAMS.
C     MODIFIED FOR ANALYSIS OF TRANSIENT,TWO-DIMENSIONAL BOUNDARY LAYERS.
      COMMON/CCFACT/FACTOR
      COMMON/CCPOOL/XMIN,XMAX,YMIN,YMAX,CCXMIN,CCXMAX,CCYMIN,CCYMAX
      DIMENSION YF(62),CF(62),YP(50),CP(50),YT(50)
      DIMENSION Q(102),QA(102),DEL(102),DELA(102)
      DIMENSION DELC(102),DE(102),DEA(102),CD(102)
      REAL K

      DATA XMIN,XMAX,YMIN,YMAX/0.0,0.1,-0.04,0.1/
      DATA W,WG,EG,EW,BETA/1.0,1.27,1.5231,1.3311,0.029/
      DATA ALFA,GAMMA,FC,DO,TMO/0.0869,0.0648,96487.0,0.00000541,0.597/
      DATA A1,A2,B1,B2/0.72927,1.28278,9.0,60.0/
      DATA CB,YMO/0.100,0.005555555/

  100 FORMAT(2I5,3F10.5)
  105 FORMAT(///*CONVENTIONAL INTERPRETATION*,/,*I =*,F5.2,5X,*DELC =*,F
     17.4,5X,*DELN =*,F7.4,//)
  110 FORMAT(2F10.4,5X,2F10.4)
  120 FORMAT(31X,2F10.4)
  125 FORMAT(//,*INCOMPLETE ITERATION*)
  130 FORMAT(//,*YIC =*,F7.4,5X,*DYS =*,F7.4,10X,*I =*,F5.2,5X,*DELC =*,
     1F7.4,5X,*DELN =*,F7.4)
  140 FORMAT(//,7X,*X*,9X,*Q*,14X,*XA*,8X,*QA*)
  150 FORMAT(///,*EXPERIMENT*,I5,9X,*Z =*,F5.1,* CM*,5X,*T =*,F6.2,* M*)
  160 FORMAT(///38X,*DATA POINTS*/38X,*YP*,8X,*CP*)
  170 FORMAT(17X,F7.4,F10.3,F10.4,2F13.6)
  175 FORMAT(//,*Q AVG =*,F8.5)
  180 FORMAT(//,34X,*INTERMEDIATE VALUES*,/,19X,*DELTA*,8X,*K*,8X,*CS*,1
     10X,*SD*,11X,*AD*)
  190 FORMAT(//,38X,*I*,8X,*DELC*)
  200 FORMAT(*EXP*,I5,/,*Z =*,F5.1,/,*T =*,F5.1)

      CALL CCBGN
      CCXMIN=200. $ CCXMAX=1100. $ CCYMIN=250. $ CCYMAX=888.
      EB=EW+BETA*CB $ F=W/EB+WG/EG $ CDM=2.0*FC*DO/TMO $ DX=0.01
      AA=2.0*CB*(1.0+ALFA+2.0*ALFA/GAMMA) $ AB=CB*(ALFA-1.0)
C     CALCULATION OF BOUNDARY LAYER THICKNESS VARIATION IN THE X-DIRECTION
      QD=1.0/(1.0+2.0*(A1/B1+A2/B2)) $ SQ=0.0
      X=0.0 $ Q(1)=QD*(1.0+A1+A2) $ PRINT 140 $ PRINT 110,X,Q(1)
      DO 2 J=1,100
      JP=J+1 $ XA=X+0.5*DX $ X=X+DX
      IF(J.GT.50) GO TO 1
      Q(JP)=QD*(1.0+A1*EXP(-B1*X)+A2*EXP(-B2*X))
      QA(J)=QD*(1.0+A1*EXP(-B1*XA)+A2*EXP(-B2*XA))
      SQ=SQ+QA(J)
      GO TO 2
    1 JJ=JP-2*(JP-51)
      Q(JP)=Q(JJ) $ QA(J)=QA(JJ) $ SQ=SQ+QA(J)
    2 PRINT 110,X,Q(JP),XA,QA(J)
      SQ=0.01*SQ $ PRINT 175,SQ
C     DATA INPUT
```

```
    3 READ 100,NE,NP,Z,T,YC
      IF(NE.EQ.0) GO TO 99
      IF(NP.LT.0) GO TO 4 $ CM=0.002182 $ GO TO 5
    4 NP=-NP $ CM=0.004364
    5 PRINT 150,NE,Z,T $ PRINT 160
      READ,(YT(I),I=1,NP)
      DO 6 I=1,NP
      YT(I)=YMD*(YT(I)-YC) $ CP(I)=CB-CM*(NP-I)
    6 PRINT 120,YT(I),CP(I)

C   CONVENTIONAL INTERPRETATION

      N=3 $ IF(NP.GT.12) N=4 $ IF(NP.GT.20) N=5
      IF(NP.GT.25) N=6 $ IF(NP.GT.30) N=7
      IA=1 $ IF(NP.LT.8) IA=0
      SX=0.0 $ SY=0.0 $ SXY=0.0 $ SXX=0.0
      DO 7 I=1,N
      J=I+IA
      SX=SX+YT(J) $ SY=SY+CP(J)
      SXY=SXY+YT(J)*CP(J)
    7 SXX=SXX+YT(J)*YT(J)
      DCDY=(N*SXY-SX*SY)/(N*SXX-SX*SX)
      SCD=CDM*(CB-ALFA*CP(2))*DCDY/(CB+GAMMA*CP(2))
      DC=CB-CP(2) $ DELN=DC/DCDY $ PRINT 105,SCD,DC,DELN

C   PARAMETER INPUT

      READ,YIC,DELTA,K,CS
      DO 8 I=1,NP
    8 YP(I)=YT(I)+YIC
      CSP=CS $ CST=CS $ CSM=3.0
      DD=-0.1*DELTA $ DK=0.2 $ DKD=0.4
      NI=0 $ SDD=1.0 $ ADP=0.0 $ PRINT 180
   10 SDK=1.0
      YM=0.050*DELTA $ IF(YM.LT.0.001) YM=0.001
      DO 12 J=1,100
      DEL(J)=Q(J)*DELTA
   12 DELA(J)=QA(J)*DELTA
      DEL(101)=DEL(1)
   15 NI=NI+1 $ IF(NI.GT.100) GO TO 90
      IF(CS.GE.CB) CS=0.9*CB $ IF(CS.LT.0.0) CS=0.0 $ IA=0

C   CALCULATION OF INTERFACIAL CONCENTRATION VARIATION IN THE X-DIRECTION

      AC=GAMMA*(CB-CS)
      DO 20 J=1,100
      A=AC*Q(J)
      DELC(J)=0.5*(AB-A+SQRT(AB*AB+A*(A+AA)))/ALFA
      IF(DELC(J).GT.CB) DELC(J)=CB
      DE(J)=BETA*DELC(J)
      A=AC*QA(J)
      DELC(J)=0.5*(AB-A+SQRT(AB*AB+A*(A+AA)))/ALFA
      IF(DELC(J).GT.CB) DELC(J)=CB
      DEA(J)=BETA*DELC(J)
   20 CONTINUE
      DE(101)=DE(1)

C NUMERICAL INTEGRATION OF THE LIGHT-DEFLECTION EQUATION

      DO 50 I=1,60
      Y=YM*(I+IA-1) $ S=0.0 $ P=0.0
```

```
      DO 40 J=1,100
      JP=J+1
      DY=S*DX $ Y=Y+DY $ YA=Y-0.5*DY
      YAR=YA/DELA(J) $ YAM=YA/DEL(J) $ YAP=YA/DEL(JP)
      ETA=EB+DEA(J)*(THETA(YAR,K)-1.0)
      DEDY=DEA(J)*GRAD(YAR,K)/DELA(J)
      DEDX=(DE(JP)*(THETA(YAP,K)-1.0)-DE(J)*(THETA(YAM,K)-1.0))/DX
      P=P+DX*ETA*SQRT(1.0+S*S)
   40 S=S+DX*(1.0+S*S)*(DEDY-S*DEDX)/ETA
      YR=Y/DEL(1) $ ETA=EB+DE(1)*(THETA(YR,K)-1.0)
      SG=TAN(ASIN(ETA*SIN(ATAN(S))/EG)) $ SA=TAN(ASIN(EG*SIN(ATAN(SG))))
      P=W*EB-P+WG*EG*(1.0-SQRT(1.0+SG*SG))-F*(1.0-SQRT(1.0+SA*SA))
      YF(I)=Y+WG*SG-F*SA $ CF(I)=CB-P/(W*BETA) $ CFR=CF(I)/CB
      IF(CFR.GE.0.95) IA=IA+1 $ IF(CFR.GE.0.98) IA=IA+1
      IF(CFR.GE.0.999) GO TO 52
   50 CONTINUE
   52 NR=I+1 $ YF(NR)=YF(I)+5.0*YM $ CF(NR)=CB

C  STANDARD DEVIATION CALCULATION

      SD=0.0 $ AD=0.0 $ L=1
      DO 60 I=1,NP
      DO 56 J=L,NR
      IF(YP(I).LT.YF(J)) GO TO 58
   56 CONTINUE
   58 L=J
      IF(J.EQ.1) L=2 $ LM=L-1
      DC=CF(L)-(YF(L)-YP(I))*(CF(L)-CF(LM))/(YF(L)-YF(LM))-CP(I)
      AD=AD+DC
   60 SD=SD+DC*DC
      AD=AD/NP $ SD=SQRT(SD/NP)
      PRINT 170,DELTA,K,CS,SD,AD

C  CS VARIATION

      IF(ABS(AD).LE.0.00001.OR.ABS((AD-ADP)/AD).LE.0.01) GO TO 65
      IF(ABS(ADP).GE.1.0E-10) CSM=(CS-CST)/(AD-ADP)
      CST=CS $ ADP=AD $ CS=CS-CSM*AD $ GO TO 15
   65 DELCS=CS-CSP $ CSP=CS $ ADP=0.0

C  K VARIATION

      IF(SDK.LE.0.0) GO TO 80 $ IF(SD.GE.SDK) GO TO 75
      SDKK=SDK $ SDK=SD $ K=K+DK
      IF(SDKK.LT.1.0) GO TO 72
      CS=CS-0.002 $ GO TO 15
   72 CS=CS+DELCS $ GO TO 15
   75 CONTINUE
      IF(SDKK.LT.1.0) GO TO 77
      K=K-2.0*DK $ DK=-DK $ SDKK=SD $ CSP=CS-DELCS $ CS=CSP-DELCS
      GO TO 15
   77 DSD=0.5+(SD-SDK)/(SDKK-2.0*SDK+SD)
      SDK=-1.0 $ K=K-DK*DSD $ CS=CS-DELCS*DSD $ GO TO 15

C  DELTA VARIATION

   80 CONTINUE
      IF(SDD.LE.0.0) GO TO 90
      RSDD=ABS((SD-SDD)/SD) $ IF(RSDD.LT.0.01) GO TO 89
      IF(SD.GE.SDD) GO TO 85
      SDDD=SDD $ SDD=SD $ DELTA=DELTA+DD
      K=K-DKD
```

```
      GO TO 10
   85 CONTINUE
      IF(SDDD.LT.1.0) GO TO 88
      DELTA=DELTA-2.0*DD $ DD=-DD $ SDDD=SD
      K=K+2.0*DKD $ DKD=-DKD
      GO TO 10
   88 DSD=0.5+(SD-SDD)/(SDDD-2.0*SDD+SD)
      SDD=-1.0 $ DELTA=DELTA-DD*DSD
      K=K+DSD*DKD
      GO TO 10
   89 SDD=-1.0 $ DELTA=DELTA-0.5*DD $ GO TO 10
   90 DYS=YP(1)-YF(1) $ IF(NI.GT.100) PRINT 125
      DELN=DELTA/K
      PRINT 190
      DC=0.0 $ SCD=0.0
      DO 95 J=1,100
      CI=CB-DELC(J)
      CD(J)=CDM*DELC(J)*(CB-ALFA*CI)/(QA(J)*DELN*(CB+GAMMA*CI))
      DC=DC+DELC(J) $ SCD=SCD+CD(J)
   95 PRINT 120,CD(J),DELC(J)
      SCD=0.01*SCD $ DC=0.01*DC
      PRINT 130,YIC,DYS,SCD,DC,DELN

C     GRAPHICAL OUTPUT

      CALL CCGRID(1,10,1,6HNOLBLS,1,14,1)
      CALL FIXLBL(5,7,2,-2,-2)
      WRITE(98,200) NE,Z,T
      CALL CCLTR(250.,800.,0,2)
      CALL CCLTR(580.,170.,0,2,11HC (M CUSO4),11)
      CALL CCLTR(100.,530.,1,2,6HY (CM),6)
      CALL CCPLOT(CP,YP,NP,6HNOJOIN,6,1)
      CALL CCPLOT(CF,YF,NR,4HJOIN,0,0)
      CALL CCNEXT
      GO TO 3
   99 CONTINUE
      CALL CCEND
      STOP
      END
```

```
      FUNCTION THETA(X,A)
C     POHLHAUSEN-TYPE BOUNDARY LAYER
      Y=X $ IF(Y.GE.1.0) GO TO 1 $ B=A
      THETA=B*Y+(4.0-3.0*B)*Y**3+(2.0*B-3.0)*Y**4 $ GO TO 2
    1 THETA=1.0
    2 CONTINUE
      RETURN
      END
```

```
      FUNCTION GRAD(X,A)
C     CALCULATES D(THETA)/DY
      Y=X $ IF(Y.GE.1.0) GO TO 1 $ B=A
      GRAD=B+3.0*(4.0-3.0*B)*Y*Y+4.0*(2.0*B-3.0)*Y**3 $ GO TO 2
    1 GRAD=0.0
    2 CONTINUE
      RETURN
      END
```

Sample Output

X	Q	XA	QA
0	2.5000		
.0100	1.9675	.0050	2.1974
.0200	1.6563	.0150	1.7917
.0300	1.4681	.0250	1.5509
.0400	1.3489	.0350	1.4021
.0500	1.2690	.0450	1.3053
.0600	1.2118	.0550	1.2382
.0700	1.1683	.0650	1.1888
.0800	1.1334	.0750	1.1500
.0900	1.1041	.0850	1.1182
.1000	1.0787	.0950	1.0910
.1100	1.0564	.1050	1.0672
.1200	1.0364	.1150	1.0461
.1300	1.0183	.1250	1.0271
.1400	1.0019	.1350	1.0099
.1500	.9870	.1450	.9943
.1600	.9735	.1550	.9801
.1700	.9611	.1650	.9672
.1800	.9498	.1750	.9553
.1900	.9395	.1850	.9445
.2000	.9301	.1950	.9347
.2100	.9214	.2050	.9257
.2200	.9136	.2150	.9174
.2300	.9064	.2250	.9099
.2400	.8998	.2350	.9030
.2500	.8938	.2450	.8967
.2600	.8883	.2550	.8910
.2700	.8833	.2650	.8857
.2800	.8787	.2750	.8809
.2900	.8745	.2850	.8766
.3000	.8707	.2950	.8726
.3100	.8672	.3050	.8689
.3200	.8640	.3150	.8655
.3300	.8611	.3250	.8625
.3400	.8584	.3350	.8597
.3500	.8559	.3450	.8571
.3600	.8537	.3550	.8548
.3700	.8517	.3650	.8527
.3800	.8498	.3750	.8507
.3900	.8481	.3850	.8489
.4000	.8465	.3950	.8473
.4100	.8451	.4050	.8458
.4200	.8438	.4150	.8445
.4300	.8426	.4250	.8432
.4400	.8415	.4350	.8421
.4500	.8405	.4450	.8410
.4600	.8396	.4550	.8401
.4700	.8388	.4650	.8392
.4800	.8381	.4750	.8384
.4900	.8374	.4850	.8377
.5000	.8367	.4950	.8370
.5100	.8374	.5050	.8370
.5200	.8381	.5150	.8377
.5300	.8388	.5250	.8384
.5400	.8396	.5350	.8392
.5500	.8405	.5450	.8401
.5600	.8415	.5550	.8410
.5700	.8426	.5650	.8421

.5800	.8438	.5750	.8432
.5900	.8451	.5850	.8445
.6000	.8465	.5950	.8458
.6100	.8481	.6050	.8473
.6200	.8498	.6150	.8489
.6300	.8517	.6250	.8507
.6400	.8537	.6350	.8527
.6500	.8559	.6450	.8548
.6600	.8584	.6550	.8571
.6700	.8611	.6650	.8597
.6800	.8640	.6750	.8625
.6900	.8672	.6850	.8655
.7000	.8707	.6950	.8689
.7100	.8745	.7050	.8726
.7200	.8787	.7150	.8766
.7300	.8833	.7250	.8809
.7400	.8883	.7350	.8857
.7500	.8938	.7450	.8910
.7600	.8998	.7550	.8967
.7700	.9064	.7650	.9030
.7800	.9136	.7750	.9099
.7900	.9214	.7850	.9174
.8000	.9301	.7950	.9257
.8100	.9395	.8050	.9347
.8200	.9498	.8150	.9445
.8300	.9611	.8250	.9553
.8400	.9735	.8350	.9672
.8500	.9870	.8450	.9801
.8600	1.0019	.8550	.9943
.8700	1.0183	.8650	1.0099
.8800	1.0364	.8750	1.0271
.8900	1.0564	.8850	1.0461
.9000	1.0787	.8950	1.0672
.9100	1.1041	.9050	1.0910
.9200	1.1334	.9150	1.1182
.9300	1.1683	.9250	1.1500
.9400	1.2118	.9350	1.1888
.9500	1.2690	.9450	1.2382
.9600	1.3489	.9550	1.3053
.9700	1.4681	.9650	1.4021
.9800	1.6563	.9750	1.5509
.9900	1.9675	.9850	1.7917
1.0000	2.5000	.9950	2.1974

Q AVG = .99793

EXPERIMENT 195 Z = 79.5 CM T = 30.00 M

DATA POINTS

YP	CP
-.0094	.0542
-.0078	.0564
-.0058	.0585
-.0033	.0607
-.0011	.0629
.0014	.0651
.0036	.0673

.0061	.0695
.0086	.0716
.0117	.0738
.0142	.0760
.0169	.0782
.0200	.0804
.0228	.0825
.0264	.0847
.0304	.0869
.0347	.0891
.0392	.0913
.0456	.0935
.0519	.0956
.0631	.0978
.0872	.1000

CONVENTIONAL INTERPRETATION
I = 1.52 DELC = .0436 DELN = .0462

	INTERMEDIATE VALUES			
DELTA	K	CS	SD	AD
.0814	2.100	.0600	.001714	-.001169
.0814	2.100	.0635	.000620	.000447
.0814	2.100	.0625	.000606	-.000007
.0814	2.300	.0605	.001648	.000521
.0814	2.300	.0594	.001836	.000073
.0814	2.300	.0592	.001879	-.000000
.0814	1.900	.0659	.000975	.000405
.0814	1.900	.0648	.000618	-.000133
.0814	1.900	.0651	.000671	-.000001
.0814	2.010	.0637	.000243	-.000038
.0814	2.010	.0638	.000241	-.000003
.0733	1.610	.0638	.001305	-.001152
.0733	1.610	.0659	.001038	.000028
.0733	1.610	.0659	.001024	-.000000
.0733	1.410	.0639	.002576	-.002243
.0733	1.410	.0681	.002133	.000198
.0733	1.410	.0677	.002034	-.000004
.0733	1.810	.0641	.000357	.000229
.0733	1.810	.0637	.000276	.000038
.0733	1.810	.0636	.000279	.000000
.0733	2.010	.0613	.001186	.000280
.0733	2.010	.0607	.001285	.000035
.0733	2.010	.0607	.001304	.000000
.0733	1.794	.0638	.000260	.000015
.0733	1.794	.0638	.000259	-.000002
.0895	2.594	.0638	.002815	.002540
.0895	2.594	.0579	.002596	.000258
.0895	2.594	.0572	.002750	.000013
.0895	2.594	.0572	.002758	.000000
.0895	2.794	.0552	.003781	.000938
.0895	2.794	.0526	.004234	.000208
.0895	2.794	.0519	.004388	.000010
.0895	2.394	.0625	.001139	.000645
.0895	2.394	.0602	.001554	-.000336
.0895	2.394	.0610	.001310	-.000006
.0895	2.194	.0648	.000602	.000450

.0895	2.194	.0637	.000252	-.000067
.0895	2.194	.0639	.000247	-.000000
.0895	1.994	.0668	.001446	.000356
.0895	1.994	.0661	.001197	-.000040
.0895	1.994	.0661	.001217	-.000000
.0895	2.189	.0639	.000250	-.000004
.0828	1.857	.0639	.001232	-.001074
.0828	1.857	.0659	.001077	-.000026
.0828	1.857	.0659	.001090	.000000
.0828	1.657	.0639	.002585	-.002276
.0828	1.657	.0681	.002255	.000204
.0828	1.657	.0678	.002148	-.000004
.0828	2.057	.0640	.000350	.000218
.0828	2.057	.0637	.000260	.000036
.0828	2.057	.0636	.000260	.000000
.0828	2.257	.0613	.001248	.000284
.0828	2.257	.0607	.001357	.000037
.0828	2.257	.0606	.001378	.000000
.0828	2.042	.0638	.000247	.000014
.0828	2.042	.0638	.000245	-.000002

I	DELC
1.5623	.0818
1.5623	.0681
1.5623	.0597
1.5623	.0544
1.5623	.0509
1.5623	.0485
1.5623	.0467
1.5623	.0453
1.5623	.0441
1.5623	.0431
1.5623	.0422
1.5623	.0414
1.5623	.0407
1.5623	.0401
1.5623	.0395
1.5623	.0390
1.5623	.0385
1.5623	.0380
1.5623	.0376
1.5623	.0373
1.5623	.0369
1.5623	.0366
1.5623	.0363
1.5623	.0361
1.5623	.0358
1.5623	.0356
1.5623	.0354
1.5623	.0352
1.5623	.0351
1.5623	.0349
1.5623	.0348
1.5623	.0346
1.5623	.0345
1.5623	.0344
1.5623	.0343
1.5623	.0342
1.5623	.0341
1.5623	.0341
1.5623	.0340

1.5623	.0339
1.5623	.0339
1.5623	.0338
1.5623	.0338
1.5623	.0337
1.5623	.0337
1.5623	.0337
1.5623	.0336
1.5623	.0336
1.5623	.0336
1.5623	.0336
1.5623	.0336
1.5623	.0336
1.5623	.0336
1.5623	.0336
1.5623	.0337
1.5623	.0337
1.5623	.0337
1.5623	.0338
1.5623	.0338
1.5623	.0339
1.5623	.0339
1.5623	.0340
1.5623	.0341
1.5623	.0341
1.5623	.0342
1.5623	.0343
1.5623	.0344
1.5623	.0345
1.5623	.0346
1.5623	.0348
1.5623	.0349
1.5623	.0351
1.5623	.0352
1.5623	.0354
1.5623	.0356
1.5623	.0358
1.5623	.0361
1.5623	.0363
1.5623	.0366
1.5623	.0369
1.5623	.0373
1.5623	.0376
1.5623	.0380
1.5623	.0385
1.5623	.0390
1.5623	.0395
1.5623	.0401
1.5623	.0407
1.5623	.0414
1.5623	.0422
1.5623	.0431
1.5623	.0441
1.5623	.0453
1.5623	.0467
1.5623	.0485
1.5623	.0509
1.5623	.0544
1.5623	.0597
1.5623	.0681
1.5623	.0818

```
YIC = -.0035     DYS = -.0023          I = 1.56     DELC =  .0395     DELN =  .

 **CCPLOT ERROR. (X(I),Y(I)) OUT OF BOUNDS. X(  18)=   .997E-01 Y(  18)=   .103
 CCHELP  CALLED FROM CCPLOT  AT 015476
 CCPLOT  CALLED FROM POBOLN  AT 005626

 **CCPLOT ERROR. (X(I),Y(I)) OUT OF BOUNDS. X(  19)=   .999E-01 Y(  19)=   .116
 CCHELP  CALLED FROM CCPLOT  AT 015476
 CCPLOT  CALLED FROM POBOLN  AT 005626

 **CCPLOT ERROR. (X(I),Y(I)) OUT OF BOUNDS. X(  20)=   .999E-01 Y(  20)=   .128
 CCHELP  CALLED FROM CCPLOT  AT 015476
 CCPLOT  CALLED FROM POBOLN  AT 005626

 **CCPLOT ERROR. (X(I),Y(I)) OUT OF BOUNDS. X(  21)=   .100E+00 Y(  21)=   .149
 CCHELP  CALLED FROM CCPLOT  AT 015476
 CCPLOT  CALLED FROM POBOLN  AT 005626
```

Sample Graphical Output

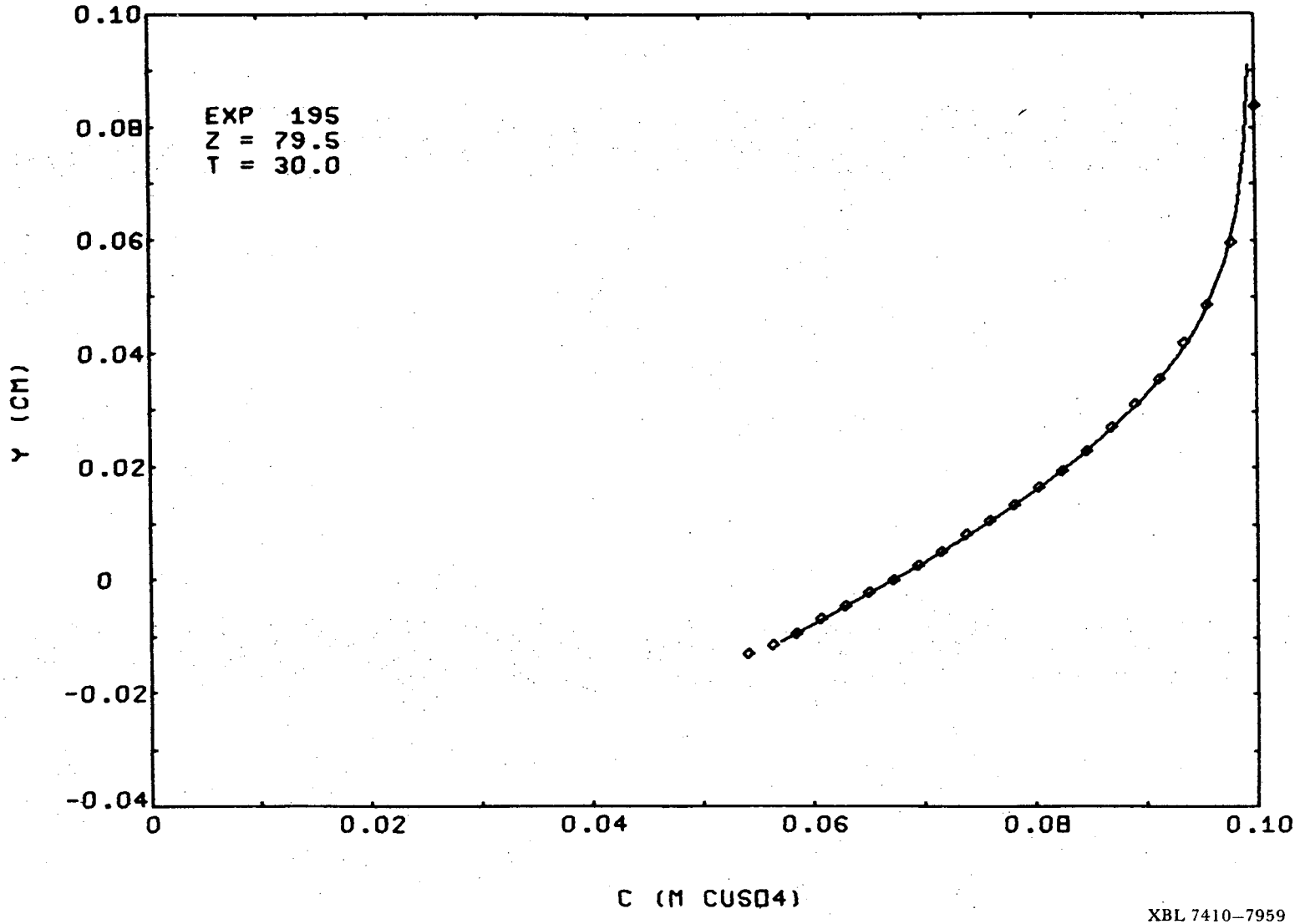

XBL 7410-7959

Key to Program POBOLN--Listing of Terms Used Differently than in POBOL

Symbol	Use	Units
A	Computation of DELC variation. See DELC and Q.	mole/liter
AA	Computation of DELC variation. See DELC and Q.	mole/liter
AB	Computation of DELC variation. See DELC and Q.	mole/liter
AC	Computation of DELC variation. See DELC and Q.	mole/liter
A1	Computation of DELTA variation. See DELTA, Q, and Fig. 1 of this Appendix.	
A2	Computation of DELTA variation. See DELTA, Q, and Fig. 1 of this Appendix.	
B1	Computation of Delta variation. See DELTA, Q, and Fig. 1 of this Appendix.	
B2	Computation of Delta variation. See DELTA, Q, and Fig. 1 of this Appendix.	
CD	Current density. Similar to POBOL, but here, CD is a function of the local concentration difference and boundary layer thickness, and thus is a function of x. It must be averaged in the x-direction. See SCD.	mA/cm^2
CFR	Reduced concentration (CF/CB) depicted by the computed interference fringe.	
CI	Local interfacial concentration CI = CB - DELC. Used to calculate the average current density.	mole/liter
CM	Multiplication factor used to relate phase (fringes) on the experimental interferogram to apparent concentration depicted by the interferogram. CM = 0.002182/fringe. If only every second fringe is read from the interferogram (signified by a negative NP value) CM = 0.004364.	mole/liter
CS	As in POBOL, CS identifies the interfacial concentration. Here, however, it signifies an average interfacial concentration from which the variable concentration difference DELC can be calculated. See DELC.	mole/liter

Symbol	Use	Units
DC	Same as in POBOL. -or- Apparent concentration difference CB-CP(2) depicted by the experimental interferogram YT, CP. CP(2) is used rather than CP(1) to account for distortion due to reflection effects (Chapter 3). (See below statement #7.) -or- Concentration difference DELC. Used as a dummy variable to sum the local DELC values in order to calculate the average DELC value. (Above statement #95.)	mole/liter
DE	Local refractive-index difference (bulk less interfacial) at one end of a segment DX (i.e., at x_j or x_{j+1} in Fig. 1 in part 2.1 of Chapter 2).	
DEA	Local refractive-index difference (bulk less interfacial) at the center of a segment DX (i.e., at x_a in Fig. 1 in part 2.1 of Chapter 2).	
DEDX	Refractive-index gradient in the x-direction. Computed from the refractive-index difference across the segment DX (between x_{j+1} and x_j, $y = y_a$).	cm^{-1}
DEDY	Refractive-index gradient in the y-direction. Computed at the center of the segment DX ($x = x_a$, $y = y_a$). See function GRAD.	cm^{-1}
DEL	Local boundary layer thickness (at $x = x_j$ or x_{j+1}). Related to the average boundary layer thickness DELTA by the function Q. See Q.	cm
DELA	Local boundary layer thickness (at $x = x_a$). Related to the average boundary layer thickness DELTA by the function QA. See QA.	mole/liter

Symbol	Use	Units
DELC	Local concentration difference (bulk less interfacial). Used to calculate DE and DEA values; i.e., DELC is calculated at either the edge of the segment DX or the center of the segment. DELC is computed in a particular manner to give a uniform current distribution in the x-direction. This computation accounts for (a) boundary layer thickness variation in the x-direction by using the local DEL or DELA values; and (b) linear variation of the diffusion coefficient and cation transport number with concentration. One restriction is imposed: if the above computation tries to make DELC larger than the bulk concentration CB, DELC is set equal to CB, i.e., negative concentrations are disallowed. This restriction can result in a slightly non-uniform current distribution: when the concentration differences try to be larger than CB near the edges of the electrode where the boundary layer is thicker, the current becomes limited to values smaller than in the center region of the electrode (a local limiting current is reached). The computations for DELC are performed between statements #15 and #20 for every iteration.	mole/liter
	-or-	
	Integrated average concentration difference (output).	mole/liter
DX	Increment width. See Fig. 1 in part 2.1. Set equal to 0.01 cm in this program, corresponding to 100 intervals. Table 1 in part 2.3 of Chapter 2 indicates that maximum errors of 0.0003 cm and 0.4 fringes could result by using only 100 intervals.	cm
ETA	Local refractive-index n = n(x,y).	
JJ, JP	Variable integers.	
K	Curve shape parameter. See function THETA.	
Q	Accounts for boundary layer thickness variation in the x-direction. Represents the local boundary layer thickness (at x_j or x_{j+1}) divided by the average boundary layer thickness. See Fig. 1 in this Appendix.	

Symbol	Use	Units
QA	Same as Q, but corresponds to a local boundary layer thickness at the center of an interval ($x = x_a$).	
QD	Multiplication factor used in the computation of Q and QA.	
S	Slope of a deflected light ray.	
SCD	Average current density.	mA/cm^2
SQ	Average value of QA, should be 1.00.	
X	Reduced horizontal distance X = x/W. Corresponds to x_j or x_{j+1} in Fig. 1 in part 2.1 of Chapter 2.	
XA	Reduced horizontal distance. Corresponding to x_a in Fig. 1 in part 2.1 of Chapter 2.	
YA	Corresponds to y_a in Fig. 1 in part 2.1 of Chapter 2.	cm
YAM	Reduced vertical distance. Corresponds to y_a (in Fig. 1 in part 2.1 of Chapter 2) divided by the local boundary layer thickness at $x = x_j$. Used in the calculation of DEDX.	
YAP	Same as above, but y_a is divided by the local boundary layer thickness at $x = x_{j+1}$.	
YAR	Same as above, but y_a is divided by the local boundary layer thickness at $x = x_a$.	
YC YMD	Numbers used to convert arbitrary distances read from film (data) to actual distances relative to the electrode surface y = 0. These calculations were done by hand to prepare the data read into program POBOL.	

REFERENCES

1. J. Happel and H. Brenner, Low Reynolds Number Hydrodynamics (Prentice-Hall, Englewood Cliffs, N.J., 1965).

2. K. W. Beach, Optical Methods for the Study of Convective Mass Transfer Boundary Layers on Extended Electrodes (Ph. D. Thesis), UCRL-20324, July 1971.

FIGURE CAPTIONS

Fig. 1. Ordinate: the function Q (or QA) used in POBOLN

Abscissa: reduced horizontal distance x/w

The open circles were calculated from hydrodynamic considerations. The interfacial fluid velocity gradient $V = (dv_z/dy)_{y=0}$ can be calculated by the method of Happel and Brenner[1] for laminar fluid flow in a rectangular duct. Such a calculation was performed by Beach[2] for duct dimensions of the flow channel described in part 1.1 of Chapter 1. Since the local boundary layer thickness should be proportional to $V^{-1/3}$ in laminar flow (see Chapter 5), we can estimate the x-variation of the boundary layer thickness variation according to the following relationship:

$$\frac{\delta_{(x)}}{\delta_{avg}} = \frac{V^{-1/3}{}_{(x)}}{(V^{-1/3})_{avg}} = Q$$

Beach's calculations[2] for V(x) were converted to the above form by using standard (e.g., Simpson's Rule) quadrature formulae to calculate $(V^{-1/3})_{avg}$. The results are presented as the open circles in Fig. 1. The solid curve was computed by a trial and error method, and its form was designed to give $Q_{avg} = 1.00$. The values of the empirical parameters were:

$$a_1 = 0.729 \qquad b_1 = 9.0$$

$$a_2 = 1.283 \qquad b_2 = 60.0$$

The solid curve Q is used to approximate the boundary layer thickness variation in POBOLN. Note that Q is symmetrical, i.e., Q(1) = Q(101), etc.

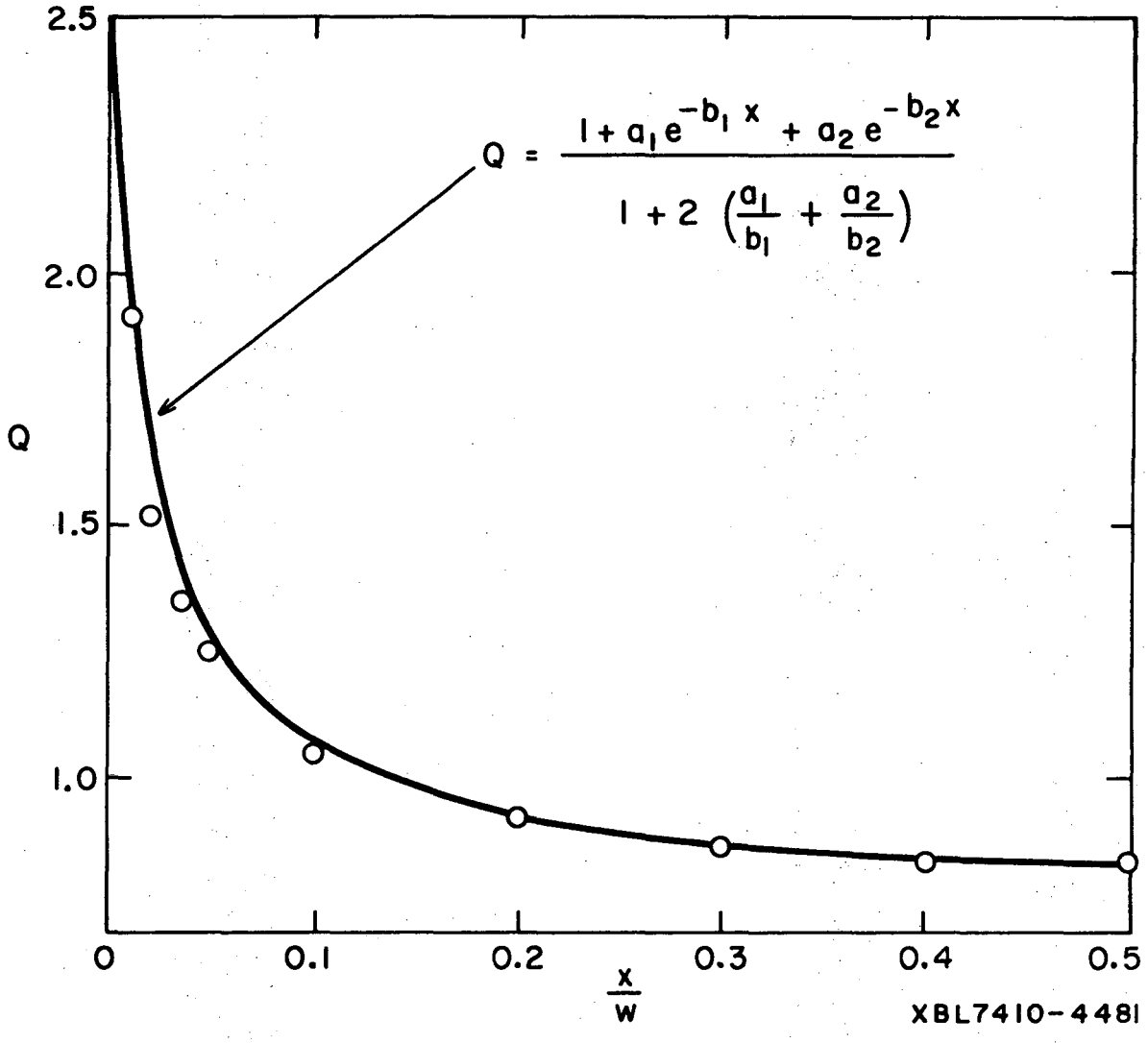
2.5
2.0
1.5
1.0
Q
0
0.1
0.2
0.3
0.4
0.5
x/w
$Q = \frac{1 + a_1 e^{-b_1 x} + a_2 e^{-b_2 x}}{1 + 2\left(\frac{a_1}{b_1} + \frac{a_2}{b_2}\right)}$
XBL7410-4481

Fig. 1

APPENDIX III. COMPUTATIONAL METHOD FOR SOLUTIONS OF FICK'S LAW OF DIFFUSION WITH VARIABLE TRANSPORT PROPERTIES

Program CRANK solves Fick's Law of Diffusion taking into account linear variations of diffusion coefficient and transference number with electrolyte concentration. The appropriate form of Fick's Law and its three boundary conditions are given in Chapter 4, Eqs. (8) through (11). This parabolic partial differential equation and its boundary conditions are cast into Crank-Nicholson finite difference representation, as described by Lapidus.[1] The resulting system of simultaneous non-linear algebraic equations is solved by the Thomas method.[2] These techniques are briefly described here, followed by a listing of program CRANK and its output: the transient concentration profiles formed by the galvanostatic electrodeposition of Cu from 0.1 M $CuSO_4$ at 10 mA/cm^2. Finally, a listing of each term used in CRANK is provided.

The time and space derivatives of dimensionless concentration θ can be approximated as follows:

$$\frac{\partial\theta}{\partial t} = \frac{\theta_{i,j+1} - \theta_{i,j}}{k} + O(k) \tag{1}$$

$$\frac{\partial\theta}{\partial x} = \frac{\theta_{i+1,j} - \theta_{i-1,j}}{2h} + O(h^2) \tag{2}$$

$$\frac{\partial^2\theta}{\partial x^2} = \frac{\theta_{i+1,j} - 2\theta_{i,j} + \theta_{i-1,j}}{h^2} + O(h^2) \tag{3}$$

where h is the spatial increment (cm) between rows i and i + 1 and k is the time increment(s) between rows j and j + 1:

$$x_i = (i - 1)\, h \tag{4}$$

$$t_j = (j - 1)\, k \tag{5}$$

Using Crank-Nicholson formulation, whereby the second derivative, Eq. (3), is represented as an average between rows i and i + 1, the parabolic partial differential differential equation (Eq. (8)) in Chapter 4 becomes:

$$\left[1 + \frac{\alpha}{4}(2\theta_{i+1,j+1} - \theta_{i-1,j+1})\right] \theta_{i-1,j+1} \tag{6}$$

$$+ \left[-2\left(1 + \frac{1}{\beta}\right) + \alpha(2\theta_{i,j+1} - \theta_{i-1,j+1} - \theta_{i+1,j+1})\right] \theta_{i,j+1}$$

$$+ \left[1 - \frac{\alpha}{4}\theta_{i+1,j+1}\right] \theta_{i+1,j+1} = 2\left(1 - \frac{1}{\beta}\right) \theta_{i,j} - \theta_{i+1,j} - \theta_{i-1,j}$$

$$+ \alpha_{i,j}(\theta_{i+1,j} + \theta_{i-1,j} - 2\theta_{i,j}) + \frac{\alpha}{4}(\theta_{i+1,j} - \theta_{i-1,j})^2$$

where $\beta = \frac{D_o k}{h^2}$. The boundary conditions (Eqs. (9) through (11)) in Chapter 4 become:

$$\theta_{i,1} = 1 \qquad (t = 0) \tag{7}$$

$$\theta_{\infty,k} = 1 \qquad (x \to \infty) \tag{8}$$

$$\frac{\theta_{2,k} - \theta_{1,k}}{h} = \frac{I(1 - t_+)_o}{mFD_o C_b} \frac{1 + \gamma\theta_{1,k}}{1 - \alpha\theta_{1,k}} \qquad (x = 0) \tag{9}$$

where m is the cation valence, I is the current density and γ, F, t_+, D, C_b and the subscript "o" have the same meanings as in Chapter 4.

The system of simultaneous nonlinear algebraic equations (Eqs. (6) through (9)) can be cast into a form amenable to solution by the Thomas method:[2]

$$a_1\theta_1 + b_1\theta_2 = d_1 \tag{10}$$

$$c_2\theta_1 + a_2\theta_2 + b_2\theta_3 = d_2$$

$$\vdots$$

$$c_i\theta_{i-1} + a_i\theta_i + b_i\theta_{i+1} = d_i$$

$$\vdots$$

$$c_n\theta_{n-1} + a_n\theta_n = d_n$$

Here, θ_i represents $\theta_{i,j+1}$, and the coefficients are given by:

$$a_i = -2\left(1 + \frac{1}{\beta}\right) + \alpha(2\theta_i - \theta_{i-1} - \theta_{i+1}) \tag{11}$$

$$b_i = 1 - \frac{\alpha}{4}\theta_{i+1}$$

$$c_i = 1 + \frac{\alpha}{4}(2\theta_{i+1} - \theta_{i-1})$$

$$d_i = 2\left(1 - \frac{1}{\beta}\right)\bar{\theta}_i - \bar{\theta}_{i+1} - \bar{\theta}_{i-1} + \alpha\bar{\theta}_i(\bar{\theta}_{i+1} + \bar{\theta}_{i-1} - 2\bar{\theta}_i) + \frac{\alpha}{4}(\bar{\theta}_{i+1} - \bar{\theta}_{i-1})^2$$

for $i = 2, 3, \ldots, n-1$ and $\bar{\theta}_i$ represents $\theta_{i,j}$. The starting values θ_i are determined by the boundary condition Eq. (7)

$$\theta_{i,1} = \theta_i = 1 \ , \ i = 1, 2, \ldots n \tag{12}$$

Now, when row k = 2 is calculated, all of the $\bar{\theta}$-values are known, defined by Eq. (12). Therefore, all of the inhomogeneous terms d_i in Eq. (11) are known, but the coefficients a_i, b_i and c_i must be guessed by assuming values of θ_i. The system of nonlinear equations (Eq. (10)) is now solved directly by the Thomas method, using Eqs. (8) and (9) to set the boundary values:

$$\left.\begin{aligned} a_1 &= -1 \\ b_1 &= +1 \\ d_1 &= \frac{hI(1 - t_+)_o}{mFD_o C_b} \frac{1 + \gamma\theta_1}{1 - \alpha\theta_1} \end{aligned}\right\} \quad (x = 0) \tag{13}$$

$$\left.\begin{aligned} a_n &= +1 \\ c_n &= 0 \\ d_n &= +1 \end{aligned}\right\} \quad (x \to \infty) \tag{14}$$

The calculated values of θ_i are then compared to the guessed values of θ_i. If the computed θ_i values fail to match the guessed θ_i value, new a_i, b_i and c_i are generated using the computed θ_i values and the process repeated. When the θ_i values finally agree (to within an arbitrary small deviation) the θ_i values for the next row k = 3 are calculated, using the θ_i values from row k = 2 (now $\bar{\theta}_i$) to compute the new d_i values and guess the new a_i, b_i and c_i values.

The computation proceeds, marching forward in time, until either zero concentration is computed at the interface x = 0 or a specified time limit is exceeded.

Program CRANK was checked by computing the concentration profiles for $I = 10\ mA/cm^2$ with $\alpha = \gamma = 0$. The resulting concentrations matched those predicted by the Sand equation[3] to within 0.0002 M $CuSO_4$ for spatial and time increments $h \leq 0.0001$ cm and $k \leq 0.1$ s.

```
      PROGRAM CRANK(INPUT,OUTPUT)

      REAL K

      DIMENSION A(902),B(902),C(902),D(902),G(902),W(902)
      DIMENSION THETA(902),THETAC(902),THETAP(902)

      DATA N,H,K/901,0.0001,0.1/
      DATA ALFA,GAMMA/0.0869,0.0648/
      DATA CD,M,FC,CB,TM,DC/10.0,2,96487.0,0.1,0.597,0.00000541/

  100 FORMAT(2F10.5)
  150 FORMAT(///,*   T =*,F5.1,* SEC*,//,7X,*X*,9X,*C*)

      A(1)=-1.0 $ B(1)=1.0 $ W(1)=A(1)
      C(N)=0.0 $ A(N)=1.0 $ D(N)=1.0 $ G(N)=1.0 $ W(N)=1.0
      BETA=DC*K/H**2 $ BETAR=1.0/BETA
      NM=N-1 $ T=0.00001
      DO 10 I=1,N
      THETA(I)=1.0 $ THETAC(I)=0.0
   10 CONTINUE
   20 T=T+K
      DO 22 I=1,N
   22 THETAP(I)=THETA(I)
   25 CONTINUE
      D(1)=H*CD*TM*(1.0+GAMMA*THETA(1))/(M*FC*DC*CB*(1.0-ALFA*THETA(1)))
      G(1)=D(1)/W(1)
      DO 30 I=2,NM
      IM=I-1 $ IP=I+1
      A(I)=-2.0*(1.0+BETAR)+ALFA*(2.0*THETA(I)-THETA(IM)-THETA(IP))
      B(I)=1.0-0.25*ALFA*THETA(IP)
      C(I)=1.0+0.25*ALFA*(2.0*THETA(IP)-THETA(IM))
      D(I)=2.0*(1.0-BETAR)*THETAP(I)-THETAP(IP)-THETAP(IM)+ALFA*(THETAP(
     1I)*(THETAP(IP)+THETAP(IM)-2.0*THETAP(I))+0.25*(THETAP(IP)-THETAP(I
     2M))**2)
      W(I)=A(I)-C(I)*B(IM)/W(IM)
      G(I)=(D(I)-C(I)*G(IM))/W(I)
   30 CONTINUE
      DO 40 I=1,NM
      J=N-I $ JP=J+1
   40 THETA(J)=G(J)-B(J)*THETA(JP)/W(J)
      SD=0.0 $ L=0
      DO 50 I=1,N
      DELT=1.0-THETA(I) $ IF(DELT.LT.0.000001) GO TO 50
      L=L+1 $ SD=SD+(THETA(I)-THETAC(I))**2
   50 THETAC(I)=THETA(I)
      SD=SQRT(SD/L) $ IF(SD.GE.0.000001) GO TO 25
      DT=T-FLOAT(IFIX(T))
      IF(ABS(DT).GT.0.001) GO TO 20 $ PRINT 150,T
      DO 60 I=1,N,50
      CONC=CB*THETA(I) $ X=H*(I-1)
   60 PRINT 100,X,CONC
      IF(THETA(1).LT.0.0) GO TO 90
      IF(T.LT.49.9) GO TO 20
   90 CONTINUE
      STOP
      END
```

```
WWWWWWWWWWWWWWWWWWWWWWWWWWWWWWWWWWWWWWWWWWWWWWWWWWWWWWWWWWWWWWWWWWWWWWWWWWWWWWWWWWWWWWW
WWWWWWWWWWWWWWWWWWWWWWWWWWWWWWWWWWWWWWWWWWWWWWWWWWWWWWWWWWWWWWWWWWWWWWWWWWWWWWWWWWWWWWW
```

Sample Output

T = 1.0 SEC

X	C
0	.08357
.00500	.09909
.01000	.09999
.01500	.10000
.02000	.10000
.02500	.10000
.03000	.10000
.03500	.10000
.04000	.10000
.04500	.10000
.05000	.10000
.05500	.10000
.06000	.10000
.06500	.10000
.07000	.10000
.07500	.10000
.08000	.10000
.08500	.10000
.09000	.10000

T = 5.0 SEC

X	C
0	.06351
.00500	.08698
.01000	.09675
.01500	.09946
.02000	.09994
.02500	.10000
.03000	.10000
.03500	.10000
.04000	.10000
.04500	.10000
.05000	.10000
.05500	.10000
.06000	.10000
.06500	.10000
.07000	.10000
.07500	.10000
.08000	.10000
.08500	.10000
.09000	.10000

T = 10.0 SEC

X	C
0	.04899
.00500	.07432
.01000	.08914
.01500	.09620
.02000	.09891
.02500	.09975
.03000	.09995
.03500	.09999
.04000	.10000
.04500	.10000
.05000	.10000
.05500	.10000
.06000	.10000
.06500	.10000
.07000	.10000
.07500	.10000
.08000	.10000
.08500	.10000
.09000	.10000

T = 20.0 SEC

X	C
0	.02901
.00500	.05528
.01000	.07413
.01500	.08635
.02000	.09346
.02500	.09717
.03000	.09889
.03500	.09961
.04000	.09988
.04500	.09997
.05000	.09999
.05500	.10000
.06000	.10000
.06500	.10000
.07000	.10000
.07500	.10000
.08000	.10000
.08500	.10000
.09000	.10000

T = 30.0 SEC

X	C
0	.01410
.00500	.04051
.01000	.06108
.01500	.07603
.02000	.08615
.02500	.09250
.03000	.09621
.03500	.09821
.04000	.09921
.04500	.09968
.05000	.09988
.05500	.09996
.06000	.09999
.06500	.10000
.07000	.10000
.07500	.10000
.08000	.10000
.08500	.10000
.09000	.10000

T = 40.0 SEC

X	C
0	.00179
.00500	.02815
.01000	.04962
.01500	.06623
.02000	.07841
.02500	.08685
.03000	.09239
.03500	.09581
.04000	.09781
.04500	.09892
.05000	.09949
.05500	.09977
.06000	.09990
.06500	.09996
.07000	.09999
.07500	.09999
.08000	.10000
.08500	.10000
.09000	.10000

Key to Program CRANK

Symbol	Use	Units
A	Coefficient, see Eq. (11).	
ALFA	Correlation coefficient for linear variation of diffusion coefficient with concentration. α in Chapter 4.	
B	Coefficient, see Eq. (11).	
BETA	Constant, $D_o k/h^2$.	
BETAR	1/BETA	
C	Coefficient, see Eq. (11). -or- Concentration (output)	mole/liter
CB	Bulk concentration.	mole/liter
CD	Current density.	mA/cm^2
CONC	Concentration.	mole/liter
D	Coefficient, see Eq. (11)	
DELT	1-THETA	
DC	Correlation coefficient for linear variation of diffusion coefficient with concentration. D_o in Chapter 4.	cm^2/s
G	Intermediate coefficient used in the Thomas method. See Reference 2.	
GAMMA	Correlation coefficient for linear variation of cation transference number with concentration. γ in Chapter 4.	
H	Spatial increment.	cm
I, IM, IP, J, JP	Variable integers.	
K	Time increment.	s
L	Variable integer.	

Symbol	Use	Units
M	Cation valence.	eq/mole
N	Number of increments H	
NM	N - 1	
SD	Standard deviation between computed θ_i and guessed θ_i.	
T	Time	s
THETA	Dimensionless concentration C/C_b.	
THETAC	Previous (guessed) values of THETA.	
THETAP	Values of THETA from the previous time step	
TM	Correlation coefficient for linear variation of cation transference number with concentration. $(1 - t_+)_o$ in Chapter 4.	
W	Intermediate coefficient used in the Thomas method. See Reference 2.	
X	Spatial coordinate.	cm

References

1. L. Lapidus, Digital Computation for Chemical Engineers (McGraw-Hill), N. Y., 1962), p. 162

2. Ibid, p. 254.

3. See Chapter 2, part 2.2.

APPENDIX IV. DERIVATION OF THE EQUATION OF LIGHT-DEFLECTION

Figure 1 illustrates the trajectory y(x) of a deflected light ray AOB as it traverses a medium of variable refractive-index n(x,y). The uv coordinate system is rotated by an angle θ from the original xy coordinates (defined in Fig. 1 of part 2.3); the tangent of the angle θ is identical to the slope dy/dx of deflected ray AOB at the origin O of the uv coordinates.

$$\frac{dy}{dx} = \tan\theta \qquad (1)$$

Within a sufficiently small region about the point O, the light ray trajectory can be approximated by a straight line in the u-direction. Figure 2 depicts the paths ABC and DE of two rays separated by a small distance Δv. The medium refractive-index varies continuously from $n = n(v_o)$ at plane ABC to a larger value $n = n(v_o + \Delta v)$ at plane DE. The light beam (i.e., the sum of all of the light rays crossing line AD) is deflected from its original propagation angle $\phi = 0$ at plane AD to a positive angle ϕ at plane EC because of the unequal velocities of rays ABC and DE. The beam propagates in a direction perpendicular to the equiphase wavefronts AD and EC, and the corresponding beam slope dv/du increases from zero at plane AD to

$$\frac{dv}{du} = \tan\phi \qquad (2)$$

at plane EC. Geometrical considerations show that the angle ϕ is directly related to the distance ε shown in Fig. 2; Eq. (2) can now be rewritten as

$$\tan\phi = \frac{dv}{du}(u_o + \Delta u) - \frac{dv}{du}(u_o) = \frac{\varepsilon}{\Delta v} \tag{3}$$

For uniform phase across a wavefront, the optical path length p of ray DE equals that of ray ABC. The optical path length is defined as the product of the local refractive index and geometrical path length, so

$$p = n(v_o)[\Delta u + \varepsilon] = n(v_o + \Delta v)[\Delta u] \quad . \tag{4}$$

Eliminating ε between Eqs. (3) and (4) gives:

$$\frac{\frac{dv}{du}(u_o + \Delta u) - \frac{dv}{du}(u_o)}{\Delta u} = \frac{n(v_o + \Delta v) - n(v_o)}{n(v_o)\cdot\Delta v} \tag{5}$$

Equation (5) can be reduced to differential form by taking limits as $\Delta u \to 0$ (left-hand side) and $\Delta v \to 0$ (right-hand side):

$$\frac{d^2v}{du^2} = \frac{1}{n}\frac{dn}{dv} \tag{6}$$

Equation (6) is a differential analogue of the well-known Schlieren equation.

Equation (6) can be expressed in terms of the original xy coordinates by inverting the coordinate rotation shown in Fig. 1. The pertinent independent variables are related in Eqs. (7) through (10) (θ = constant).

$$u = x\cos\theta + y\sin\theta \tag{7a}$$

$$v = -x\sin\theta + y\cos\theta \tag{7b}$$

$$x = u\cos\theta - v\sin\theta \tag{8a}$$

$$y = u\sin\theta + v\cos\theta \tag{8b}$$

$$du = \frac{\partial u}{\partial x}\,dx + \frac{\partial u}{\partial y}\,dy = \cos\theta\,dx + \sin\theta\,dy \tag{9a}$$

$$dv = \frac{\partial v}{\partial x}\,dx + \frac{\partial v}{\partial y}\,dy = -\sin\theta\,dx + \cos\theta\,dy \tag{9b}$$

$$\frac{\partial}{\partial v} = \frac{\partial y}{\partial v}\,\frac{\partial}{\partial y} + \frac{\partial x}{\partial v}\,\frac{\partial}{\partial x} = \cos\theta\,\frac{\partial}{\partial y} - \sin\theta\,\frac{\partial}{\partial x} \tag{10}$$

The slope dv/du can be obtained by dividing Eq. (9b) by Eq. (9a)

$$\frac{dv}{du} = \frac{\frac{dy}{dx} - \tan\theta}{1 + \frac{dy}{dx}\tan\theta} \tag{11}$$

and the second derivative can be found by applying the chain rule of differentiation to Eq. (11) and using Eq. (9a):

$$\frac{d^2v}{du^2} = \frac{dx}{du}\,\frac{d}{dx}\left(\frac{dv}{du}\right) = \frac{dx}{\cos\theta\,dx + \sin\theta\,dy} \tag{12}$$

$$\left[\frac{\left(1 + \frac{dy}{dx}\tan\theta\right)\frac{d^2y}{dx^2} - \left(\frac{dy}{dx} - \tan\theta\right)\tan\theta\,\frac{d^2y}{dx^2}}{\left(1 + \frac{dy}{dx}\tan\theta\right)^2}\right]$$

$$= \frac{d^2y}{dx^2}\,\frac{1 + \tan^2\theta}{\cos\theta\left(1 + \frac{dy}{dx}\tan\theta\right)^3}$$

Now, for <u>any</u> location along the ray trajectory, Eq. (1) can be used to relate the slope dy/dx to the rotation angle θ (θ variable). Equation (12) becomes

$$\frac{d^2v}{du^2} = \frac{d^2y}{dx^2}\left[1 + \left(\frac{dy}{dx}\right)^2\right]^{-3/2} \quad , \tag{13}$$

and Eq. (10) transforms into

$$\frac{\partial}{\partial v} = \left[1 + \left(\frac{dy}{dx}\right)^2\right]^{-1/2}\left[\frac{\partial}{\partial y} - \frac{dy}{dx}\,\frac{\partial}{\partial x}\right] \tag{14}$$

Combining Eqs. (6), (13) and (14) yields the light-deflection equation for rectangular coordinate systems

$$\frac{d^2y}{dx^2} = \frac{1}{n}\left[1 + \left(\frac{dy}{dx}\right)^2\right]\left[\frac{\partial n}{\partial y} - \left(\frac{dy}{dx}\right)\frac{\partial n}{\partial x}\right] \quad . \tag{15}$$

Furthermore, the optical path length p can be expressed in differential form:

$$dp = n\,du = n\,\frac{du}{dx}\,dx \tag{16}$$

Using Eqs. (1), (9a) and (16), the differential optical path length can be expressed in terms of xy coordinates:

$$dp = n\left[1 + \left(\frac{dy}{dx}\right)^2\right]^{1/2} dx \quad , \tag{17}$$

which in integral form becomes

$$p(x) = \int_o^x n\left[1 + \left(\frac{dy}{dx}\right)^2\right]^{1/2} dx \tag{18}$$

FIGURE CAPTIONS

Fig. 1. Coordinate systems.

x,y coordinate system defined by Fig. 1 in part 2.3

u,v coordinate system rotated from the x,y coordinate system by an angle θ

AOB deflected ray trajectory

θ angle of ray deflection

O origin of the u,v coordinate system

Fig. 2. Ray deflection in the u,v coordinate system.

ABC,DE ray trajectories

ϕ angle of deflection

Δv incremental distance between rays ABC and DE

Δu incremental propagation distance

u_o, v_o origin of the u,v coordinate system

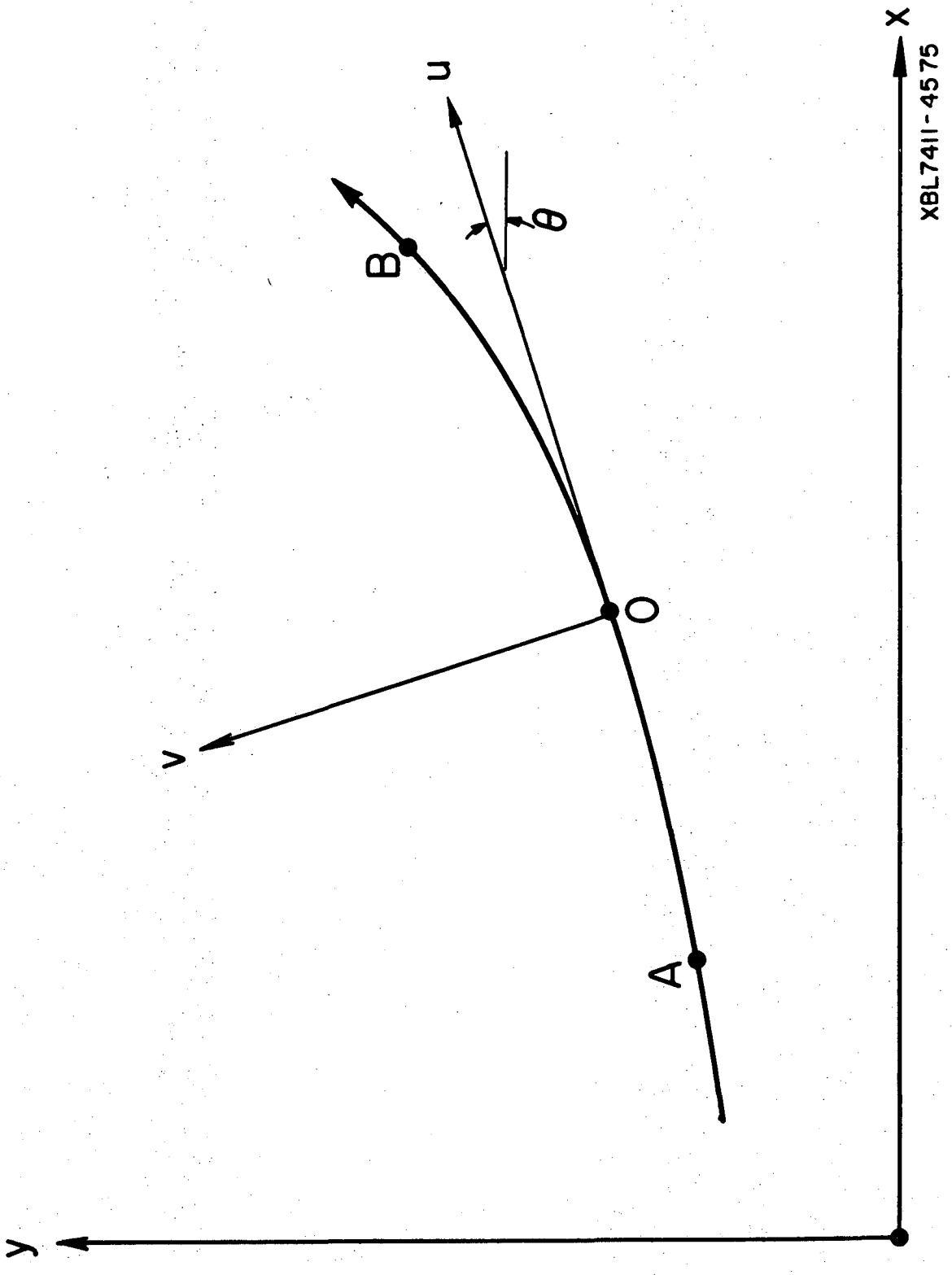

Fig. 1

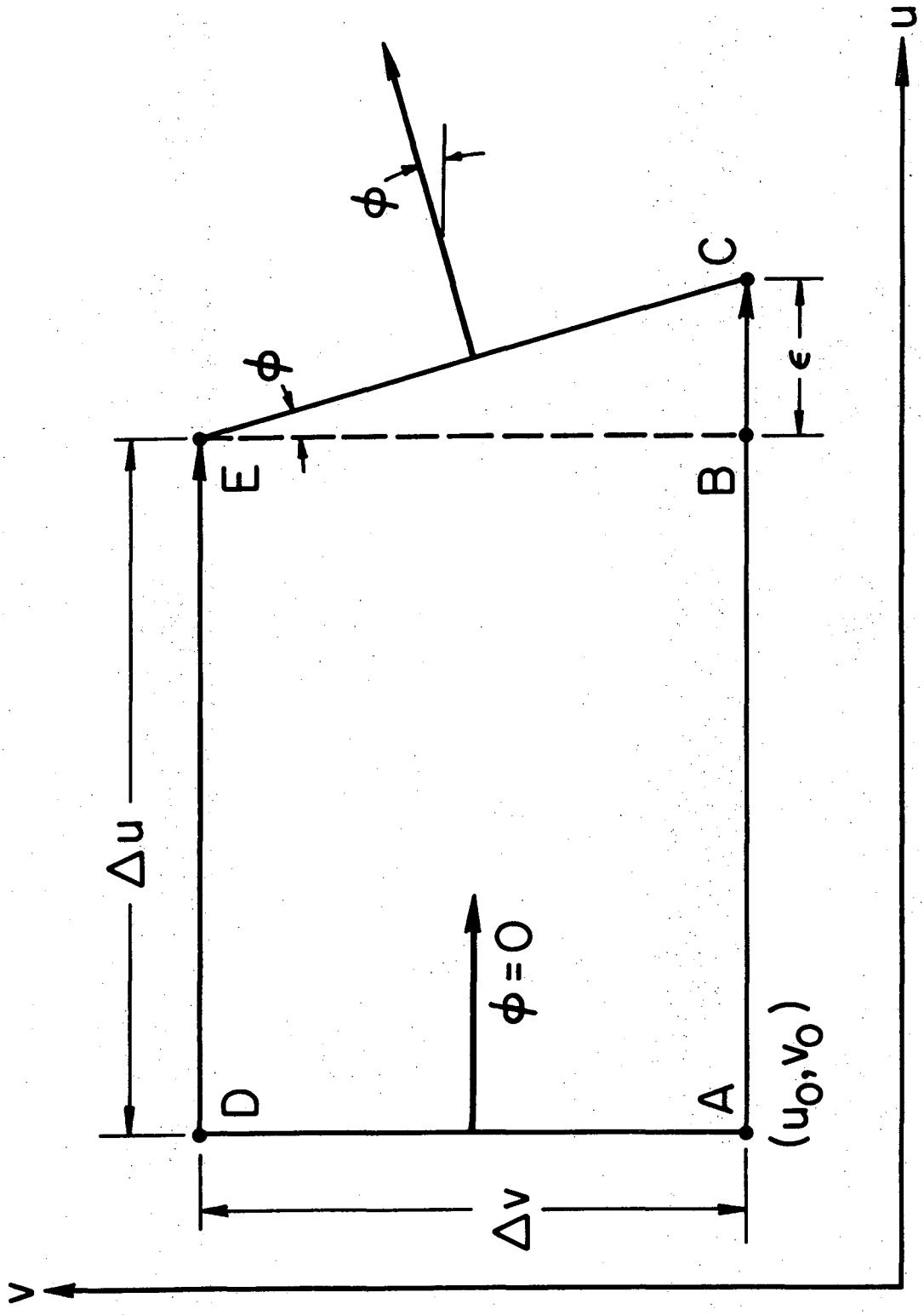

XBL7411-4581

Fig. 2

APPENDIX V.
LIGHT-DEFLECTION ERRORS IN THE INTERFEROMETRY OF ELECTROCHEMICAL MASS TRANSFER BOUNDARY LAYERS

F. R. McLarnon, R. H. Muller and C. W. Tobias

Inorganic Materials Research Division, Lawrence Berkeley Laboratory and Department of Chemical Engineering; University of California Berkeley, California 94720

ABSTRACT

The effect of light-deflection on interferograms of electrochemical mass transfer boundary layers can result in substantial errors if interferograms are interpreted in the conventional way. Corrections in boundary layer thickness, interfacial concentration and interfacial concentration gradient for the convection-free electrodeposition of Cu from aqueous $CuSO_4$ have been calculated to provide estimates for a wide range of experimental conditions.

Key Words

Interferometry; Refraction; Diffusion; Mass Transfer

INTRODUCTION

Concentration profiles of single solutes in electrolytes near working electrodes can, in principle, be quantitatively observed by interferometric techniques. Such observations are useful in the study of transport processes and in the analysis of different measures designed to provide uniform accessibility and increased reaction rates at electrodes. Some of the advantages of interferometry compared to other means of observing boundary layers and local transport rates are: high resolution for concentration changes (typically 10^{-5} M) and; the possibility of continuous observation without disturbance (e.g., of flow), not restricted to conditions of limiting current.

In the conventional interpretation of interferograms, local changes in the phase depicted by the interferogram are taken as a direct measure of local refractive index variations in the object. Such an interpretation is often not valid because it assumes that light travels along a straight line through the specimen. Refractive index variations normal to the propagation direction of a light beam produce a deflection of the beam (refraction, Schlieren effect) that results in two types of distortions in the interferogram: a) Geometrical distortion due to displacement of the beam normal to its propagation direction. This effect falsifies conventional interpretation of distance on the interferogram and causes displacement of the apparent electrode/electrolyte interface. b) Phase distortion due to increased geometrical path length and passage of the beam through regions of varying refractive-index. Quantitative concentration profiles,

therefore, often cannot be derived by the conventional interpretation of interferograms.

Figure 1 schematically shows the trajectories of two light rays traversing a cathodic concentration boundary layer. Ray ABC is only slightly deflected and stays within the boundary layer over its path AB because it propagates near the edge of the boundary layer where the refractive-index gradient is small. Ray DEF, which enters the electrolyte where the refractive-index gradient is high, is deflected so much that it leaves the boundary layer at the intersection with line GH (and then travels along a straight line) before leaving the electrolyte at point E. A deflected ray will contribute to the interferogram only if it passes through the aperture of the objective lens. For instance, if ray DEF were to be deflected at any higher angle, it would not pass through the objective lens and, therefore, would not contribute to the interferogram. The corresponding part of the boundary layer would then not be visible on the interferogram.

Details of computational techniques, that have been developed to account for the effect of light-deflection on interferograms of one-dimensional boundary layers, have been described elsehwere.[1,2] Suffice it to say that for any concentration profile, the shapes of (double beam) interference fringes can now be calculated taking into account effects of light deflection. It has been found that distortions in the interferogram depend strongly on the position of the plane of focus of the imaging objective lens. Although for each concentration profile a plane of focus can be found[3] for which the location of the electrode surface is not distorted on the interferogram, it is preferable to use a more

easily defined plane of focus at a fixed location and accept the resulting displacement of the electrode shadow. For the observation of cathodic boundary layers (to be considered here) we recommend[2] to focus on the inside of the cell wall on the light-entrance side of the cell, where suitable targets can be inscribed. (For anodic boundary layers, it would be preferable to focus on the inside of the cell wall on the light-exit side.)

It is the purpose of this paper to present calculations of light-deflection errors for the interferometric observation of boundary layers so that investigators may estimate errors to be expected under a wide range of experimental conditions.

LIGHT-DEFLECTION ERRORS

Figure 2 shows the experimental interferogram of a concentration boundary layer formed by constant-current electrolysis. Superimposed are the theoretical concentration profile, AE, derived by use of the Sand[4] equation, and an interference fringe, BF, computed from the concentration profile by taking light-deflection effects into account.

The ordinate on Fig. 2 denotes distance from the true (undistorted) image of the electrode surface. Local changes in the phase of transmitted light, visible as displacements of originally straight interference fringes, have been related to local concentration changes, as shown on the abscissa. The relationship has been based on the conventional interpretation of interferograms that assumes straight-line light propagation. Thus, local changes in phase have been linearly related to changes in concentration (or refractive index) at the corresponding point in the image.

If the interferogram was free of light-deflection effects, the interference fringes would follow the theoretical concentration profile AE. The figure illustrates that the apparent location B of the interface on the interferogram has receded from its original position A, identified by $y = 0$. Also, the apparent concentration change over the boundary layer is smaller than the true change.

Conventional interpretation of the interferogram in Fig. 2 would therefore lead to a boundary layer thickness that is too large. If we define the extent of the boundary layer as the region containing 90% of the concentration variation, the error e_t in boundary layer thickness can be defined in terms of the ordinates of the points shown in Fig. 2 as

$$e_t = (y_F - y_B) - (y_E - y_A)$$

Similarly, the apparent interfacial concentration is too high and the error can be formulated as a difference of abscissas

$$e_c = C_B - C_A \quad .$$

The interfacial concentration (refractive index) gradient is too low. The error can be represented by the difference in slope of the two curves at the interface

$$e_g = \left.\frac{dC}{dy}\right|_B - \left.\frac{dC}{dy}\right|_A \quad .$$

In addition to the above <u>absolute</u> errors in the interferometry of boundary layers, it is often desirable to estimate the <u>relative</u> errors. Such relative errors in boundary layer thickness, interfacial concentration and interfacial concentration gradient, as shown in Figs. 8-13, are defined here as

$$\varepsilon_t = \frac{e_t}{y_E}$$

$$\varepsilon_C = \frac{e_c}{C_b - C_A}$$

$$\varepsilon_g = \frac{e_g}{\left.\frac{dC}{dy}\right|_A} \quad .$$

CONVECTION-FREE BOUNDARY LAYERS

Diffusion boundary layers free of convection effects offer a useful model for optical investigation since the concentration profiles are easily derived, and experimental results can serve to test the optical calculations. Convection-free transport conditions are common in electrochemical studies, and the results can be used as a basis for convective transport studies.

The convectionless electrodeposition of a metal cation from a stagnant layer of an aqueous binary salt electrolyte is described by the time-dependent diffusion equation in one dimension*

$$\frac{\partial C}{\partial t} = D \frac{\partial^2 C}{\partial y^2} \quad . \tag{1}$$

The current density is related to the interfacial concentration gradient by

$$i = \frac{zFD}{1-t_+} \left.\frac{\partial C}{\partial y}\right|_{y=0} \quad . \tag{2}$$

*Concentration-independent diffusivity will be assumed. Solutions for variable diffusivity can also be obtained, although not in a convenient closed form.

For potentiostatic electrodeposition, the boundary conditions are

$$C = C_s \quad \text{at} \quad y = 0 \, , \; t > 0 \tag{3}$$

$$C = C_b \quad \text{at} \quad t = 0 \, , \; \text{all} \; \; y \tag{4}$$

$$C = C_b \quad \text{as} \quad y \to \infty \, . \tag{5}$$

The solution, first obtained by Cottrell,[5] is

$$\theta = \text{erf} \; \zeta \tag{6}$$

$$i = \frac{zF(\Delta C)}{1-t_+} \sqrt{\frac{D}{\pi t}} \tag{7}$$

where erf ζ is the error function of dimensionless distance

$$\zeta = \frac{y}{2\sqrt{Dt}} \, , \tag{8}$$

$\Delta C = C_b - C_s$ and the dimensionless concentration

$$\theta = \frac{C - C_s}{\Delta C} \, . \tag{9}$$

For galvanostatic electrodeposition, the boundary conditions to Eq. (1) are:

$$\frac{\partial C}{\partial y} = \text{constant at} \quad y = 0 \, , \; t > 0 \tag{10}$$

$$C = C_b \quad \text{at} \quad t = 0 \, , \; \text{all} \; \; y \tag{11}$$

$$C = C_b \quad \text{as} \quad y \to \infty \, .$$

The solution, first obtained by Sand,[4] is

$$\theta = 1 + \sqrt{\pi}\,\zeta(1 - \text{erf}\,\zeta) - e^{-\zeta^2} \tag{13}$$

$$\Delta C = \frac{2i(1 - t_+)}{zF}\sqrt{\frac{t}{\pi D}} \tag{14}$$

Concentration profiles for use in the light-deflection analysis, with electrodeposition of Cu from aqueous $CuSO_4$ serving as a model, have been calculated. Equations (6) and (7) and Eqs. (13) and (14) have been used in this computation. The interfacial concentration has been set $C_s = 0$, and the values of the bulk concentration were $C_b = 0.01$, 0.10 or 0.20 M $CuSO_4$ ($\Delta C = 0.01$, 0.10 or 0.20). For constant potential calculations, time t is varied to give different concentration profiles and interfacial mass flux rates. For constant current calculations, various current densities are used (substituting Eq. (2) into Eq. (10)) to give different concentration profiles and interfacial mass flux rates. (Note that specification of i and ΔC fixes t through Eq. (14).) A diffusion coefficient[6] $D = 6\times10^{-6}$ cm^2/sec and Cu^{++} transference number[7] $t_+ = 0.36$ (typical values for 0.1M $CuSO_4$ at 25°C) are used in all calculations. Representative concentration profiles employed in the optical analysis are shown in Figs. 3 and 4.

ERROR CALCULATIONS

Cell dimensions and optical constants must be specified in order to compute interferograms from concentration profiles. The electrode, which is assumed here to fully occupy the space between the glass sidewalls, was assigned widths of 1.0, 2.5, 5.0, 10.0 and 20.0 mm. In order to model our experimental cell, the glass sidewalls were assumed to be 12.7 mm wide with a refractive-index of 1.5231. However, refraction in the glass sidewalls has a negligible effect on light-deflection errors.[3] Light of 632.8 mm wavelength is assumed incident parallel to the planar electrode surface and perpendicular to the glass sidewalls. The plane of focus is chosen as the plane where light enters the electrolyte. Electrolyte refractive-index was experimentally found to be a linear function of $CuSO_4$ concentration at 632.8 nm wavelength and 25°C:

$$n = 1.3311 + 0.029\ C \qquad (15)$$

Interferograms similar to the dashed line in Fig. 2 are now calculated from concentration profiles using the above-mentioned computational technique.[1]

Absolute errors in boundary layer thickness, interfacial concentration and interfacial concentration gradient are shown in Figs. 5, 6 and 7, respectively for a 10 mm wide electrode. Current density (interfacial refractive-index gradient) was chosen as abscissa because it is an easily measured variable. Note that a positive error means that the value of a variable on the interferogram is larger than the true value.

Relative errors in boundary layer thickness, interfacial concentration and interfacial concentration gradient are shown in Figs. 8-13. Figures 8-10 also demonstrate the dependence of errors on concentration difference ΔC. The effect of electrode width is illustrated in Figs. 11-13.

DISCUSSION

Figures 5-7 show that for a 10 mm wide electrode, the light-deflection errors depend strongly on current density and concentration difference ΔC and only weakly on the specific boundary condition (potentiostatic or galvanostatic). For current densities in the order of 1 mA/cm^2, the errors are independent of ΔC and boundary condition. The weak dependence on boundary condition can be ascribed to the similarity between the respective concentration profiles; compare Figs. 3 and 4. Above about 2 mA/cm^2 for ΔC = 0.01 M $CuSO_4$, about 7 mA/cm^2 for ΔC = 0.1 M and about 10 mA/cm^2 for ΔC = 0.2 M, the light rays entering the boundary layer at the electrode surface are deflected so much that they leave the boundary layer before they leave the electrolyte (as ray DEF in Fig. 1). This effect causes an error extremum in the curves of Figs. 5 and 6 and a knee in the curves of Fig. 7. The abrupt changes in the character of the error curves are due to the straight paths traversed by the deflected rays once they leave the boundary layer; at lower current densities the rays are continuously changing direction within the boundary layer. (Figure 2 illustrates an interferogram in which rays entering the cell near the electrode surface are deflected out of the boundary layer.) As infinite current density is approached, the error in boundary layer thickness approaches zero, the error in interfacial concentration approaches ΔC and the error in interfacial concentration gradient approaches negative infinity.

The trend toward apparent negative concentrations (i.e., on the interferogram) seen in Figs. 6, 9 and 12 is a result of the choice of focal plane position. For focus in the center of the cell, for instance, no such negative errors would occur.

Figures 8-10 show that, contrary to what one might expect, relative errors are generally smaller for larger concentration difference ΔC. However, for large concentration differences, interferogram interpretation can be impeded by crowding of the fringes near the interface.

Figures 11-13 show that similar to absolute errors derived analytically for constant concentration gradients of unlimited extent,[3] relative errors strongly diminish with decreasing cell width, but are negligible only for electrodes thinner than a few mm.

Figures 5-13 can be used to estimate light deflection errors in experimental interferograms if all deflected portions of the test beam are accepted by the objective lens. The maximum angle ϕ_{max} of light deflection within a boundary layer is given by[2,3]

$$\tan \phi_{max} = \sqrt{\left(\frac{n_b}{n_s}\right)^2 - 1} \qquad (16)$$

and the maximum angle of deflected light emanating from the specimen cell can be calculated by substituting numerical values of refractive-index (e.g., Eq. (15)) into Eq. (16) and accounting for refraction in the glass sidewall. For example, the objective lens aperture must accept illumination at angles up to 1.59° for ΔC = 0.01 M $CuSO_4$, up to 4.65° for ΔC = 0.10 M and up to 7.14° for ΔC = 0.20 M.

CONCLUSIONS

Light deflection effects in the interferometry of electrochemical mass transfer boundary layers can lead to serious errors in the derivation of concentration profiles unless appropriate corrections in the interpretation of interferograms are employed. The magnitude of errors encountered may be estimated from the data presented in Figs. 5-13, but the accurate interpretation of interferograms with significant light-deflection effects requires individual optical analysis.[2] Light-deflection errors are small (<10%) for small current densities (below 2.5 mA/cm^2 for a 1 cm wide electrode) or narrow electrodes (less than 2.5 mm for up to 10 mA/cm^2).

ACKNOWLEDGEMENTS

This work was conducted under the auspices of the U. S. Atomic Energy Commission.

REFERENCES

1. K. W. Beach, R. H. Muller and C. W. Tobias, J. Opt. Soc. Am. 63, 559 (1973).

2. K. W. Beach, Optical Methods for the Study of Convective Mass Transfer Boundary Layers on Extended Electrodes (Ph.D. Thesis), UCRL-20324, July 1971.

3. R. H. Muller in Advances in Electrochemistry and Electrochemical Engineering, R. H. Muller, ed. (Wiley-Interscience, New York, 1973), Vol. 9, pp. 326-353.

4. H. J. S. Sand, Phil. Mag. (6) 1, 45 (1901).

5. F. G. Cottrell, Z. Physikal. Chem. 42, 385 (1903).

6. W. G. Eversole, H. M. Kindsvater and J. D. Peterson, J. Phys. Chem. 46, 370 (1942)

7. J. J. Fritz and C. R. Fuget, J. Phys. Chem. 62, 303 (1958).

NOMENCLATURE

C	concentration [mole/liter]
C_b	bulk concentration [mole/liter]
C_s	interfacial concentration [mole/liter]
D	diffusion coefficient [cm^2/sec]
e_t	absolute error in boundary layer thickness [mm]
e_c	absolute error in interfacial concentration [M $CuSO_4$]
e_g	absolute error in interfacial concentration gradient [M $CuSO_4$ cm^{-1}]
F	Faraday constant [coul/equiv]
i	current density [A/cm^2]
n	refractive-index
n_b	bulk refractive-index
n_s	interfacial refractive-index
t	time after current (voltage) switch-on [s]
t_+	cation transference number
y	distance from electrode [mm]
z	cation valence
ΔC	$C_b - C_s$ [mole/liter]
ε_t	relative error in boundary layer thickness
ε_c	relative error in interfacial concentration
ε_g	relative error in interfacial concentration gradient
ζ	dimensionless distance (Eq. (8))
θ	dimensionless concentration (Eq. (9))
ϕ_{max}	maximum angle of deflection within a boundary layer

FIGURE CAPTIONS

Fig. 1. Schematic of light ray trajectories in a cathodic concentration boundary layer: refractive-index increases in the direction away from the electrode surface.

ABC Trajectory of a ray that remains inside the boundary layer.

DEF Trajectory of a ray that is deflected out of the boundary layer.

GH Edge of the boundary layer.

Fig. 2. Experimental interferogram of a concentration boundary layer during galvanostatic deposition of copper on a 10 mm wide electrode. i = 10.0 mA/cm^2, C_b = 0.1M $CuSO_4$ and t = 10.0 s.

——— Theroretical concentration profile AE corresponding to experimental conditions (calculated from Eq. (13)).

----- Computed interference fringe BF corresponding to theoretical concentration profile.

A True interfacial concentration and position.

B Apparent interfacial concentration and position.

E True (90%) boundary layer edge (position where θ = 0.9).

F Apparent boundary layer edge.

Fig. 3. Concentration profiles for potentiostatic conditions.

——— ΔC = 0.1M $CuSO_4$

----- ΔC = 0.2M $CuSO_4$

a i = 10.0 mA/cm^2, t = 17.5 s

b i = 20.0, t = 4.4 s

c i = 30.0, t = 1.9 s

d i = 10.0, t = 70.0 s

e i = 20.0, t = 17.5 s

f i = 30.0, t = 7.8 s

Fig. 4. Concentration profiles for galvanostatic conditions. ΔC and i designation as in Fig. 3.

a t = 43.2 s

b t = 10.8 s

c t = 4.8 s

d t = 172.7 s

e t = 43.2 s

f t = 19.2 s

Fig. 5. Absolute error in boundary layer thickness. Electrode width = 10.0 mm.

——— potentiostatic boundary condition

------- galvanostatic boundary condition

a ΔC = 0.01 M $CuSO_4$

b ΔC = 0.10 M $CuSO_4$

c ΔC = 0.20 M $CuSO_4$

Fig. 6. Absolute error in interfacial concentration. Designations as in Fig. 5.

Fig. 7. Absolute error in interfacial concentration gradient. Designations as in Fig. 5.

Fig. 8. Relative error in boundary layer thickness for various concentration differences. Electrode width = 10.0 mm, potentiostatic boundary condition.

a ΔC = 0.01 M $CuSO_4$

b ΔC = 0.10 M $CuSO_4$

c ΔC = 0.20 M $CuSO_4$

Fig. 9. Relative error in interfacial concentration for various concentration differences. Designations as in Fig. 8.

Fig. 10. Relative error in interfacial concentration gradient for various concentration differences. Designations as in Fig. 8.

Fig. 11. Relative error in boundary layer thickness for different electrode widths. ΔC = 0.1 M $CuSO_4$, potentiostatic boundary condition.

a electrode width = 20.0 mm

b 10.0 mm

c 5.0 mm

d 2.5 mm

e 1.0 mm

Fig. 12. Relative error in interfacial concentration for different electrode widths. Designations as in Fig. 11.

Fig. 13. Relative error in interfacial concentration gradient for different electrode widths. Designations as in Fig. 11.

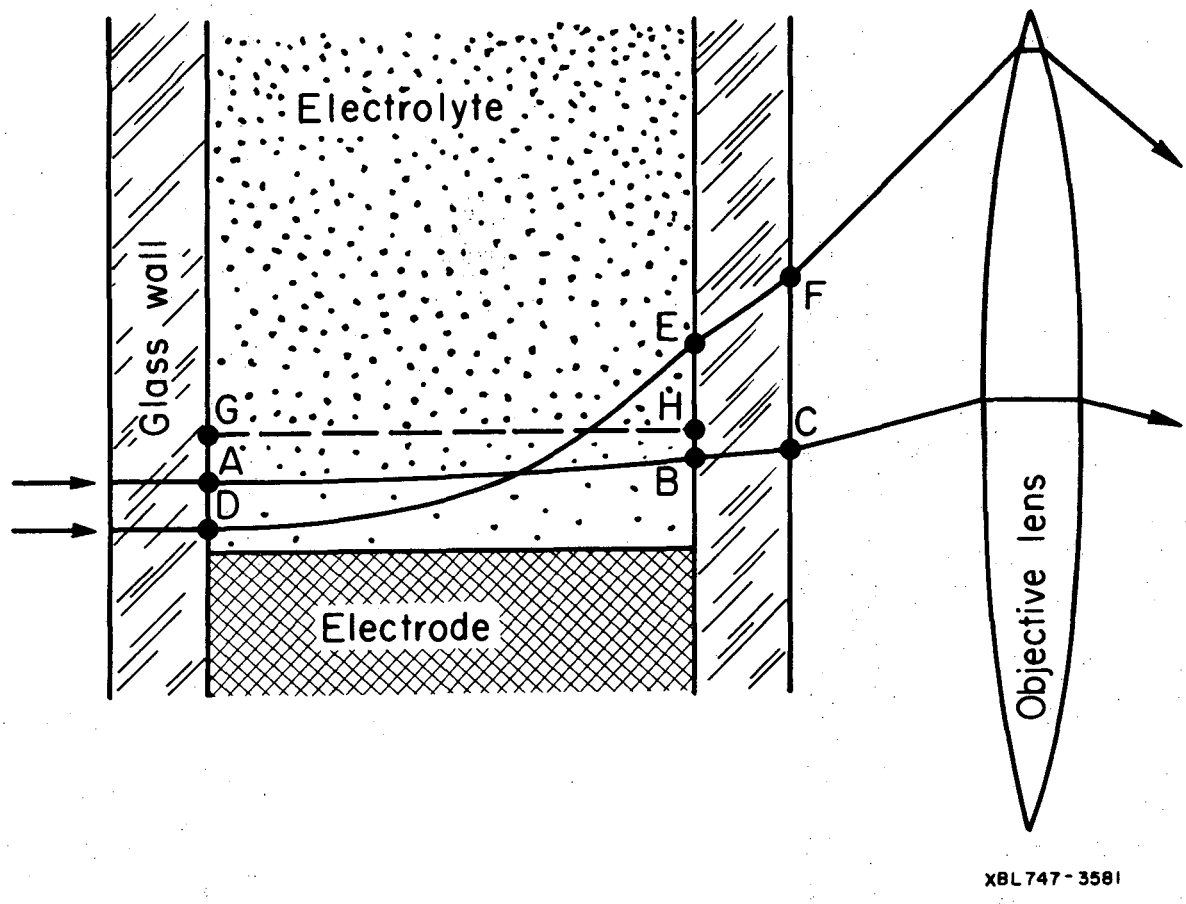
Electrolyte
Glass wall
G
H
A
B
D
E
F
C
Electrode
Objective lens
XBL747-3581

Fig. 1

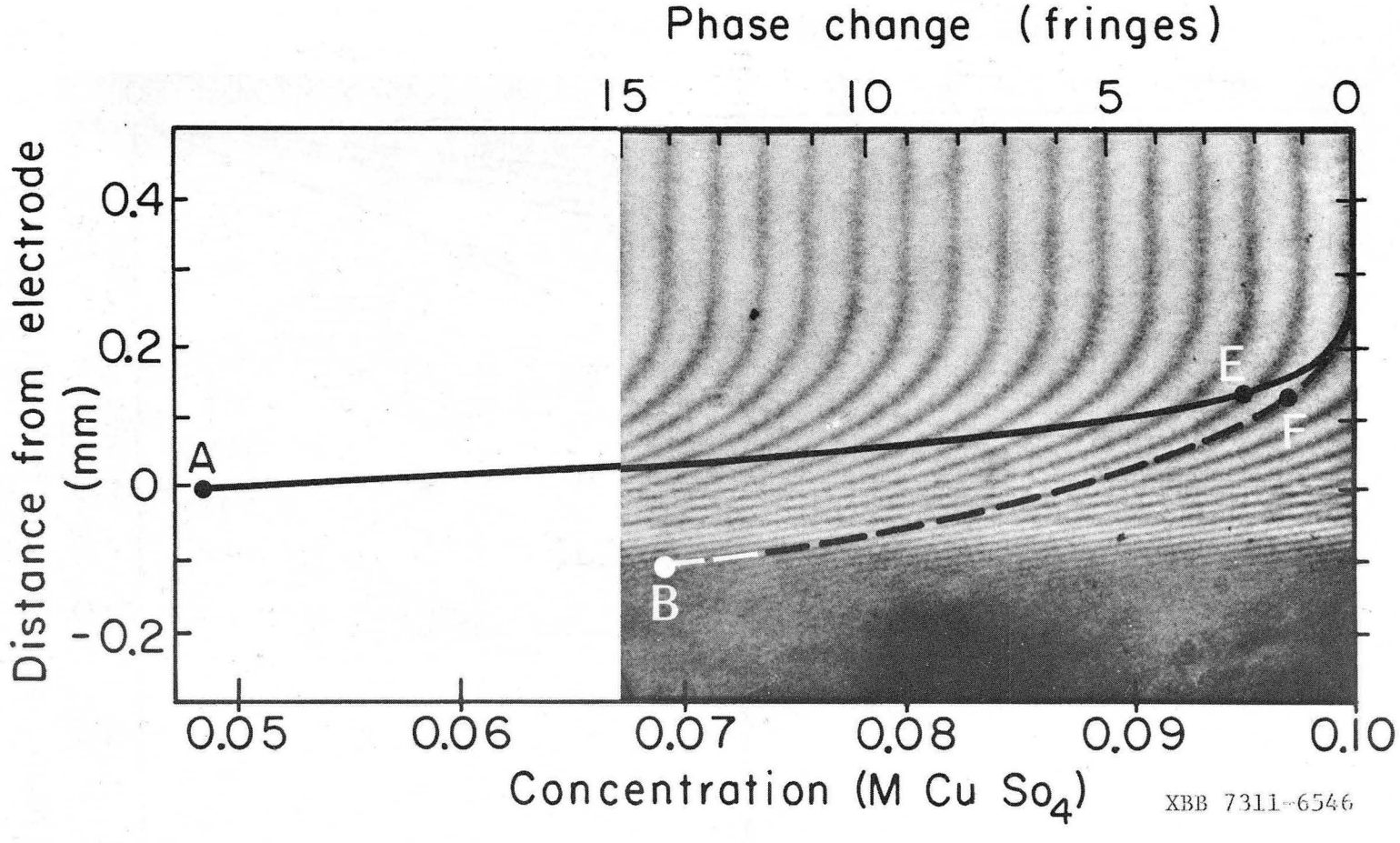

Fig. 2

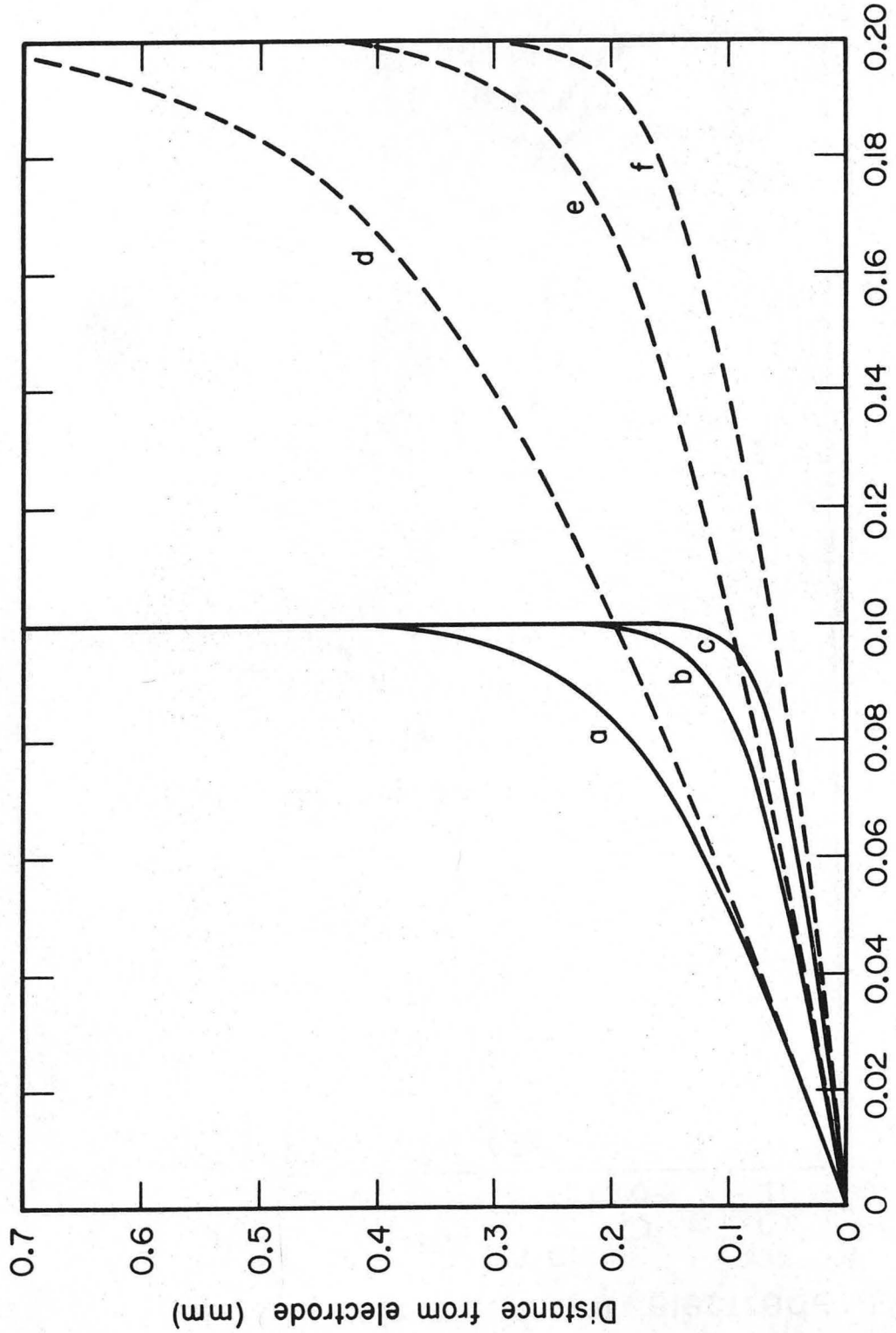

XBL739-4134

Fig. 3

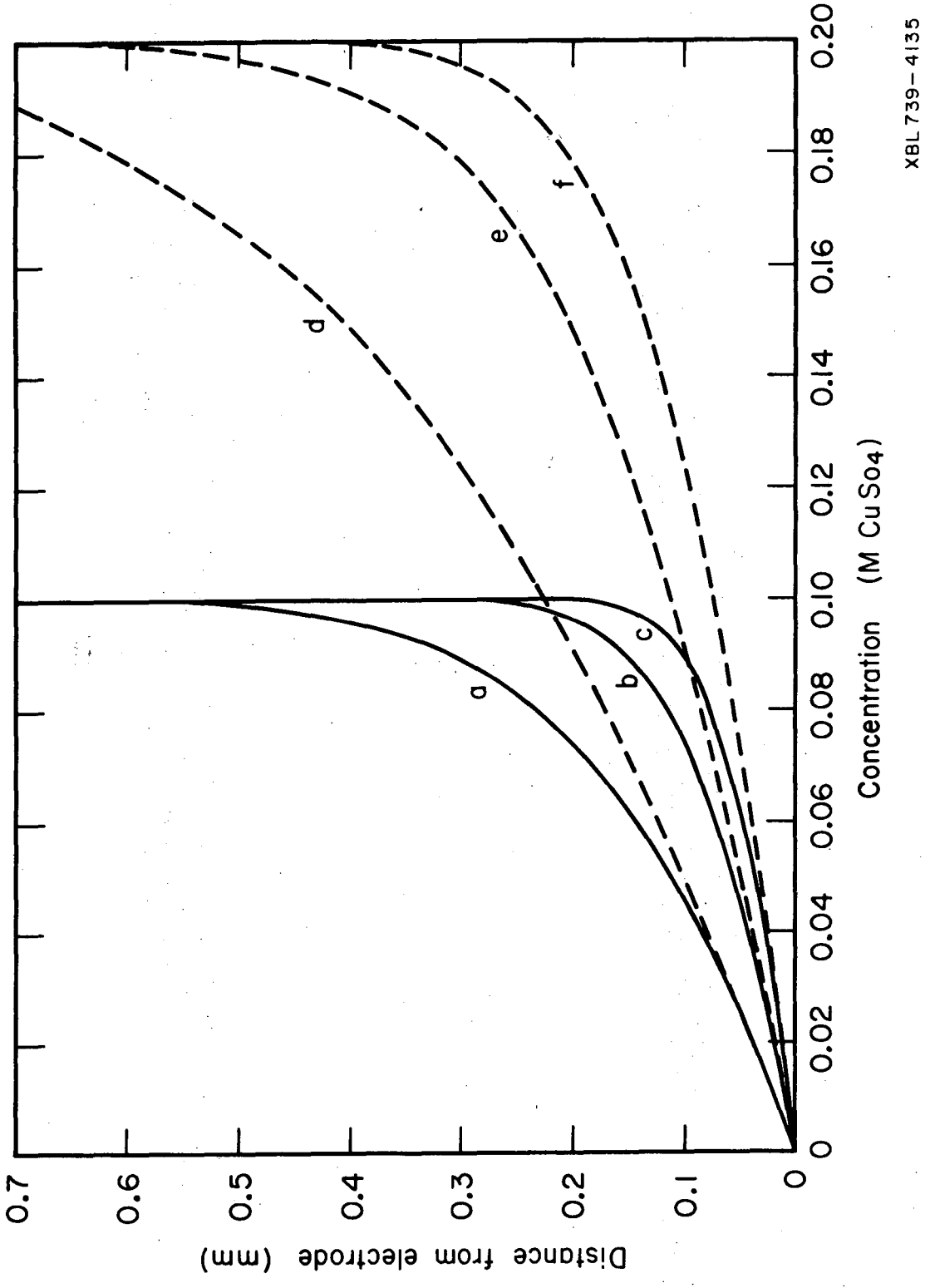

XBL 739-4135

Fig. 4

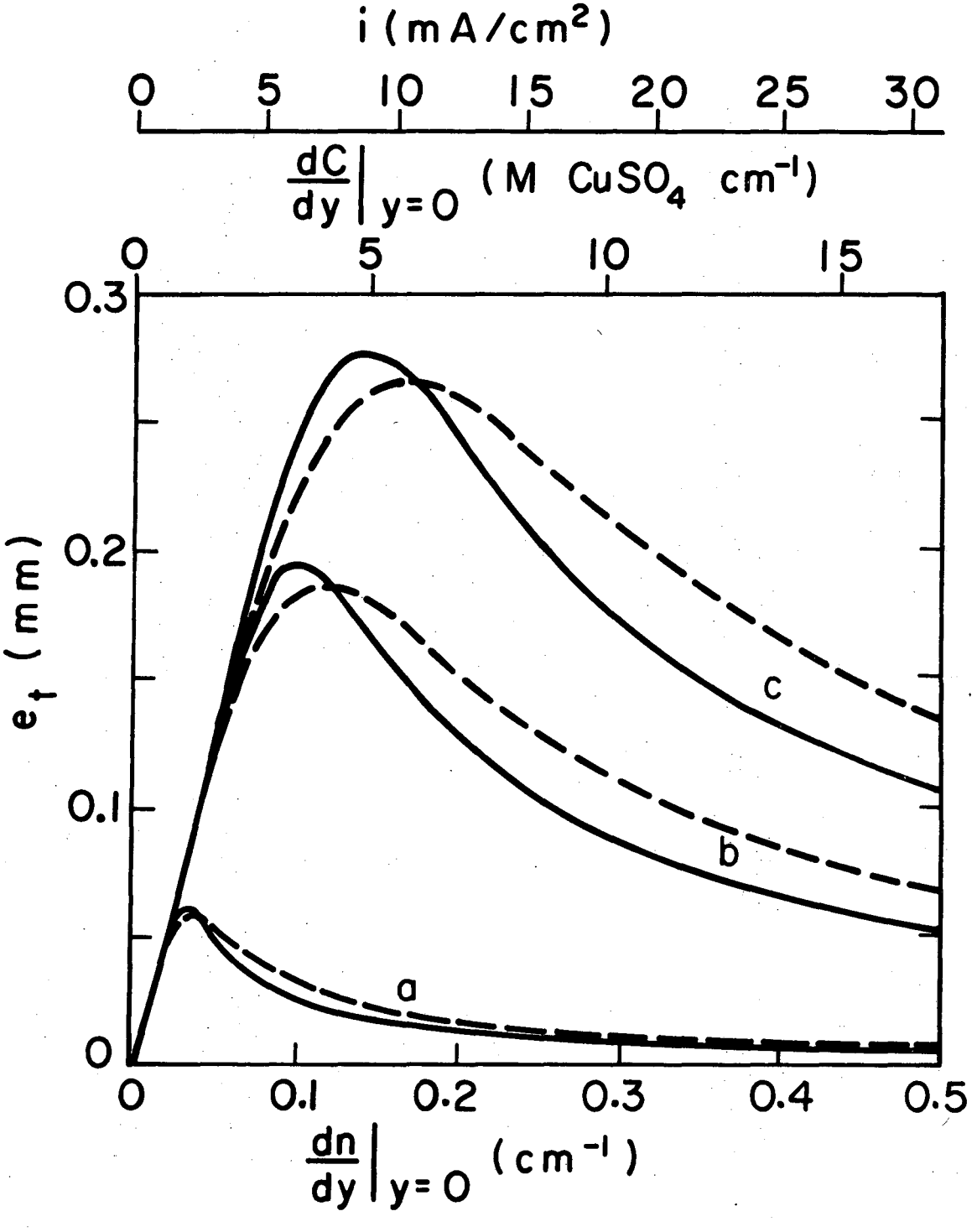
i (mA/cm²)
0
5
10
15
20
25
30
dC/dy | y=0 (M CuSO4 cm⁻¹)
0
5
10
15
0.3
0.2
0.1
0
et (mm)
a
b
c
0
0.1
0.2
0.3
0.4
0.5
dn/dy | y=0 (cm⁻¹)
XBL741-2170

Fig. 5

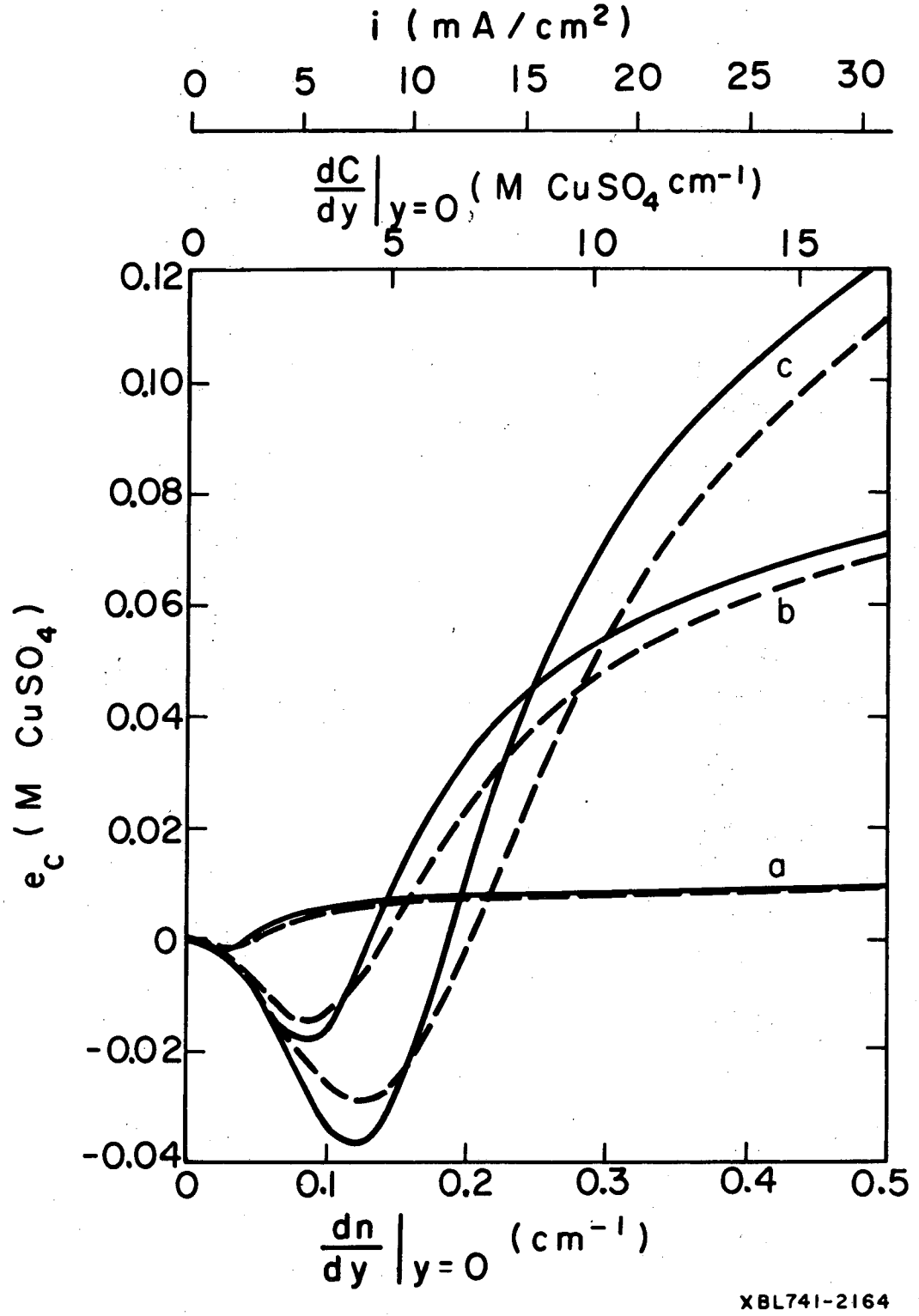

Fig. 6

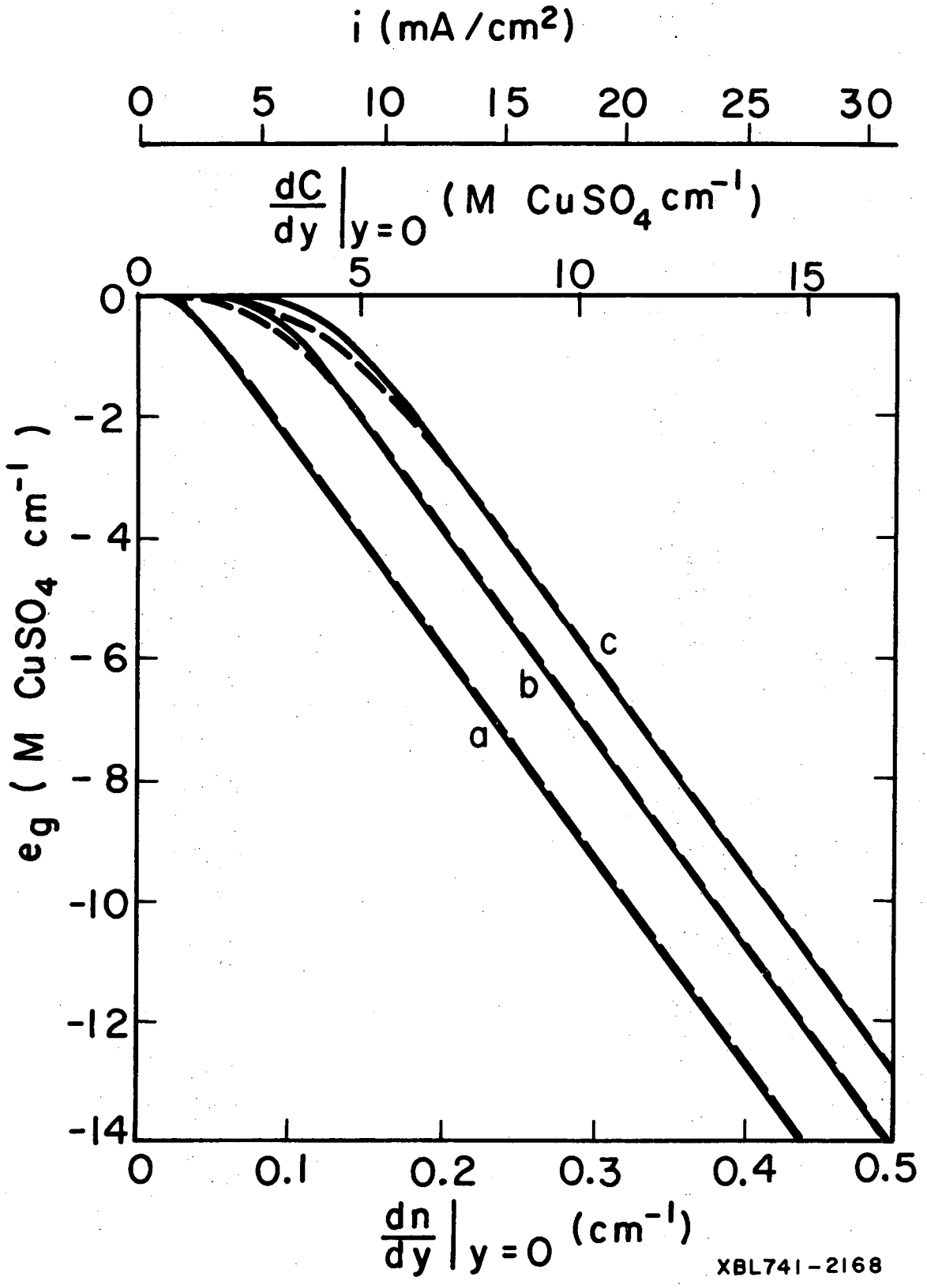
i (mA/cm²)
0
5
10
15
20
25
30
dC/dy |y=0 (M CuSO4 cm⁻¹)
0
5
10
15
eg (M CuSO4 cm⁻¹)
0
-2
-4
-6
-8
-10
-12
-14
a
b
c
0
0.1
0.2
0.3
0.4
0.5
dn/dy |y=0 (cm⁻¹)
XBL741-2168

Fig. 7

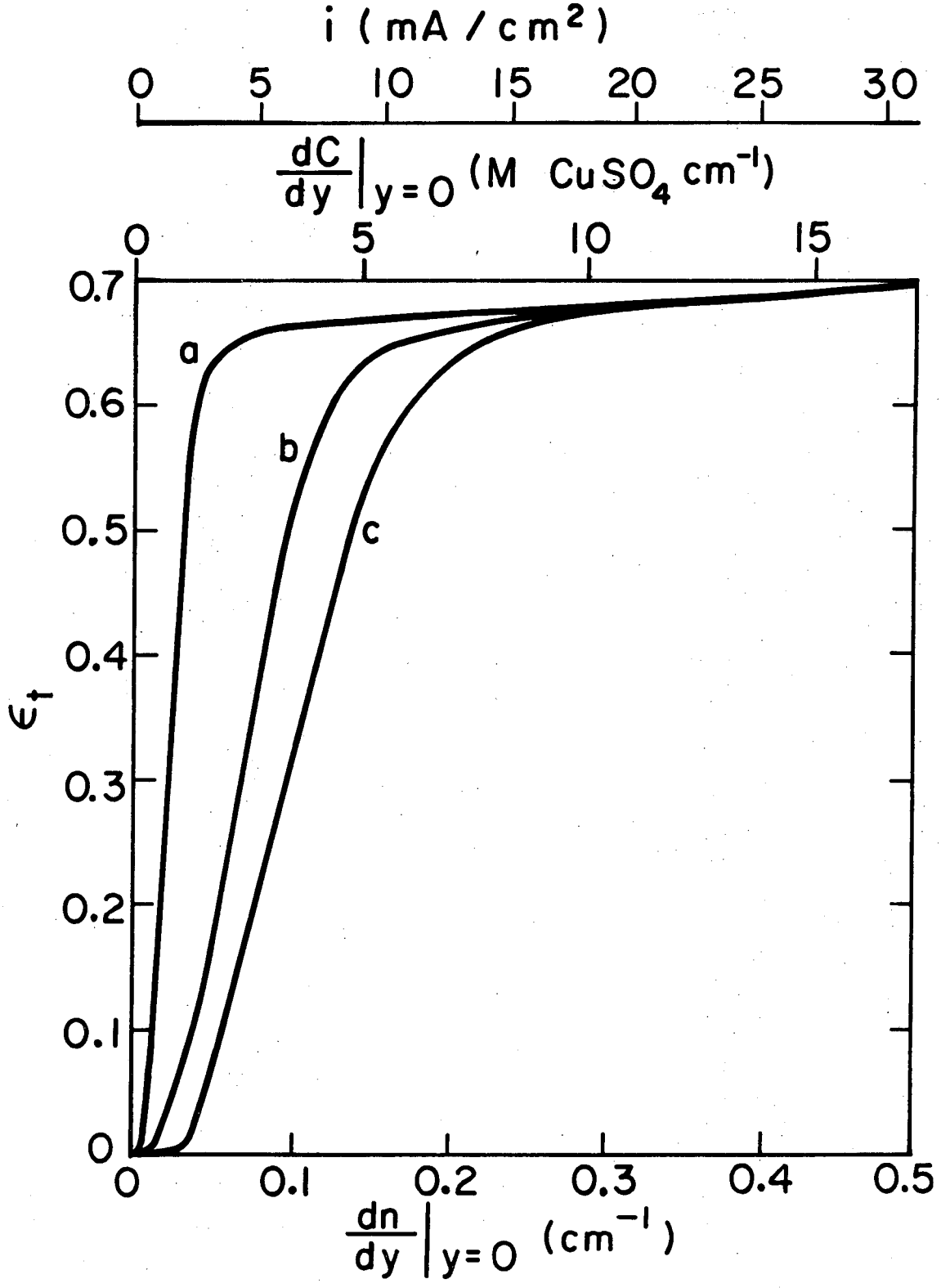

Fig. 8

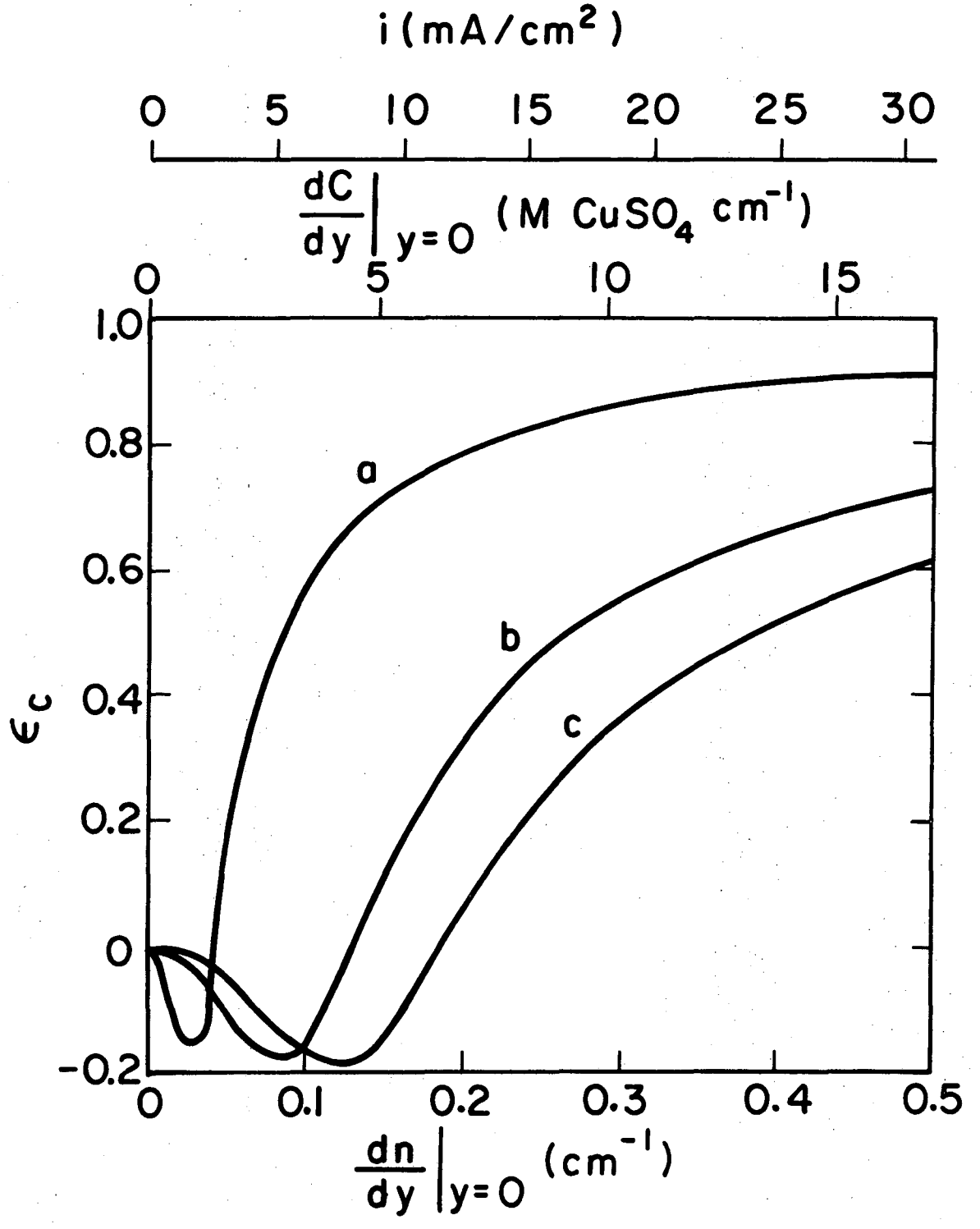
i (mA/cm²)
0
5
10
15
20
25
30
dC/dy | y=0 (M CuSO4 cm⁻¹)
0
5
10
15
1.0
0.8
0.6
0.4
0.2
0
-0.2
εc
a
b
c
0
0.1
0.2
0.3
0.4
0.5
dn/dy | y=0 (cm⁻¹)
XBL741-2166

Fig. 9

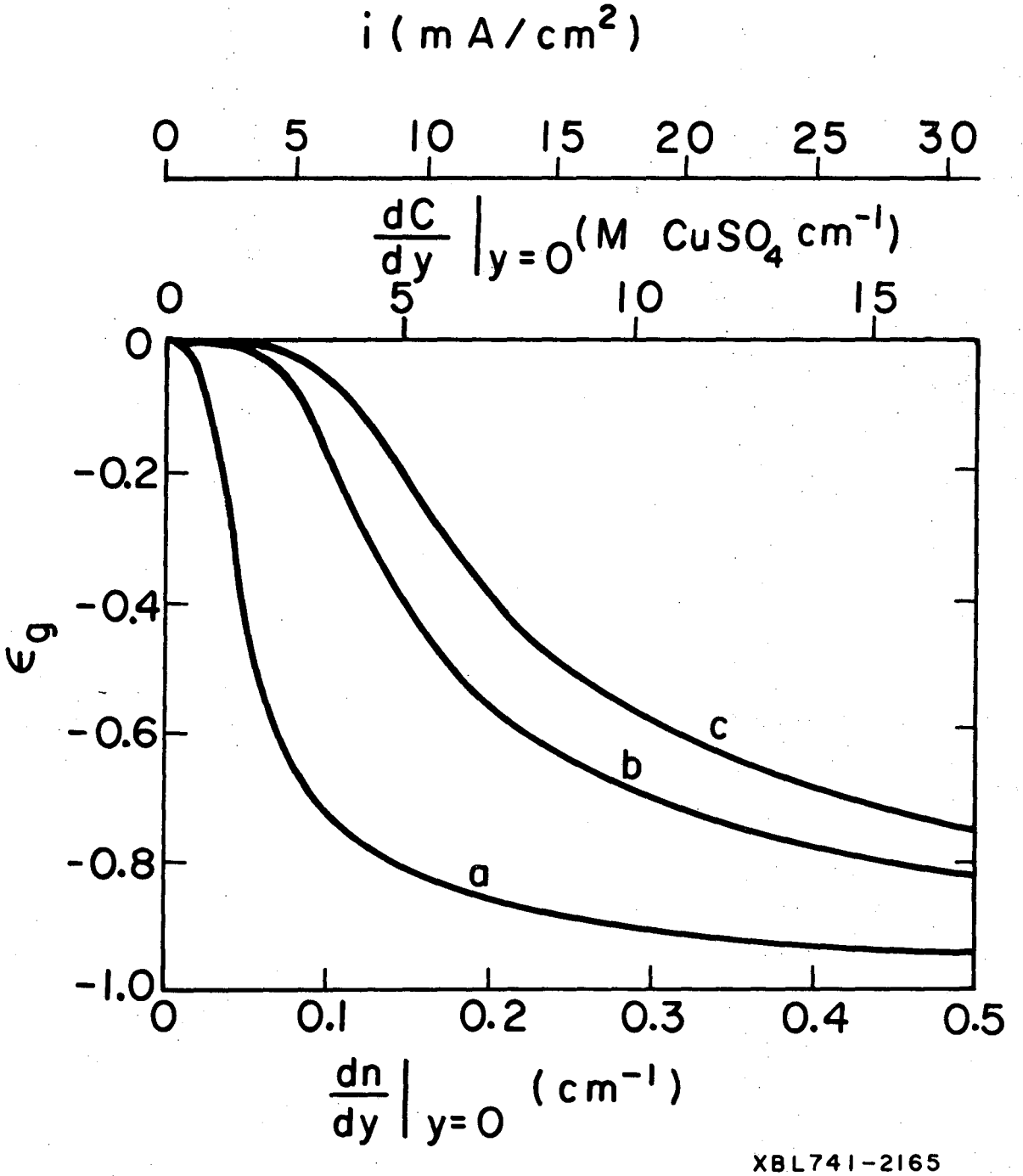

Fig. 10

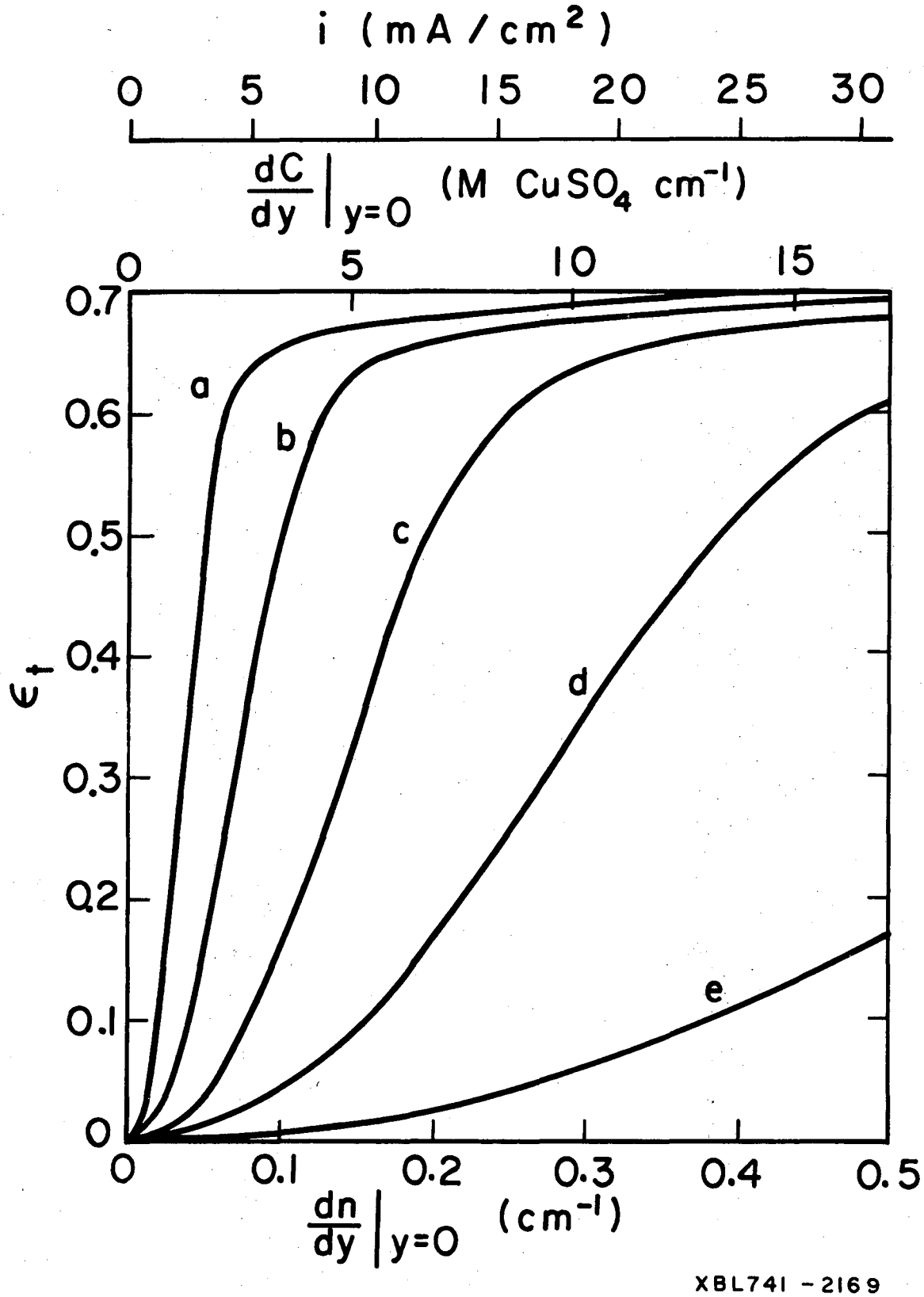
i (mA / cm²)
0
5
10
15
20
25
30
dC/dy |y=0 (M CuSO4 cm⁻¹)
0
5
10
15
0.7
0.6
0.5
0.4
0.3
0.2
0.1
0
εt
a
b
c
d
e
0
0.1
0.2
0.3
0.4
0.5
dn/dy |y=0 (cm⁻¹)
XBL741 - 2169

Fig. 11

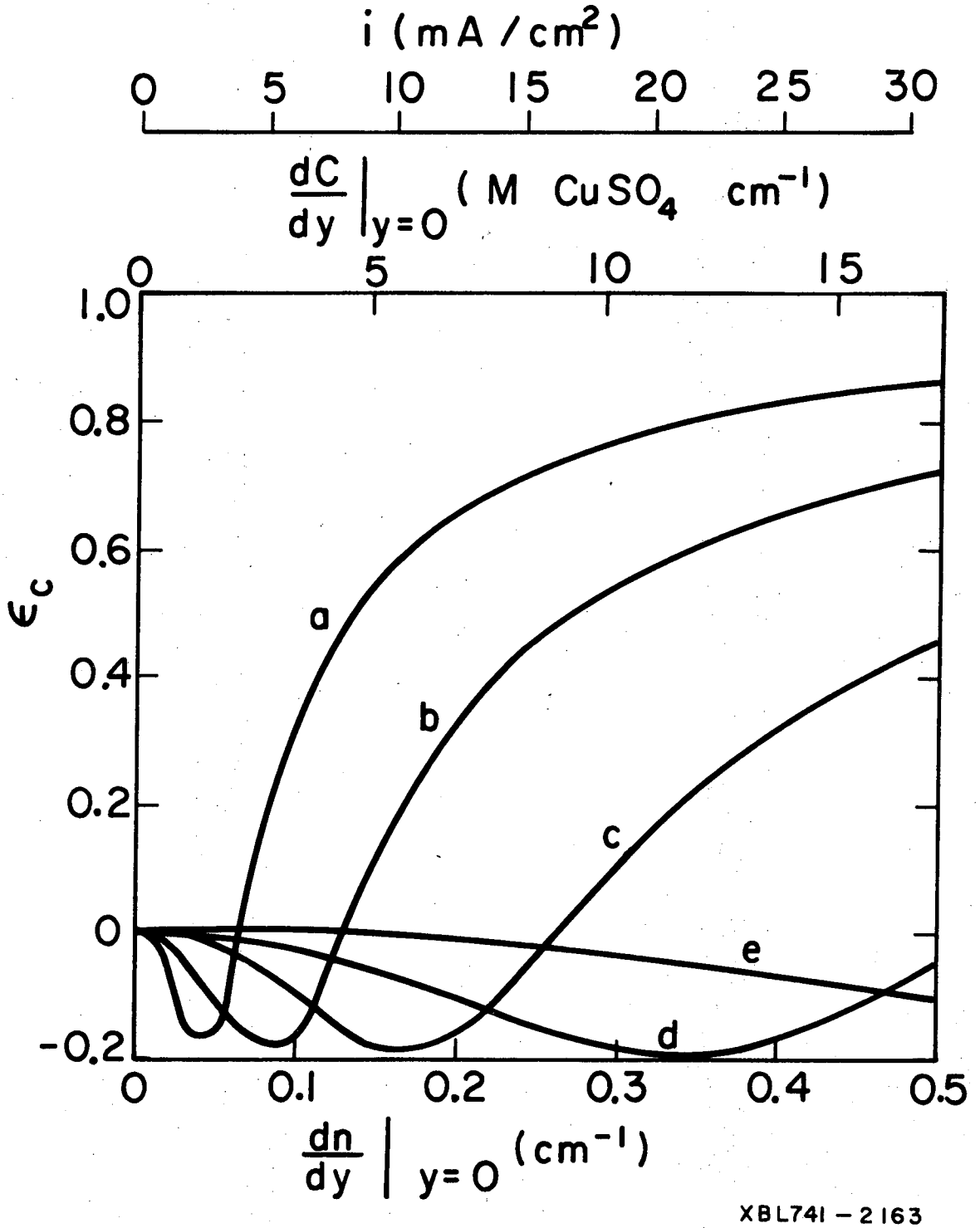

Fig. 12

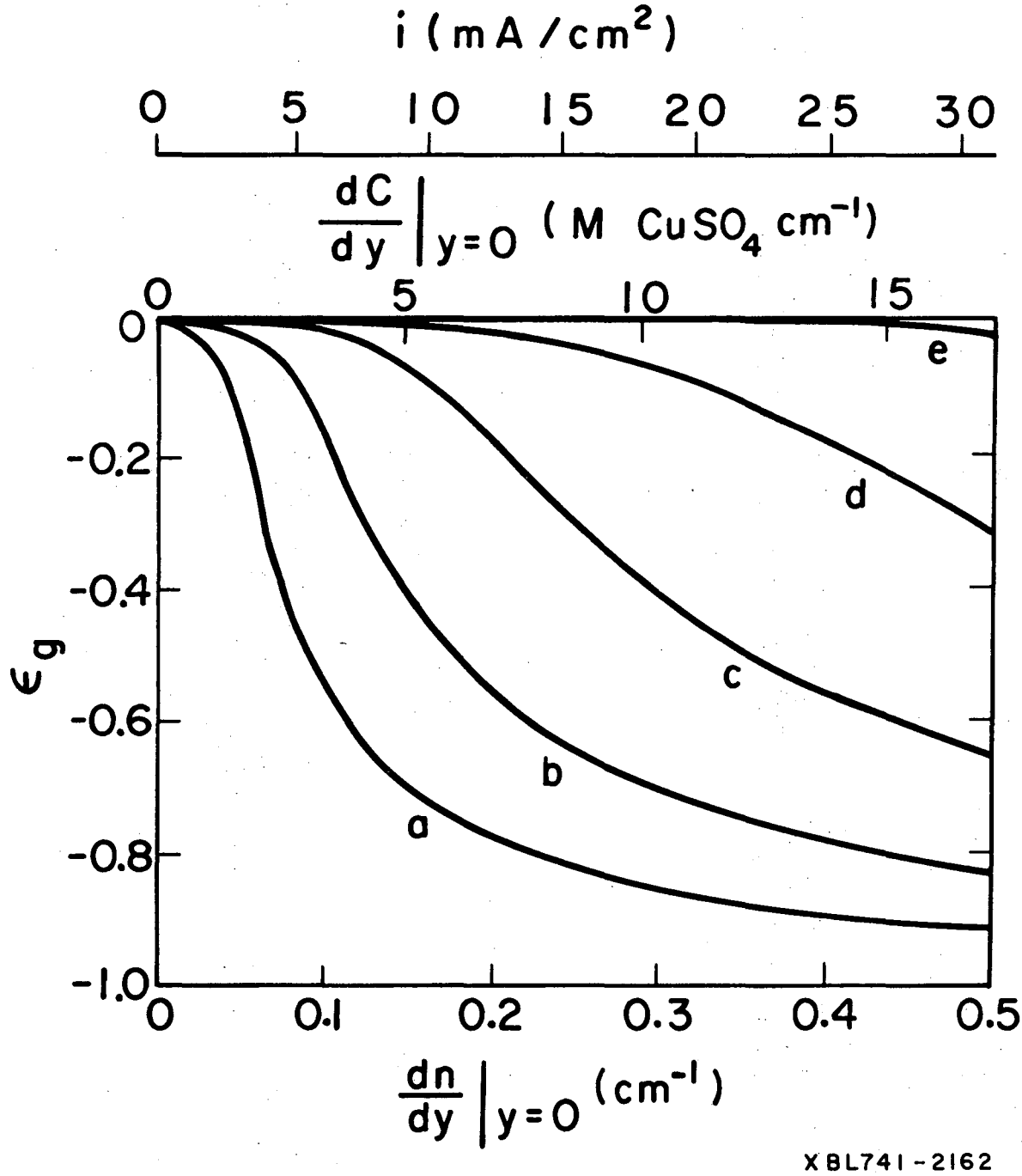
i (mA/cm²)
0
5
10
15
20
25
30
dC/dy |y=0 (M CuSO4 cm⁻¹)
0
5
10
15
εg
0
-0.2
-0.4
-0.6
-0.8
-1.0
a
b
c
d
e
0
0.1
0.2
0.3
0.4
0.5
dn/dy |y=0 (cm⁻¹)
XBL741-2162

Fig. 13

APPENDIX VI. SOLUTION OF THE CONVECTIVE-DIFFUSION EQUATION

Equations (2) and (3) in part 5.1 can be solved using a similarity variable η:

$$\eta = y\left(\frac{\beta}{9Dz}\right)^{1/3} \quad , \tag{1}$$

$$C = C_b - \gamma\left(\frac{9Dz}{\beta}\right)^{1/3} \cdot f(\eta) \quad , \tag{2}$$

where β is the interfacial velocity gradient

$$\beta = \left.\frac{\partial v}{\partial y}\right|_{y=0} \quad . \tag{3}$$

The electrolyte velocity can be approximated by $v = \beta y$ within the diffusion layer and f is a function of η only. All other terms are defined in Chapter 5. Equations (2) and (3) in part 5.1 now transform into

$$\frac{d^2 f}{d\eta^2} + 3\eta\left(\eta \frac{df}{d\eta} - f\right) = 0 \tag{4}$$

$$f = 0 \text{ as } \eta \to \infty \tag{5a}$$

$$\frac{df}{d\eta} = -1 \text{ at } \eta = 0 \quad , \tag{5b}$$

for which the solution is:

$$f(\eta) = \frac{1}{\Gamma\left(\frac{2}{3}\right)} \left(e^{-\eta^3} - 3\eta \int_{\eta}^{\infty} x e^{-x^3}\, dx\right) \quad . \tag{6}$$

The local concentration difference $\Delta C = C_b - C_s$ can be computed from Eqs. (2) and (6):

$$\Delta C(z) = \frac{\gamma}{\Gamma\left(\frac{2}{3}\right)} \left(\frac{9Dz}{\beta}\right)^{1/3} \tag{7}$$

Equation (7) can be derived directly from Eq. (113-2) on page 331 of Ref. 1.

A first approximation for the Nusselt number distribution can be obtained by substitution of the values $\beta = 6v_{avg}/h$ and $d_e = 2h$ into Eq. (7) above and Eqs. (5) and (6) in part 5.1:

$$Nu(z) = \frac{36^{1/3}}{3}\,\Gamma\left(\frac{2}{3}\right)\left(Re\ Sc\ \frac{d_e}{z}\right)^{1/3} \tag{8}$$

$$= 1.4904\left(Re\ Sc\ \frac{d_e}{z}\right)^{1/3}$$

Equation (8) corresponds to the solution of the convective-diffusion equation for uniform current distribution along infinitely wide parallel plates.

The finite cross-section of the flow channel (2.54×1.00 cm) requires the use of an average velocity gradient

$$\beta_{avg}^{1/3} = \frac{1}{w}\int_0^w \beta^{1/3}\,dx \tag{9}$$

and the hydraulic diameter of the duct

$$d_e = \frac{2hw}{h+w} \tag{10}$$

Rousar et al.[2] have tabulated correction factors that account for the variation (Eq. (9)) of the interfacial velocity gradient, and their results show that a correction factor (equal to 0.78 for h = 2.54 and w = 1.00) should multiply the constant term in Eq. (8). Therefore,

$$Nu(Z) = 1.161\left(Re\ Sc\ \frac{d_e}{z}\right)^{1/3} \tag{11}$$

Equation (11) approximates Eq. (4) in part 5.1 to within 6%.

A dimensionless concentration profile can be obtained by combining Eqs. (2), (6) and (7):

$$\theta = \frac{C - C_s}{C} = 1 - e^{-\eta^3} + 3\eta \int_{\eta}^{\infty} x e^{-x^3} \, dx \qquad (12)$$

The integral in Eq. (12) can be evaluated in terms of the Incomplete Gamma Function, tabulated in Ref. (3):

$$\int_{\eta}^{\infty} x e^{-x^3} \, dx = \frac{1}{3} \int_{\eta^3}^{\infty} t^{-1/3} \, e^{-t} \, dt \qquad (13)$$

The computed concentration profile Eq. (12) is listed in Table 1 in terms of a reduced (distance) variable $Y = \eta/1.5$, where the numerical value 1.5 was chosen to give $\theta(Y = 1) = 1.0$. Table 1 also catalogues the dimensionless concentration profile Eq. (13) in part 5.1. The latter profile corresponds to the solution[1,2] to the convective-diffusion equation for constant interfacial concentration, and inspection of Table 1 shows that the profiles are very similar.

Table 1. Dimensionless concentration profiles.

Y	θ Computed from Eq. (12) in this Appendix. Y = η/1.50	θ Computed from Eq. (13) in part 5.1 Y = y/1.70
0	0	0
0.067	0.133	0.126
0.114	0.224	0.215
0.246	0.457	0.465
0.390	0.675	0.695
0.491	0.800	0.817
0.605	0.903	0.914
0.667	0.939	0.948
0.841	0.993	0.990
1	1	1

REFERENCES

1. J. S. Newman, Electrochemical Systems (Prentice-Hall, Inc., Englewood Cliffs, N. J., 1973).

2. J. Rousar, J. Hostomsky and V. Cezner, J. Electrochem. Soc. 118, 881 (1971).

3. M. Abramowitz and J. Stegun, eds., Handbook of Mathematical Functions, National Bureau of Standards, Washington, 1964, pp. 255-262, 978-983.

TECHNICAL INFORMATION DIVISION
LAWRENCE BERKELEY LABORATORY
UNIVERSITY OF CALIFORNIA
BERKELEY, CALIFORNIA 94720